THE INFRARED EMISSION SPECTRUM
OF THE ATMOSPHERE

DISSERTATION

Presented in Partial Fulfillment of the Requirements
for the Degree Doctor of Philosophy in the
Graduate School of The Ohio State
University

By

RAYMOND WILLIAM SLOAN, A. B., M. S.

****

The Ohio State University
1955

Approved by:

Dudley Williams
Adviser
Department of Physics and Astronomy

ACKNOWLEDGMENTS

The research reported in this dissertation has been sponsored in part by the Geophysics Research Directorate, Air Forces Cambridge Research Center, Air Research and Development Command, under Contract AF19(122)-65 with the Ohio State University Research Foundation. The author served in the capacity of a research associate while doing the experimental work covered by this dissertation.

Greatest appreciation is expressed to Professor Dudley Williams for his guidance and suggestions during the investigation and to Dr. John H. Shaw for his suggestions and contributions. It is a pleasure to acknowledge the assistance of Daniel Elleman, David Althoen and Robert Hansen in various parts of the work. Appreciation is also expressed to Mr. Carl McWhirt and associates of the Department of Physics and Astronomy Machine Shop for their splendid cooperation in building various special parts for the experimental work.

TABLE OF CONTENTS

LIST OF TABLES

LIST OF FIGURES

THE INFRARED EMISSION SPECTRUM OF THE ATMOSPHERE

I. Introduction

Among the major radiative factors governing the "heat balance" at the earth's surface are: (1) direct solar radiation reaching the earth's surface after penetration of the atmosphere, (2) other radiation reaching the earth from the sky, and (3) radiation leaving the earth's surface. The present study is concerned with the second of these factors. The sky radiation includes (a) radiation from extra-terrestrial sources including stars, moon, planets, and the dust particles causing zodiacal light, (b) radiation due to electronic excitation of atoms and molecules in the atmosphere, (c) solar radiation scattered during its passage through the atmosphere, and (d) "thermal" radiation from the atmosphere. The contributions of (a) and (b) to the heat balance are negligible as compared with the contributions of (c) and (d).

The present report gives a description of apparatus for measuring the infrared radiation in the wavelength interval between 4 μ and 15.5 μ reaching the earth's surface from the sky and gives the results obtained during the year 1954. At night the radiation is almost entirely "thermal" radiation from the atmosphere. During daylight hours the observed radiation also includes scattered infrared radiation of solar origin. With the apparatus described, it is possible to obtain quantitative measurements of sky radiation in various spectral regions in the infrared. This has been done under various atmospheric conditions.

II. Earlier Studies

There have been many investigations of undispersed nocturnal sky radiation.[1] The methods employed have usually involved a measurement of the temperature T^S attained by a blackened object such as a thermometer bulb or thermocouple junction exposed to the sky and shielded by mirrors from ground surface radiation. When thermal equilibrium is attained, the intensity R^S of the sky radiation can be obtained from the relation $R^S = \sigma(T^S)^4$. Such measurements give no information concerning the spectral distribution of the sky radiation but only an effective sky radiation temperature T^S. If T^S is to be a measure of thermal radiation from the atmosphere, measurements must be made at night in order to avoid the effects of direct and scattered solar radiation.

A refinement of this type of measurement was made by Strong,[2] who employed reststrahlen techniques to obtain effective sky radiation temperatures T^S_λ for various wavelength intervals between 8 μ and 12 μ. Strong was thus able to make a rough determination of the spectral distribution of sky radiation in this portion of the infrared. Strong's reststrahlen system had a relatively small field of view so that T^S_λ for various small portions of the sky could be determined. In determining T^S_λ, laboratory blackbodies at 100° C and 0° C were used for calibration purposes.

---

[1] Compendium of Meteorology, Am. Met. Soc., Boston, Mass., 34-49 (1951).

[2] J. Strong, J. Frank. Inst. 232, 1 (1941).
J. Strong, J. Opt. Soc. Amer. 29, 520 (1939).

Studies of dispersed sky radiation were made by Adel,[3] who used his measurements to obtain effective radiation temperatures for ozone and other atmospheric gases.* In Adel's work a conventional prism spectrograph with an opaque "chopper" was employed to obtain the "emission spectrum of the earth," which was actually a spectrum representing the net exchange of radiation between the spectrograph and the sky. As the thermocouple and other parts of the spectrograph were at 300° K, the observed spectrum represented the emission spectrum of a blackbody at 300° K as modified by the downcoming radiation from the sky. By comparison of such a spectrum with the "lunar spectrum," which represented the net exchange of radiation between the spectrograph and the atmosphere plus the radiation reaching the spectrograph from the moon, Adel was able to make estimates of the effective radiation temperatures of various atmospheric gases by assuming that the gases were in radiative equilibrium.

Butler[4] at the Naval Research Laboratory made extensive spectroscopic studies of the radiative exchange between a thermocouple and the sky under various atmospheric conditions during day and night. Beam interruption techniques were not employed in the prism spectrograph used by Butler. Absolute calibration of the spectrograph and its

---

[3] A. Adel, Astrophys. J. 103, 19 (1946).
A. Adel, Astrophys. J. 105, 406 (1947).
A. Adel, Cent. Proc. Roy. Meteor. Soc., London, p. 5 (1950).
A. Adel, "Effective Radiation Temperatures of the Ozoneosphere Over New Mexico," Geophysical Research Papers No. 2 (1949).

[4] C. P. Butler, "On the Exchange of Radiant Energy Between the Earth and Sky," NRL Report 3984, June 11, 1952.

*The term "effective radiation temperature" is used in a somewhat different sense by Adel.

associated amplifiers and recorder was made in terms of two laboratory blackbodies at different temperatures; the two sources were a steam-heated blackened cone and a piece of melting ice, which were used to approximate blackbodies at 100° and 0° C.

Butler's work gave quantitative information on the exchange of radiation between the earth (thermocouple) and the sky. The spectra, however, were obtained under conditions giving rather low resolution. The present work was undertaken with a view to obtaining a sky spectrum with a spectrograph giving higher resolution and to developing a more convenient system that would provide for the direct measurement of sky radiation.

III. Apparatus and Experimental Procedures

In the methods previously employed for absolute measurements of sky radiation it was necessary to keep the temperature of the detecting system constant during observation periods and to record radiation from blackbodies at two or more known temperatures. It is desirable to incorporate equivalent basic calibration information of this type into the measuring system and also to develop an instrument which detects incident sky radiation rather than the net transfer of radiation between the sky and the receiver. In order to eliminate the effects of thermocouple zero drift, it is advantageous to employ interrupted beam techniques.

Some of these desirable features have been incorporated in the instrument shown schematically in Figure 1. A Perkin-Elmer single-pass spectrograph S, equipped with a sodium-chloride prism, is used

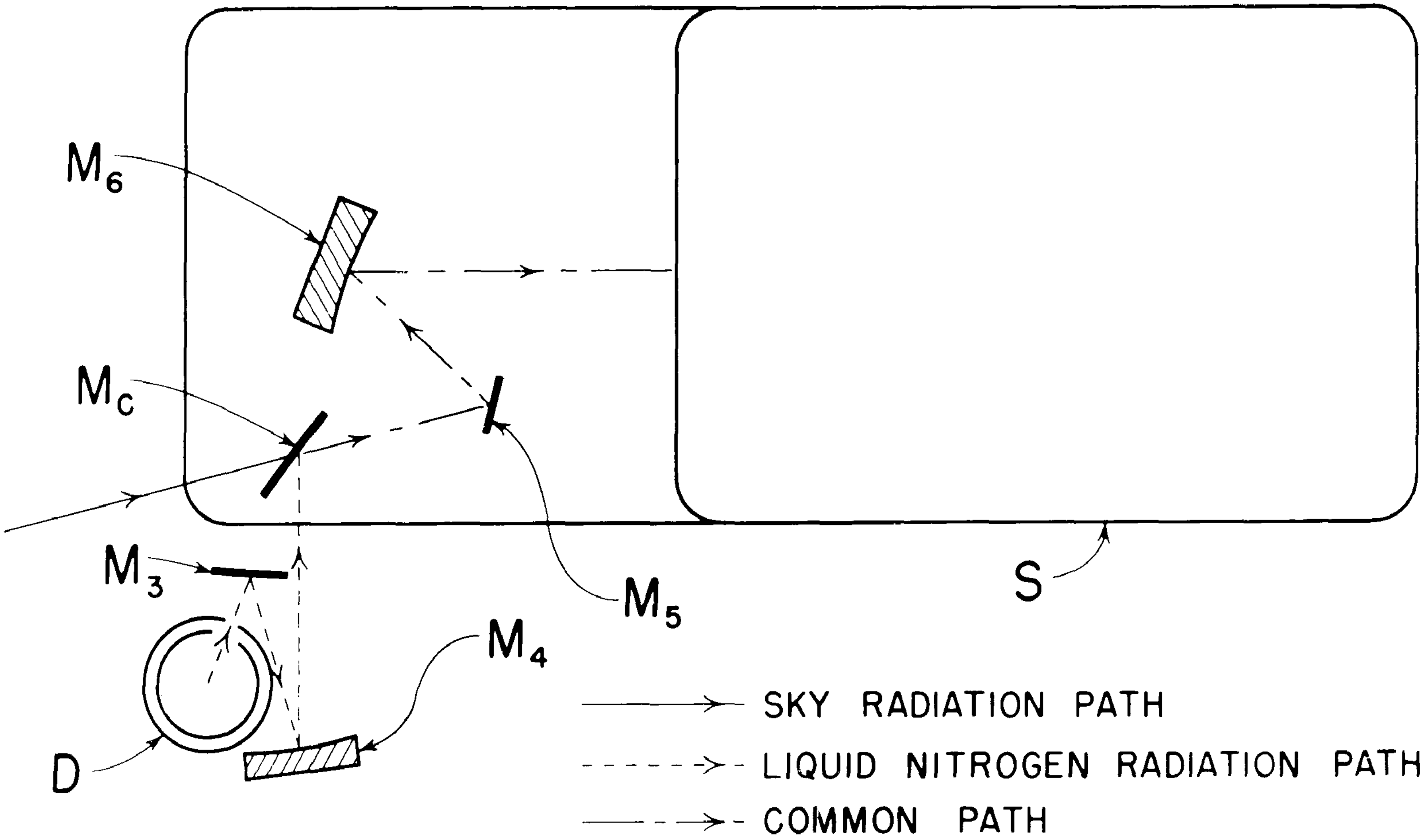

Figure 1. Optical arrangement for automatic comparison of sky spectrum with the spectrum of a "blackbody" at liquid nitrogen temperatures.

for dispersing the radiation. The usual opaque radiation "chopper" is replaced by a chopper with a mirror surface M_c. During one half the chopper rotation cycle sky radiation is admitted to the spectrograph slit after reflection by mirrors M_5 and M_6; during the second half cycle, radiation from a blackbody D at a know temperature is admitted to the spectrograph slit after reflection by mirrors M_3, M_4, M_c, M_5 and M_6. Thus, the signal produced in the thermocouple is proportional to the difference in the radiation flux incident on the thermocouple during the two half cycles. Since the radiation flux from the blackbody D is known, one of the standard radiation references is established by the use of the mirror chopper.

It is desirable to measure the intensity of the sky radiation directly; since the signal from the thermocouple is proportional to the difference between the incident flux of the sky radiation and the blackbody radiation flux at the thermocouple, the desired response to sky radiation can be obtained provided the intensity of the blackbody radiation can be reduced to "zero." This is accomplished in practice by using a blackbody at liquid-nitrogen temperature, since with the present detecting system the near infrared flux from such a source cannot be distinguished from that of a blackbody at absolute zero.*

The actual source used as a low temperature blackbody is a one-liter, open-mouthed Dewar vessel with a blackened cone at the bottom. The level of the liquid nitrogen is kept at a distance of one or two inches from the top of the vessel, and a region close to the surface

---

*R_λ for the liquid nitrogen blackbody is 0.3% R_λ for a 0° C blackbody at 15 microns and still less at shorter wavelengths.

of the refrigerant is imaged at the spectrograph slit. The radiation reaching the spectrograph from the blackbody D is not pure blackbody radiation, since the chopper blade is not a perfect reflector and therefore has a weak emission spectrum and since the CO_2 and water vapor in the laboratory air between D and M_c emit radiation some of which is "chopped" and reaches the entrance slit. The emissivity of the chopper blade is very small ($\varepsilon \cong 0.02$) and does not introduce serious errors. The radiation from laboratory air between D and M_c is compensated by similar radiation from an air column of equal length in the path of sky radiation through the laboratory. The assumption that the liquid-nitrogen blackbody has "zero" radiant flux introduces errors no larger than four per cent of the radiant flux from a blackbody at room temperature in spectral regions remote from the strong CO_2 and H_2O vibration-rotation bands. Part of this error is caused by reflection of "room radiation" at the surface of the liquid nitrogen.

Sky radiation is directed to the spectrograph by the mirror system shown in Figure 2. Radiation incident on a large plane mirror M_1 is reflected to an off-axis parabaloidal mirror M_2, which produces an image at the chopper position. The radiation passing the chopper is reflected by plane mirror M_5 to M_6, which forms an image at the entrance slit of the spectrograph as shown in Figure 1.

Plane mirror M_1 can be rotated about the axis indicated in Figure 2. This rotation provides for a study of sky radiation from the zenith and from small portions of the sky at various zenith distances. Zenith distances as large as 75° toward the east and 84° toward the west can be attained; these correspond to approximately

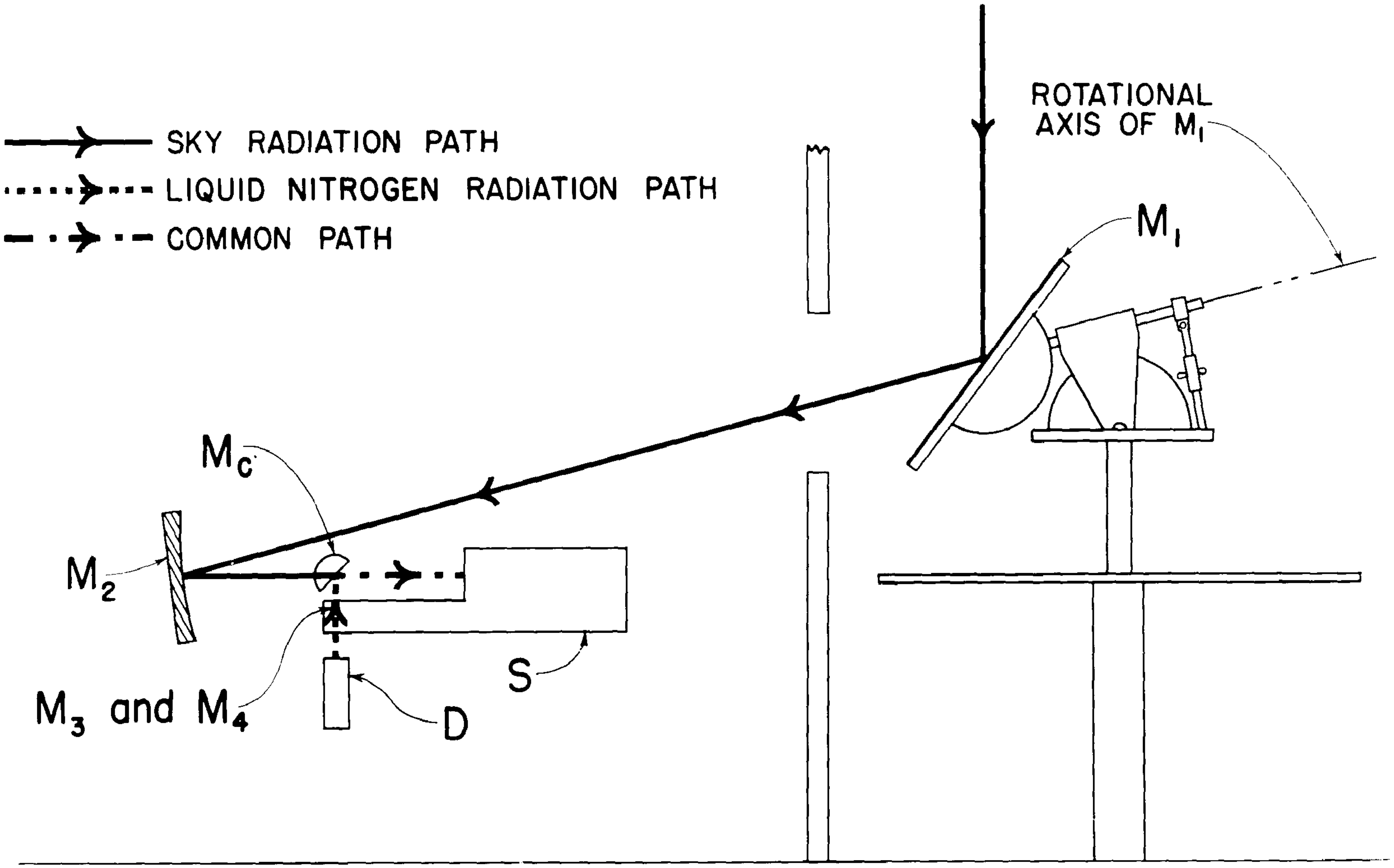

Figure 2. Optical arrangement for directing sky radiation to the spectrograph.

4 to 10 air masses, respectively.

The outside mirror M_1 was the only mirror exposed to direct solar radiation and was not shaded during the day. This mirror was tilted toward the north and the data revealed no evidence of scattering of direct solar radiation by this mirror surface in the wavelength region considered here. It is believed, however, that shading of this mirror from solar radiation for future experiments would be a wise precaution and would permit accurate measurements of small-angle scattering of solar radiation in the atmosphere. This small-angle scattering of solar radiation was not investigated in the present study.

As a result of the temperature difference between the air inside and outside the laboratory, the large laboratory air path traversed by the sky radiation did introduce some error into the measurements for spectral regions near the strong CO_2 and H_2O vapor absorption bands. Fortunately the sky radiation in these spectral regions was found to resemble that of a blackbody at ground level air temperature and appropriate corrections could be made. The observed records were corrected whenever the temperature difference between indoor and outdoor air was large.

Another point worthy of consideration involves the mirror chopper. Close examination reveals that the straight edge of this mirror may direct spurious radiation from the laboratory to the spectrograph during a small portion of the half-cycle during which sky radiation enters the spectrograph. This occurs as a result of the fact that the angle between the mirror chopper and the sky radiation path is not 90° and as a result of the finite thickness of the mirror chopper.

Calculations reveal that the time interval during which this stray radiation reaches the spectrograph is less than one percent of the period of a chopper rotation. If one assumes that the stray radiation is blackbody radiation at room temperature, the effect of the brief "flash" of stray radiation during each chopper cycle will be at most only two percent of that due to the radiation from the 300° K comparison laboratory blackbody discussed below, since the stray radiation is admitted to the spectrograph during a time interval only one-fiftieth as great as that during which desired radiation is admitted.

It is extremely important that mirrors M_1, M_2, M_3, M_4 and M_c be kept clean and freshly aluminized to minimize emission of radiation from them which can influence the recorded spectra. The sky radiation and the radiation from the liquid-nitrogen blackbody experience the same number of reflections except for one additional reflection of the latter at the mirror chopper M_c.

As described above, the liquid-nitrogen blackbody provides one standard source of radiation. It is necessary to employ at least one additional standard source. In the present instrument a laboratory blackbody at room temperature is used at frequent intervals during each observation day. The radiation from this blackbody is directed by two mirrors through the chopper into the spectrograph along the path normally traversed by the sky radiation.

Figure 3 is a block diagram of the detecting and recording system used. The 13 cps signal from the thermocouple was amplified by the preamplifier located close to the thermocouple. The resulting signal was then passed to the amplifier (Perkin-Elmer Model 81), which

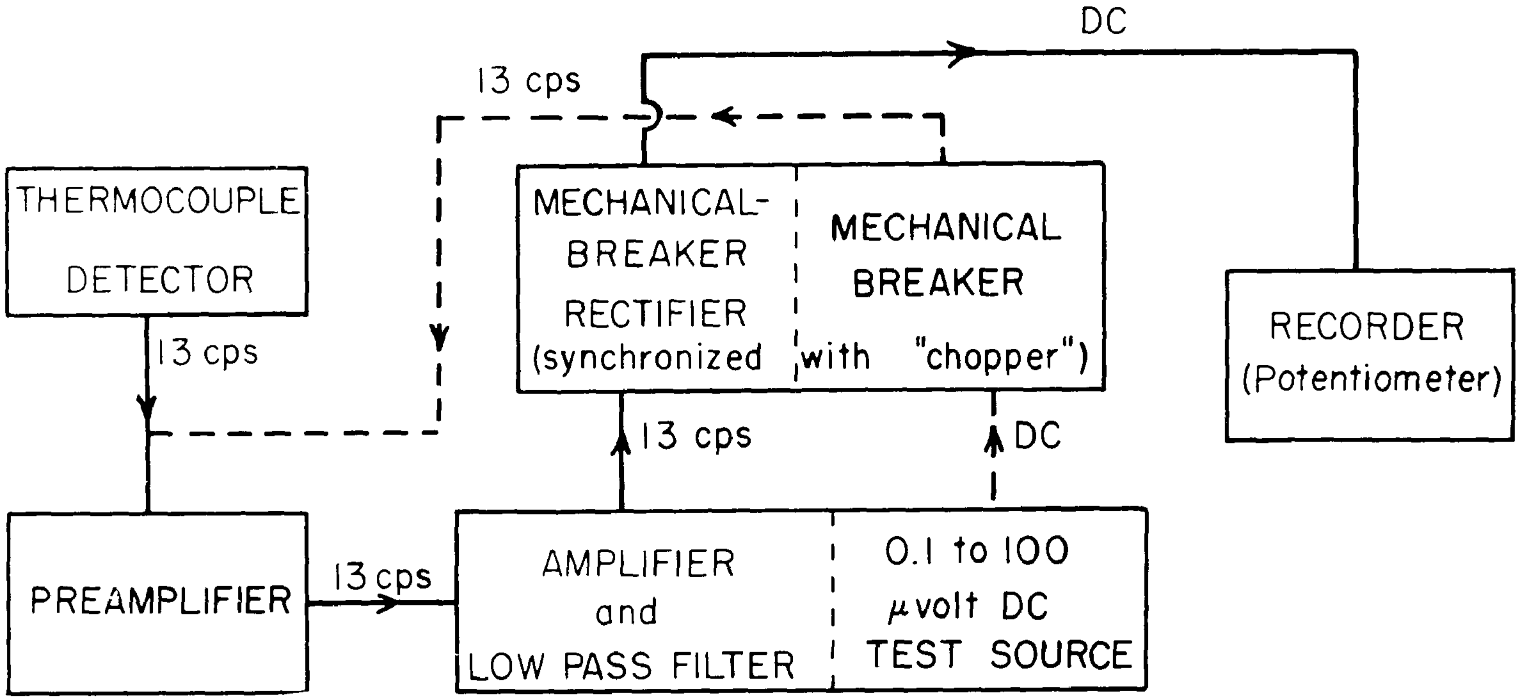

DETECTING AND AMPLIFYING SYSTEM

Figure 3. Schematic diagram of the detecting and amplifying system.

increased the signal level to the order of 10 millivolts or less. This 13 cps signal was then rectified by the mechanical-breaker, full-wave rectifier which was synchronized with the radiation "chopper." The DC signal produced was then used to actuate a Leeds and Northrup potentiometer-type recorder. A 0.1 to 100 microvolt DC test source was provided in the amplifier unit. This test signal, when used, was converted to 13 cps by the mechanical breaker synchronized with the radiation chopper and was then led to the input stage of the preamplifier. The time constant of the total system, preamplifier to recorder, was about two seconds.

The laboratory blackbody illustrated in Figure 4 consists of a black anodized aluminum tube, twelve inches long and three inches in diameter. The bottom of this tube is sealed by an inverted circular cone C of black anodized aluminum with an apex angle of about 75 degrees. A brass water jacket J encloses the sides and bottom of the tube. A means of circulating the water to heat or cool the tube is provided. Two thermometer wells W extend to convenient depths in the water jacket and two iron-constantan thermocouples (not shown) permit temperature measurements of the inside and outside surfaces of the aluminum tube. A small rectangular opening O at the end of the tube can be imaged at the spectrograph slit as described above. The nearly complete enclosure of the blackbody tube and the high thermal capacity of the water in the jacket assist in stabilizing the temperature and hence the radiation of the laboratory blackbody.

It should be noted that the angular aperture of the entire instrument is limited by the optical system of the spectrograph itself.

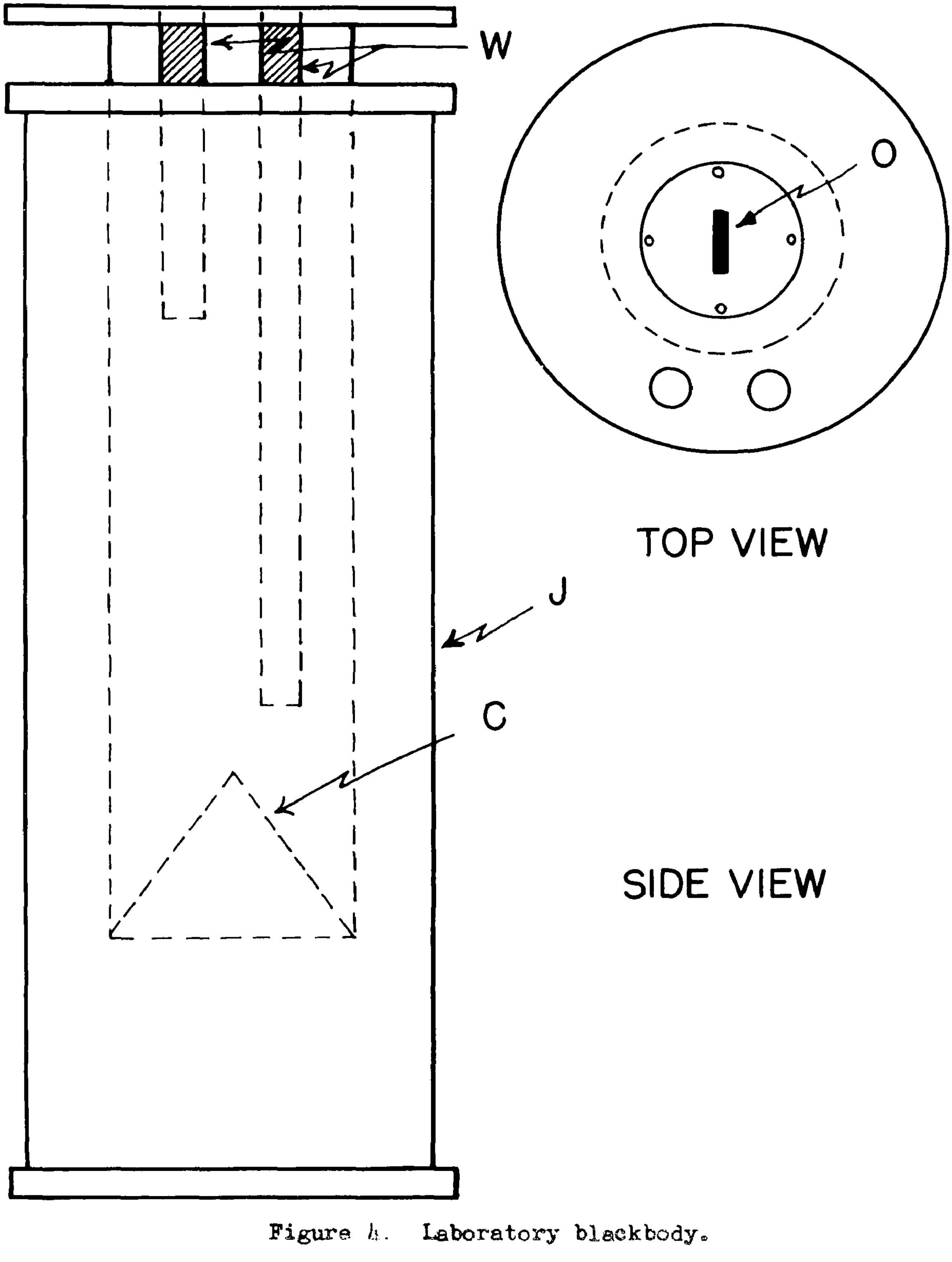

Figure 4. Laboratory blackbody.

All external mirrors are sufficiently large to fill the spectrograph collimator. Thus, the effective aperture of the instrument is the same for all radiation measurements.

The solid angle subtended by the portion of the sky imaged at the entrance slit of the spectrograph is extremely small. For the slit-width employed in most of the work this solid angle is approximately 5×10^{-6} steradians. In the long dimension of the slit, the angle subtended was of the order of 10^{-2} radians or approximately 0.6 degrees.

Photographs of the apparatus are shown in Figures 5 through 7. Figure 5 shows the mount for mirror M_1 located outside the laboratory building. The axis of rotation is visible in the photograph. Protective covers were provided for the mirror and mirror mount when the instrument was not in use, and a heater was employed in cold weather to prevent condensation on the mirror. The mirror was cleaned with a mild detergent at one-week intervals. Dust particles were removed each day by means of a dry nitrogen stream. Mirror M_1 was re-aluminized at intervals of approximately three months.

Figure 6 gives a view of the instrument located inside the laboratory. The black line shows the general path of the sky radiation to the position of the mirror chopper. The off-axis parabaloidal mirror M_2, indicated in Figure 2, is obscured by the black box in the foreground and is noted by the black broken lines. The black box contained provisions for hot or cold water which could be circulated through the water jacket of the laboratory blackbody located to the immediate left of the spectrograph. Beneath the spectrograph is the thermocouple amplifier. On the extreme right is the recorder, beside which is the

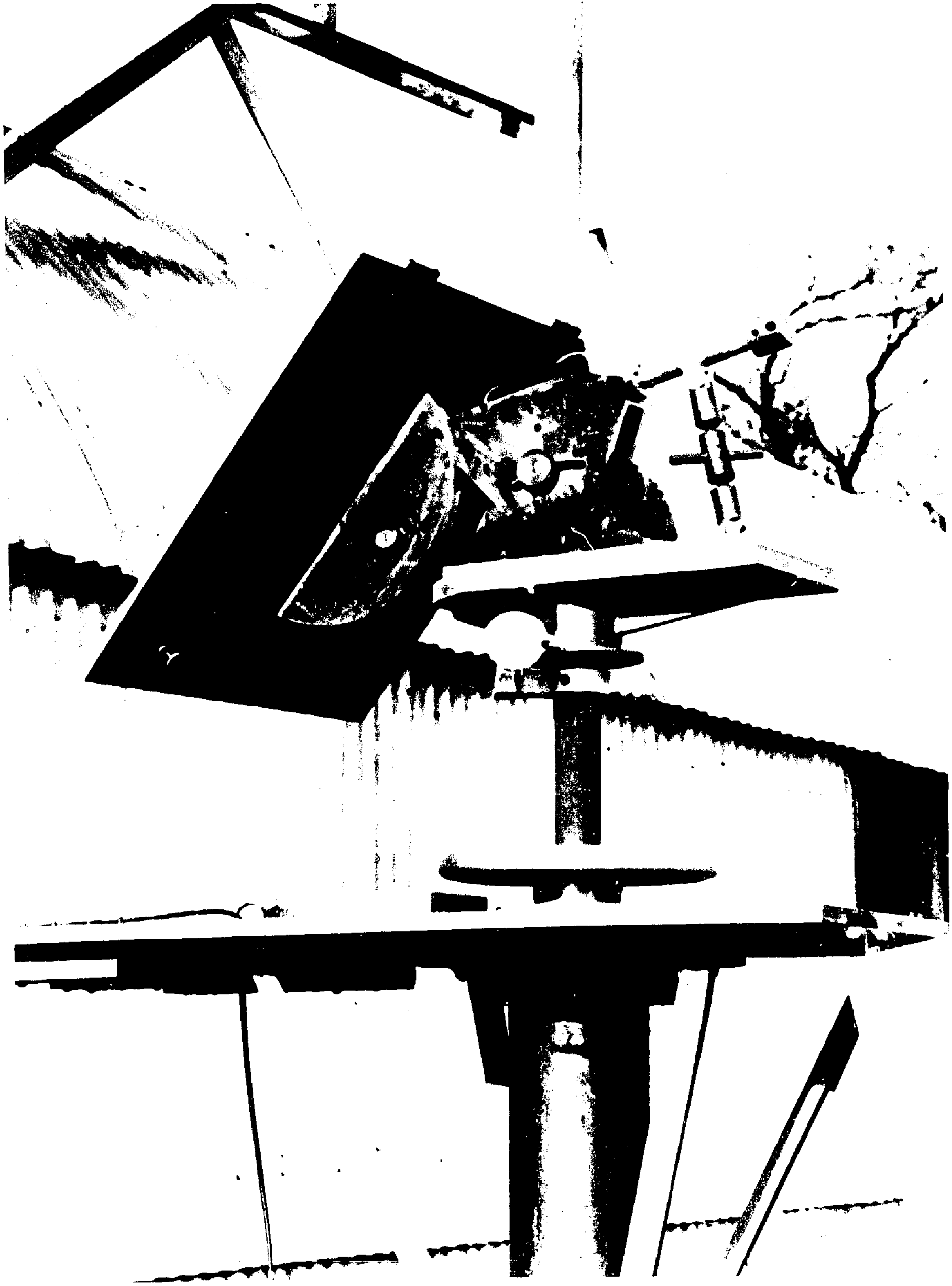

Figure 5. Outside mirror mount.

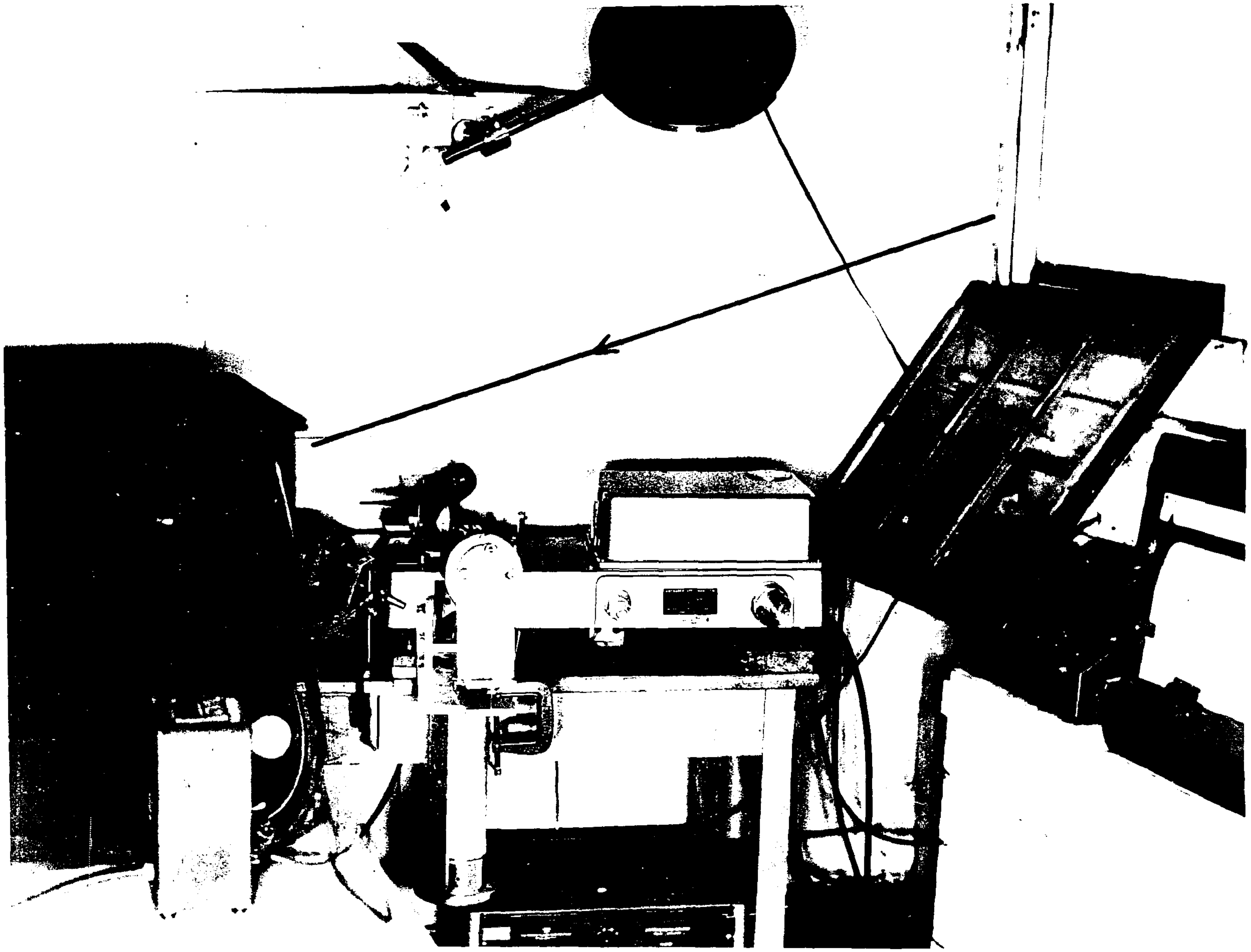

Figure 6. Instruments in the laboratory

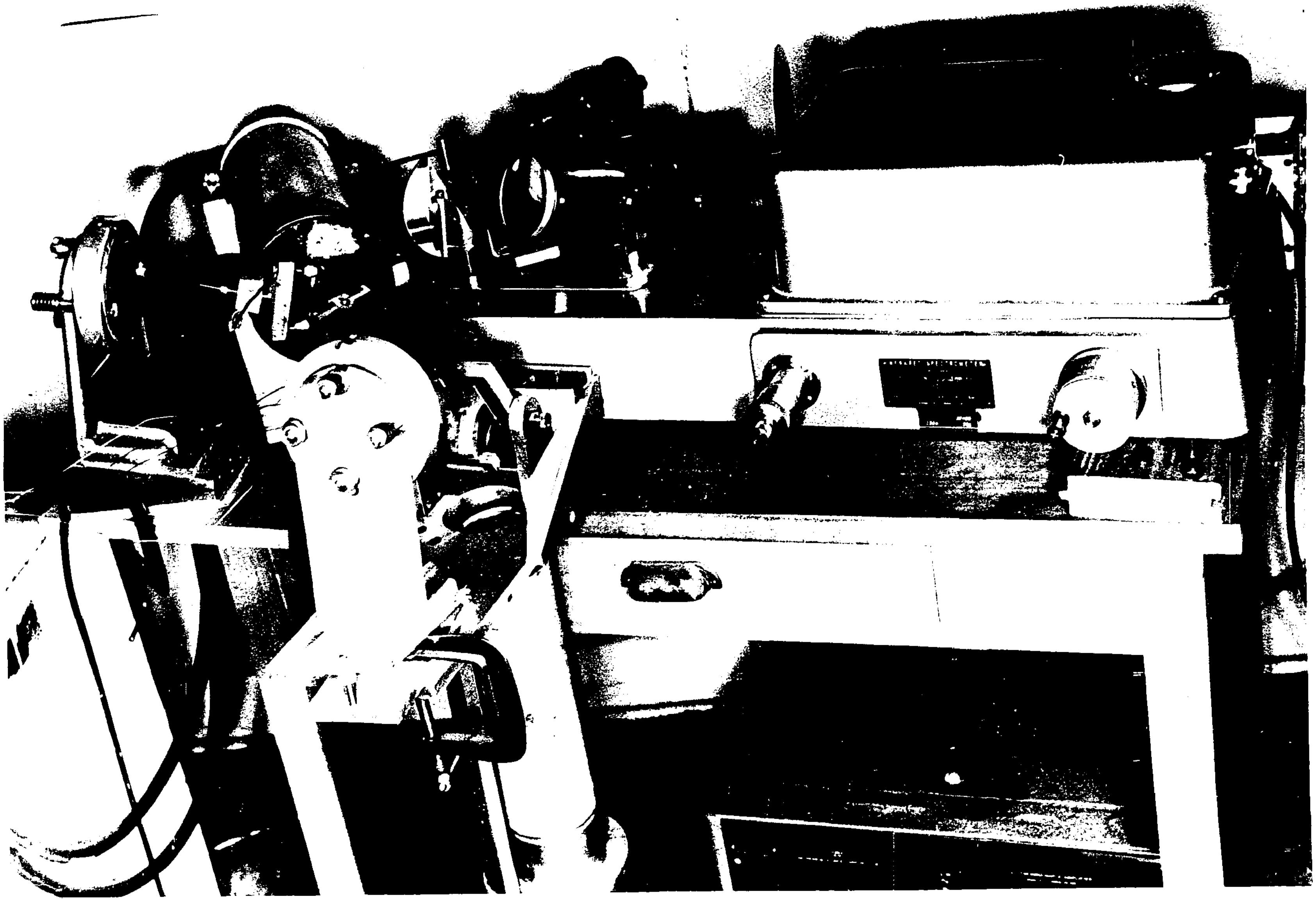

Figure 7. Spectrograph with modifications

wavelength-drive control box for the spectrograph. Above the spectrograph is a circular plane mirror which, when lowered into the path normally traversed by the sky radiation, was used to direct solar radiation from a coelostat to the spectrograph.

A close-up view of the spectrograph and associated equipment is given in Figure 7. The mirror at the left is the spherical focusing mirror for the laboratory blackbody radiation and is shown in position for the recording of this radiation. This mirror mount is hinged at the far side to permit alternate recording of sky radiation and laboratory blackbody radiation with minimum adjustment between recordings. The liquid-nitrogen blackbody is at the left end and in front of the spectrograph.

IV. Typical Spectra

Typical zenith sky spectra in the region 3 to 15.5 μ are shown in Figure 8 along with a solar spectrum included for comparison. In obtaining all the data presented in this figure, the spectrograph slit-width and scanning rate were kept constant; the same is true for the amplifier gain setting and time constants, except in the case of the comparison solar spectrum, for which the gain setting had to be reduced. In obtaining the solar spectrum, it was necessary to employ a glass chopper to minimize recorder deflections due to the scattering of shorter wavelength radiation (less than 3 μ) inside the spectrograph. The scanning time for each spectrum shown was approximately fifteen minutes.

The well known atmospheric CO_2 absorption bands at 15 μ and

Figure 8. Typical zenith sky spectra with a solar spectrum for comparison. The dashed curve above each tracing was obtained with a laboratory blackbody of temperature T_B. The "ground temperature" T_o was measured by automatic recording in a standard screen. Water vapor concentrations (g/m^3) six feet above ground level have the following values for various parts of the figure: (b) 8.0, (c) 8.4, (d) 4.0, (e) 15.2 and (f) 19.1.

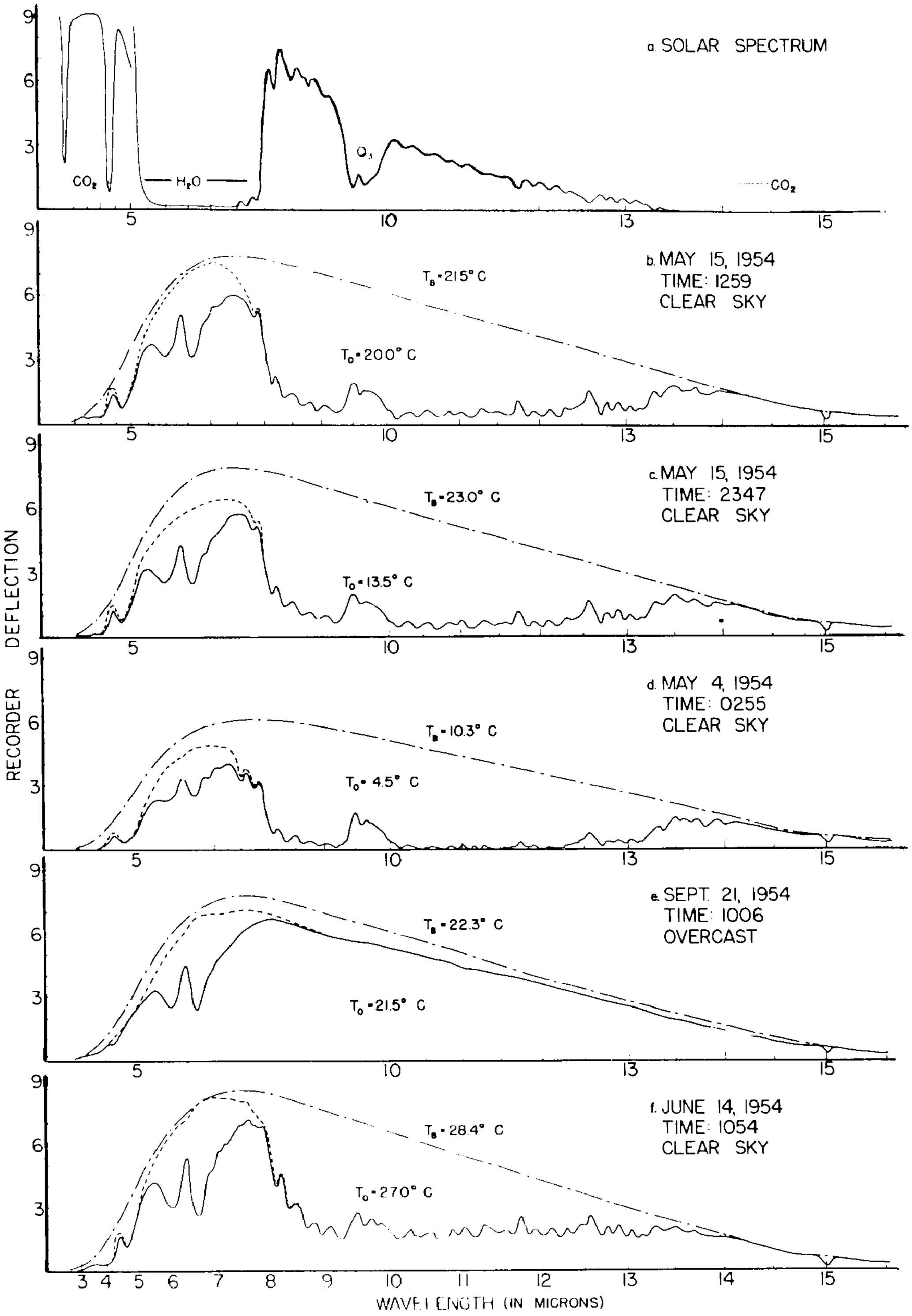

Figure 8. Typical zenith sky spectra with a solar spectrum for comparison.

4.3 μ, the water vapor absorption band at 6.3 μ, and the ozone absorption band at 9.6 μ appear as deflection minima in the solar spectrum and are labeled in Figure 8(a). The additional strong band at 2.7 μ is caused by overlapping absorption bands of CO_2 and water vapor. Most of the small deflection minima appearing in the 10 to 14 μ region of the solar spectrum are produced by groups of pure rotational absorption lines of water vapor, while those in the 7 to 9 μ region are due to rotational lines associated with the 6.3 μ vibration-rotation band. Comparison with the high-dispersion studies of Benedict, Shaw, and Claassen[5] providesa basis for this identification.

The tracing shown in Figure 8(b) represents the zenith sky spectrum as observed on a clear day of moderate humidity with ground-level air temperature $T_o = 20.0^o$ C. The topmost curve in this part of the figure represents the spectrum of a blackbody at temperature $T_B = 21.5^o$ C corrected for absorption by CO_2 and H_2O vapor between the chopper and the detector. The dotted curve just above the tracing of the sky spectrum represents an attempt to make a similar correction for CO_2 and water vapor absorption, the assumption being that the sky radiation is absorbed to the same extent as the blackbody radiation in the 4.3 μ, 6.3 μ, and 15 μ regions. Scattered solar radiation of wavelengths shorter than 3 μ produce larger recorder deflections not shown in the figure.

Examination of Figure 8(b) reveals that for every strong

---

[5] W. S. Benedict, H. H. Claassen and J. H. Shaw, J. Res. Nat. Bu. Stan. 49, 91-132 (1952).

deflection maximum in the sky-radiation spectrum there is a corresponding minimum in the solar spectrum, which appears as a result of absorption by atmospheric gases. Thus, major emission bands appear in the sky spectrum at 4.3 μ, 6.3 μ, 9.6 μ, and 15 μ produced by the atmospheric gases listed above. There are a number of relatively strong emission maxima between 7 and 14 μ that are probably caused by water vapor; these emission maxima appear more prominently in the sky radiation tracing than the corresponding minima in the solar spectrum, but corresponding minima in the solar spectrum can always be found. The emission maximum at 12.6 μ is due, in part, to a weak CO_2 vibration-rotation band, which has been identified in high-dispersion solar studies;[6] there are several other CO_2 bands between 13 and 14 μ, which cause emission maxima.

Figure 8(c) gives the sky spectrum for a clear night ($T_o = 13.5^\circ$ C) and a comparison blackbody spectrum ($T_B = 23.0^\circ$ C). The marked similarity between this night sky spectrum and the day sky spectrum in Figure 3(b) is striking. There is some decrease in the intensity of the 6.3 μ water vapor emission, but the other major features remain almost unchanged. Comparison of Figures 8(b) and 8(c) shows that the only clear evidence of scattered solar radiation of wavelengths longer than 3 μ is found in the region between 3 and 4 μ.

The tracing in Figure 8(d) gives the sky spectrum observed on a cold night of low humidity. The decreased emission by water vapor in the 6.3 μ region and in the region between 8 and 13 μ is readily apparent, although emission by ozone is apparently as intense as

---

[6] J. H. Shaw, M. L. Oxholm and H. H. Claassen, Astrophys. J. 116, 554 (1952).

that shown in Figures 8(b) and (c).

The sky spectrum observed on a uniformly overcast day is shown in Figure 8(e). The "ceiling" on this day was at 500 to 700 feet above ground. The observed spectrum is almost continuous and resembles that of a blackbody. In Figure 8(f) is shown a sky spectrum obtained on a hot humid day. The increase in water vapor emission is obvious.

In Figure 9 are shown sky spectra obtained at different zenith distances on a single night. The upper portion of this figure gives a solar spectrum for comparison. In the lower part of the figure, the four sky spectra are plotted on the same wavelength and recorder-deflection scales. The sky spectrum tracing, obtained at the largest zenith distance, corresponding to an atmospheric path of 7 air masses, shows the largest recorder deflection. Below this tracing are shown tracings for other directions corresponding to 1, 3, and 5 air masses respectively. The most pronounced spectral change observed as the zenith distance is increased is the increase in sky emission in the spectral region between 8 and 14 μ.

V. Determination of Radiant Flux from the Sky

One of the important factors in a detailed study of heat balance at the earth's surface is the determination of the absolute intensity of the sky radiation in various wavelength intervals under different atmospheric conditions. Estimates of this absolute radiation intensity for the spectral range 4 to 15.5 μ can be made in fair approximation from the present measurements. It should be emphasized that for any given set of blackbody and sky spectra the slitwidth was maintained constant.

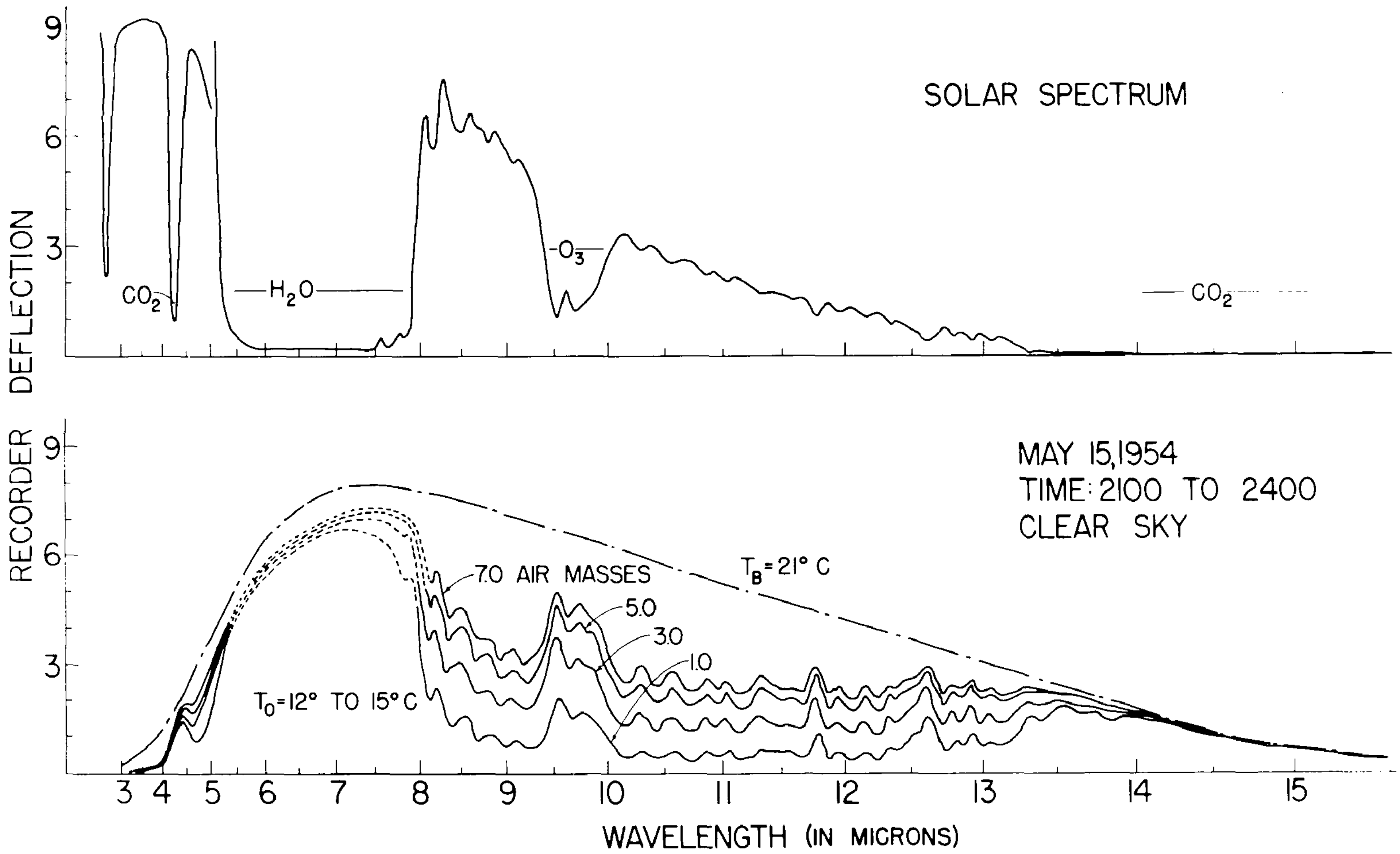

Figure 9. Sky spectra observed at various zenith distances on a clear night.

The first step is a determination of the relation between recorder deflections D_λ and spectral emissive power or radiant flux per unit wavelength interval per unit solid angle R_λ for various wavelengths. This can be done by observing the deflections $D_\lambda^B(T)$ produced by radiation from a blackbody at temperature T and by using the relation

$$D_\lambda^B(T) = K_\lambda R_\lambda^B(T) , \qquad (1)$$

where $R_\lambda^B(T)$ is the value of blackbody spectral emissive power given by the Planck radiation law and K_λ is a proportionality constant for a given slitwidth and amplifier gain. This instrumentation parameter K_λ was actually determined for three different blackbody temperatures (0° C, 20° C, and 50° C); the three values obtained were in agreement to ± 2% for spectral regions remote from the fundamental vibration-rotation bands of CO_2 and H_2O, where emission and absorption by these gases in the laboratory may influence the observed recorder deflections.

Once K_λ is determined as a function of wavelength, the spectral emissive power R_λ^S for a given part of the sky can be obtained from observed recorder deflections D_λ^S with the relation

$$R_\lambda^S = D_\lambda^S / K_\lambda . \qquad (2)$$

The spectral emissive power R_λ^S so obtained is a function of the zenith distance and atmospheric conditions. For a given zenith distance, the emissive power of the sky, R_{1-2}^S for the wavelength interval of the observed spectral range λ_1 to λ_2 can be determined by graphical integration

$$R^{s}_{1-2} = \int_{\lambda_1}^{\lambda_2} R^{s}_{\lambda}\, d\lambda . \qquad (3)$$

It should be noted that the dimensions of R^{S}_{1-2} are different from those of R^{S}_{λ}. R^{S}_{1-2} represents the radiant flux density per unit solid angle in the spectral region between λ_1 and λ_2.

VI. Procedure for Analyzing Records

The first step in the analysis of the sky spectra was the determination of the radiation calibration parameter K_{λ} at one half micron intervals from 4.0 to 15.5 µ with the use of the laboratory blackbody spectra. From these values a curve of K_{λ} as a function of λ was drawn as shown in Figure 10, and dotted curves were made over the CO_2 and H_2O vapor absorptions in an attempt to extrapolate to vacuum conditions within the spectrograph. This extrapolation was transferred to each laboratory blackbody spectrum with the aid of equation (1) and was then transferred to each sky spectrum with the assumption of equal absorption for sky and blackbody radiation. This extrapolation permitted the observer to follow changes in absorption by CO_2 and H_2O vapor in the instrument and afforded a K_{λ} which was relatively independent of these absorptions. It should be noted that this extrapolation could not be easily applied directly to the laboratory blackbody spectra since the deflection maximum occurred in the 6.3 µ water band region.

In the calculation of the value R^{S}_{1-2} from the sky spectrum, one may combine equations (2) and (3) to obtain

$$R^{S}_{1-2} = \int_{\lambda_1}^{\lambda_2} (D^{s}_{\lambda} / K_{\lambda})\, d\lambda . \qquad (4)$$

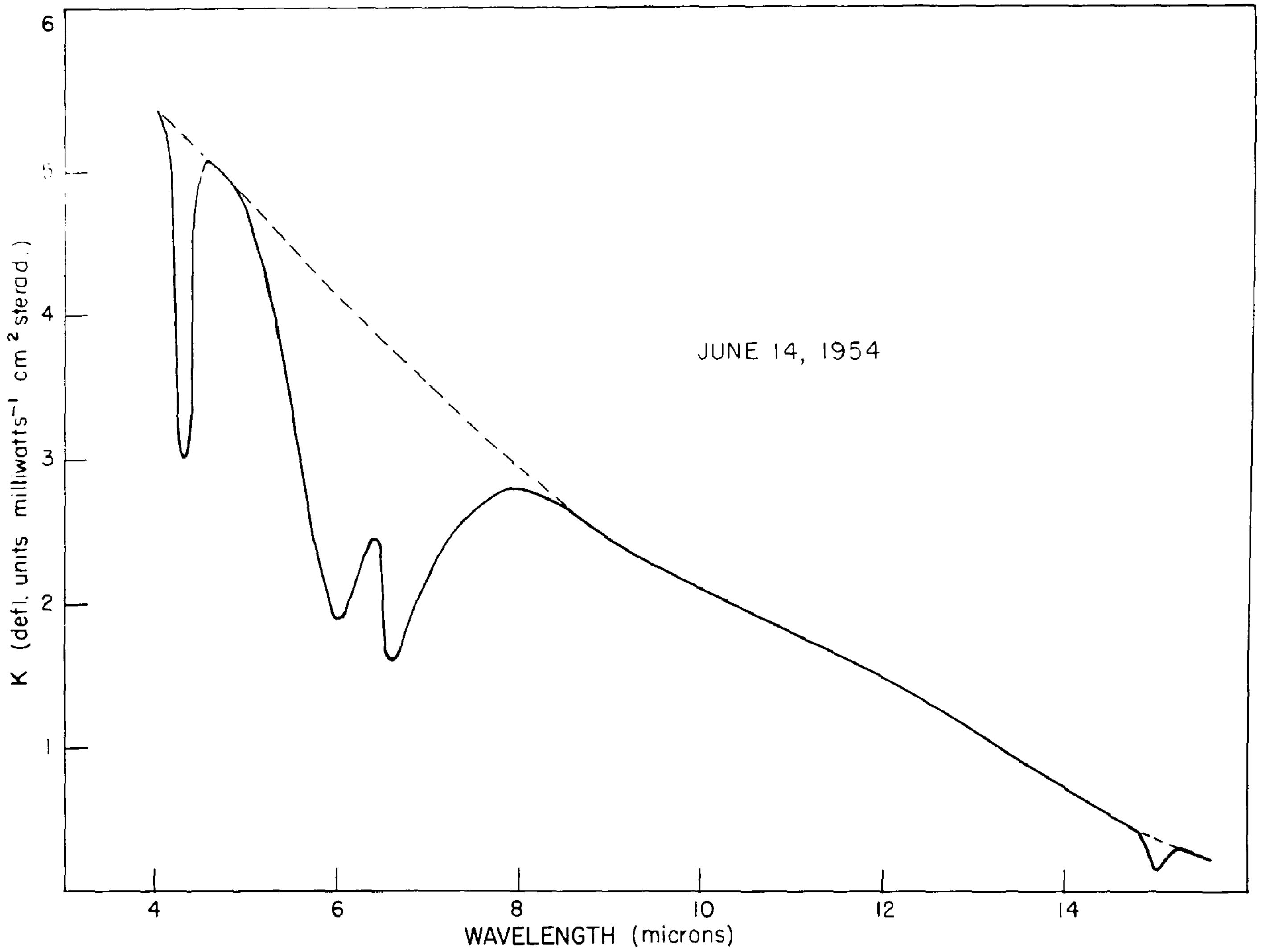

Figure 10. Radiation calibration curve for the spectrograph.

The direct integration in equation (4) from the observed sky spectrum and the curve corresponding to that in Figure 10 was not feasible without the aid of automatic computing devices. Instead the two curves were subdivided into n parts and the following relation was used:

$$R^{s}_{1-2} \approx \sum_{i=1}^{n} (\overline{D^{s}_{\lambda}})_i \, (\overline{1/K_{\lambda}})_i \, \Delta\lambda_i \, , \qquad (5)$$

where i denotes the ith interval, the barred terms are average values in the interval and $\Delta\lambda_i$ is the length of the interval. The average values were obtained by planimeter measurements. The value of n was increased by successive subdivisions until further subdivision produced no variations in the values R^{S}_{1-2} larger than those introduced by the errors of the experimental measurements. In the final analysis $\Delta\lambda_i$ was one half micron between 4.0 and 7.5 µ and between 12.0 and 15.5 µ. Between 7.5 and 12.0 µ $\Delta\lambda_i$ was one-quarter micron.

It should be noted that the value of R^{S}_{λ} given in equation (2) depends upon the slitwidth of the spectrograph and will in general differ from the true value $R^{S'}_{\lambda}$. It is desirable that R^{S}_{1-2} of equation (3) approximate the true value

$$R^{s'}_{1-2} = \int_{\lambda_1}^{\lambda_2} R^{s'}_{\lambda} \, d\lambda \, . \qquad (6)$$

In practice a given recorder deflection D_{λ} may be represented by

$$D_{\lambda} = \int_{-\infty}^{+\infty} g_{\lambda}(\alpha) \, R_{\lambda} \, d\alpha \, , \qquad (7)$$

where $g_{\lambda}(\alpha)$ is a transmission or slit function defined for each wavelength α for a given central wavelength setting λ. Note that $g_{\lambda}(\alpha)$

is dependent upon all elements of the spectrograph from the chopper to the detector, including the air in the spectrograph. Combining equation (1) and equation (7) one obtains

$$K_\lambda = \frac{\int_{-\infty}^{+\infty} g_\lambda(\alpha)\, R_\alpha^B \, d\alpha}{R_\lambda^B} . \qquad (8)$$

For the slitwidths used in the present study $g_\lambda(\alpha)$ may be assumed symmetric about λ and R_λ^B is approximately linear over the spectral slit intervals for all wavelengths longer than 7 µ. Thus R_α^B may be represented by $R_\lambda^B + k_1\,(\alpha - \lambda)$, where k_1 is a constant. Since $g_\lambda(\alpha)$ is symmetric about λ the term $k_1\,(\alpha - \lambda)\; g_\lambda(\alpha)$ yields nothing in the integration of equation (8) and one may write

$$K_\lambda = \int_{-\infty}^{+\infty} g_\lambda(\alpha)\, d\alpha . \qquad (9)$$

Substitution of

$$D_\lambda^S = \int_{-\infty}^{+\infty} g_\lambda(\alpha)\, R_\alpha^{S'}\, d\alpha \qquad (10)$$

and equation (9) in equation (4) gives the following relation for the measured value of R_{1-2}^S:

$$R_{1-2}^S = \int_{\lambda_1}^{\lambda_2} 1/K_\lambda \int_{-\infty}^{+\infty} g_\lambda(\alpha)\, R_\alpha^{S'}\, d\alpha\, d\lambda . \qquad (11)$$

A radiation calibration curve such as the one given in Figure 10, provides experimental evidence that K_λ was continuous and non-zero in the wavelength interval of the present study. It is reasonable to assume that the slit function $g_\lambda(\alpha)$ is continuous in both λ and α for all appropriate values throughout the ranges of integration of equation

(11) and that the true emissive power of the sky, $R^{S'}_{\alpha}$ is continuous at all wavelengths. It is permissible to interchange the order of integration of equation (11) to obtain

$$R^{S}_{1-2} = \int_{-\infty}^{+\infty} R^{S'}_{\alpha} \int_{\lambda_1}^{\lambda_2} [g_\lambda(\alpha)/K_\lambda]\, d\lambda\, d\alpha. \quad (12)$$

In this form a given value of the spectral emissive power $R^{S'}_{\alpha}$ is sampled by a normalized slit function integrated over the wavelength interval λ_1 to λ_2. These values are then integrated over all possible values of α. Note that $g_\lambda(\alpha)/K_\lambda$ is normalized over the limits of α by equation (9) and hence the value of the inside integral of equation (12) may be different from one.

Since the slit function has all its non-zero values in a finite interval it will suffice to perform the integrations as follows:

$$R^{S}_{1-2} = \int_{\lambda_1-\delta\lambda_1}^{\lambda_2+\delta\lambda_2} R^{S'}_{\alpha} \int_{\lambda_1}^{\lambda_2} [g_\lambda(\alpha)/K_\lambda]\, d\lambda\, d\alpha, \quad (13)$$

where $\delta\lambda_i$ is the extent of the non-zero values of $g_\lambda(\alpha)$ about λ_i.
In mwhere $\delta\lambda_i$ is the extent of the non-zero values of $g_\lambda(\alpha)$ about λ_i.
to vary only slightly with λ over a spectral interval sampled by the spectrograph since this is true for both K_λ and the spectral slitwidth. In equation (13) the inside integral, which will serve as a weight function, will have a general form indicated in Figure 11. The variation of this function from the value one in the central portion of the curve depends upon the variation of the normalized slit function over the spectral slit interval and upon the possible overlapping of

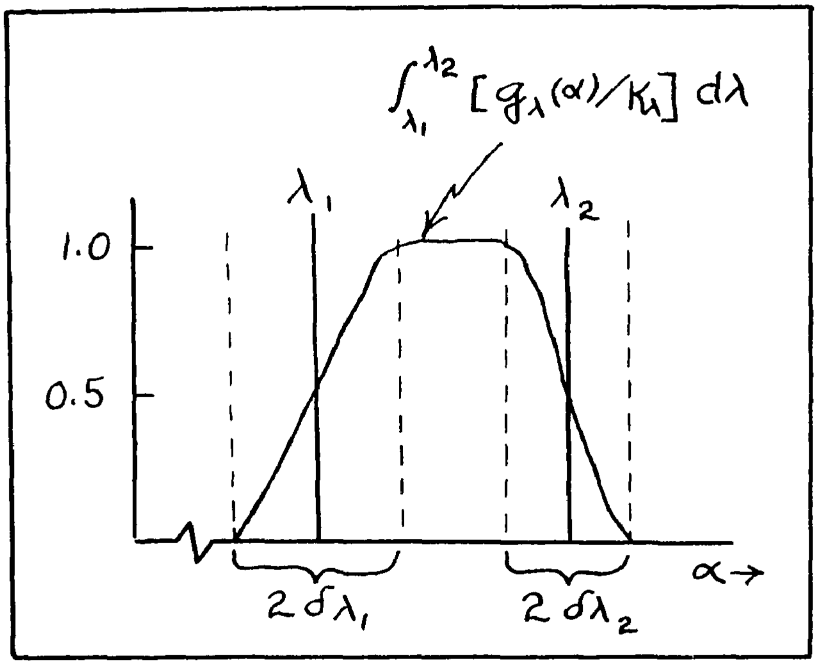

Figure 11. General form of the integrated slit function or weight function.

the regions around λ_1 and λ_2, indicated by the dashed lines. It is evident that the major differences between R^S_{1-2} of equation (13) and the true value $R^{S'}_{1-2}$ of equation (6) will be introduced around the extremities λ_1 and λ_2. Some values of $R^{S'}_\alpha$ will be sampled which lie outside the wavelength interval λ_1 to λ_2 at the expense of incomplete sampling of some of the values inside the interval. Hence it is indicated that R^S_{1-2} will generally be a closer approximation to $R^{S'}_{1-2}$ for increasing values of $\lambda_1 - \lambda_2 / \delta\lambda$ and for values of $R^{S'}_\alpha$ which tend to be symmetric about λ_1 and λ_2 in the spectral slit interval sampled by the spectrograph.

From the above considerations, it becomes apparent that the resolution of the spectrograph is extremely important in the study of sky radiation for small wavelength intervals. It must be admitted that even with the improved resolution obtained with the present instrument, the values of R^S_{1-2} obtained for the smaller wavelength intervals in this investigation may differ from the true values $R^{S'}_{1-2}$; this is particularly true in the region 8.0 to 8.5 μ, at the long-wavelength limit of the intense water vapor band centered at 6.3 μ.

In the wavelength region 4 to 7 μ the assumptions concerning $g_\lambda(\alpha)$ and $R^B_\lambda(T)$ fail completely. Fortunately the radiation from the sky in this wavelength region resembles that of a blackbody, except for certain small intervals between 4 and 5 μ in which blackbody radiation is relatively weak for temperatures of the order of 300° K. The error introduced into R^S_{1-2} for the wavelength region 4.0 to 15.5 μ by errors in the values of R^S_{1-2} for this questionable region, 4 to 7 μ, is estimated to be less than two per cent. It should be noted that no values of R^S_{1-2} are reported which include this region except for the entire range 4.0 to 15.5 μ indicated above.

VII. Observations of the Zenith Sky

Among the first sets of spectra recorded was a twenty-four hour observation of a clear zenith sky. Except where noted a clear sky will be implied for observations mentioned hereafter. For this particular set a laboratory blackbody spectrum was recorded for every two zenith sky spectra, in a cyclic fashion. From these observations it was found that one blackbody spectrum was required for every four or five sky spectra to make adequate radiation calibration and estimates of absorptions by CO_2 and H_2O vapor within the spectrograph.

Figure 12 shows curves of the temperatures T_o and of the value πR^S_{1-2} from the zenith sky for this twenty-four hour period. The correlation between these curves is quite evident. Corresponding curves for the radiation from various wavelength intervals are given in Figure 13. These latter curves demonstrate the type of variations

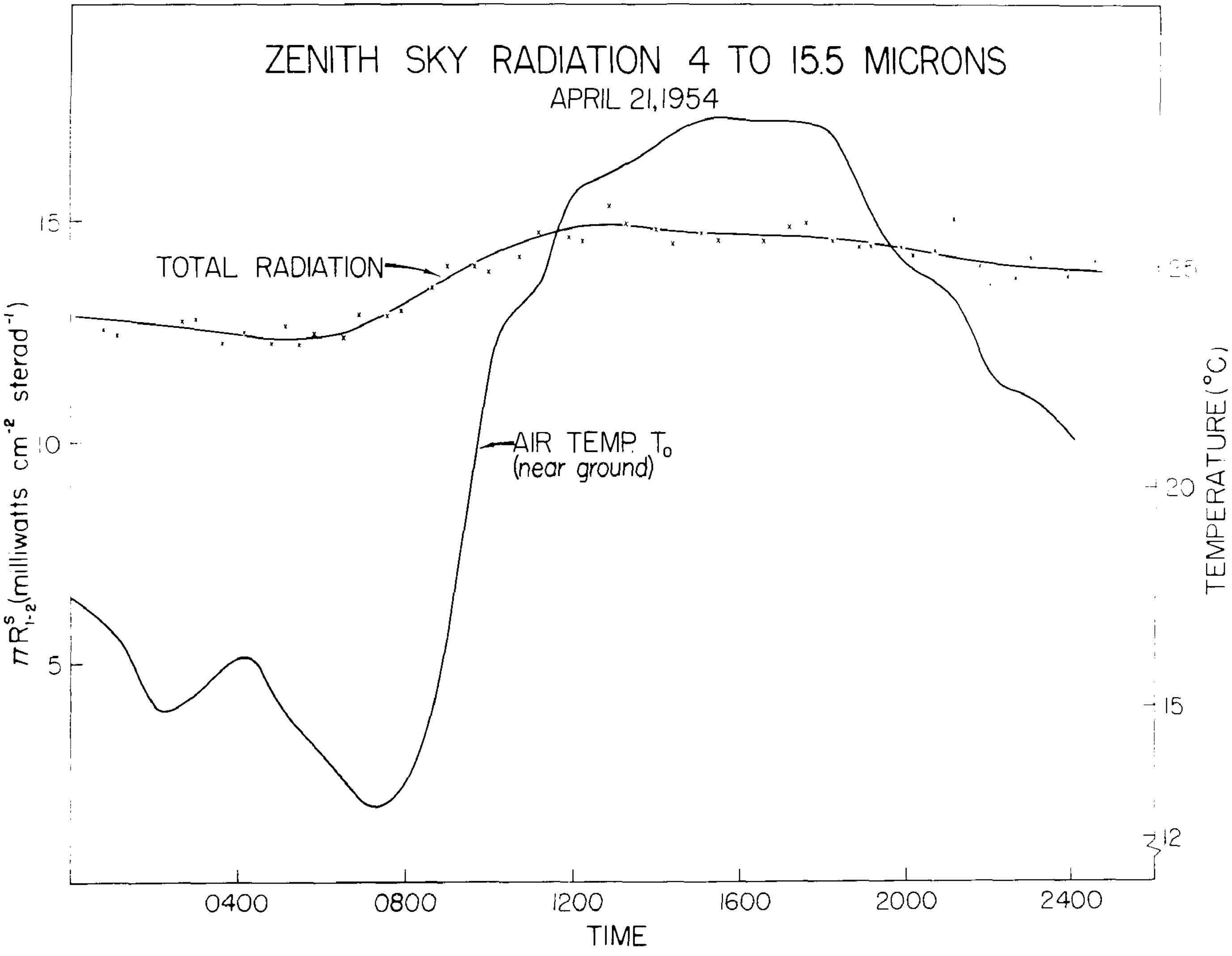

Figure 12. Zenith sky radiation from 4 to 15.5 μ and temperature T_0 for a twenty-four hour period.

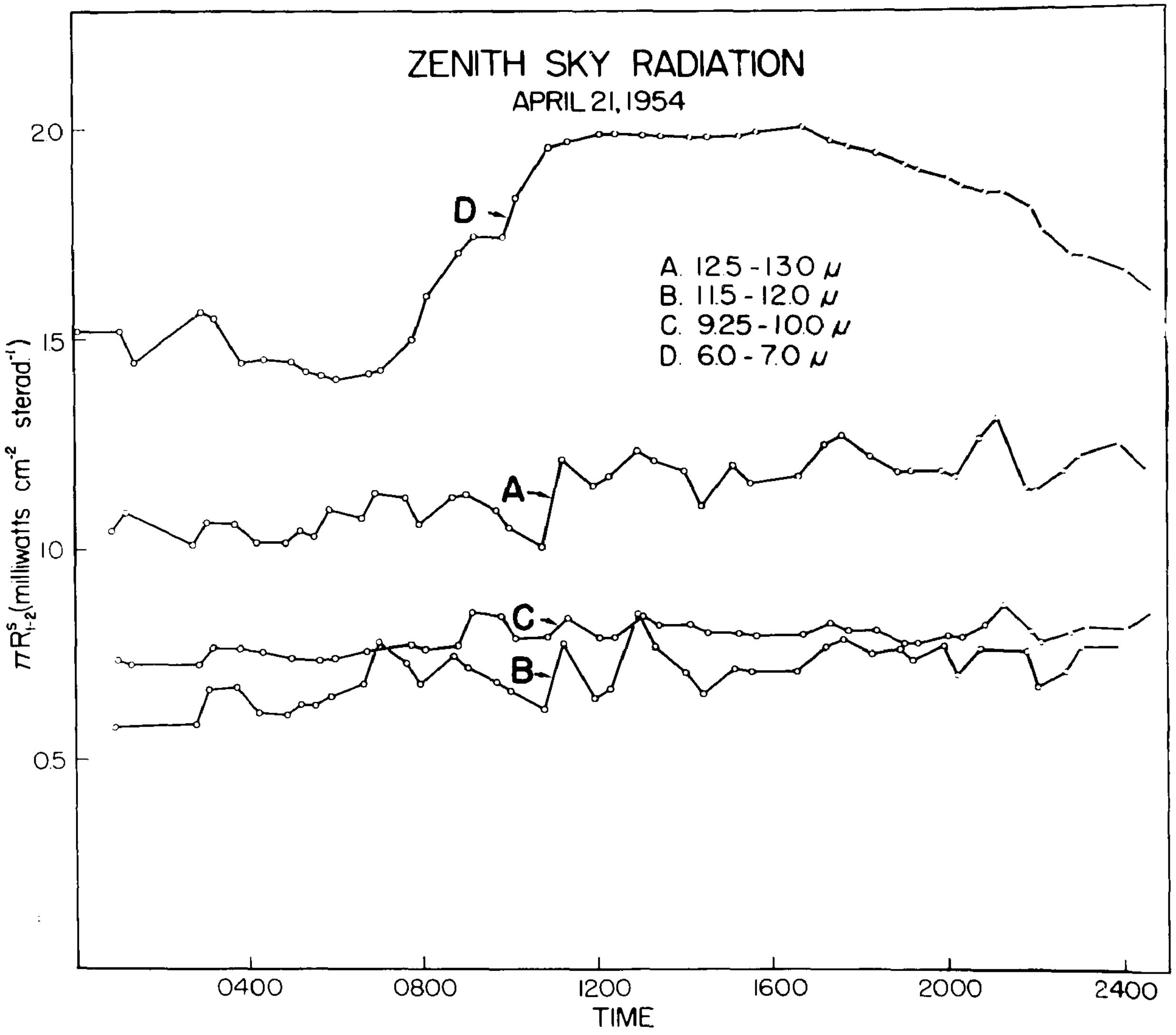

Figure 13. Zenith sky radiation for various wavelength intervals in a twenty-four hour period.

in emission which can occur in the wavelength region 8 to 13 μ. Although these variations were still present in the region of the 9.6 μ ozone band they were less pronounced. Since this region has a relative minimum absorption by water vapor with respect to adjacent regions[7] it is presumed that at least part of the variations are due to changes in water vapor concentration and perhaps to changes in upper air temperature which were not correlated with the meteorological data taken at the ground level.

In an effort to find a relation independent of temperature, the radiation ratio of the emissive power of the zenith sky $R^S_{1-2}(Z)$ to the emissive power of a blackbody at ground level air temperature $R^B_{1-2}(T_o)$ were tabulated for all of the appropriate spectra observed. These values for the wavelength interval 4.0 to 15.5 μ have been plotted for their various absolute humidities in Figure 14. The dashed line was inserted to indicate the general trend. A true curve should contain some non-zero second derivative with respect to humidity (probably negative) but with the variations present the error in estimation might be more than the deviation from the line shown. It was noted that the radiation ratio for this and smaller wavelength intervals was not entirely independent of T_o. For a clear sky and for similar conditions of humidity and pressure the radiation ratio was generally higher at night than in the daytime and the per cent change apparently increased with the transparency of the wavelength region.

Part of these variations in the radiation ratio from the mean

---

[7] W. S. Benedict, H. H. Claassen and J. H. Shaw, J. Res. Nat. Bu. Stan. 49, 91-132 (1952).

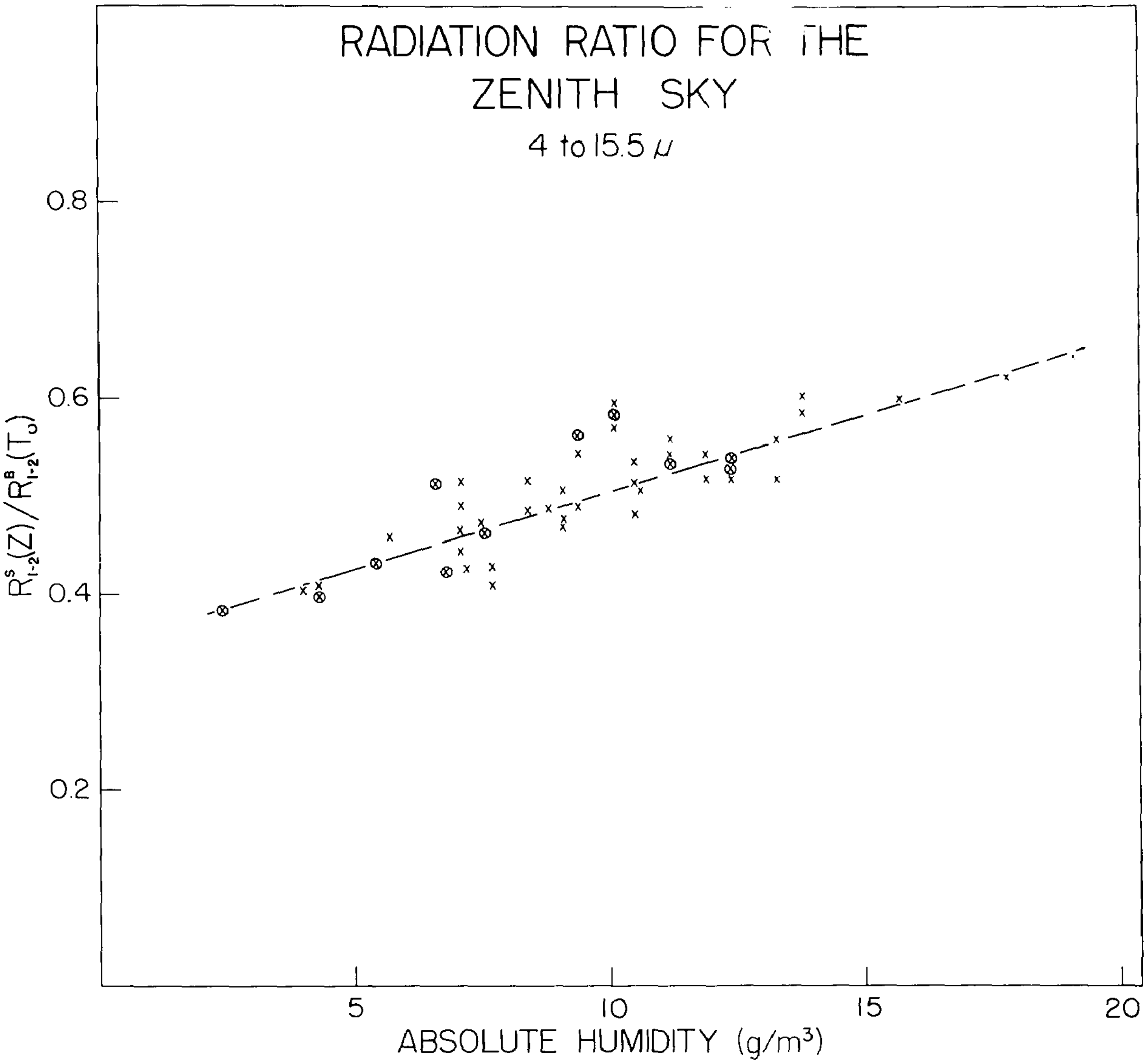

Figure 14. Radiation ratio of zenith sky radiation at various absolute humidities over a nine months period.

values might be correlated with temperature and humidity of the air at altitudes above the six foot level at which meteorological data were taken for the present study. Such information was not available, however. In future studies, radiosonde data would be desirable.

VIII. Sky Radiation Measurements

It is desirable to obtain estimates of the radiation from the hemisphere of sky on the earth. Since the heating effect on the earth's surface by radiation from the atmosphere is of great meteorological importance, the intensity of radiation on a horizontal plane surface near the ground is a convenient measure of the heating effect. With the present data it is possible to estimate this radiation intensity $\underline{R}^{S}_{1-2}(\Sigma)$ for various spectral regions λ_1 to λ_2. Since the data required for a given estimate of $\underline{R}^{S}_{1-2}(\Sigma)$ were obtained over a period of time, during which the temperature and humidity change, it is desirable that each estimate should represent an average value over the observation period.

To obtain an idea of the behavior of the sky radiation as a function of zenith distance or "air mass" the values of the radiation ratio $R^{S}_{1-2}/ R^{B}_{1-2}(T_0)$ were plotted as a function of the square root of the air mass as shown in the sample curves of Figures 15 and 16. The square root of the air mass was used since the emission of radiation from air was expected to be proportional to the absorption of radiation by air, which for the wavelength region 8.0 to 12.0 μ is known to be approximately proportional to the square root of the air mass. Similar curves for the observed spectra for various observation periods

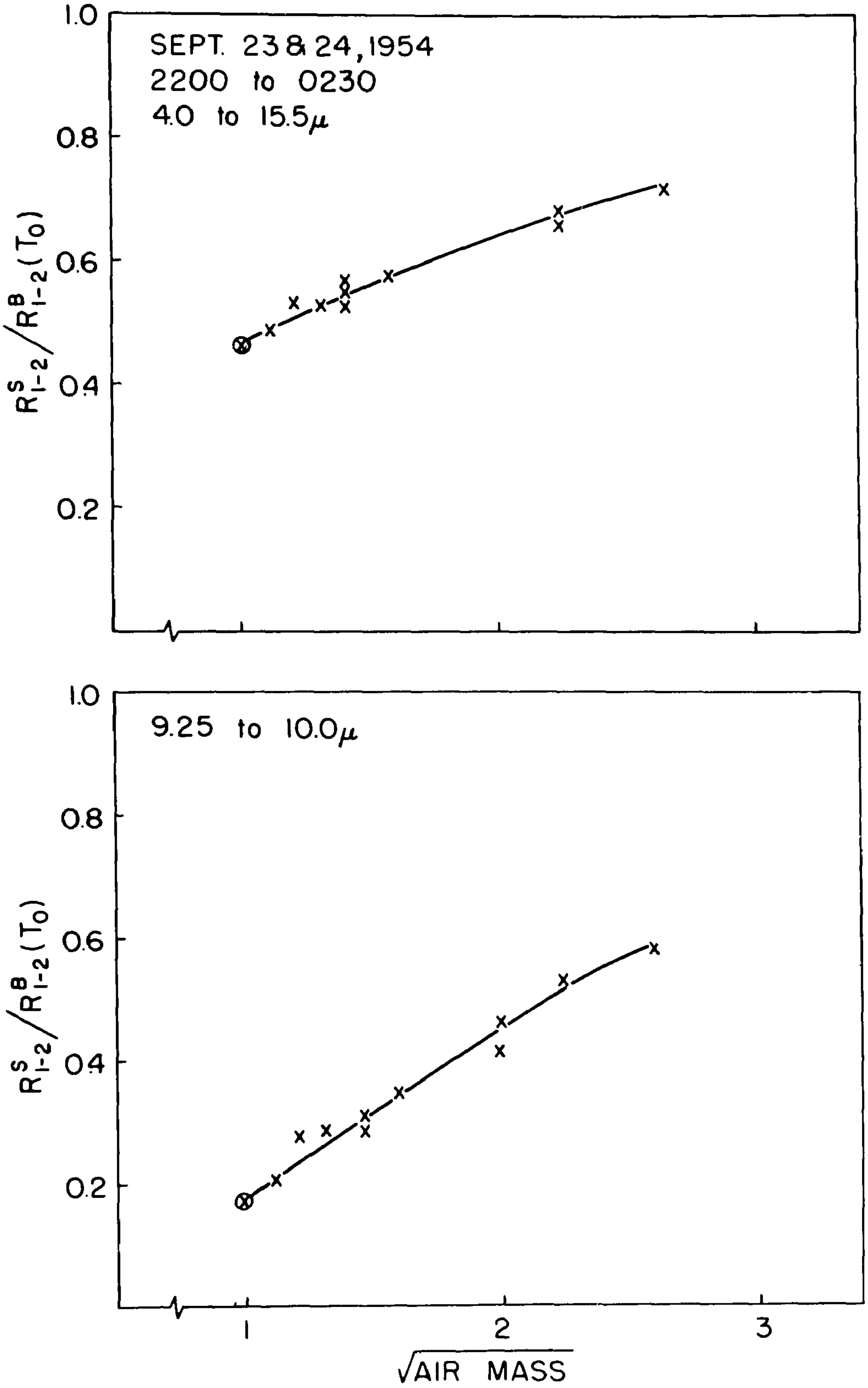

Figure 15. Radiation ratio as a function of the square root of the air mass.

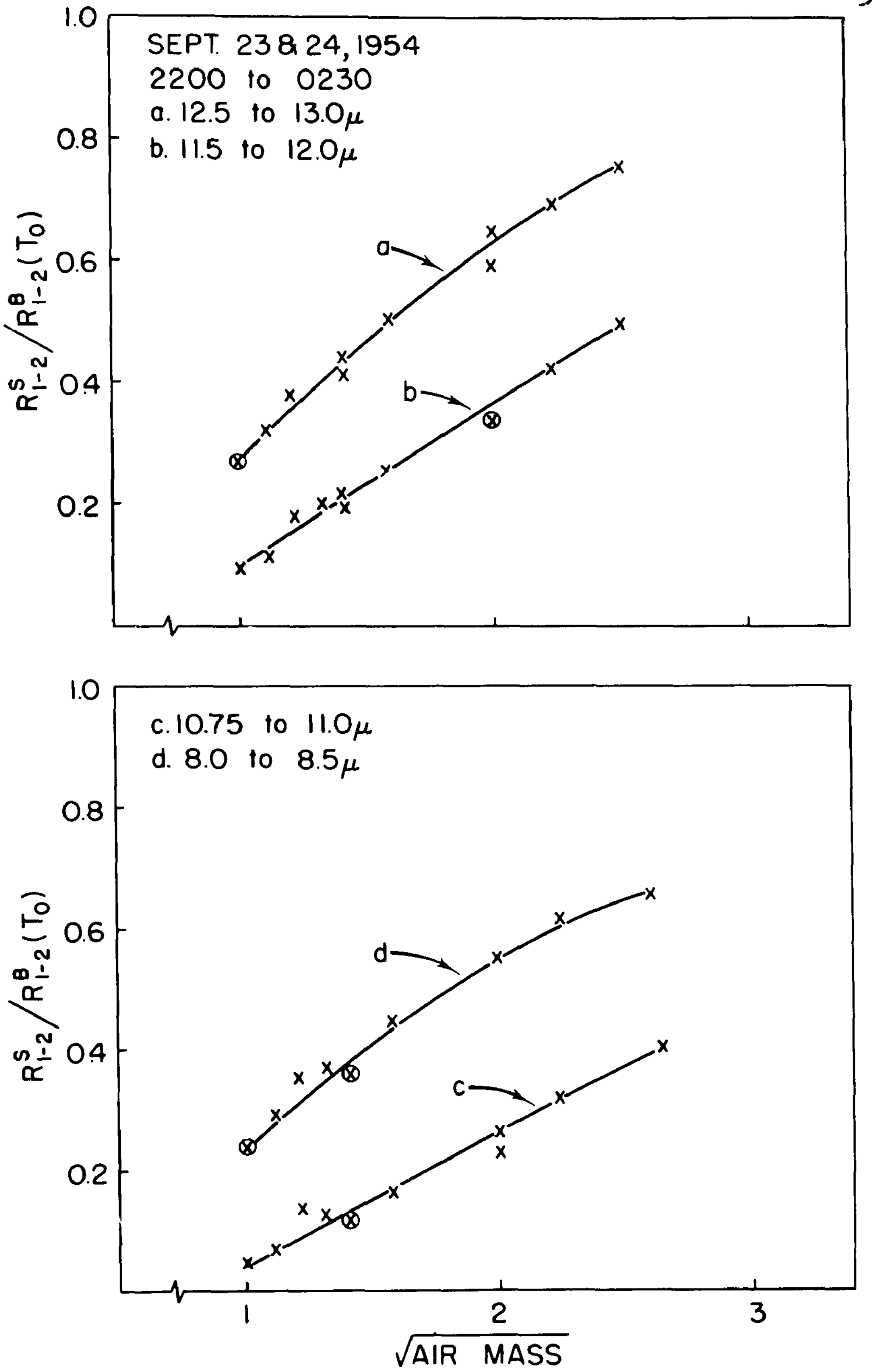

Figure 16. Radiation ratio as a function of the square root of the air mass.

are given in Appendix IV. These curves varied from nearly a straight line to curves having upward or downward curvature. In general for high humidities, occurring during the warmer months, these curves tended toward concave downward (negative second derivative) i.e., $R^S_{1-2}/R^B_{1-2}(T_o)$ tended toward a function of a power of the air mass less than one half. In the cooler months of low humidity the value of $R^S_{1-2}/R^B_{1-2}(T_o)$ tended toward a function of a power of the air mass greater than one half, particularly in the more transparent regions. Stratified conditions such as clouds which tended to increase radiation from the sky produced the effect noted during the warmer months.

At the tops of Figures 17 through 19 are given sample curves of the values of πR^S_{1-2} as functions of zenith distance. Corresponding curves for the other observed spectra are given in Appendix V. The dashed portion within the last ten degree interval of the zenith distance are estimated values which could not be measured due to obstructions near the horizon. The value assumed for the zenith distance of 90^o was the average value of $\pi R^B_{1-2}(T_o)$ for the observation period. In regions of the zenith distance for which there was no observed spectrum, the appropriate value of the radiation ratio from the curve corresponding to those given in Figures 15 and 16 were multiplied by the average value of $\pi R^B_{1-2}(T_o)$ to estimate πR^S_{1-2}. To transfer from air mass A. M. to zenith distance z one may use the relation

$$z = \sec^{-1}(A.M.) \qquad (14)$$

for the values of air mass associated with the present observations.

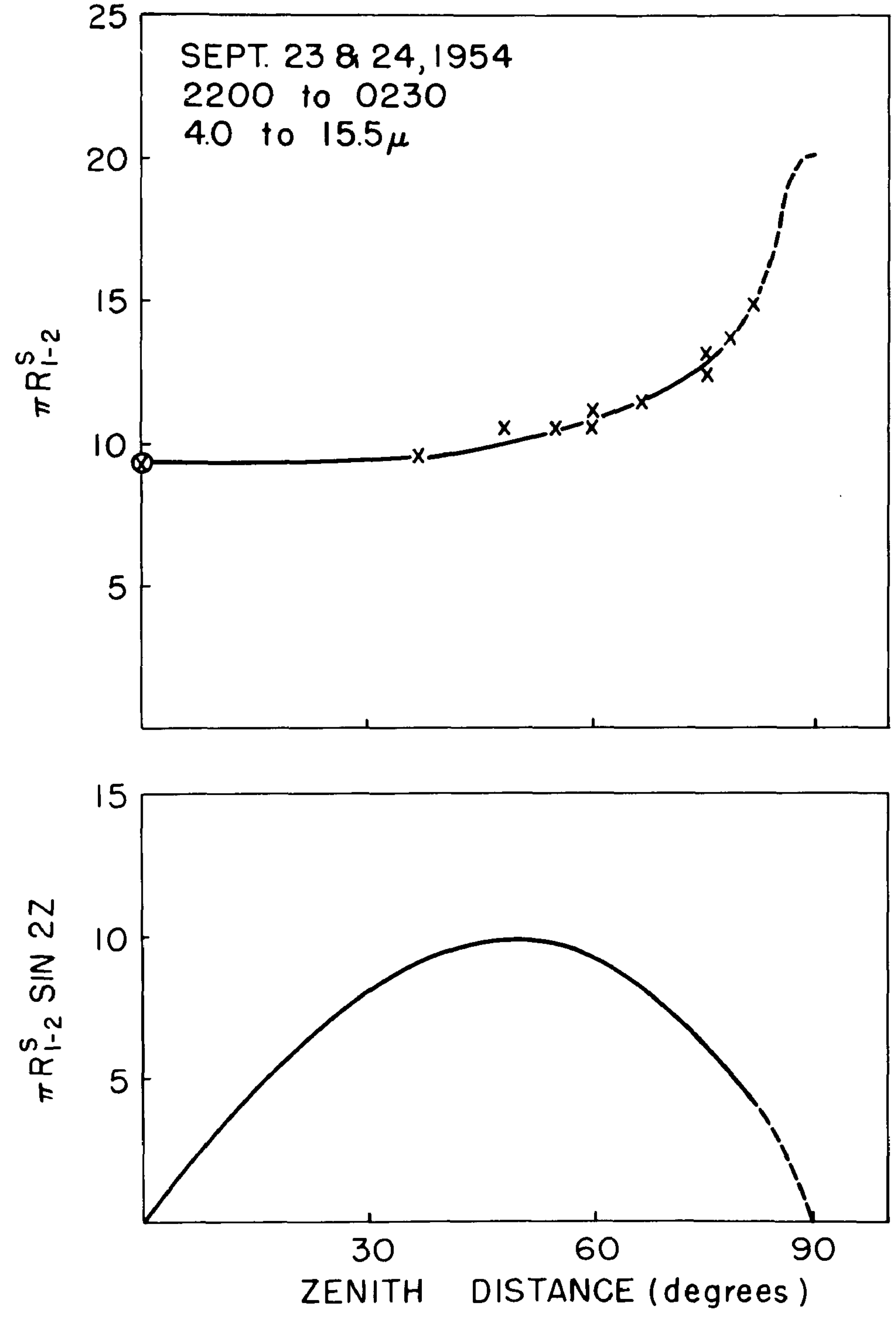

Figure 17. Radiation as a function of zenith distance.

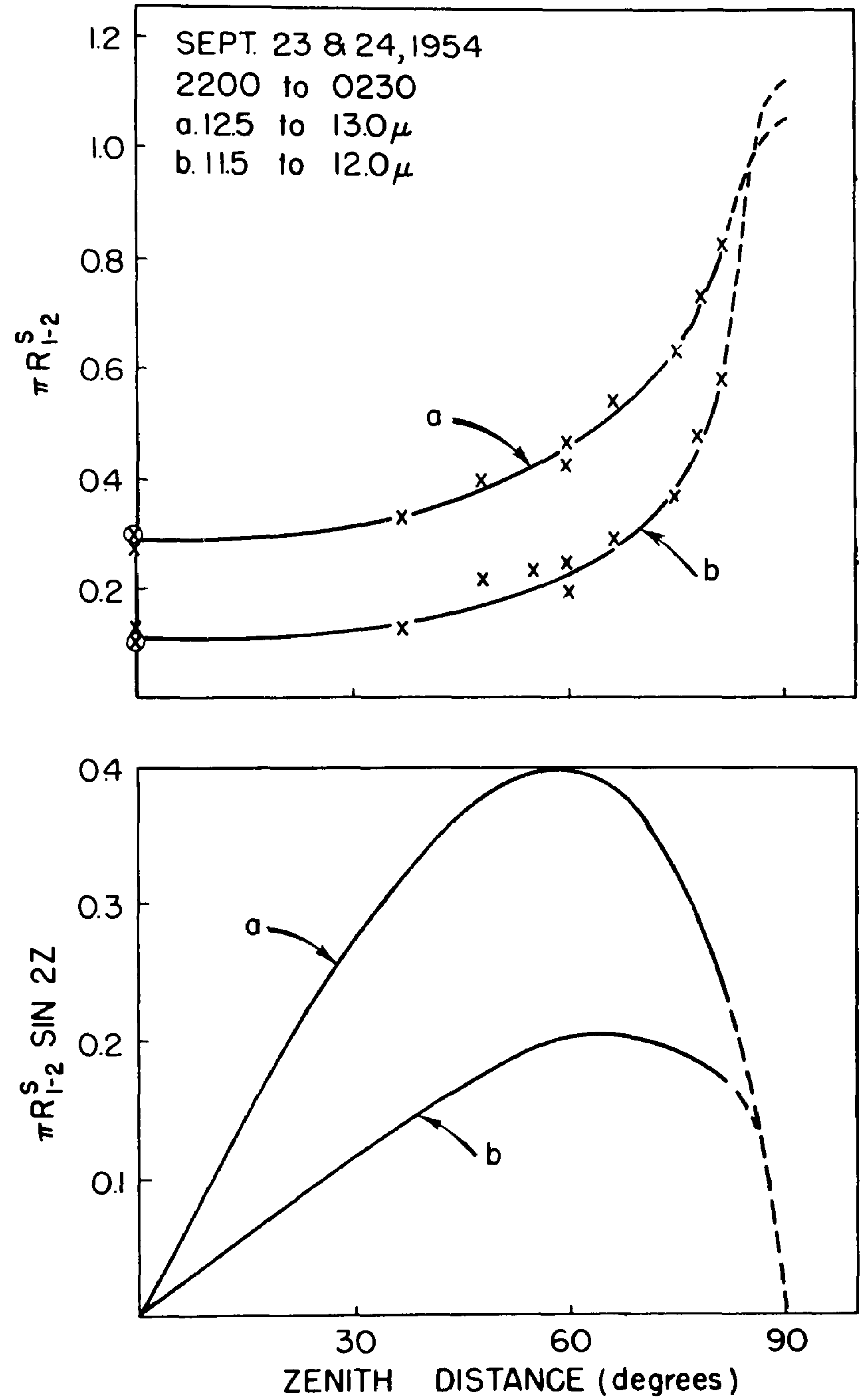

Figure 18. Radiation as a function of zenith distance.

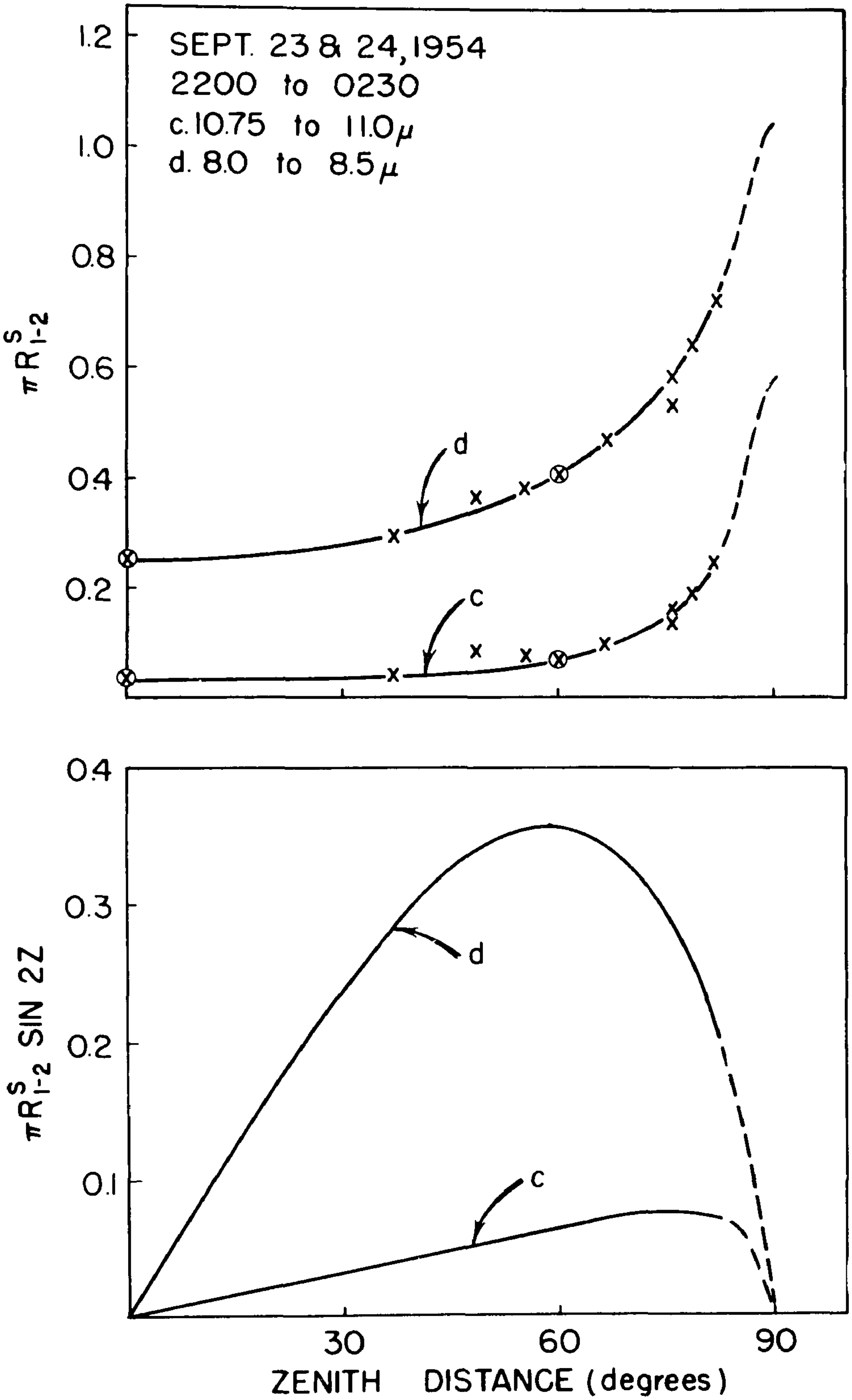

Figure 19. Radiation as a function of zenith distance.

With the values from the curves at the top of Figures 17 through 19, it is possible to estimate the radiation crossing a unit horizontal area. The element of solid angle of the sky is given by $2\pi \sin z \, dz$ and from the element the energy per second crossing a unit area normal to the path defined by z will be $2\pi R^S_{1-2} \sin z \, dz$. This must be multiplied by the cos z for the projection of the area normal to the path onto the horizontal surface. The radiation intensity on the horizontal surface will be

$$\underline{R}^S_{1-2}(\Sigma) = \int_0^{\pi/2} 2\pi R^S_{1-2} \sin z \cos z \, dz \tag{15}$$

which with a substitution of the relation

$$2 \sin z \cos z = \sin 2z \tag{16}$$

becomes

$$\underline{R}^S_{1-2}(\Sigma) = \int_0^{\pi/2} \pi R^S_{1-2} \sin 2z \, dz. \tag{17}$$

Each curve at the bottom of Figure 17 through 19 is the integrand in equation (17) plotted as a function of zenith distance. The planimetered area is therefore proportional to $\underline{R}^S_{1-2}(\Sigma)$. To calibrate the planimetered area one may planimeter a rectangle extending from zero to a known value, say r, along the ordinate and from zero to $\pi/2$ or 90 degrees along the abscissa. The area of this rectangle is $\pi/2$ times the area under an r sin 2z curve where r is the known value along the ordinate. The area under the latter corresponds to a radiation value

$$\underline{R}^{B}_{1-2}(\Sigma) = r, \tag{18}$$

which is obtained by substituting r in place of πR^{S}_{1-2} in equation (17). Therefore the area of the rectangle corresponds to radiation intensity of r $\pi/2$. By equating the ratios of corresponding values one obtains the following equation:

$$\underline{R}^{S}_{1-2}(\Sigma) = \pi r A_s / 2 A_r, \tag{19}$$

where A_S is the planimetered area under the curve of πR^{S}_{1-2} sin 2z and A_r is the planimetered area of the rectangle.

It was found from the planimetered areas A_S, that incomplete knowledge of πR^{S}_{1-2} for zenith distances from 82 to 90 degrees could not cause appreciable error in $\underline{R}^{S}_{1-2}(\Sigma)$. In most cases, for variations of πR^{S}_{1-2} in this region of zenith distances, the difference in areas was difficult to measure with a planimeter.

The true importance of the various zenith distances to the estimate of $\underline{R}^{S}_{1-2}(\Sigma)$ is revealed by the curve of πR^{S}_{1-2} sin 2z. A curve obtained from a sky radiating uniformly in all directions would have a maximum at 45 degrees. Since the spectral emissive power increases with zenith distance, the maxima are shifted to larger values of zenith distance. In a given wavelength region and generally in a comparison among various wavelength regions the maximum value of πR^{S}_{1-2} sin 2z was shifted toward the horizon for decreasing values of the radiation ratio.

In connection with this varied importance of the zenith distance of the sky path to the estimate of $\underline{R}^{S}_{1-2}(\Sigma)$, it is evident that variations and errors in πR^S_{1-2} will not be properly weighted if the curve of πR^S_{1-2} were drawn directly over measured values; e.g. an error or variation in a sky spectrum of a 50 degree zenith distance would influence the estimate of $R^S_{1-2}(\Sigma)$ more than a corresponding error or variation in a sky spectrum from either zero or 80 degrees, while the probability of occurrence of an error or variation is about the same for all three spectra. Where such variations occurred, the values of πR^S_{1-2} predicted by the corresponding radiation ratio curve were used. The method used to find this new value of πR^S_{1-2} has been described in this section. Since it was easier to approximate an unbiased average by the radiation ratio curve the estimated value of $\underline{R}^S_{1-2}(\Sigma)$ which resulted, was more representative of the period of observation.

For future experiments, in addition to the observations of continuous spectra of the sky, it would be desirable to make observation of a radiation from a given wavelength region as a continuous function of zenith distance. In this manner the time element involved for each of these curves would be reduced considerably.

In the curves of Figures 15 through 19 and of Appendix IV and Appendix V the measured values have been noted by an "x." Where two or more values were too close to be plotted this symbol has been circled "⊗."

The values of $\underline{R}^S_{1-2}(\Sigma)$ have been computed for the curves in Appendix V and appear in a tabular form in that section together with the temperature, humidity and radiation ratio for the appropriate time interval. In Figure 20 the values of the radiation ratio for the wavelength interval 4.0 to 15.5 μ have been plotted as a function of

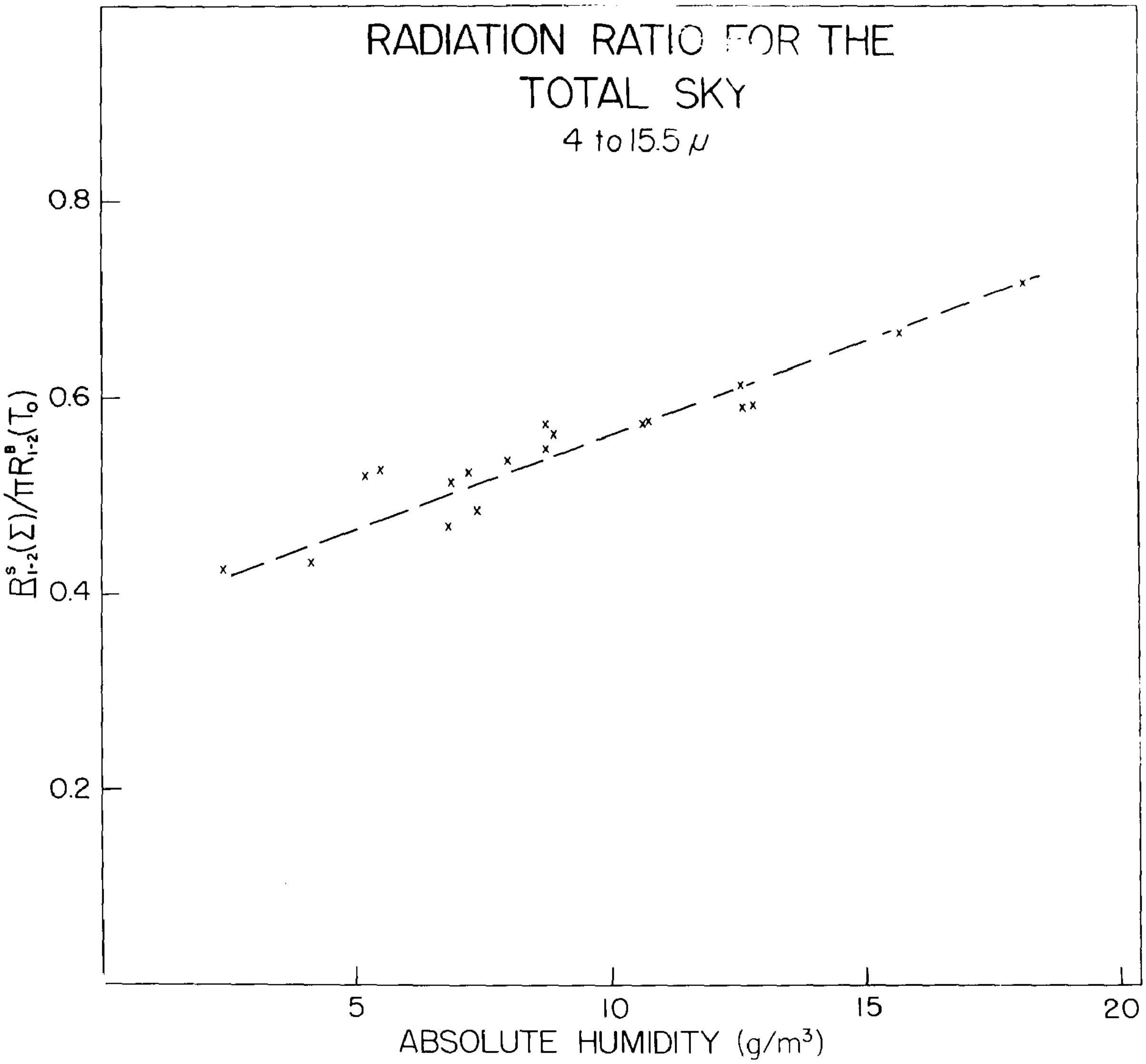

Figure 20. Radiation ratio of the total sky for various absolute humidities (4 to 15.5 μ).

humidity. The dashed line was inserted to indicate the general trend of the measured values. Figures 21 and 22 show these values for the four smaller wavelength intervals indicated.

Note that the dashed line in Figure 20 would intercept the origin at about 0.37. Unfortunately this cannot be interpreted as an estimate of the average contribution of CO_2 to the total emission in this wavelength region since the behavior of the curve is not known close to the ordinate axis. There is no evidence of appreciable changes in CO_2 concentration in the present measurements. However, it must be noted that a study of CO_2 is rather difficult with the present measurements, since emission in the 15 u region does not change appreciably with any existing variations in CO_2 concentration and since emission in the regions of the weaker bands of CO_2 are overlapped by emissions of other gases, largely water vapor. The ordinate intercepts of the other curves (Figures 21 and 22) tend closer to the origin, particularly for the 10.75 to 11.0 μ and the 11.5 to 12.0 μ regions. The wavelength region from 12.5 to 13.0 μ may contain emission from CO_2 due to a very weak absorption band around 12.6 μ. Some radiation from methane and nitrous oxide due to very strong bands around 7.7 μ may be included in the measured values of R^S_{1-2} for the wavelength region 8.0 to 8.5 μ. The true behavior of the curves for these two regions just mentioned is not well established by the present data and therefore an estimate of their ordinate intercepts will not be attempted.

IX. Observations in the Region of the 9.6 μ Ozone Band

Figure 23 shows the appearance of the sky spectrum in the

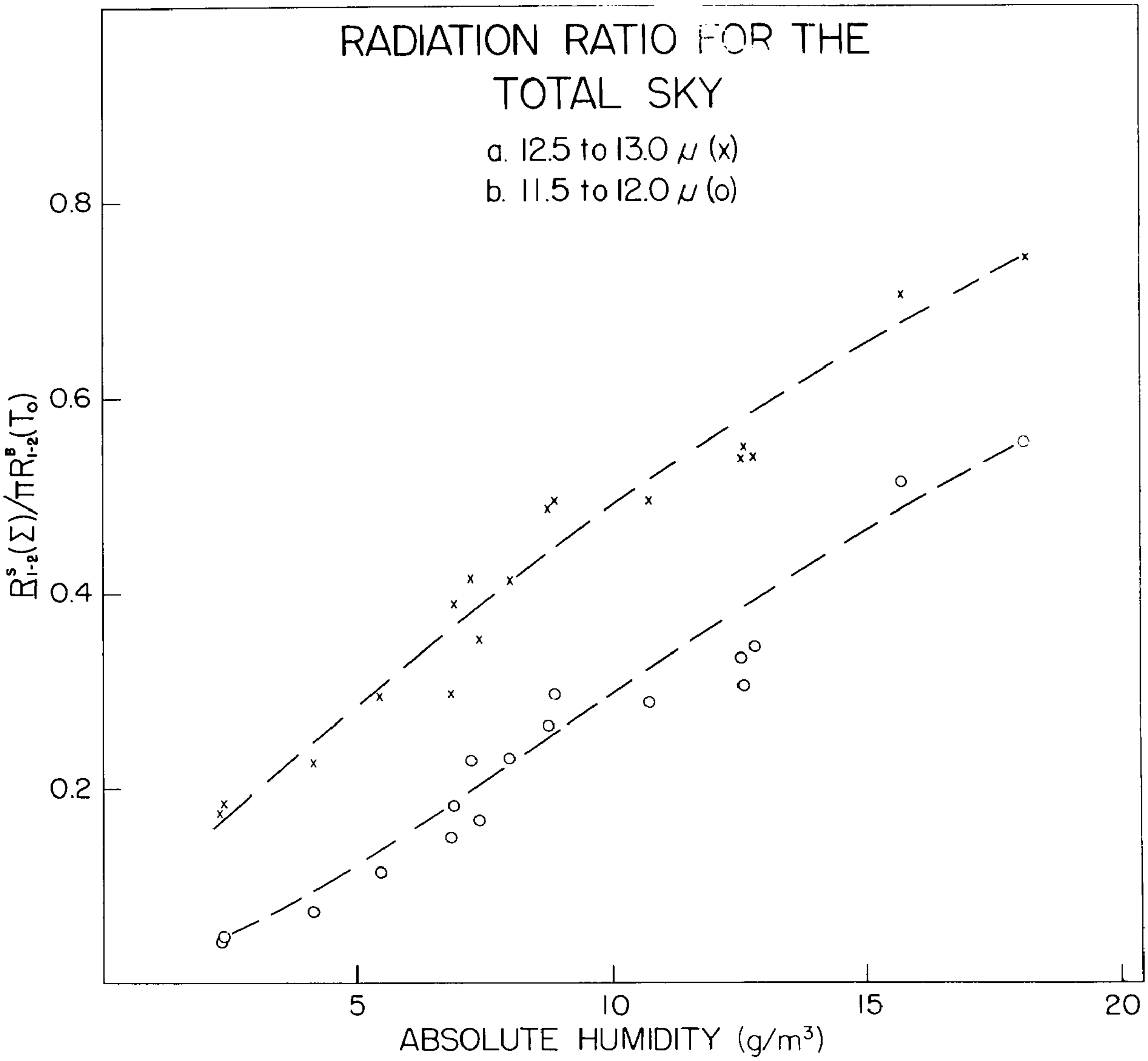

Figure 21. Radiation ratio of the total sky for various absolute humidities (11.5 to 12.0 μ and 12.5 to 13.0 μ).

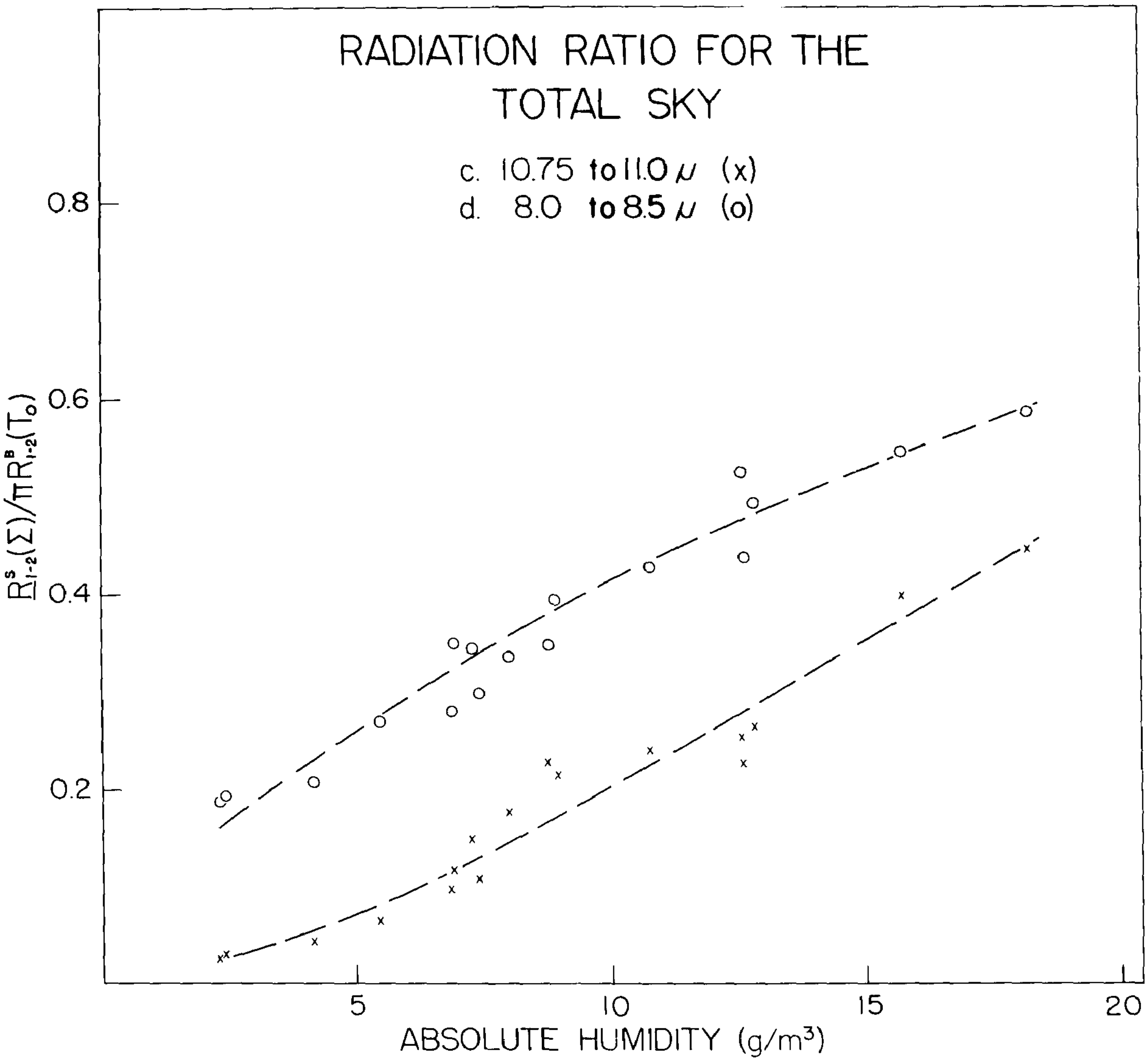

Figure 22. Radiation ratio of the total sky for various absolute humidities (8.0 to 8.5 μ and 10.75 to 11.0 μ).

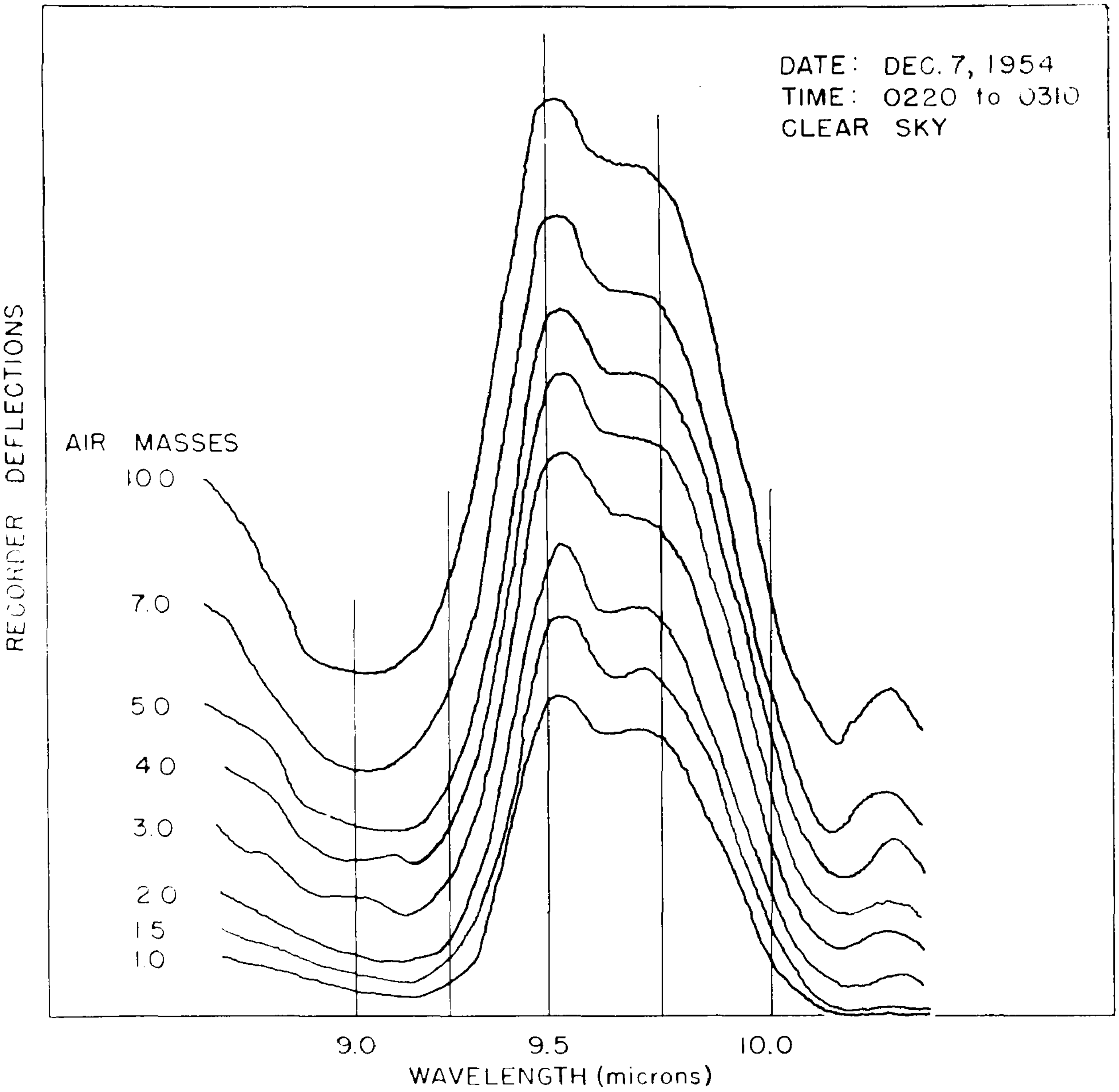

Figure 23. Recorded spectra for various air masses in the region of the 9.6 μ ozone band.

region of the 9.6 μ ozone band for the various air masses listed. The slitwidth of the spectrograph was 0.75 mm. The ground level air temperature T_o was -8.5° C (16.5° F) and the absolute humidity was about 2.4 g/m^3. The data shown required approximately forty-five minutes for observation.

The values of πR^S_{1-2} for the wavelength region 9.25 to 10.0 μ were found for spectra observed throughout the year and the curves described in Section VIII are given in Appendix IV and Appendix V. Figure 24 shows the radiation as a function of zenith distance for a period in which the recordings of Figure 23 were included. The solid curves correspond to the total radiation measured and the irregular-dash curve correspond to an estimate of the radiation from the ozone reaching the earth's surface.

The estimate of radiation from the ozone reaching the earth's surface $R^S_{1-2}(O_3)$ was made by attempting to subtract the background radiation which is probably due to emission from CO_2 and H_2O vapor. For the data in Figure 23 a line was drawn from the deflection value around 9.0 μ to the first maximum beyond the ozone band (about 10.25 μ). The radiation represented above this line was the estimated value for radiation from the ozone reaching the earth's surface. It is believed that this estimate represents a lower limit of radiation from ozone because: (1) Some of the effect of radiation from ozone was sampled outside the wavelength region 9.25 to 10.0 μ, due to the large spectral slitwidth of the spectrograph used on this particular night. This would tend to decrease the measured value from the true value; (2) The absorption bands and lines of other atmospheric gases are weak in this

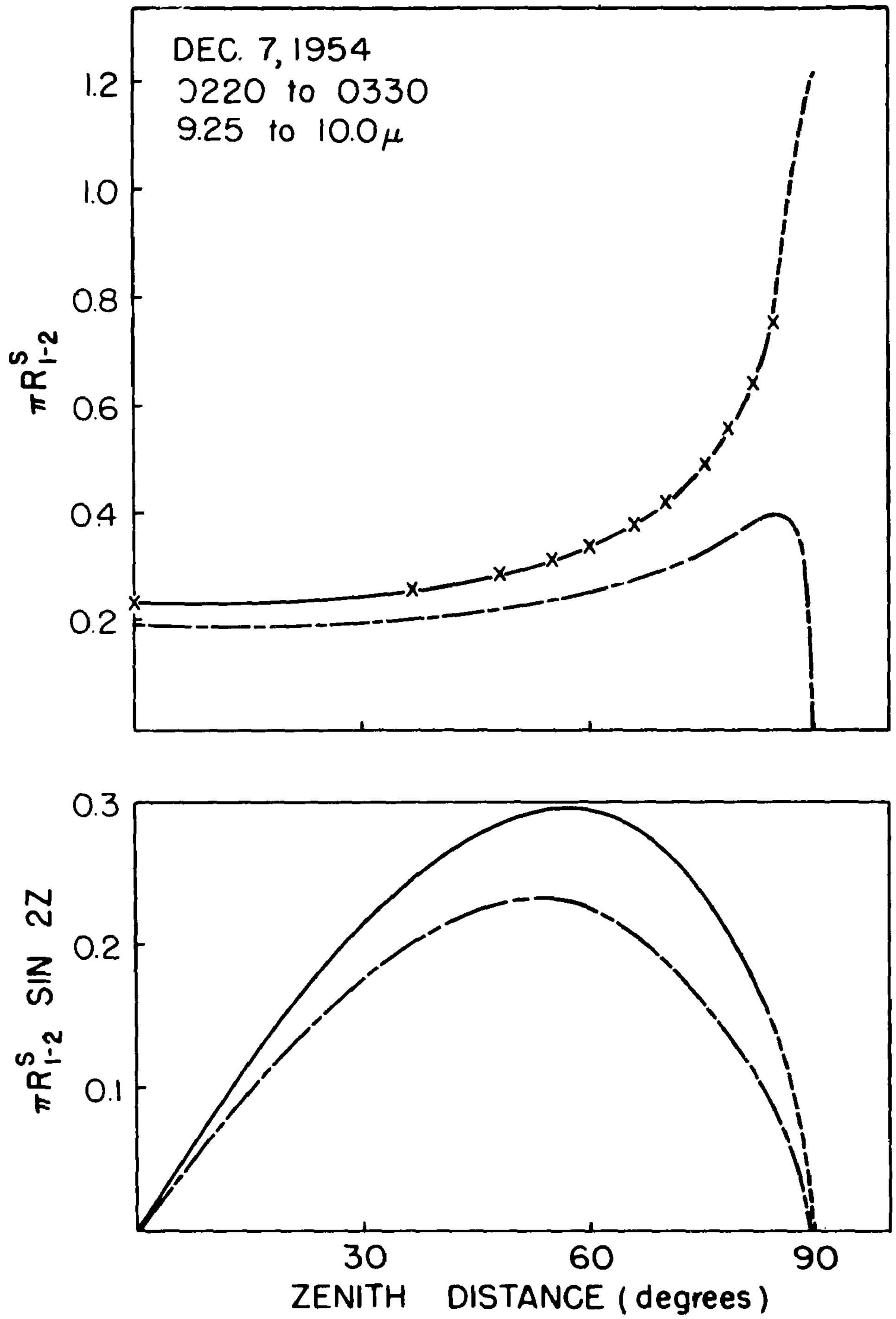

Figure 24. Radiation as a function of zenith distance in the region of the 9.6 μ ozone band.

region and it is doubtful that they could contribute as much to emission as is accounted for by the removed background radiation; (3) Emissions which are outside of the 9.25 to 10.0 µ region may be sampled in the spectral interval of the spectrograph for central wavelength settings within the region, but the contributions to recorder deflections within this wavelength region should at least be less than the deflections outside this wavelength region.

There are two weak CO_2 bands[8] at 9.4 µ and 10.4 µ, the latter of which may be contributing to the emission maximum at 10.25 µ. Since the line for the estimation was drawn from this maximum, the influence of the emission from the 9.4 µ band should be more than accounted for by the background radiation removed.

For the remaining data of this ozone region, the average values of the radiation obtained for the two adjoining quarter-micron intervals was multiplied by three and this value was subtracted from the total radiation to obtain the estimated value $R^S_{1-2}(O_3)$. This condition proved to be about the same as that described above when it was applied to the recordings shown in Figure 23.

The emissive power of the sky R^S_{1-2} and the estimated emissive power of the ozone $R^S_{1-2}(O_3)$ in the region 9.25 to 10.0 µ can be transformed to the effective radiation temperatures T^S_{1-2} and $T^S_{1-2}(O_3)$ respectively. The effective radiation temperature corresponding to an emissive power in a given wavelength interval may be defined as the temperature at which a blackbody would exhibit the same emissive power

---

[8] G. Herzberg, Infrared and Raman Spectra of Polyatomic Molecules (D. Van Nostrand Company, New York, New York, 1945), p. 274.

normal to its surface for the same wavelength interval. The effective radiation temperature for a hemisphere of sky $T^S_{1-2}(\Sigma)$ will be defined as the temperature of a horizontal plane blackbody for which a radiation balance would exist between its upper surface and the sky in the wavelength interval of study. Figure 25 shows the effective radiation temperatures as a function of the zenith distance for the same data represented in Figure 24 and discussed at the beginning of the present section. The corresponding effective radiation temperatures of the sky $T^S_{1-2}(\Sigma)$ for the total measured radiation in this region and the estimated radiation from ozone are -59.5° and -67° C respectively. These latter temperatures are lower than the "effective temperatures" of the ozone (around -40° C) measured by Adel,[9] who endeavored to take account of the effective emissivity of the ozone.

Thus far, only the "integrated" values of the emissive power R^S_{1-2} have been used to estimate the effective radiation temperature in the wavelength region 9.25 to 10.0 μ. By estimating the emissive power per unit wavelength interval R^S_λ, given by D^S_λ / K_λ, one may find the temperature of a blackbody for which the corresponding value R^B_λ is the same. Since the measurement involves a finite spectral slitwidth, this temperature represents an effective radiation temperature of the sky which has been weighted in the spectral slit interval about λ by a spectral slit function. It is noteworthy that with the subtraction of the deflection due to CO_2 and H_2O vapor emission in the manner described in this section, the remaining deflection at the maximum of the ozone

---

[9] A. Adel, Geophysical Research Papers No. 2 (1949).

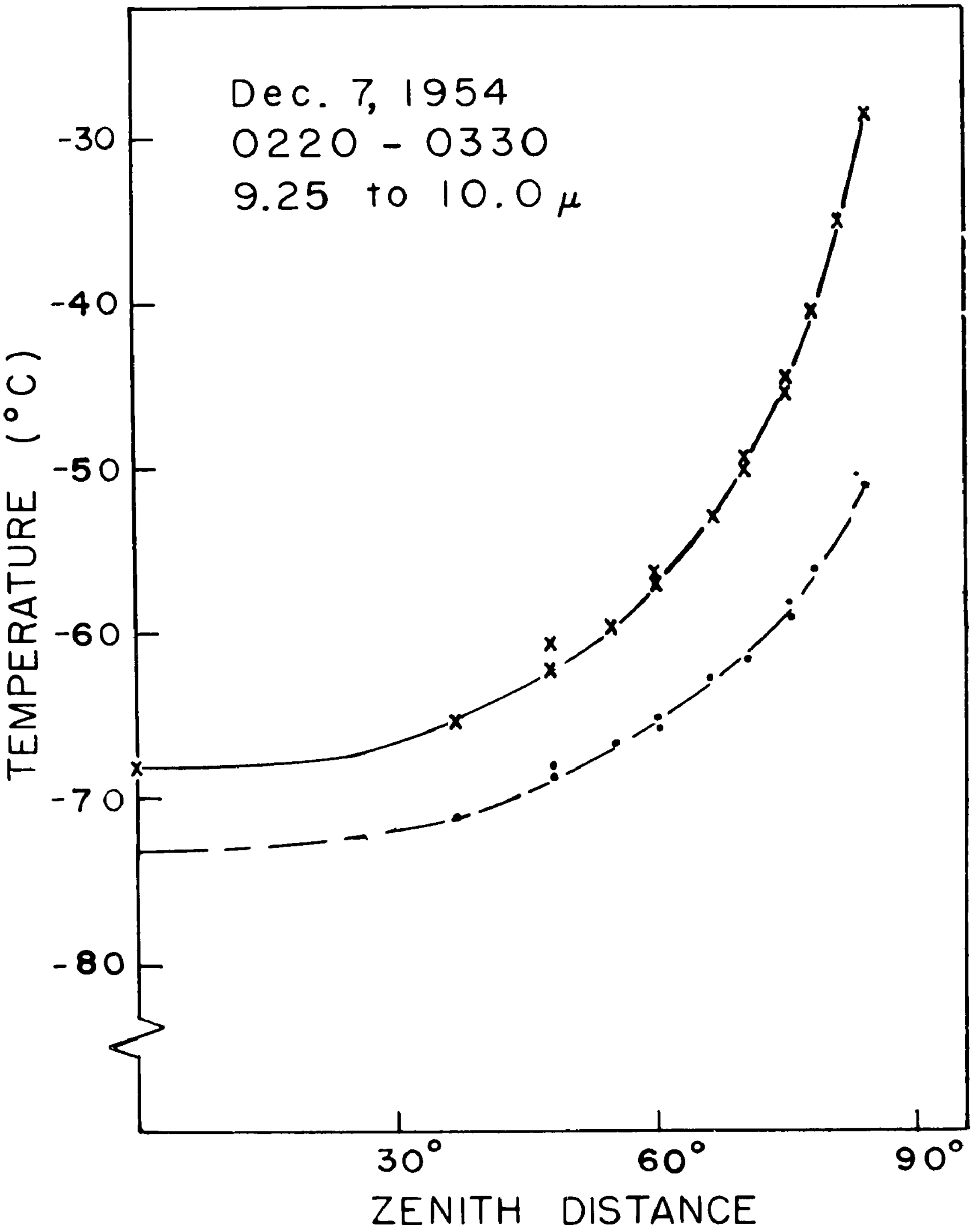

Figure 25. Effective radiation temperature as a function of zenith distance in the region of the 9.6 μ ozone band.

emission corresponds to emissive powers per unit wavelength interval of a blackbody at temperatures as high as -10° C. In particular this temperature was found from the recorded spectrum at ten air masses in Figure 23 of this section. Since the recorder deflection is a maximum in this wavelength region one may expect this temperature to be lower than the corresponding true maximum effective radiation temperature which could be more closely approximated from spectra with improved resolution.

In the present data a definite correlation was indicated between water vapor density and radiation from the sky in the 9.6 μ region, while Adel found "no systematic connection between water vapor content" and the effective temperature of the ozone for his observations. This may be explained in part by the fact that Adel's measurements were made in a relatively dry climate and at higher elevations than Columbus, Ohio. Also, for large spectral slitwidths emission and absorption by water vapor tend to be presented as a smooth spectrum around this ozone band. Thus extrapolations to the "background" would tend to decrease any effects of water vapor absorption and emission on the final estimate of the effective temperature of the ozone.

X. Summary

The use of the mirror chopper and the "blackbody" at liquid-nitrogen temperatures as integral parts of the spectrograph permitted direct measurements of dispersed sky radiation. Although the present measurements were confined to the wavelength region 4 to 15.5 μ, the region can probably be extended to 25 μ with the use of a potassium bromide prism in place of the sodium chloride prism used for the present data. The improvement in resolution with this spectrograph permitted observations of some of the smaller emission maxima in the wavelength region 8 to 13 μ, which to the author's knowledge were not observed previously in this type of spectra. Also the increased resolution provided increased accuracy in the measurement of radiant flux for various spectral intervals. In regard to the absolute accuracy of the radiant flux measurements, there was no detectable constant error from analysis of laboratory blackbody spectra for temperatures from 0° C to 50° C. It is estimated that the assumed zeros of the recorded spectra represent radiation values differing from the true zero by not more than four per cent of the radiation from a blackbody at room temperature. This estimate is valid only for wavelength regions remote from the fundamental vibration-rotation bands of CO_2 and H_2O.

The only notable diurnal change in the sky spectra recorded was associated with the regions of strong absorption in which the emission from the atmosphere resembles that of a blackbody at ground level air temperature. No marked changes in radiation were noted at sunrise or sunset in the wavelength region studied. The most noteworthy changes in sky radiation occurred in the wavelength region 8 to 13 μ in which the radiation increased with the air mass, absolute humidity and cloud formations. The measured values of radiation from an overcast sky with "ceiling" of 1,000 feet or less were usually ninety per cent or more of the radiation from a blackbody at the ground level air temperature in the wavelength region of these observations. For increased ceiling the radiation value decreased and the cloud formations usually became less homogeneous, making measurements with the present instrument difficult to interpret. There was some evidence of an increase in radiation from cirrus clouds at 25,000 feet but the increase was small and was at times completely obscured by changes in sky radiation which existed in the absence of visible clouds.

The seasonal trends in the radiation from a clear sky were noted. Clear-sky radiation was found to be a function of the ground level air temperature and absolute humidity. No attempt was made to obtain an analytic relation between radiation, temperature, and humidity from the present data but general trends were established by experimental observations. Until some knowledge of the contribution to the sky radiation by the air layers at various altitudes is available, the correlation of sky radiation with the parameters, temperature and humidity will probably remain incomplete. It would be desirable to measure temperature, pressure and humidity at various altitudes, simultaneously with sky radiation measurements, in an effort to obtain this knowledge.

Sky radiation measurements in the wavelength region of the 9.6 u ozone band indicate that CO_2 and H_2O vapor contribute to the radiation in this region for the values of ground level humidity and pressure associated with the present data. In a solar spectrum the contribution of these two gases to absorption is nearly obscured by the strong absorption of the ozone of the upper atmosphere. For atmospheric emission, however, the importance of these two gases is increased considerably due to their high temperatures relative to the temperatures of the ozone layer.

It was found during the course of this investigation that in addition to the suggestions noted earlier certain other improvements in future work could be made. Measurements of the total undispersed radiation could be made simultaneously with the present measurements if both sides of the present chopper were aluminized. Additional equipment is, of course, implied but the additional detecting and amplifying system does not require a high sensitivity. The construction of an insulated enclosure with thermostat-controlled heating for the spectrograph housing is desirable to reduce noise and to permit the sky radiation measurements to be made out of doors in order to prevent the influence of the laboratory path on the measurements. Direct measurements of the radiation as a function of zenith distance could be made by rotating the plane mirror in a continuous manner for a given wavelength setting of the spectrograph. In this way the time represented in the curves of this type for the present data would be reduced considerably. It is also desirable that continuous temperature and humidity measurements be taken at the site of the observations. However, it is not believed that this is as important as obtaining temperature, pressure and humidity at higher altitudes. It is further suggested that the sky spectrum be observed at high altitudes to study its features in a dry and less dense atmosphere.

APPENDIX I Spectograph Calibrations and Spectral Slitwidth

The wavelength calibration was made from 3 to 16 μ by observations of the absorption bands and lines of CO_2 and H_2O vapor in the laboratory path and of NH_3 in an absorption cell. A Nernst glower was used as the source of radiation.

Figure 26 shows the curves of the spectral slitwidth as a function of the wavelength setting.[10] The spectral slitwidth indicated here is an estimate of the wavelength interval between half-amplitude points of the slit function. A sensitive thermocouple (sensitivity of 7 or 8 microvolts per microwatt) with relatively low noise level was employed to maintain the smaller physical slitwidth 0.45 mm, noted in this figure. However, the gradual decrease in sensitivity which was most marked during months of high humidity, finally necessitated the use of the larger slitwidth 0.75 mm, for the observations on the night of December 6 and 7.

Figure 27 shows curves of $\pi R_\lambda^B(T)$ as a function of wavelength for temperatures from 0° C to 50° C. The points used to plot these curves were computed from the tables by Lowan and Blanch[11] of the Planck radiation function

$$\pi R_\lambda^B = c_1 \lambda^{-5} \left(e^{c_2/\lambda T} - 1 \right)^{-1}, \tag{20}$$

---

[10] "Instruction Manual, Infrared Spectrometer, Model 12c," Appendix (The Perkin-Elmer Corporation, Glenbrook, Connecticut, 1950).

[11] A.N. Lowan and G. Blanch, J. Opt. Soc. Amer. <u>30</u>, 70 (1940).

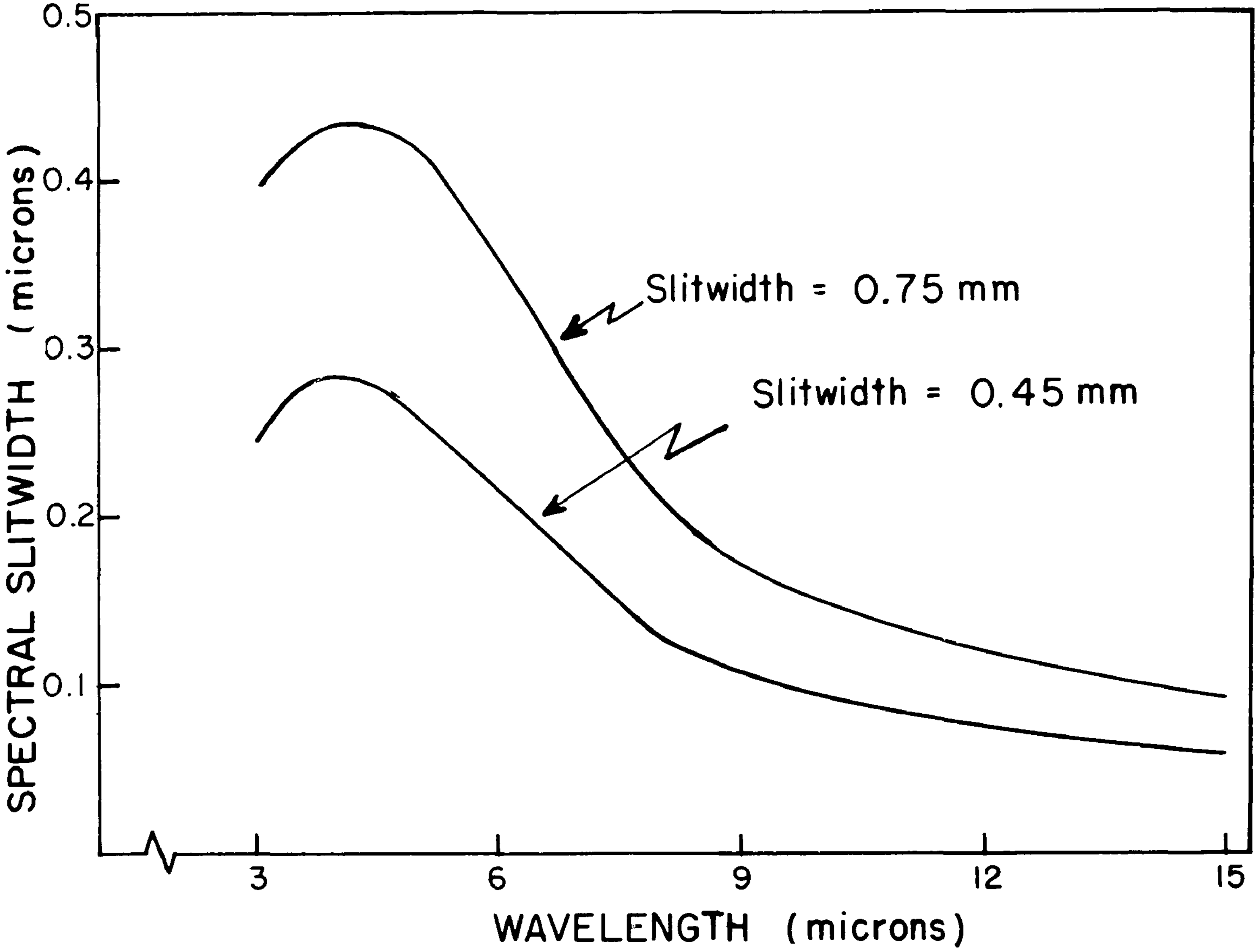

Figure 26. Spectral slitwidth as a function of wavelength.

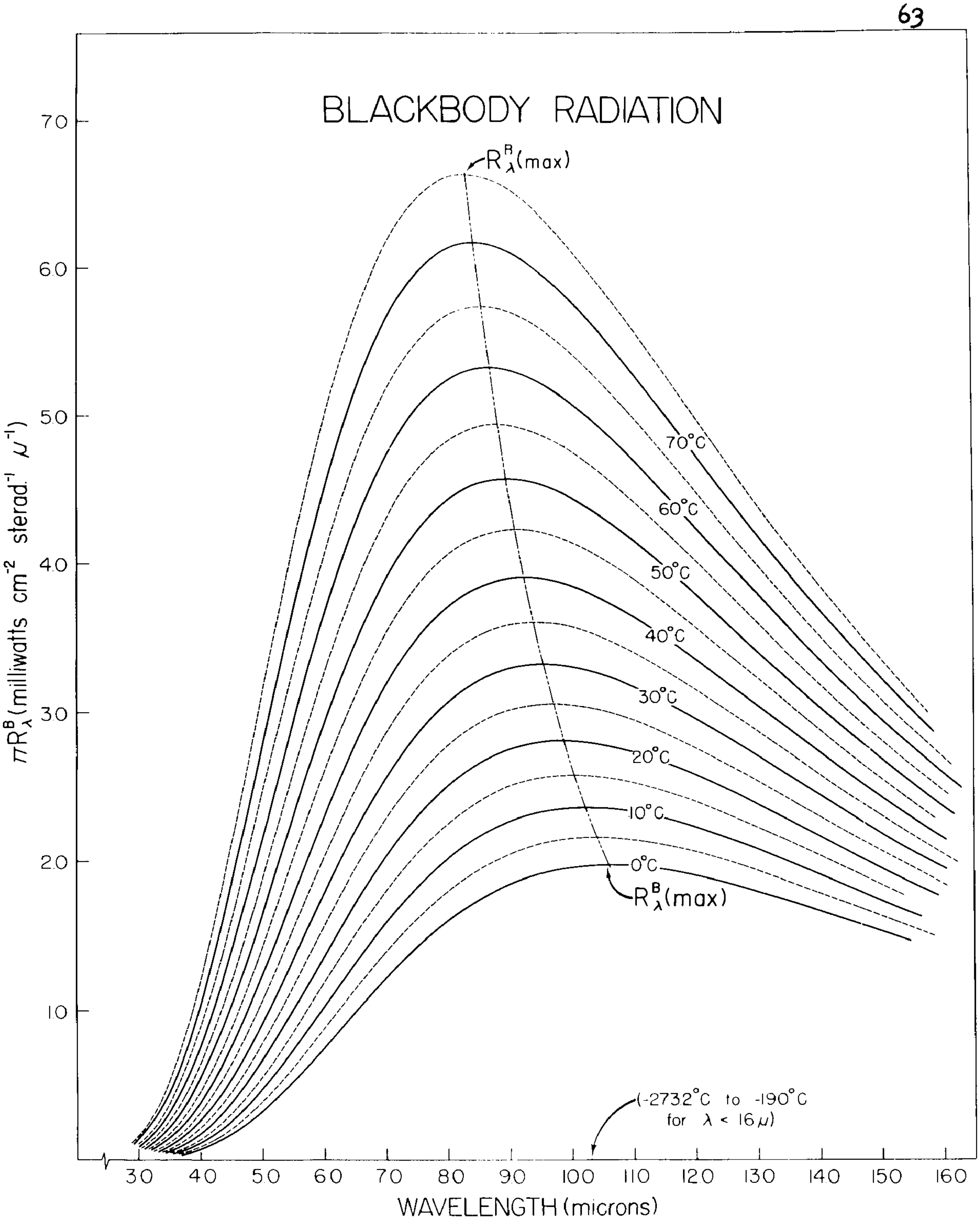

Figure 27. Curves of the Planck radiation function in terms of wavelength.

where C_1 and C_2 are constants. If πR_λ^B has the units of watts per cm^2 per cm wavelength interval then $C_1 = 3.732 \times 10^{-12}$ watts cm^2, $C_2 = 1.436$ cm °K and λ is given in cm. The values of $\pi R_{\lambda\ (max)}^B(T)$ and $\pi R_{0-\infty}^B(T)$ necessary to use the tables were found from corresponding values for T = 1,000° K and the use of Wien's law and the Stephan-Boltzman law respectively. A table of $\pi R_\lambda^B(T)$ was made from the curves of Figure 27 for every half-micron interval of λ and for 5° C intervals of T. Linear interpolation was used to find $\pi R_\lambda^B(T)$ for the temperature of the laboratory blackbody to the nearest tenth degree centigrade. With this value the radiation calibration constant was then found as described in section VI.

APPENDIX II Sources of Error in Radiation Measurements Within the Spectrograph

Most of the sources of error in connection with the measurements by the present instrument have been discussed in the text. Two additional types of error should be noted, however, which may arise due to events inside the spectrograph housing. The first type of error arises from the introduction of undispersed "chopped" radiation into the path of the exit slit and the thermocouple detector. This type of error is constant for all wavelength settings of the spectrograph. The major cause of this error is scattering of radiation by the first mirror following the entrance slit. The second type of error arises from the introduction of dispersed radiation of undesired wavelengths into the path of the exit slit and thermocouple detector. The dispersion of this radiation of wavelengths not included in the normal spectral interval, it is not well defined. Nevertheless this error does favor certain spectral regions and may change with the wavelength settings of the spectrograph and with the differences of the observed spectra. This error is caused by scattering of undispersed radiation at various reflecting surfaces, by so called "ghost reflections" of dispersed radiation at the surfaces of the prism and by a second pass of some of the radiation through the dispersing arrangement.

Since scattering usually increases with frequency, one would expect the first type of error mentioned above to increase with radiation of shorter wavelengths. Now in the solar spectrum more than ninety-eight per cent of the radiant energy is of wavelengths below the wavelength region of this study. Thus in a recording of the solar spectrum the error due to scattering of undispersed radiation is relatively large for the wavelength region 4.0 to 15.5 μ as compared to the corresponding error in the present data on sky radiation. From considerations of recordings of the solar spectrum taken with the alternate use of an opaque chopper and a glass chopper, this error is negligible for the present data.

It was also noted from the solar spectrum that the magnitude of the total observed error was relatively constant but did increase slightly toward the shorter wavelength settings of the spectrograph. This was the only conclusive observation of an error of the second type and this error as noted above was negligible for the present data. This does not preclude the possibility of an error of the second type arising from "second-pass" radiation, which for the present spectrograph would be of wavelengths longer than those of the principal radiation being observed. For the present data one would expect to find such an error by studies of radiation of wavelengths 4 to 5 μ, for which the emissive power of the sky and of a blackbody at temperatures of the order of 300° K are low compared to their emissive power at longer wavelengths. Unfortunately the low resolving power of the present spectrograph in this wavelength region prevented accurate estimates of this error, but from the observation of sky spectra of different air masses it is estimated that this error would not contribute more than one per cent error to the value of R^S_{1-2} for the wavelength region 4.0 to 15.5 μ.

APPENDIX III Observations on December 6 and 7, 1954

There were three essential differences in conditions the night of December 6 and 7, 1954, from those of preceding observation periods. (1) The outside air temperature was lower, (2) the absolute humidity was lower and (3) a larger slitwidth was used, partly because of the decreased radiation from the sky and partly because of the decrease in sensitivity of the thermocouple. The low air temperature proved to be of considerable consequence in obtaining accurate and readable spectra.

It was noted that after the laboratory window had been opened for an hour or more, the "noise" of the recording began to increase. It was found that increased heating of the spectrograph by its own electric heater and by an additional electric heater on the back of the spectrograph housing decreased the noise considerably and prolonged the period in which readable spectra could be recorded. Although no verifying experiments have been conducted, it is believed that normal instrument vibrations and the increase of temperature gradients inside the spectrograph were the joint cause of most of this noise.

During the night of December 6 and 7, some negative deflections were observed in the recordings of the sky spectrum in the wavelength region between 10 and 12 μ. The radiation represented by these negative deflections was not in excess of two per cent of blackbody radiation at laboratory temperatures. These negative deflections were probably caused by (1) non-zero radiation from the liquid-nitrogen path and (2) the large difference in temperature between the outside mirror

M_1 of Figure 2 in the text and the mirrors inside. In either case the true zero of the recording would be depressed from the zero indicated by the shutter which excludes all interrupted radiation to the thermocouple. In the case of (1) one may assume the true zero to be depressed by the value

$$D_\lambda^{(1)} = \varepsilon^{(1)} R_\lambda^B(T_L)/K_\lambda , \qquad (21)$$

where T_L is the temperature of the laboratory and $\varepsilon^{(1)}$ is a parameter which may depend on λ. Note that $\varepsilon^{(1)}$, a function of wavelength, cannot be determined definitely without complete knowledge of the radiation in the liquid-nitrogen path. For simplicity $\varepsilon^{(1)}$ is assumed to be constant. For the second case the depression of the true zero may assume the form

$$D_\lambda^{(2)} = \varepsilon^{(2)} [R_\lambda^B(T_L) - R_\lambda^B(T_o)]/K_\lambda , \qquad (22)$$

where $\varepsilon^{(2)}$ is a parameter perhaps dependent upon λ, but for simplicity is also assumed to be constant. With the knowledge of the maximum negative deflection, T_L, T_o and K_λ one may examine the possible values of $\varepsilon^{(1)}$ and $\varepsilon^{(2)}$ with the use of equations (21) and (22) respectively. If one asserts that the maximum negative deflection represents the true zero and that all of the depression of the true zero is due to non-zero radiation from the liquid-nitrogen path then a value for $\varepsilon^{(1)}$ of 0.013 results. For the assertion that the difference between T_L and T_o is the cause of the depressed zero $\varepsilon^{(2)}$ has a value of 0.043. Now it is true that the maximum negative deflection may not represent the true depressed zero. The point to be emphasized here, however, is the plausibility of these values. The value of 0.013 for $\varepsilon^{(1)}$ is quite plausible since either the radiation reflected from the surface of the liquid nitrogen or radiation from the additional mirror in the liquid-nitrogen path might explain this value. On the other hand, a value of 0.043 for $\varepsilon^{(2)}$ is higher than expected, since the emissivity of the outside mirror was not expected to be above 0.03. It was assumed, therefore, that the depression of the true zero was a linear combination of these two effects and the recorder deflections of this night were modified by adding the deflection

$$D_\lambda^{(1)+(2)} = \left\{0.0065\, R_\lambda^B(T_L) + 0.0215\left[R_\lambda^B(T_L) - R_\lambda^B(T_0)\right]\right\} / K_\lambda . \qquad (23)$$

The choice of constants was purely arbitrary at this point and divided the depressed zero equally between the two causes mentioned. No attempt was made to modify deflections of previous data or the calibration constant K_λ , since the corrections would be small and of necessity would be based upon incomplete knowledge.

It should also be noted that a wavelength calibration shift was observed as the temperature of the spectrograph changed. Under the normal temperature changes of the laboratory this effect is not observed, since the exit mirror on the prism mount is temperature compensated to decrease this shift. The magnitude and direction of the shift was not difficult to follow with the aid of the sky spectrum and did not introduce serious error into the observed values.

APPENDIX IV Curves of Radiation Ratio as a Function of the Square Root of the Air Mass

This appendix contains Figures 28 through 70 which consist of curves of the radiation ratio as a function of the square root of the air mass for the various wavelength intervals selected. The date, period and wavelength interval are noted on each page. Unless otherwise indicated the sky was clear for the observed spectra. The term "clear sky" is used here to denote a homogeneous blue sky, free of visible clouds in the small region of observation. It is possible that high, thin haze and high cloud formations were not detected at times and that some of these conditions existed for parts of the data presented for a clear sky. It was noted, however, that high cirrus clouds produced only a small increase in radiation in the wavelength region 8 to 12 μ. The temperature and humidity for most of the observation periods associated with these curves are given in the tables in Appendix V.

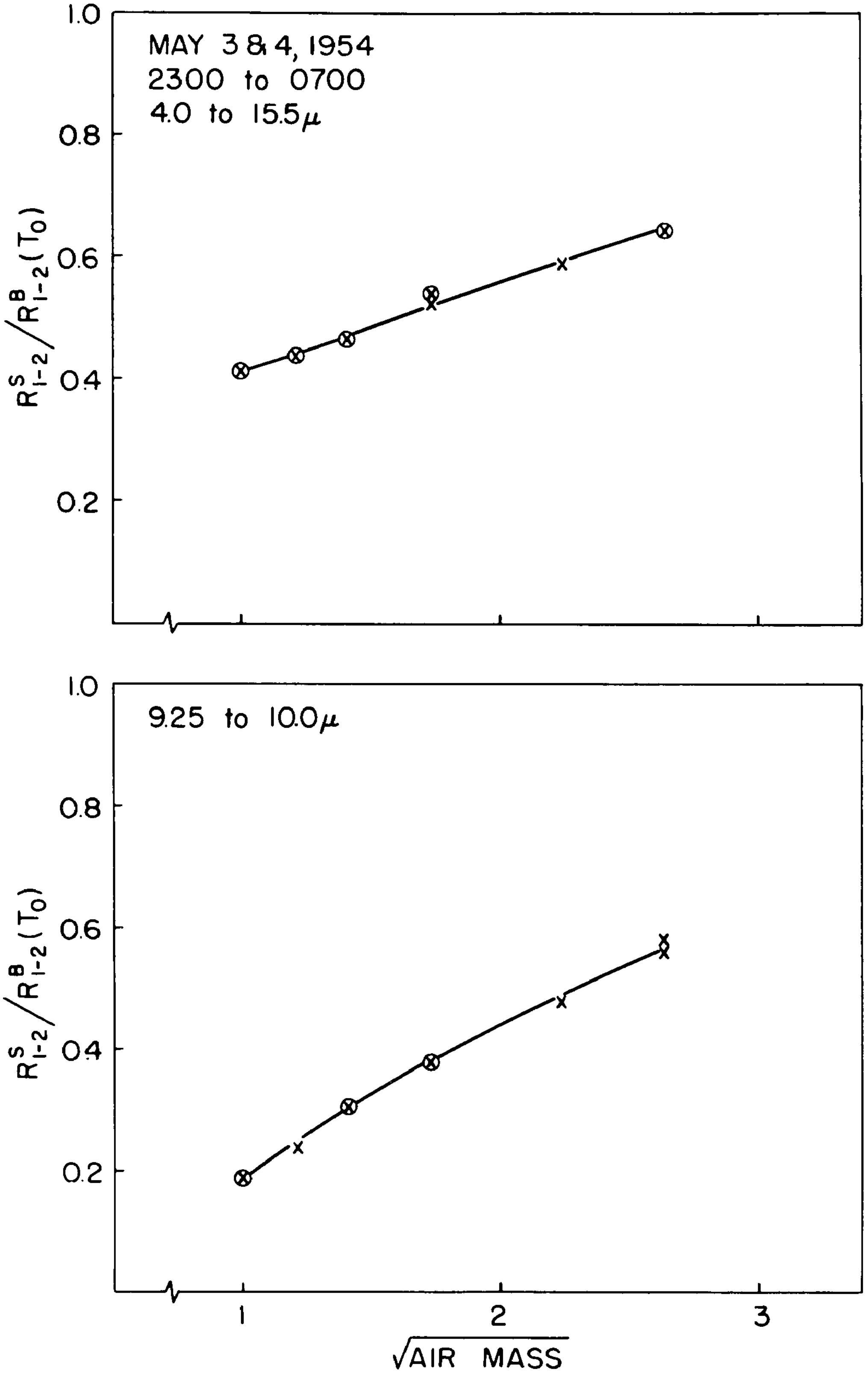
MAY 3 & 4, 1954
2300 to 0700
4.0 to 15.5μ
9.25 to 10.0μ
$R^S_{1-2} / R^B_{1-2}(T_0)$
1.0
0.8
0.6
0.4
0.2
1
2
3
√AIR MASS

Figure 28.

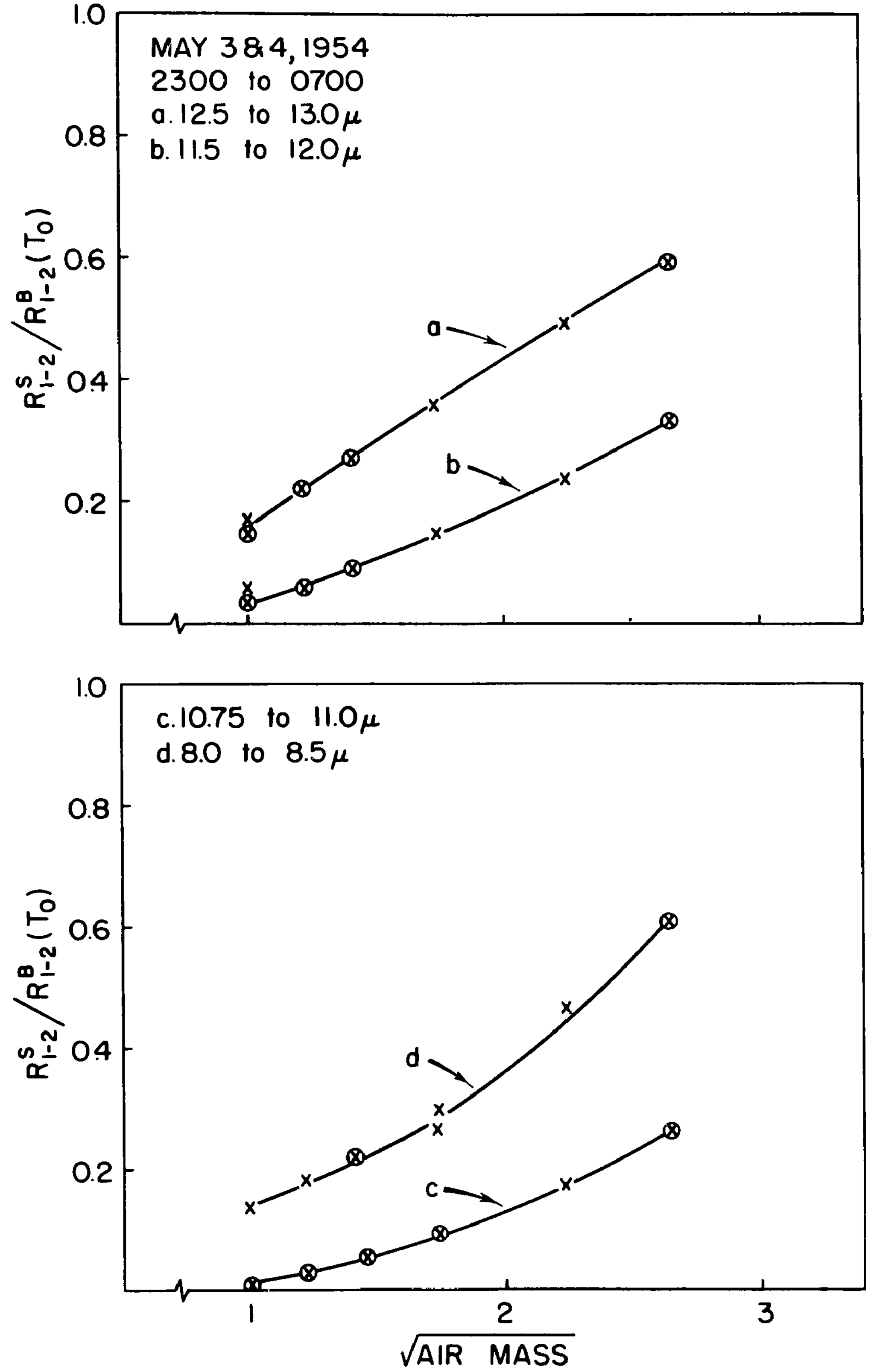
MAY 3&4, 1954
2300 to 0700
a. 12.5 to 13.0μ
b. 11.5 to 12.0μ
c. 10.75 to 11.0μ
d. 8.0 to 8.5μ
a
b
c
d
1.0
0.8
0.6
0.4
0.2
1
2
3
$R^S_{1-2} / R^B_{1-2}(T_0)$
√AIR MASS

Figure 29.

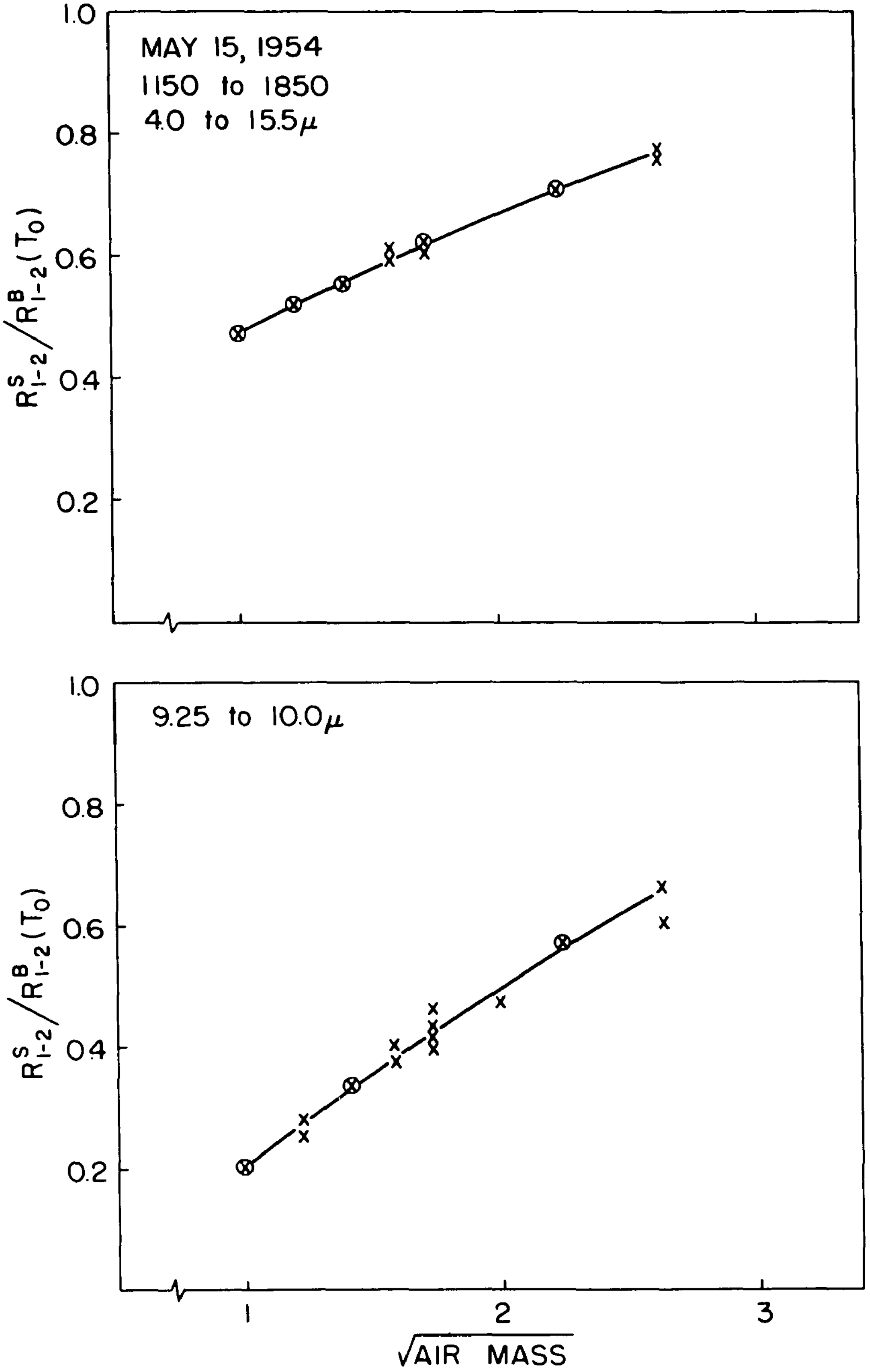
MAY 15, 1954
1150 to 1850
4.0 to 15.5μ
9.25 to 10.0μ
$R^S_{1-2}/R^B_{1-2}(T_0)$
1.0
0.8
0.6
0.4
0.2
1
2
3
$\sqrt{\text{AIR MASS}}$

Figure 30.

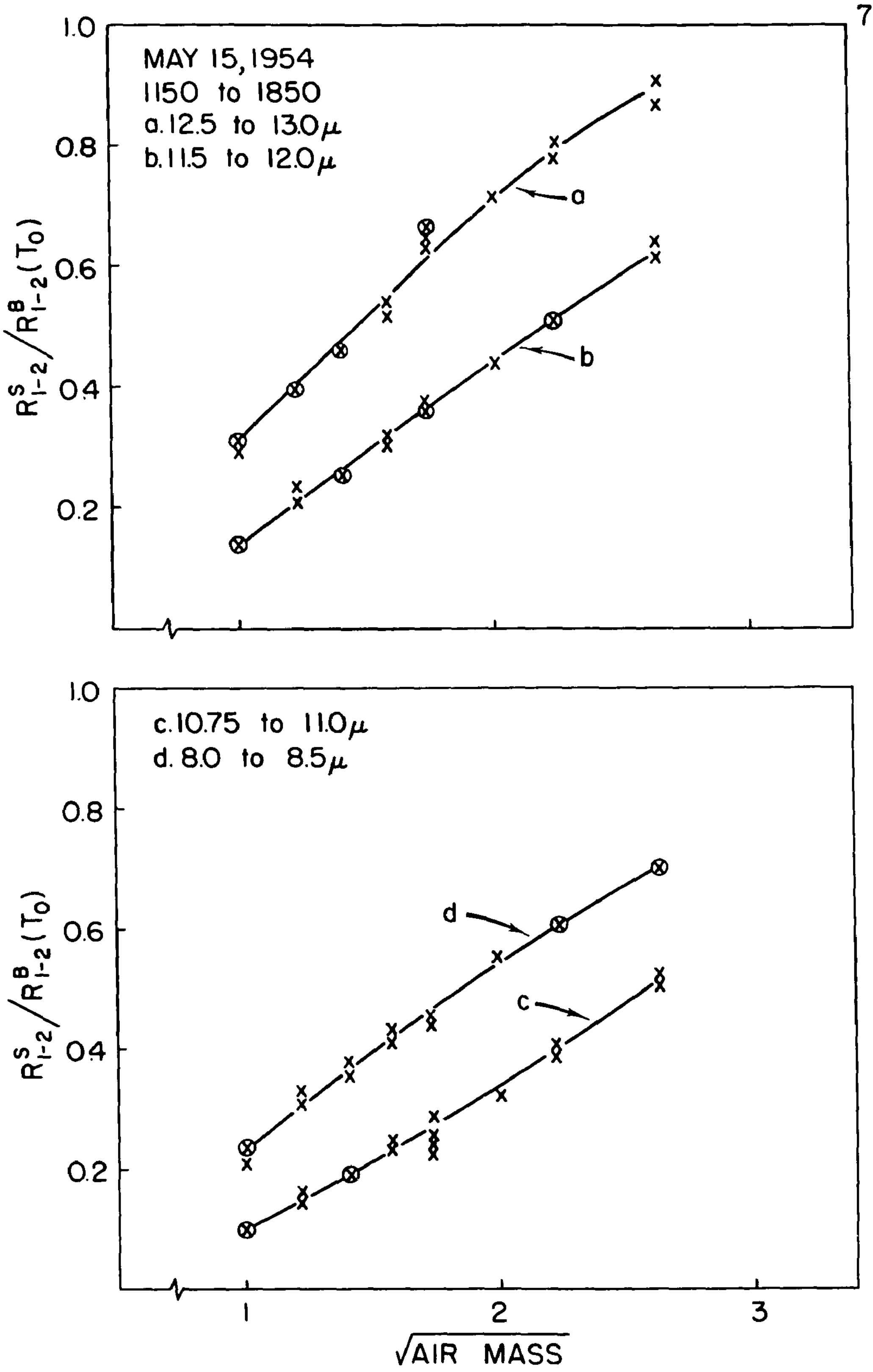
MAY 15, 1954
1150 to 1850
a. 12.5 to 13.0μ
b. 11.5 to 12.0μ
a
b
c. 10.75 to 11.0μ
d. 8.0 to 8.5μ
d
c
1.0
0.8
0.6
0.4
0.2
$R^{S}_{1-2}/R^{B}_{1-2}(T_0)$
1
2
3
$\sqrt{\text{AIR MASS}}$

Figure 31.

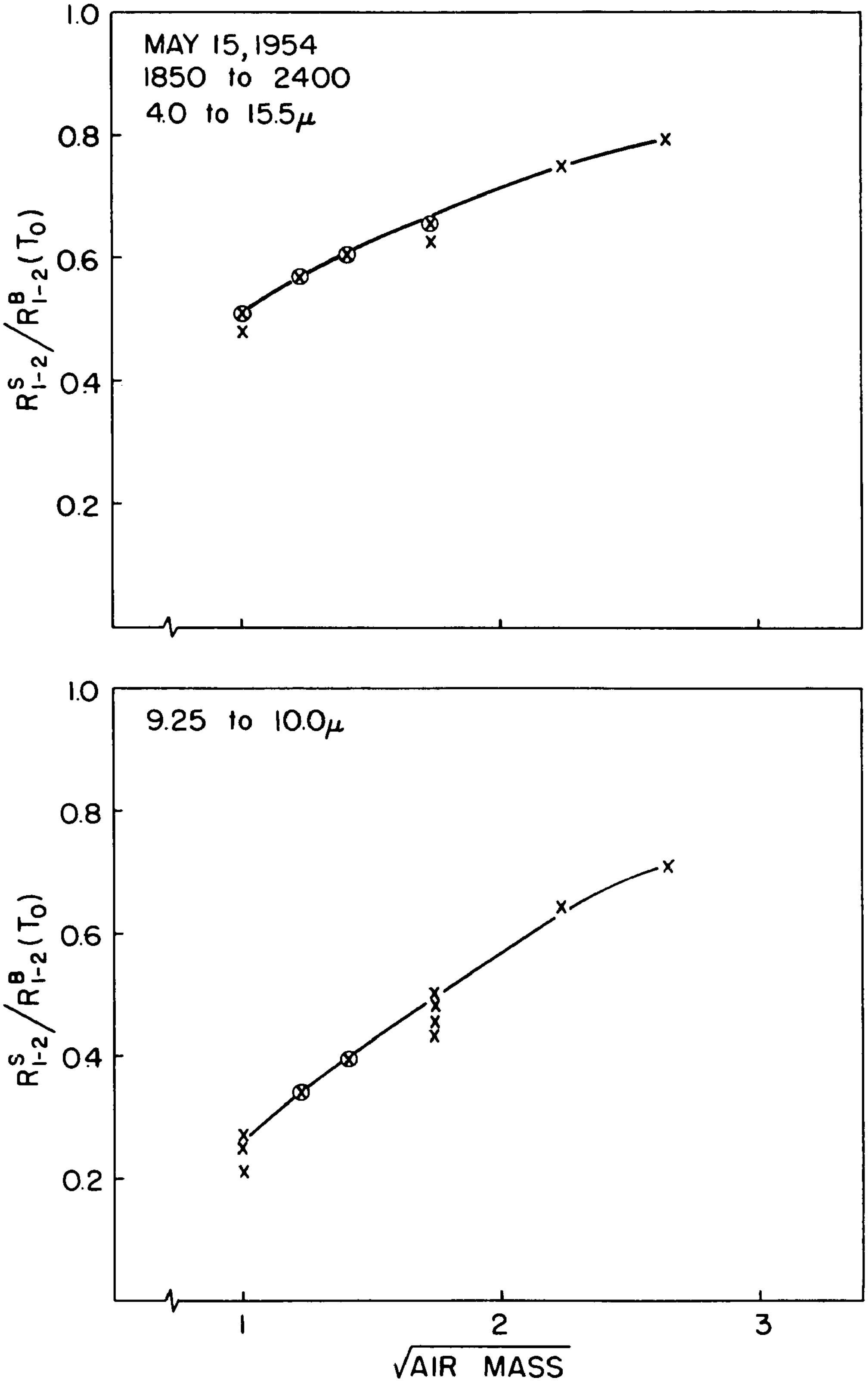
MAY 15, 1954
1850 to 2400
4.0 to 15.5μ
9.25 to 10.0μ
$R^S_{1-2}/R^B_{1-2}(T_0)$
1.0
0.8
0.6
0.4
0.2
1
2
3
√AIR MASS

Figure 32.

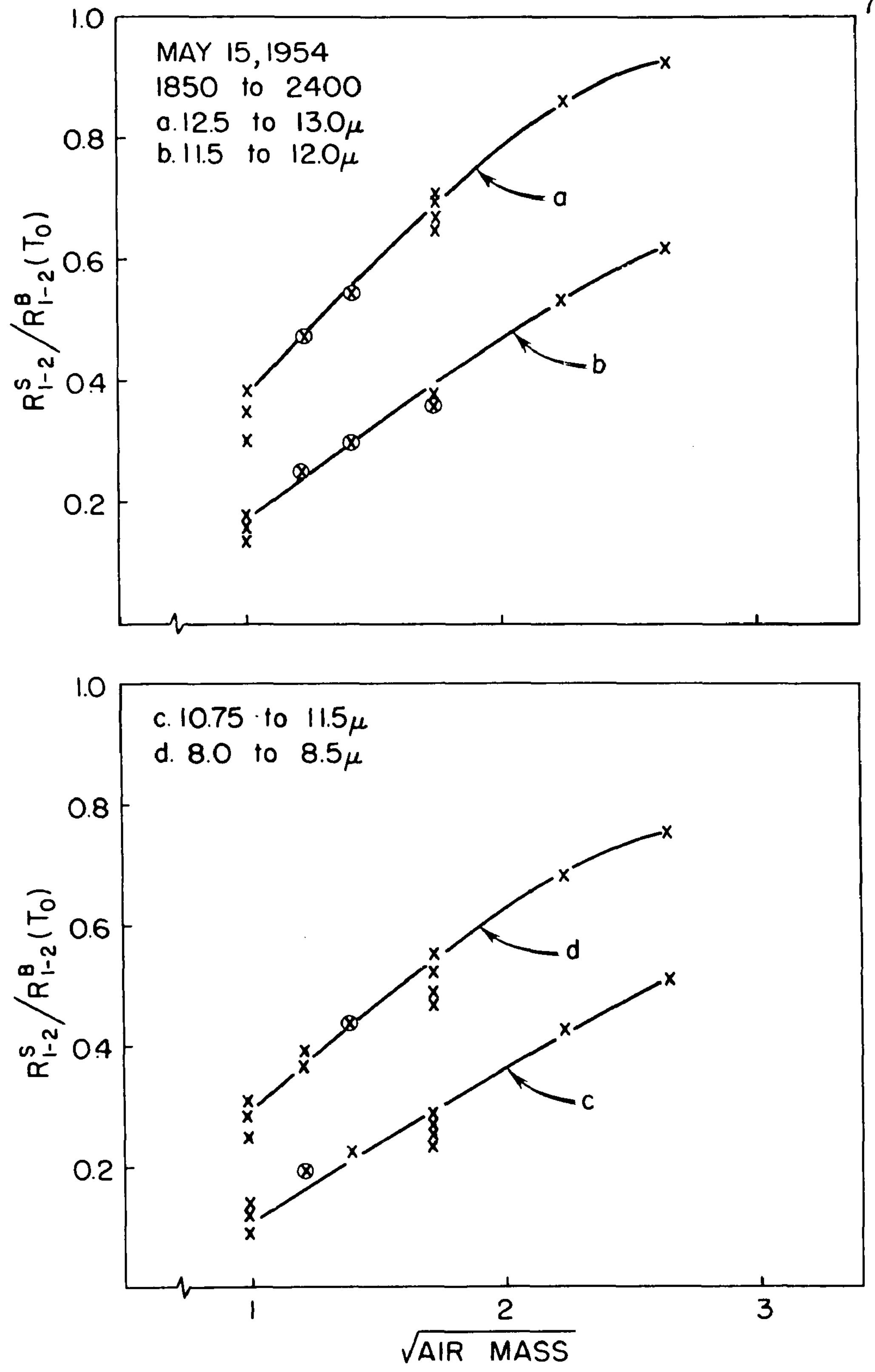
MAY 15, 1954
1850 to 2400
a. 12.5 to 13.0μ
b. 11.5 to 12.0μ
a
b
c. 10.75 to 11.5μ
d. 8.0 to 8.5μ
d
c
$R^S_{1-2}/R^B_{1-2}(T_0)$
1.0
0.8
0.6
0.4
0.2
1
2
3
$\sqrt{\text{AIR MASS}}$

Figure 33.

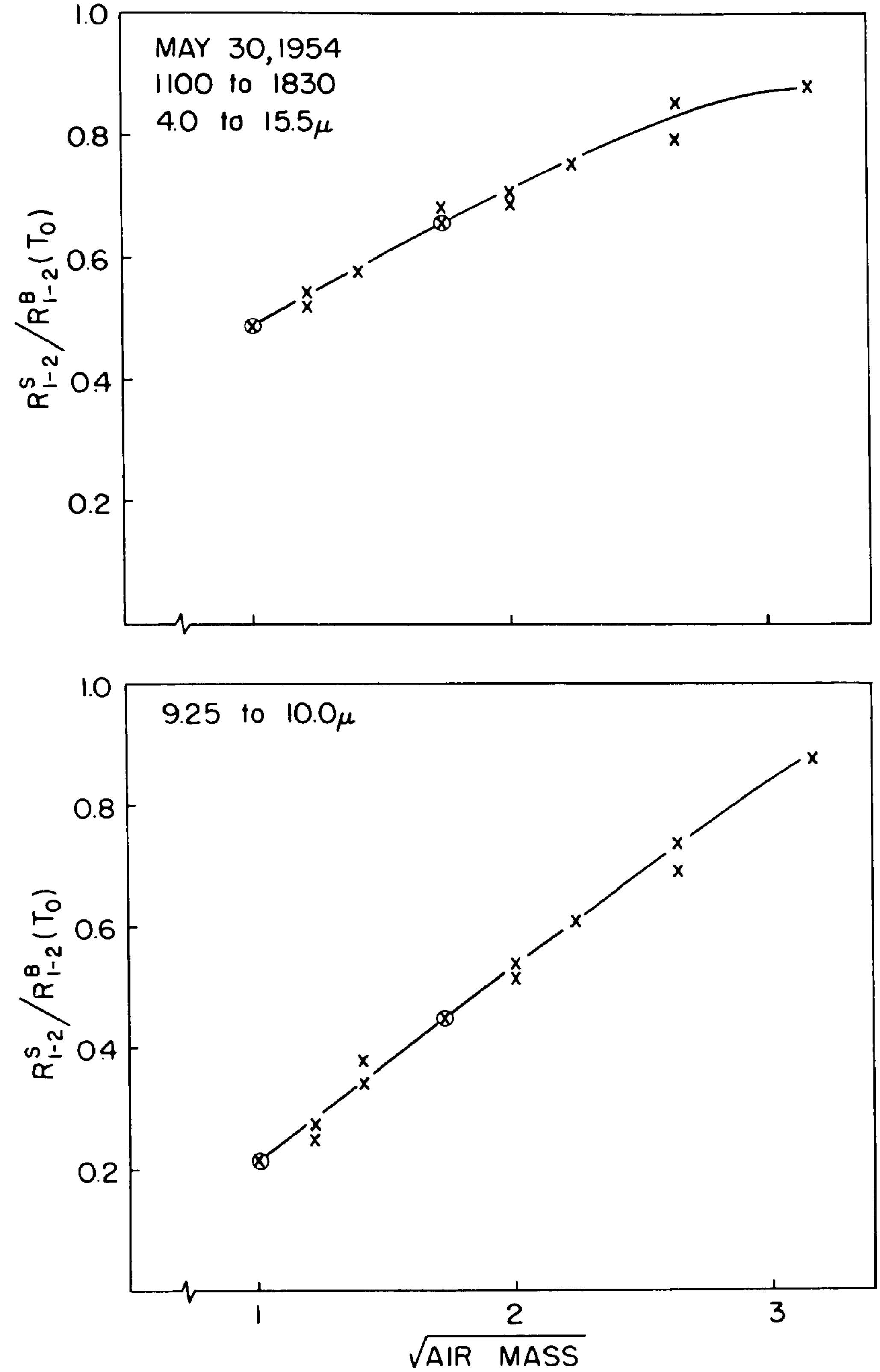
MAY 30, 1954
1100 to 1830
4.0 to 15.5μ
1.0
0.8
0.6
0.4
0.2
$R^S_{1-2}/R^B_{1-2}(T_0)$
9.25 to 10.0μ
1.0
0.8
0.6
0.4
0.2
$R^S_{1-2}/R^B_{1-2}(T_0)$
1
2
3
√AIR MASS

Figure 34.

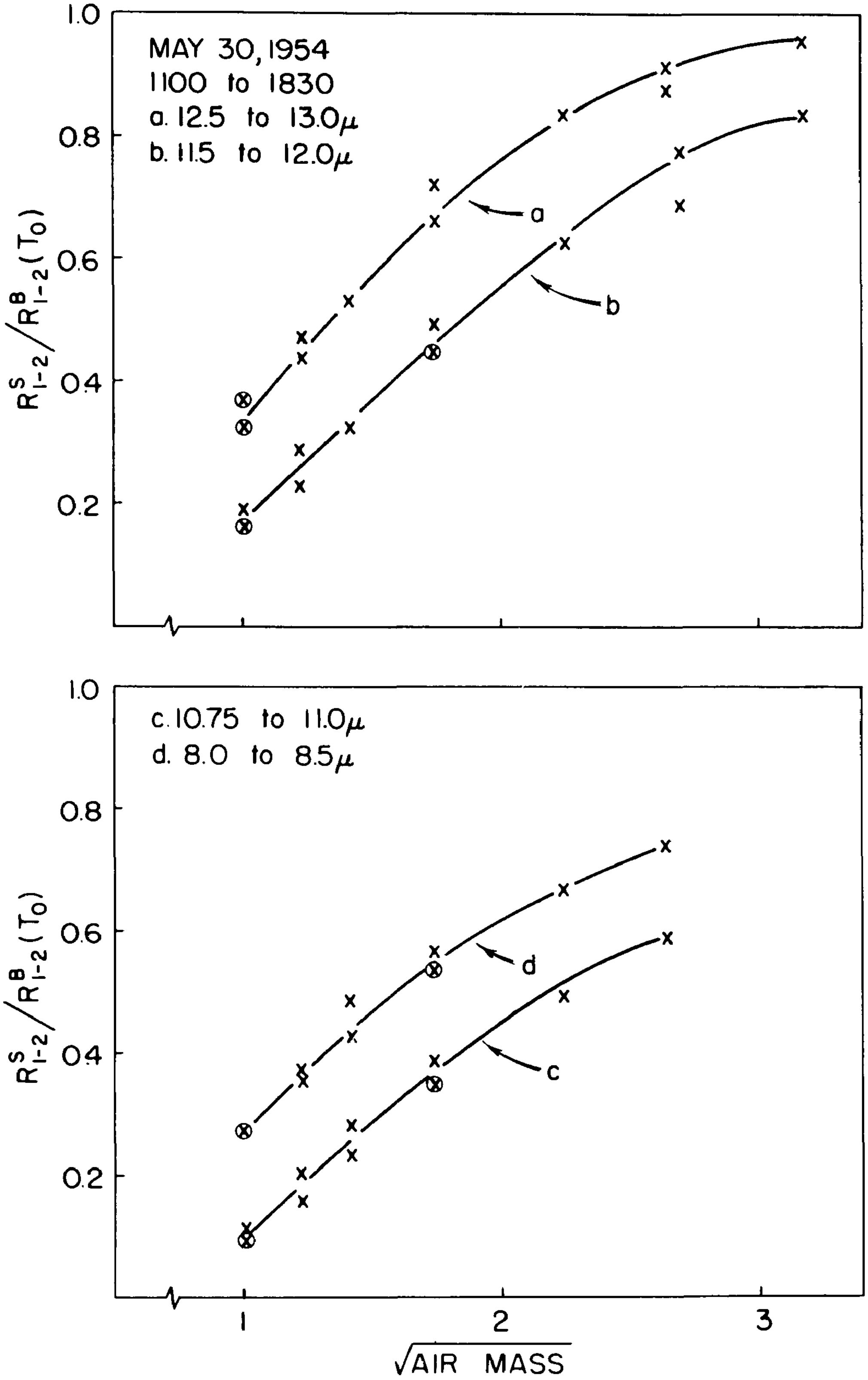
MAY 30, 1954
1100 to 1830
a. 12.5 to 13.0μ
b. 11.5 to 12.0μ
c. 10.75 to 11.0μ
d. 8.0 to 8.5μ
a
b
c
d
$R^S_{1-2}/R^B_{1-2}(T_0)$
1.0
0.8
0.6
0.4
0.2
1
2
3
√AIR MASS

Figure 35.

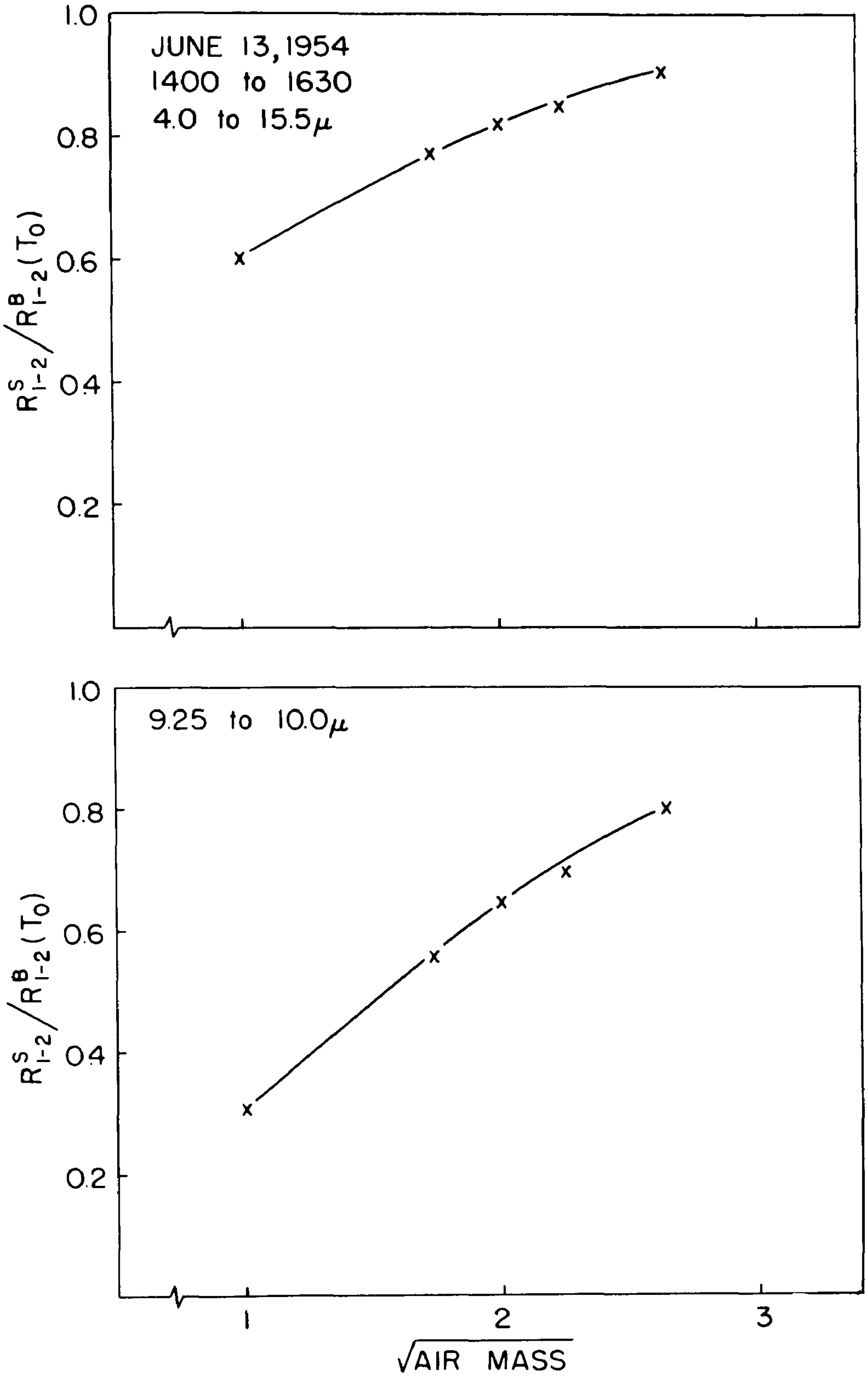
JUNE 13,1954
1400 to 1630
4.0 to 15.5μ
9.25 to 10.0μ
$R^S_{1-2}/R^B_{1-2}(T_0)$
1.0
0.8
0.6
0.4
0.2
1
2
3
√AIR MASS

Figures 36.

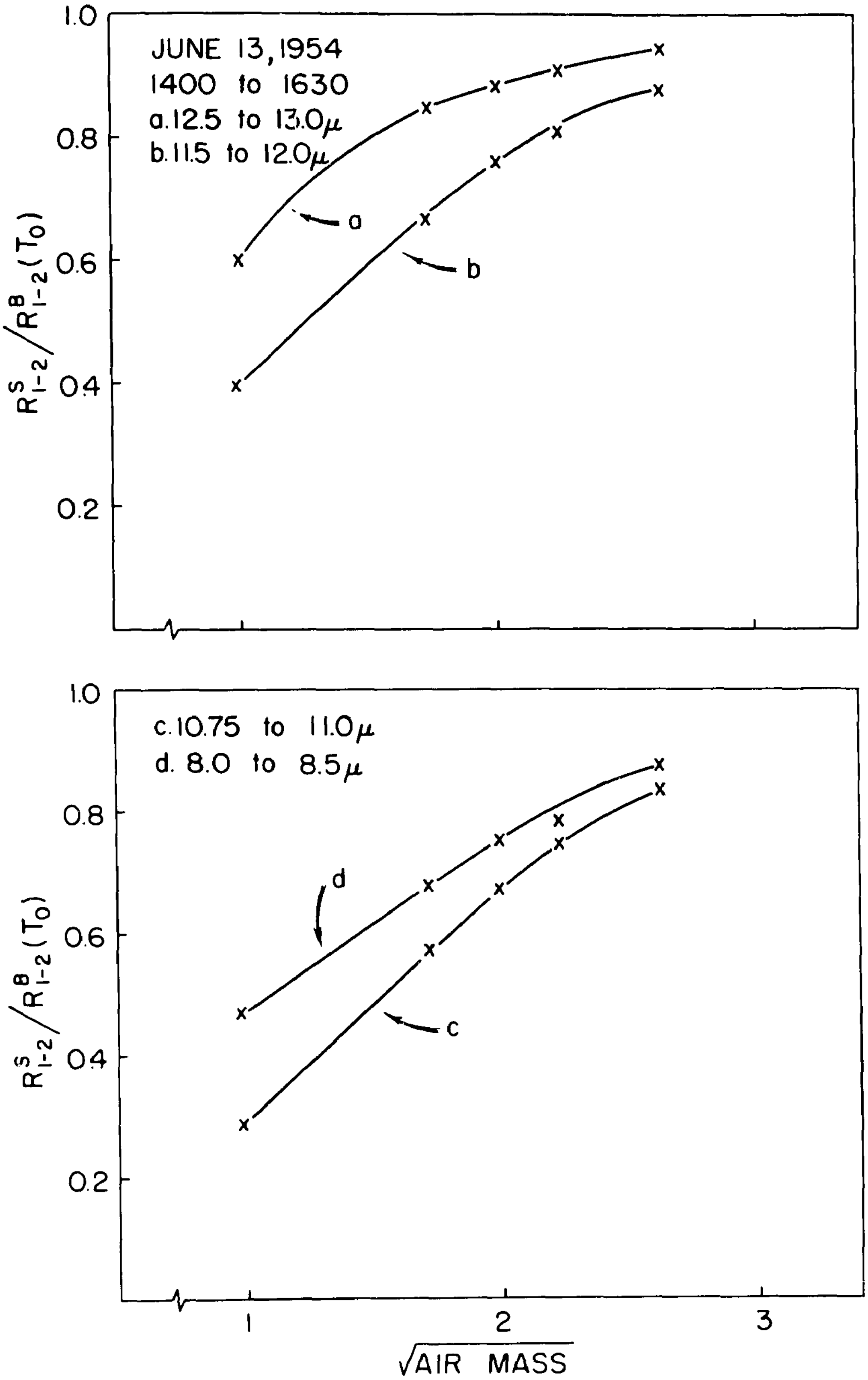
1.0
0.8
0.6
0.4
0.2
$R^S_{1-2} / R^B_{1-2}(T_0)$
JUNE 13, 1954
1400 to 1630
a. 12.5 to 13.0μ
b. 11.5 to 12.0μ
a
b
c. 10.75 to 11.0μ
d. 8.0 to 8.5μ
d
c
1
2
3
√AIR MASS

Figure 37.

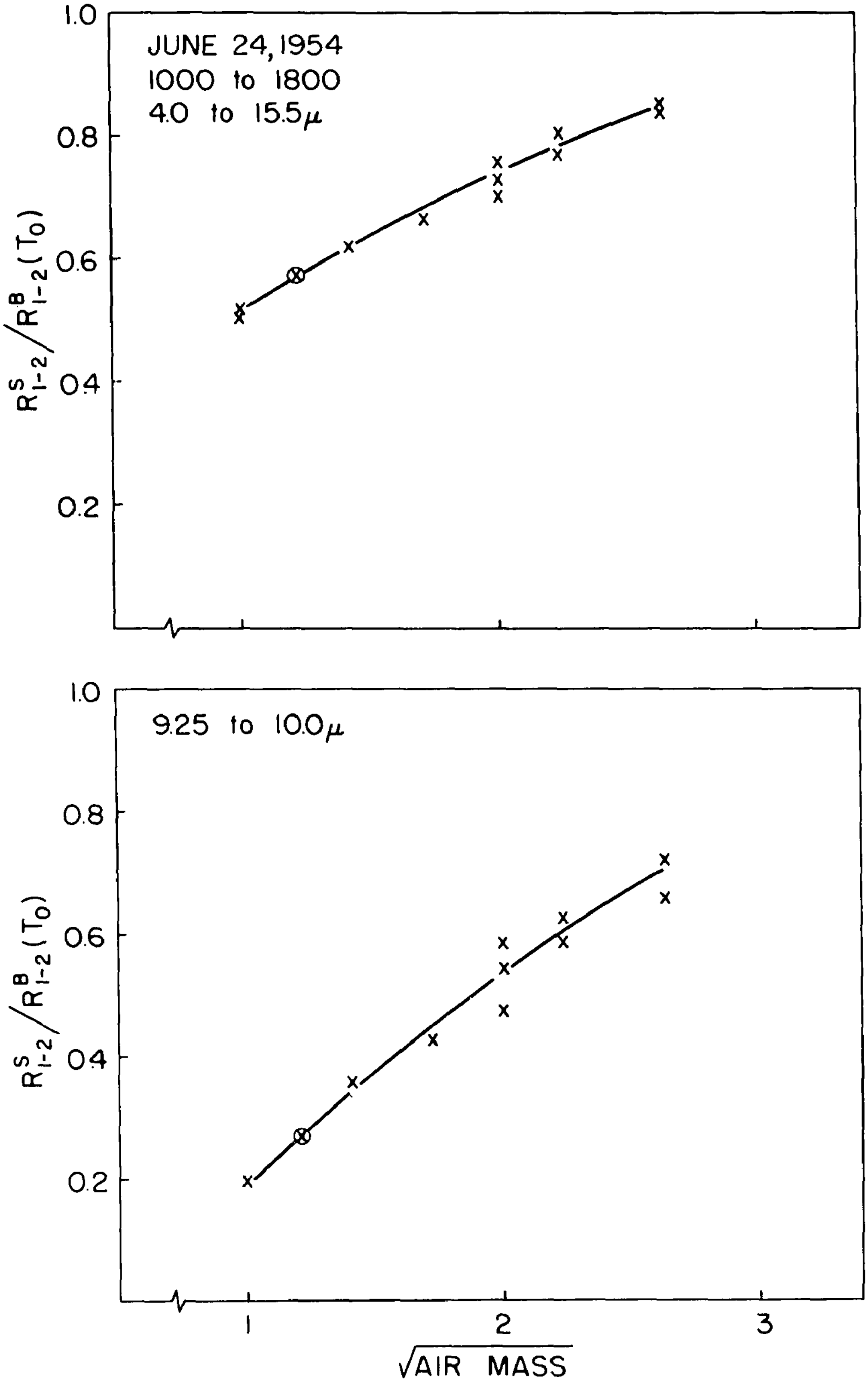
JUNE 24, 1954
1000 to 1800
4.0 to 15.5μ
9.25 to 10.0μ
1.0
0.8
0.6
0.4
0.2
$R^S_{1-2}/R^B_{1-2}(T_0)$
1
2
3
√AIR MASS

Figure 38.

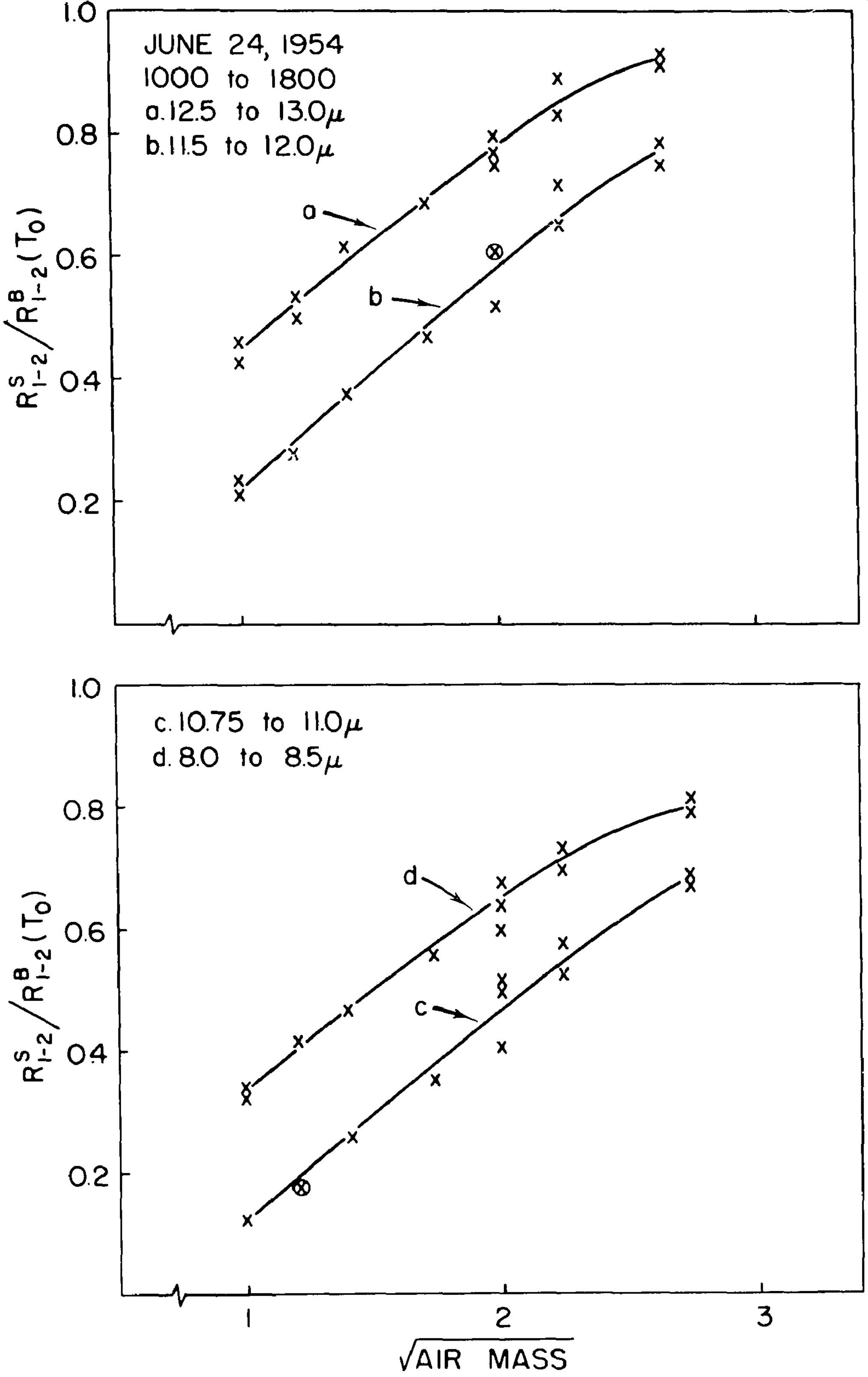
JUNE 24, 1954
1000 to 1800
a. 12.5 to 13.0μ
b. 11.5 to 12.0μ
a
b
c. 10.75 to 11.0μ
d. 8.0 to 8.5μ
d
c
1.0
0.8
0.6
0.4
0.2
$R^S_{1-2} / R^B_{1-2}(T_0)$
1
2
3
√AIR MASS

Figure 39.

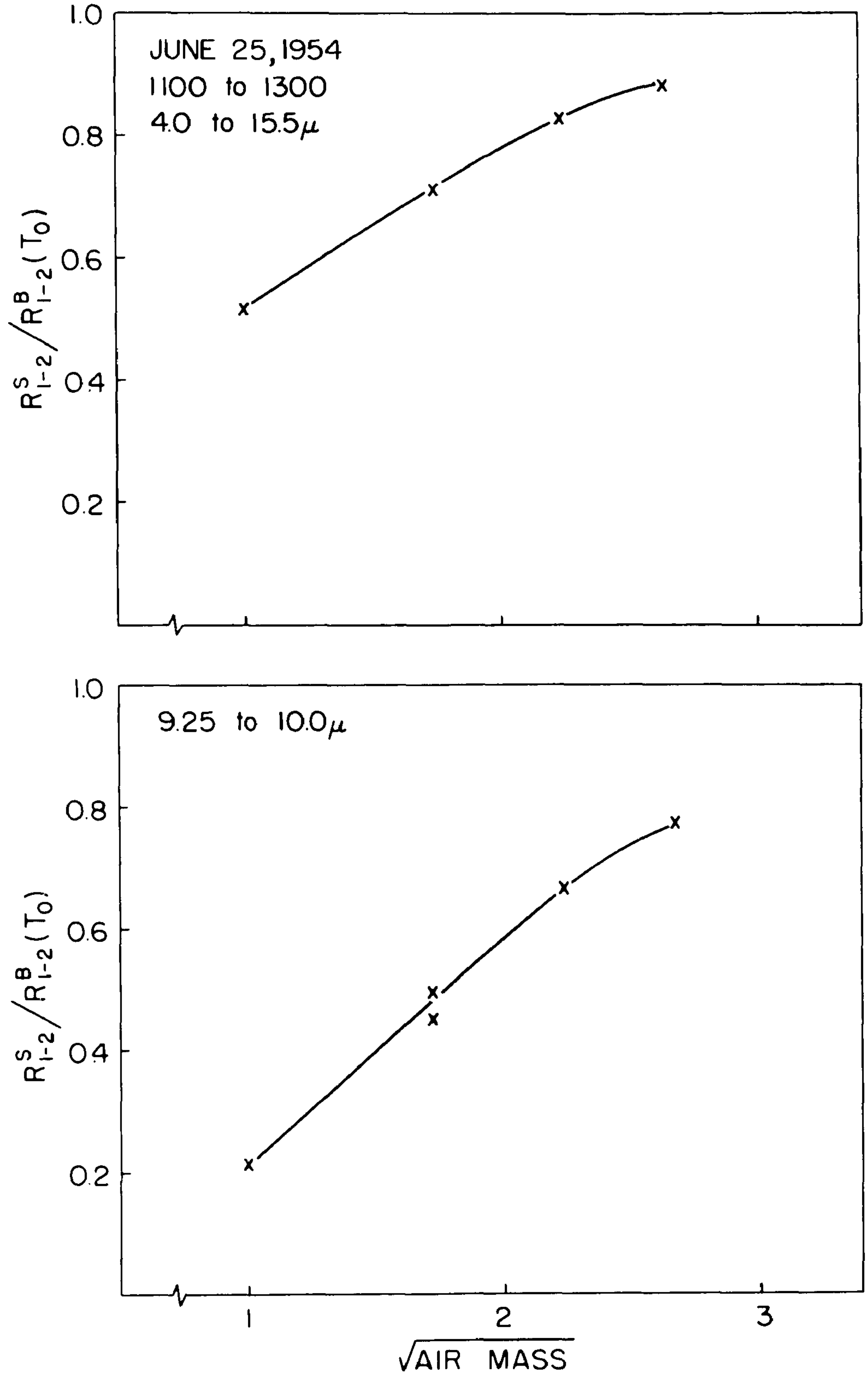
JUNE 25, 1954
1100 to 1300
4.0 to 15.5μ
9.25 to 10.0μ
1.0
0.8
0.6
0.4
0.2
$R^S_{1-2}/R^B_{1-2}(T_0)$
1
2
3
$\sqrt{\text{AIR MASS}}$

Figure 40.

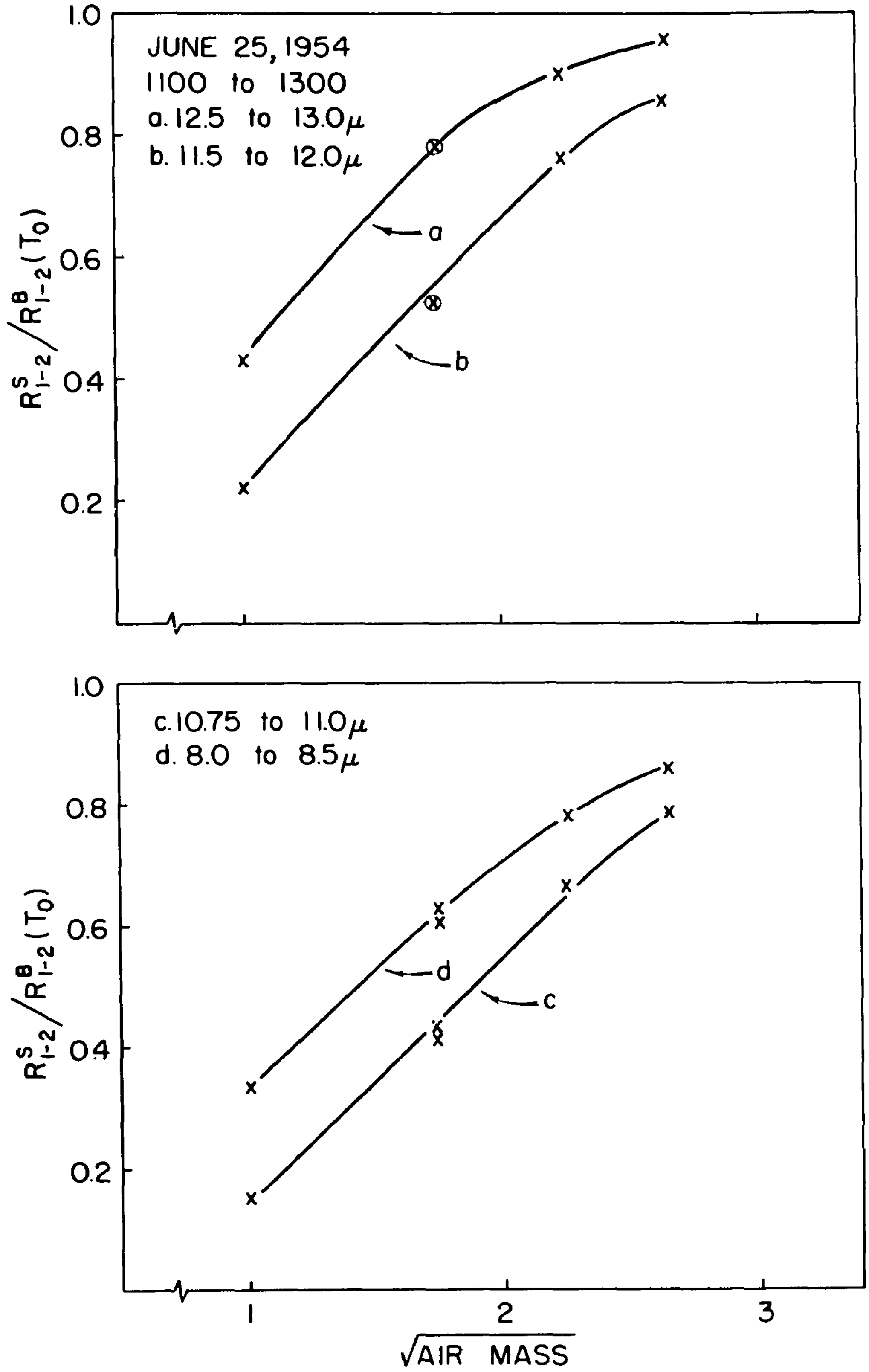
JUNE 25, 1954
1100 to 1300
a. 12.5 to 13.0μ
b. 11.5 to 12.0μ
a
b
c. 10.75 to 11.0μ
d. 8.0 to 8.5μ
d
c
$R^S_{1-2} / R^B_{1-2}(T_0)$
1.0
0.8
0.6
0.4
0.2
1
2
3
√AIR MASS

Figure 41.

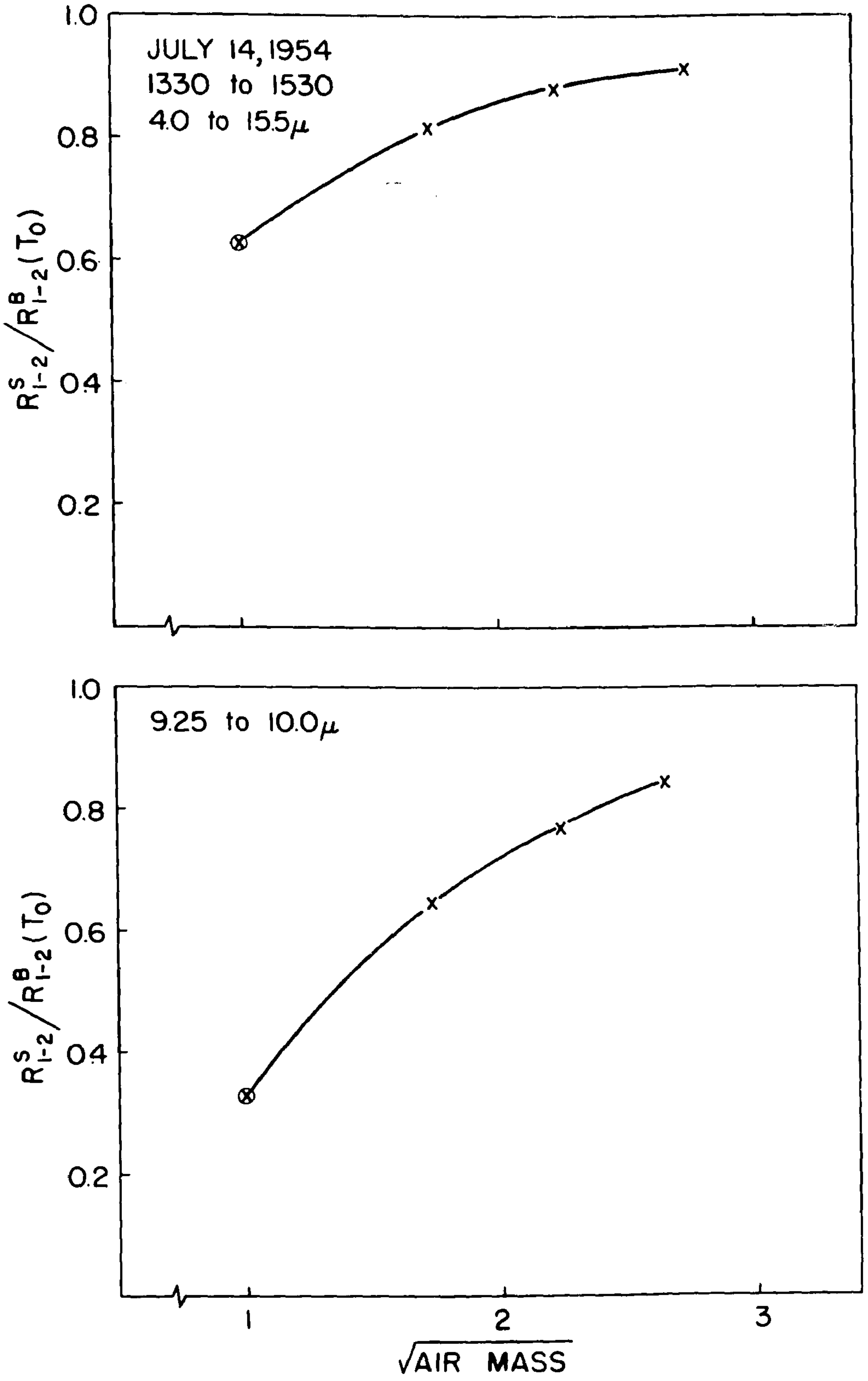
JULY 14, 1954
1330 to 1530
4.0 to 15.5μ
9.25 to 10.0μ
$R^S_{1-2}/R^B_{1-2}(T_0)$
1.0
0.8
0.6
0.4
0.2
1
2
3
√AIR MASS

Figure 42.

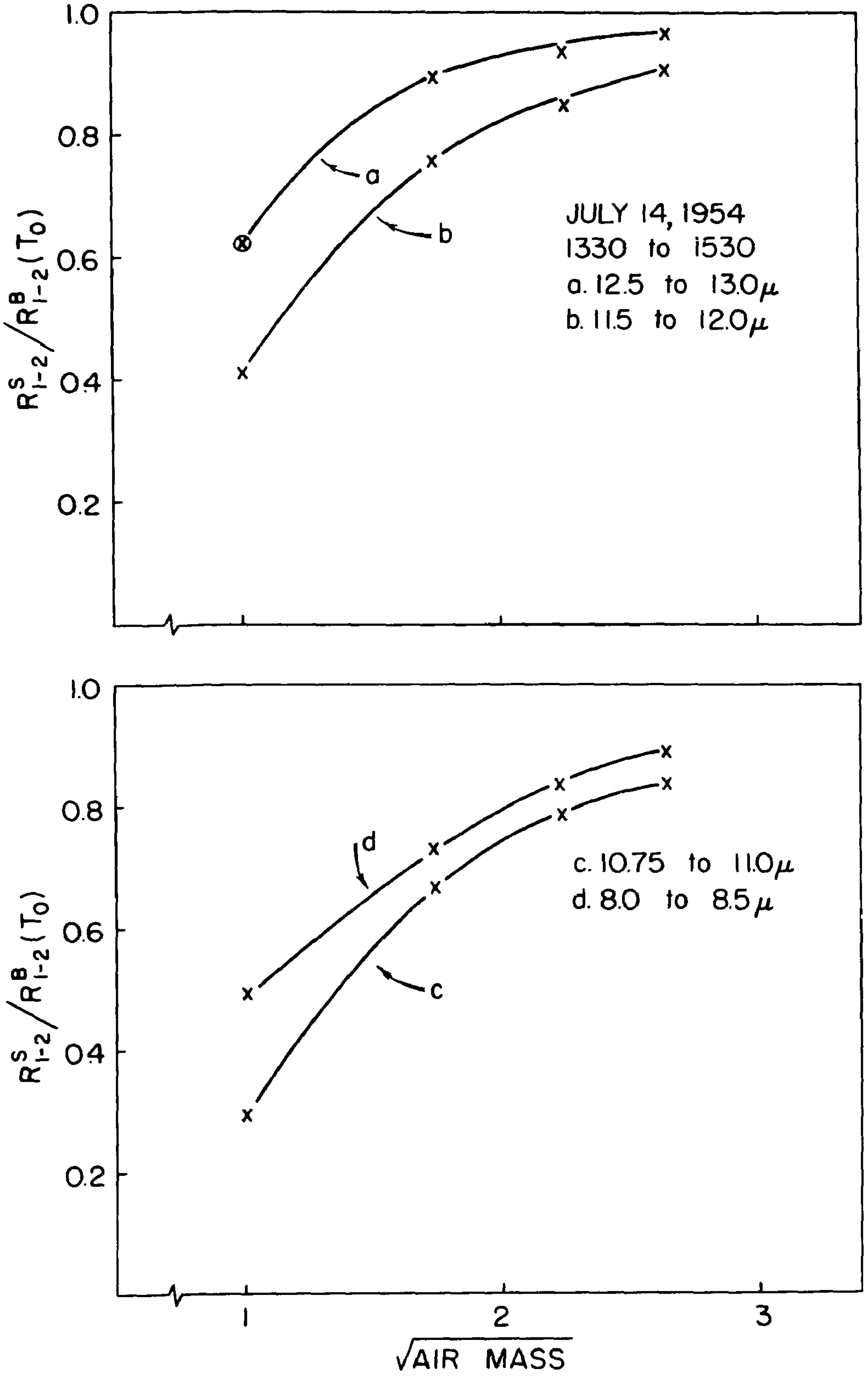
1.0
0.8
0.6
0.4
0.2
$R^S_{1-2}/R^B_{1-2}(T_0)$
a
b
JULY 14, 1954
1330 to 1530
a. 12.5 to 13.0μ
b. 11.5 to 12.0μ
1.0
0.8
0.6
0.4
0.2
$R^S_{1-2}/R^B_{1-2}(T_0)$
d
c
c. 10.75 to 11.0μ
d. 8.0 to 8.5μ
1
2
3
√AIR MASS

Figure 43.

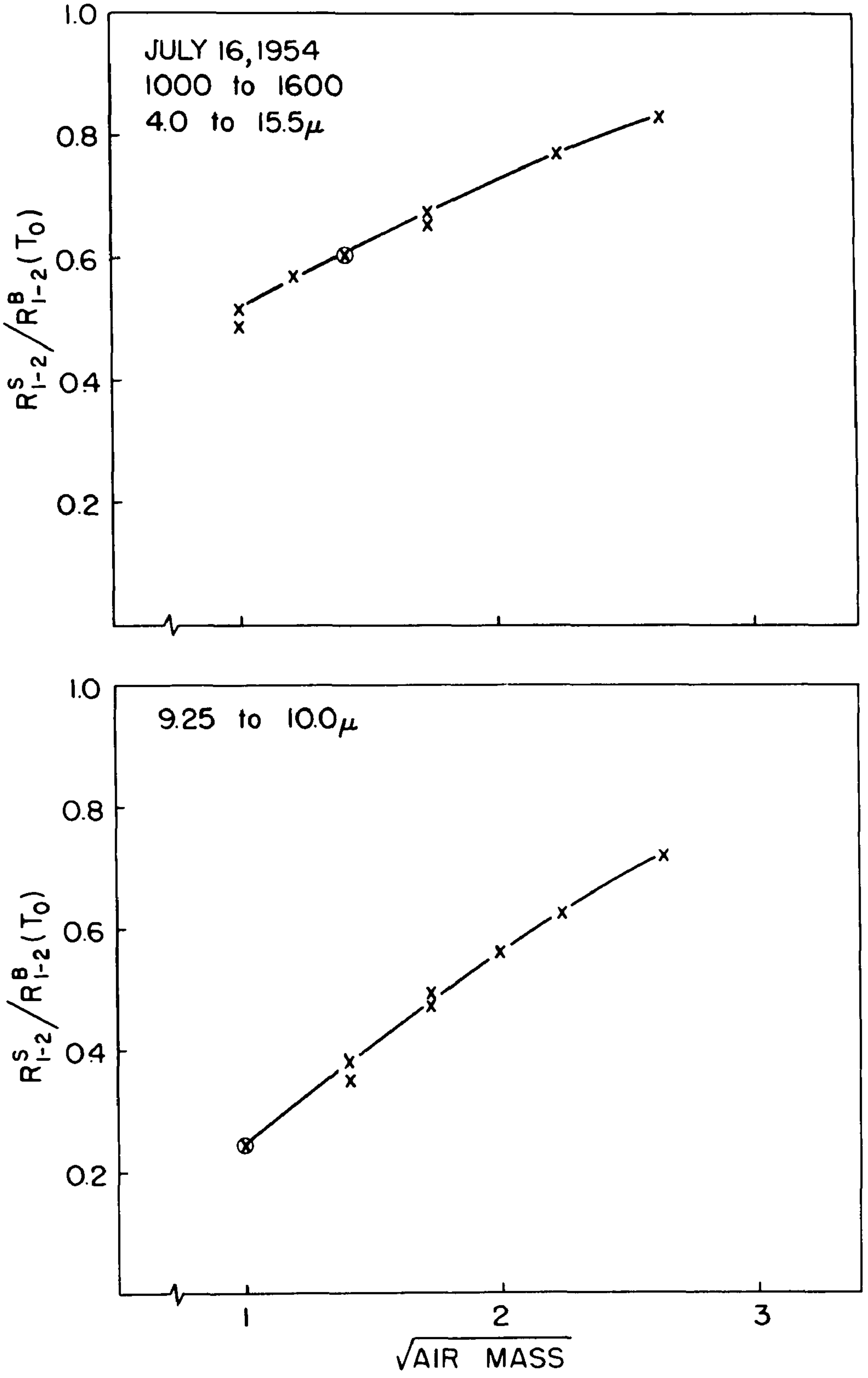
JULY 16, 1954
1000 to 1600
4.0 to 15.5μ
9.25 to 10.0μ
$R^S_{1-2} / R^B_{1-2}(T_0)$
1.0
0.8
0.6
0.4
0.2
1
2
3
$\sqrt{\text{AIR MASS}}$

Figure 44.

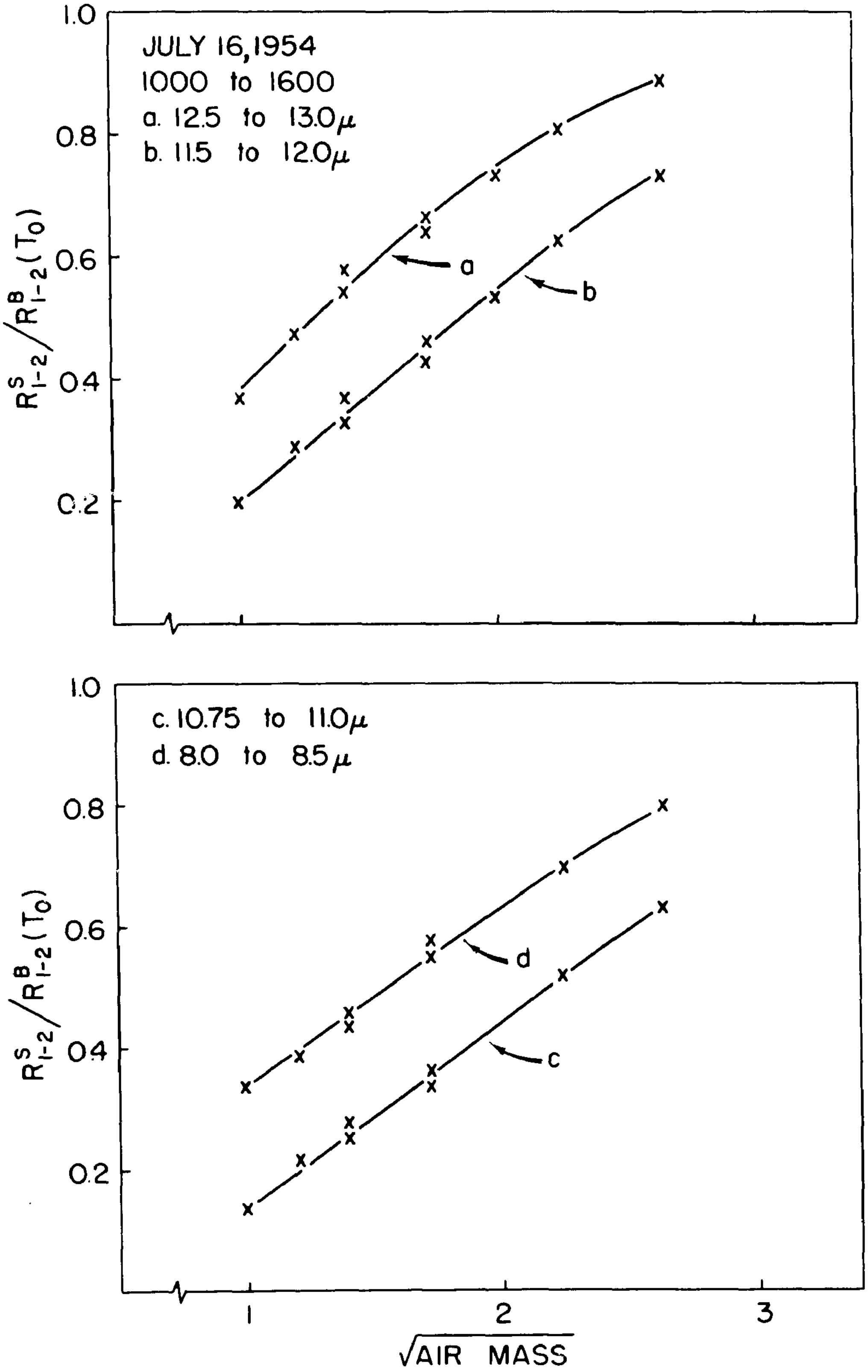
1.0
0.8
0.6
0.4
0.2
$R^S_{1-2}/R^B_{1-2}(T_0)$
JULY 16,1954
1000 to 1600
a. 12.5 to 13.0μ
b. 11.5 to 12.0μ
a
b
1.0
0.8
0.6
0.4
0.2
$R^S_{1-2}/R^B_{1-2}(T_0)$
c. 10.75 to 11.0μ
d. 8.0 to 8.5μ
d
c
1
2
3
√AIR MASS

Figure 45.

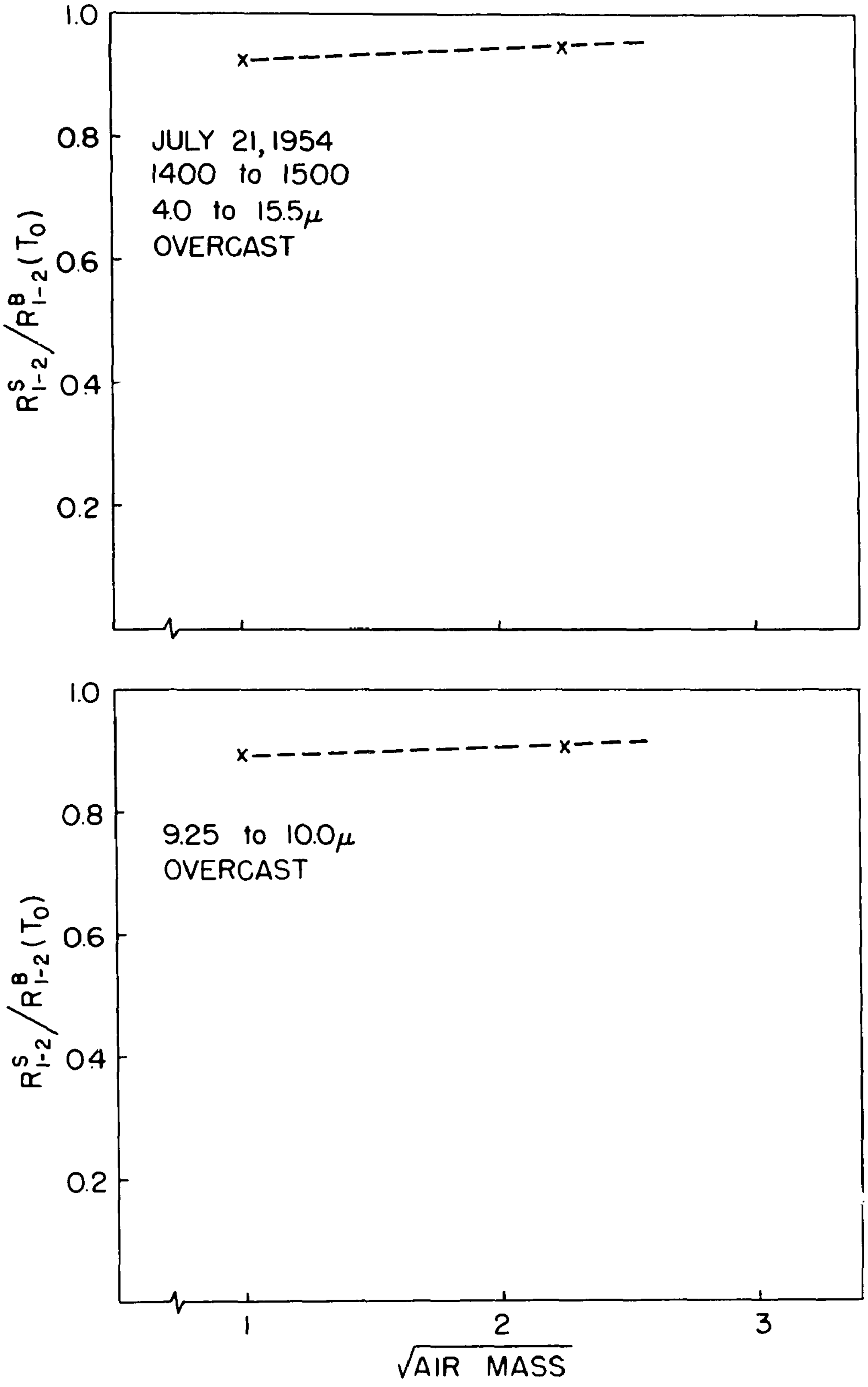
1.0
0.8
0.6
0.4
0.2
$R^S_{1-2}/R^B_{1-2}(T_0)$
JULY 21, 1954
1400 to 1500
4.0 to 15.5μ
OVERCAST
1.0
0.8
0.6
0.4
0.2
$R^S_{1-2}/R^B_{1-2}(T_0)$
9.25 to 10.0μ
OVERCAST
1
2
3
$\sqrt{\text{AIR MASS}}$

Figure 46.

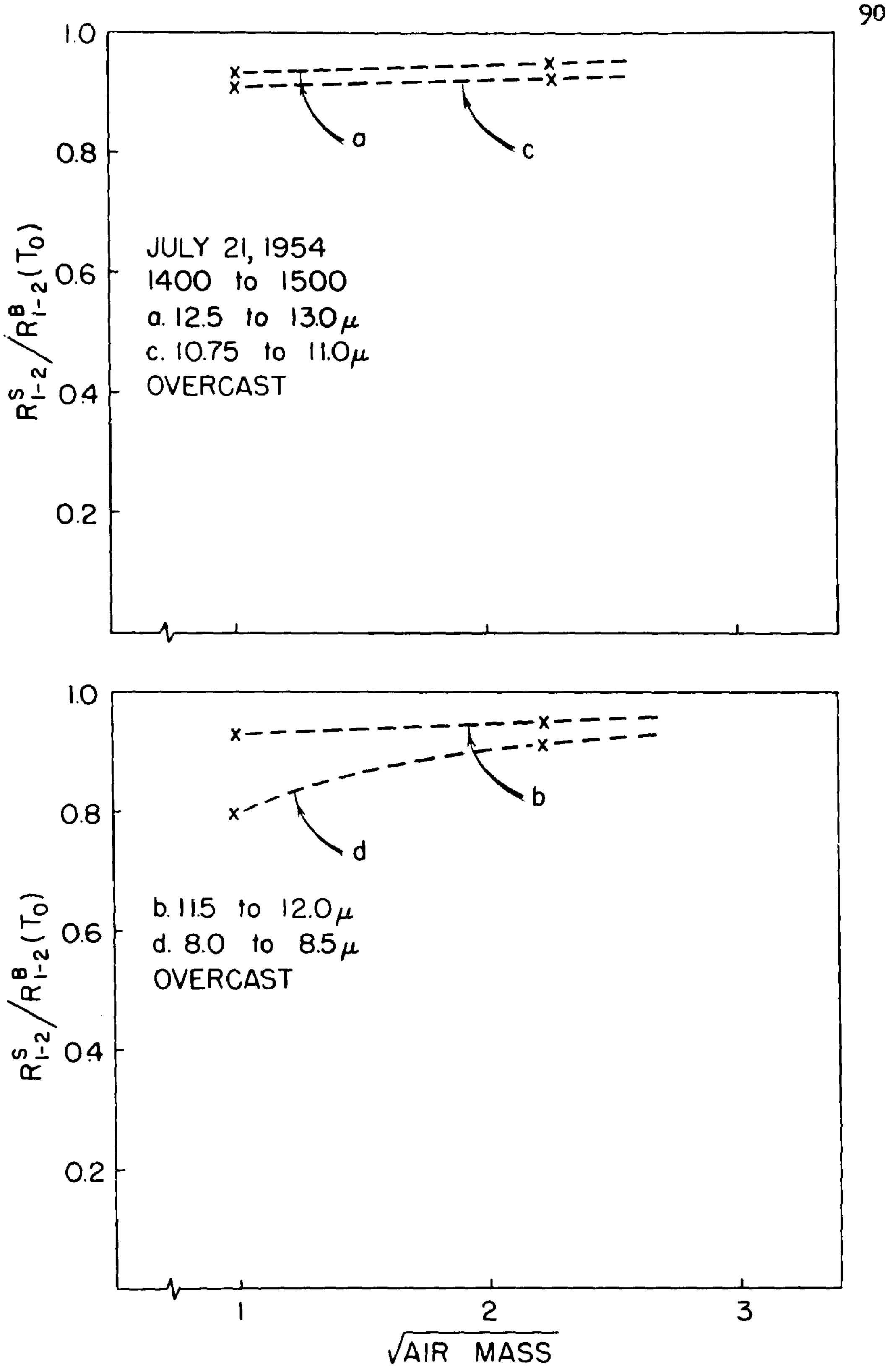
1.0
0.8
0.6
0.4
0.2
$R^S_{1-2}/R^B_{1-2}(T_0)$
a
c
JULY 21, 1954
1400 to 1500
a. 12.5 to 13.0μ
c. 10.75 to 11.0μ
OVERCAST
1.0
0.8
0.6
0.4
0.2
$R^S_{1-2}/R^B_{1-2}(T_0)$
b
d
b. 11.5 to 12.0μ
d. 8.0 to 8.5μ
OVERCAST
1
2
3
$\sqrt{\text{AIR MASS}}$

Figure 47.

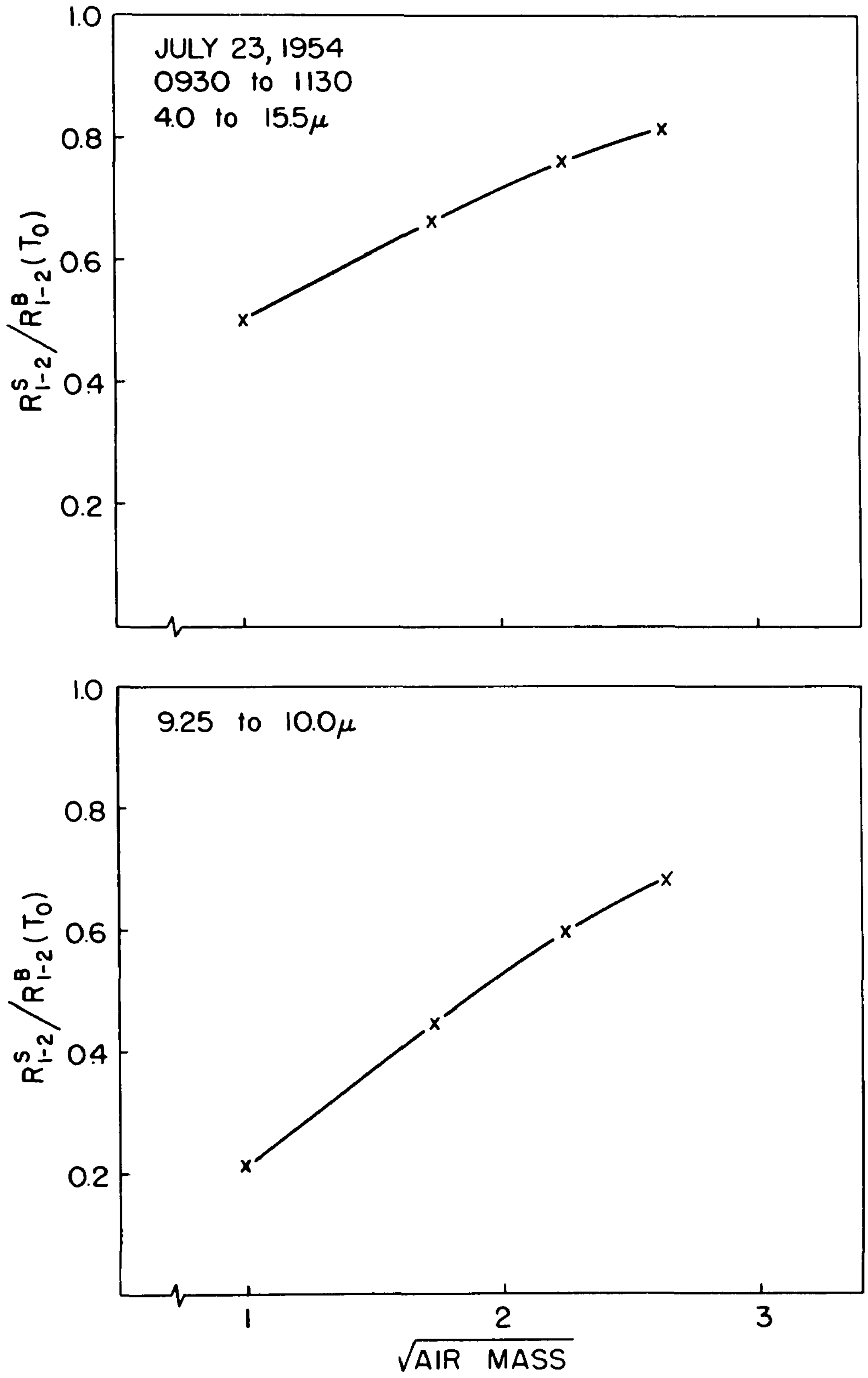
JULY 23, 1954
0930 to 1130
4.0 to 15.5μ
9.25 to 10.0μ
$R^{S}_{1-2}/R^{B}_{1-2}(T_0)$
1.0
0.8
0.6
0.4
0.2
1
2
3
√AIR MASS

Figure 48.

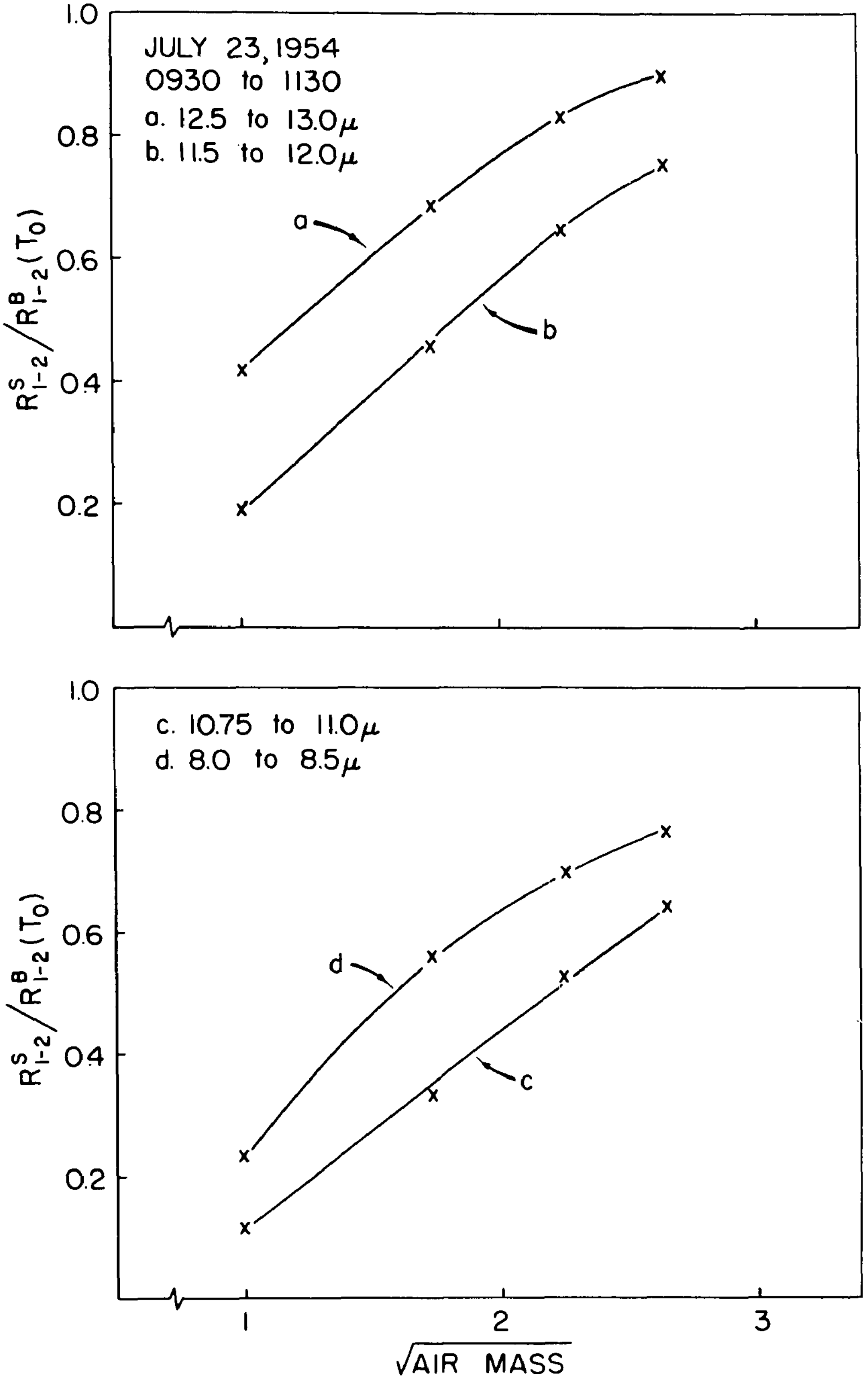
1.0
0.8
0.6
0.4
0.2
JULY 23, 1954
0930 to 1130
a. 12.5 to 13.0μ
b. 11.5 to 12.0μ
a
b
$R^S_{1-2}/R^B_{1-2}(T_0)$
1.0
0.8
0.6
0.4
0.2
c. 10.75 to 11.0μ
d. 8.0 to 8.5μ
d
c
$R^S_{1-2}/R^B_{1-2}(T_0)$
1
2
3
$\sqrt{\text{AIR MASS}}$

Figure 49.

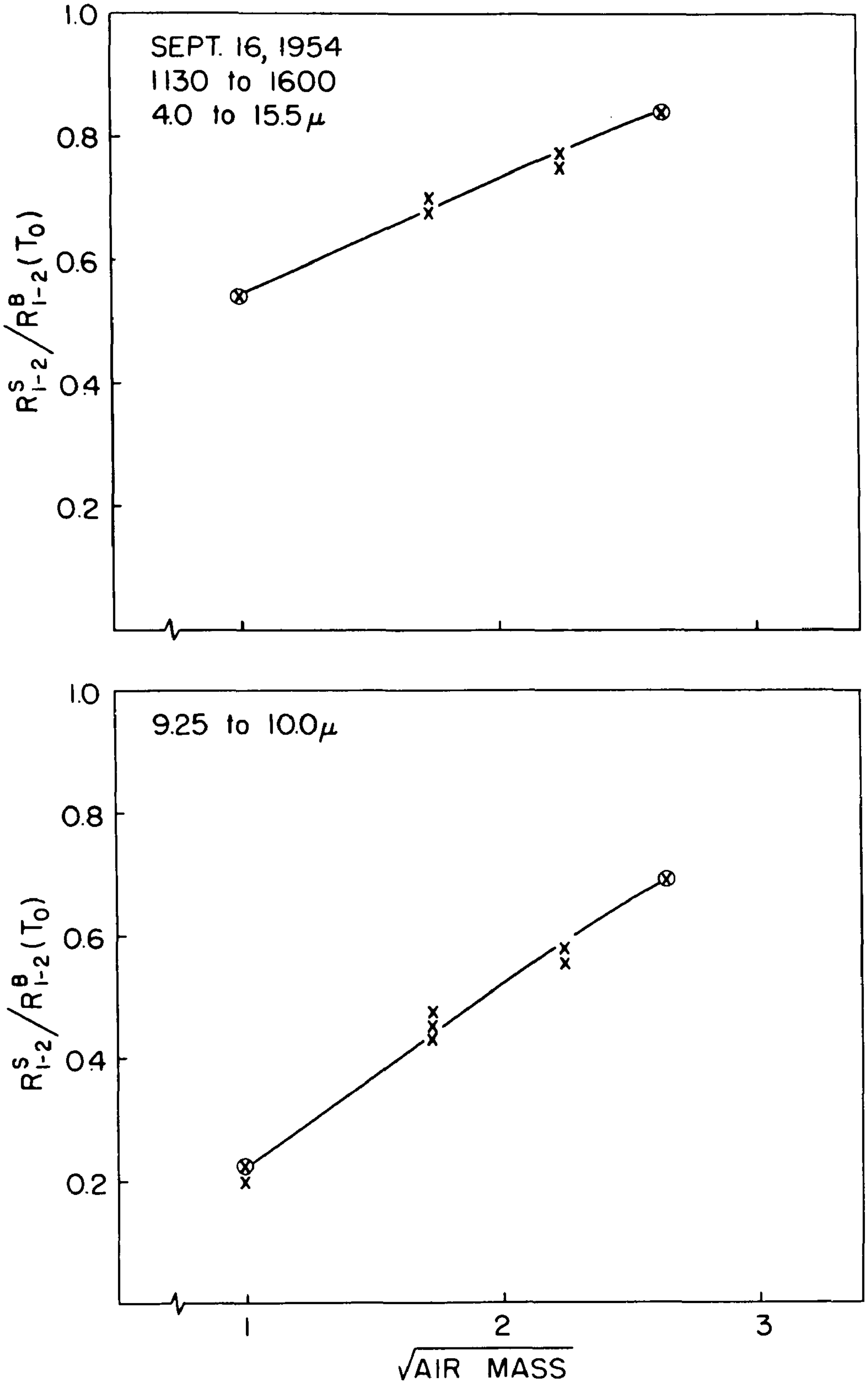
SEPT. 16, 1954
1130 to 1600
4.0 to 15.5μ
9.25 to 10.0μ
$R^S_{1-2}/R^B_{1-2}(T_0)$
1.0
0.8
0.6
0.4
0.2
1
2
3
$\sqrt{\text{AIR MASS}}$

Figure 50.

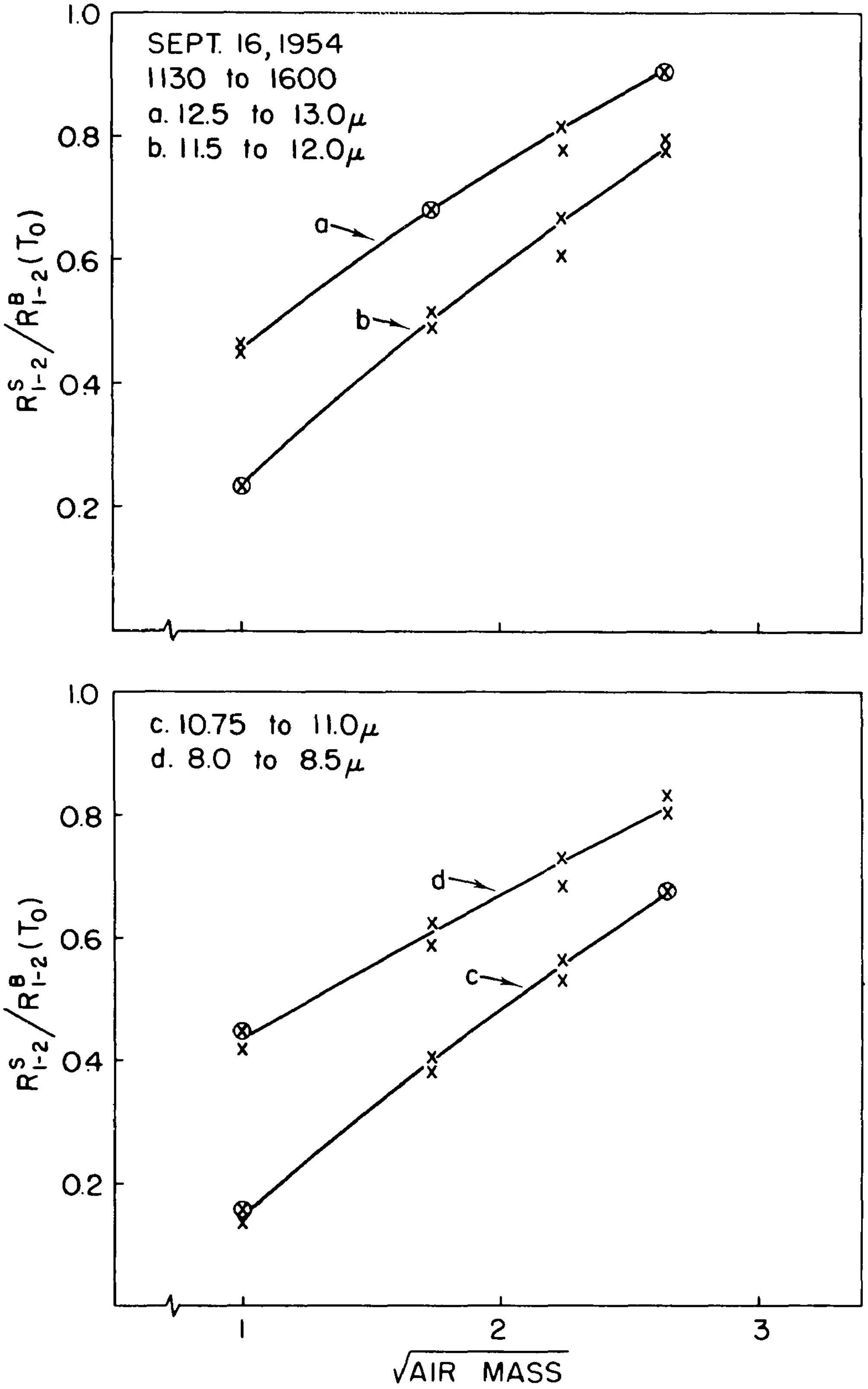
SEPT. 16, 1954
1130 to 1600
a. 12.5 to 13.0μ
b. 11.5 to 12.0μ
a
b
c. 10.75 to 11.0μ
d. 8.0 to 8.5μ
d
c
$R^S_{1-2}/R^B_{1-2}(T_0)$
1.0
0.8
0.6
0.4
0.2
1
2
3
√AIR MASS

Figure 51.

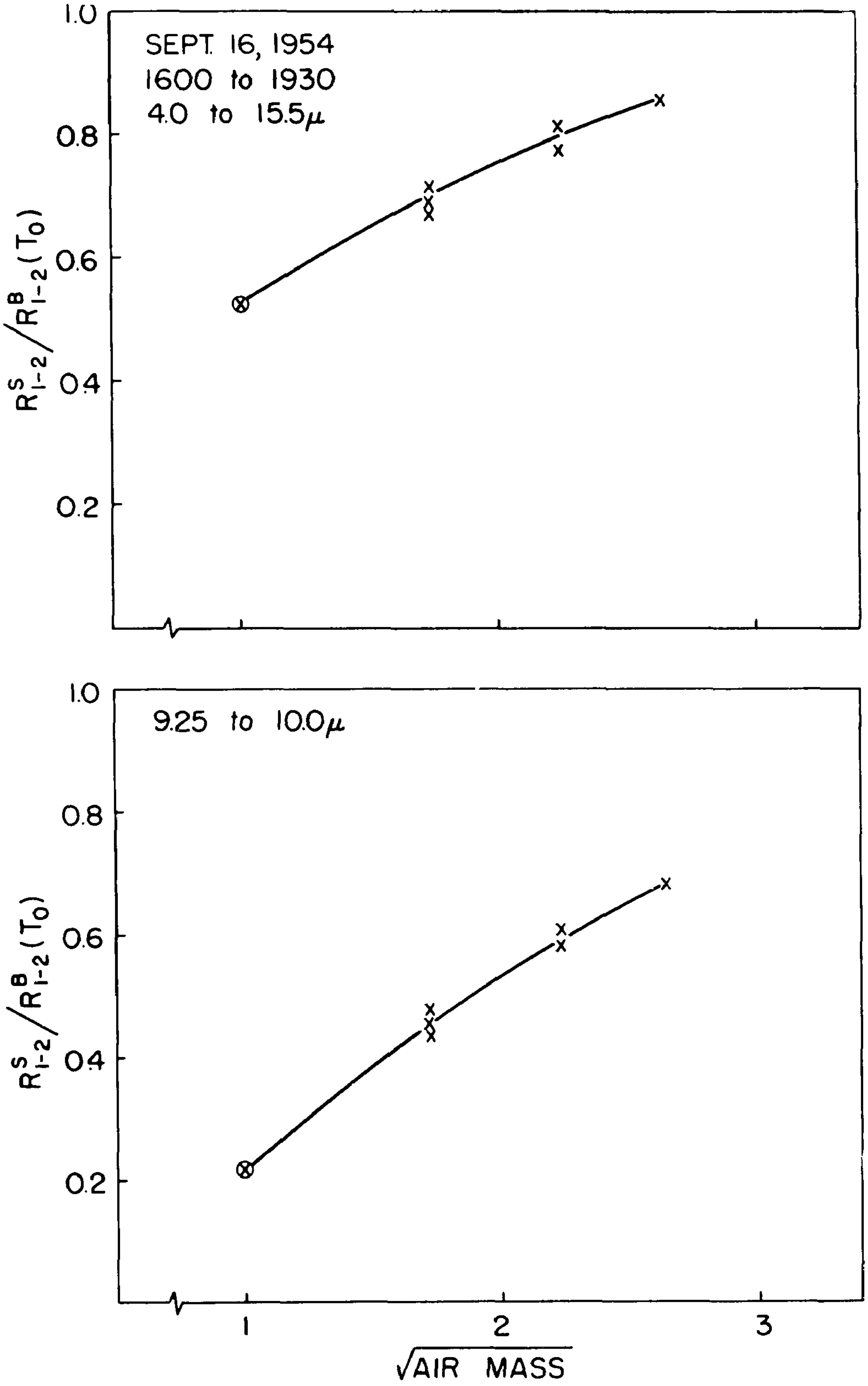
SEPT. 16, 1954
1600 to 1930
4.0 to 15.5μ
9.25 to 10.0μ
$R^S_{1-2}/R^B_{1-2}(T_0)$
1.0
0.8
0.6
0.4
0.2
1
2
3
√AIR MASS

Figure 52.

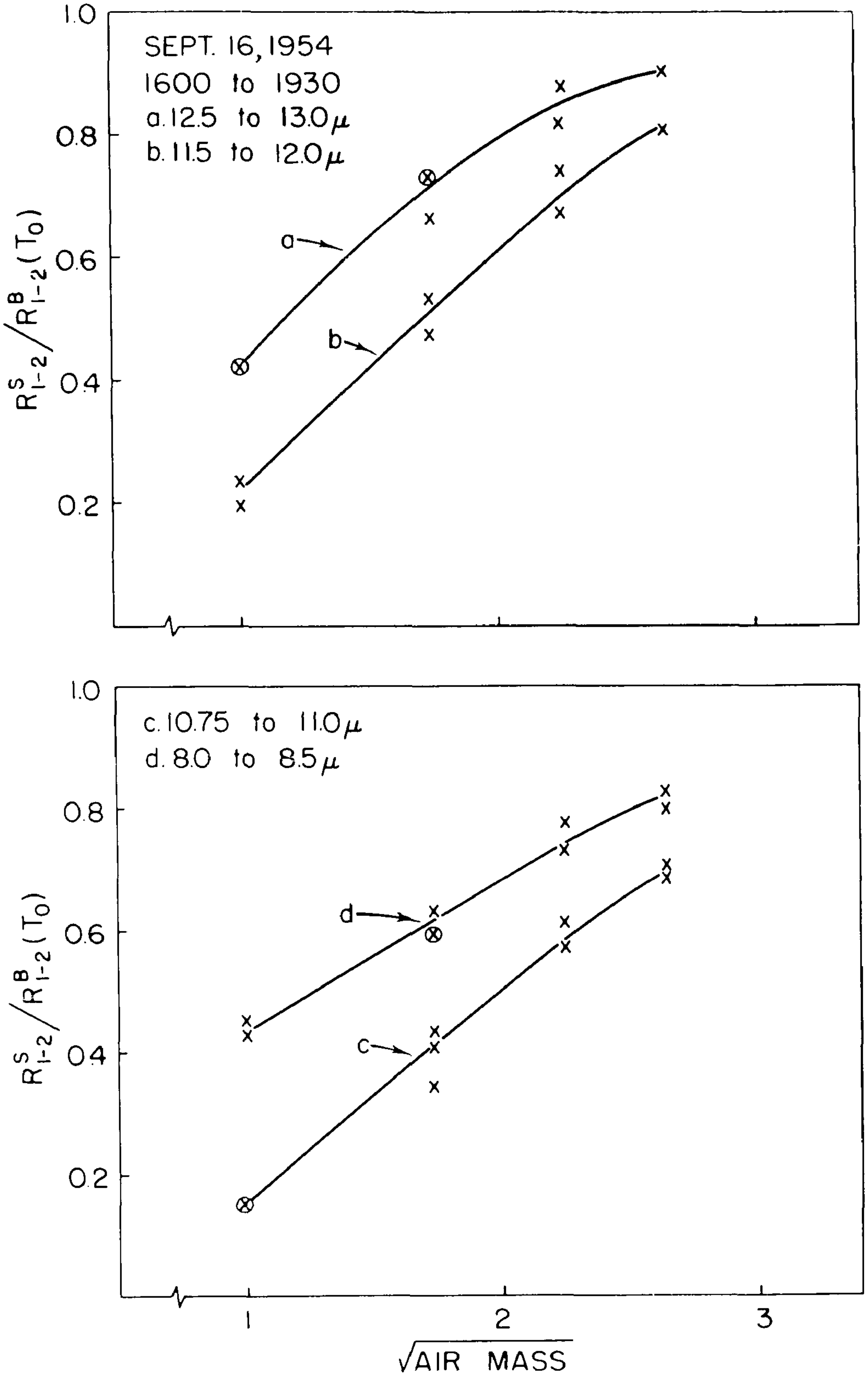
1.0
0.8
0.6
0.4
0.2
SEPT. 16, 1954
1600 to 1930
a. 12.5 to 13.0 μ
b. 11.5 to 12.0 μ
a
b
$R^S_{1-2}/R^B_{1-2}(T_0)$
1.0
0.8
0.6
0.4
0.2
c. 10.75 to 11.0 μ
d. 8.0 to 8.5 μ
d
c
$R^S_{1-2}/R^B_{1-2}(T_0)$
1
2
3
√AIR MASS

Figure 53.

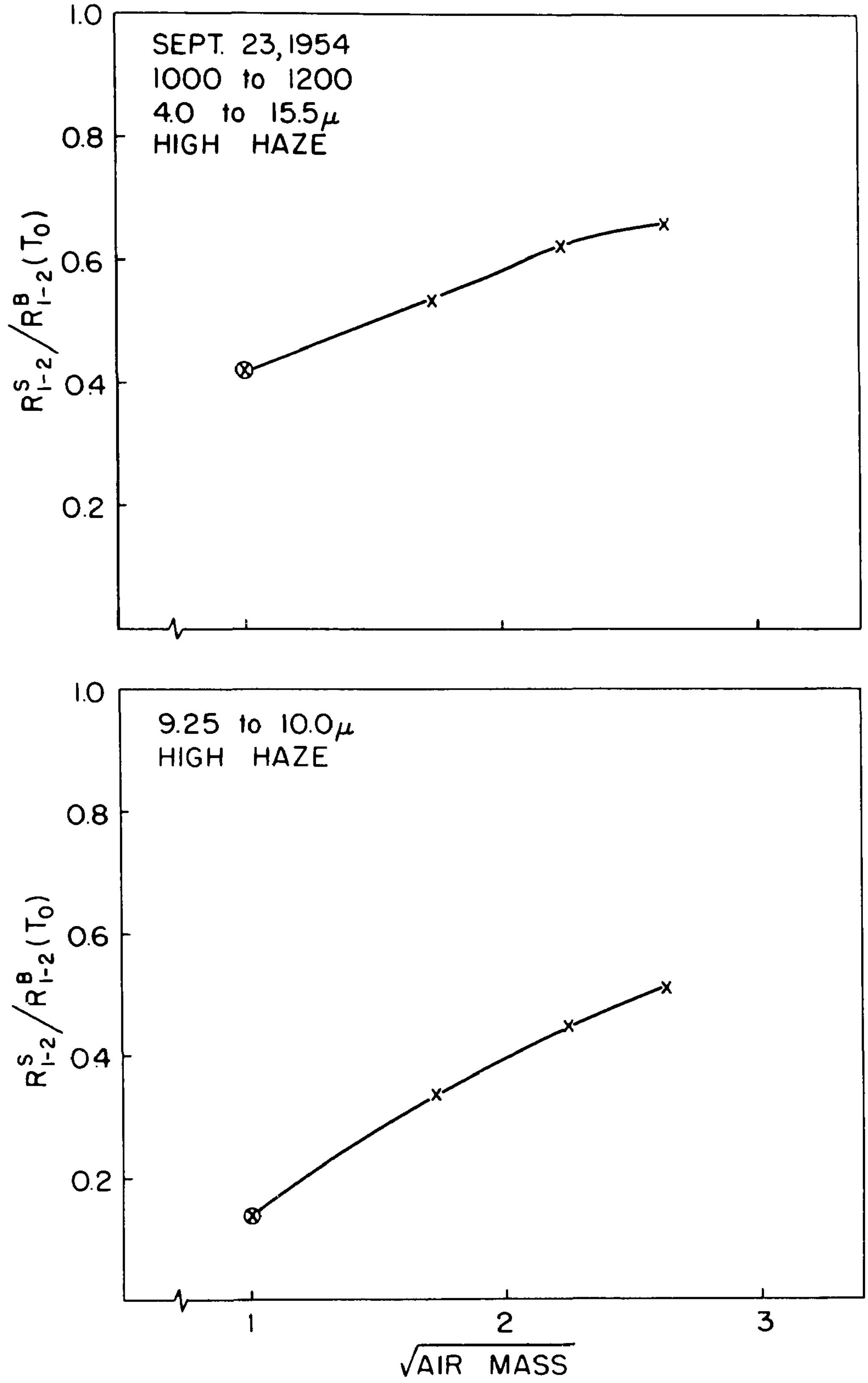
SEPT. 23, 1954
1000 to 1200
4.0 to 15.5μ
HIGH HAZE
1.0
0.8
0.6
0.4
0.2
$R^S_{1-2}/R^B_{1-2}(T_0)$
9.25 to 10.0μ
HIGH HAZE
1.0
0.8
0.6
0.4
0.2
$R^S_{1-2}/R^B_{1-2}(T_0)$
1
2
3
√AIR MASS

Figure 54.

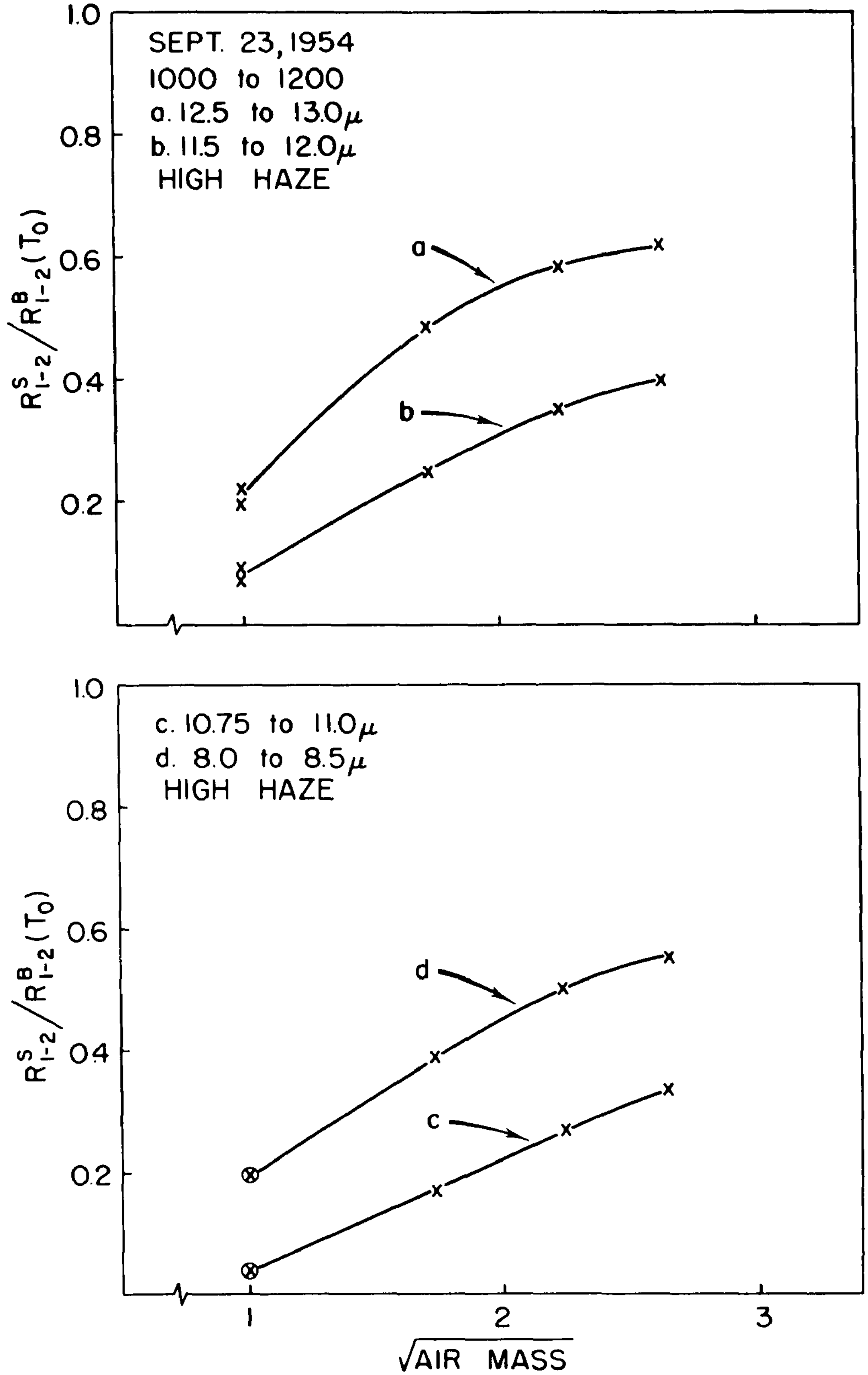
1.0
0.8
0.6
0.4
0.2
$R^S_{1-2}/R^B_{1-2}(T_0)$
SEPT. 23, 1954
1000 to 1200
a. 12.5 to 13.0μ
b. 11.5 to 12.0μ
HIGH HAZE
a
b
c. 10.75 to 11.0μ
d. 8.0 to 8.5μ
HIGH HAZE
d
c
1
2
3
√AIR MASS

Figure 55.

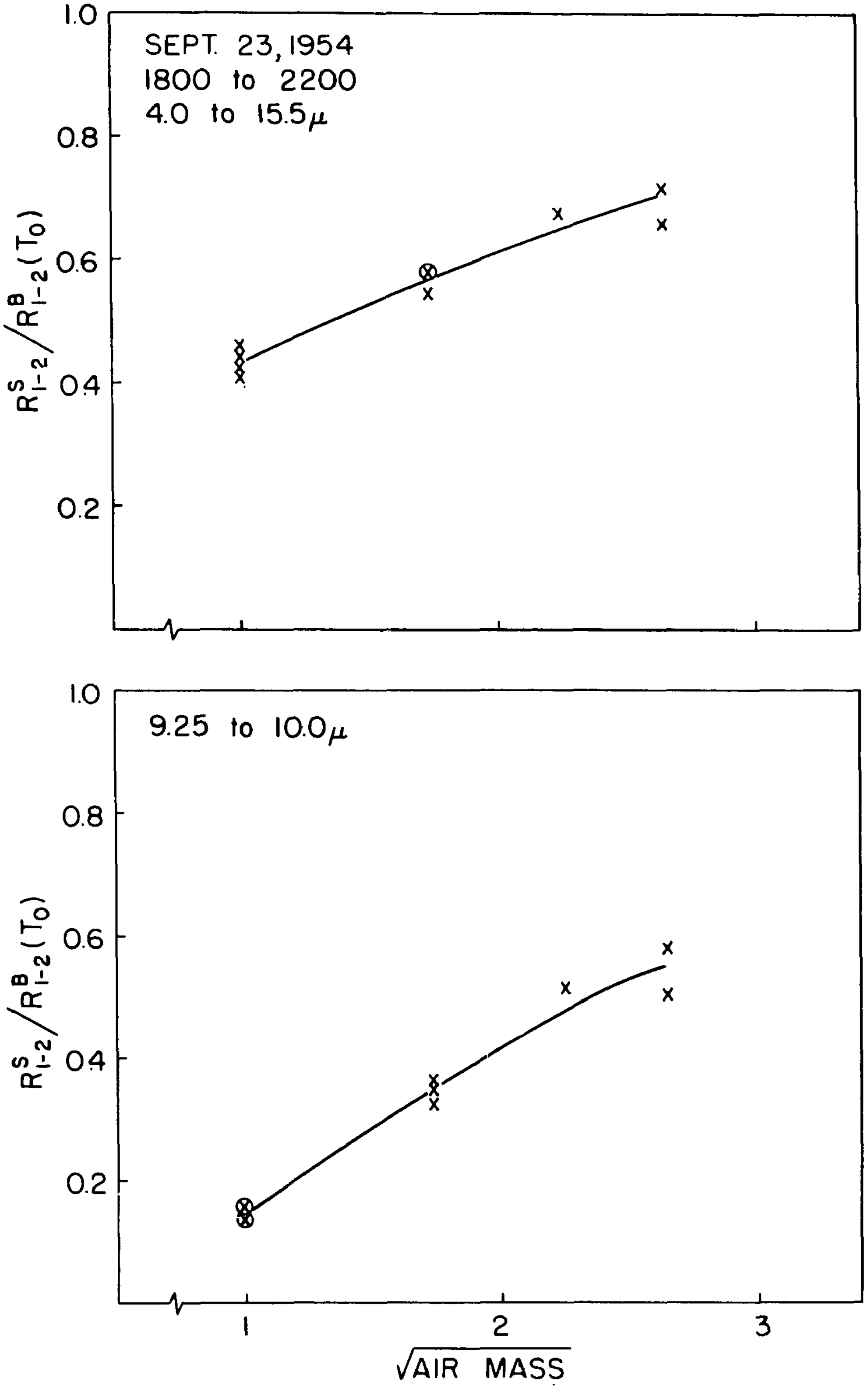
SEPT. 23, 1954
1800 to 2200
4.0 to 15.5μ
9.25 to 10.0μ
1.0
0.8
0.6
0.4
0.2
R^S_{1-2}/R^B_{1-2}(T_0)
1
2
3
√AIR MASS

Figure 56.

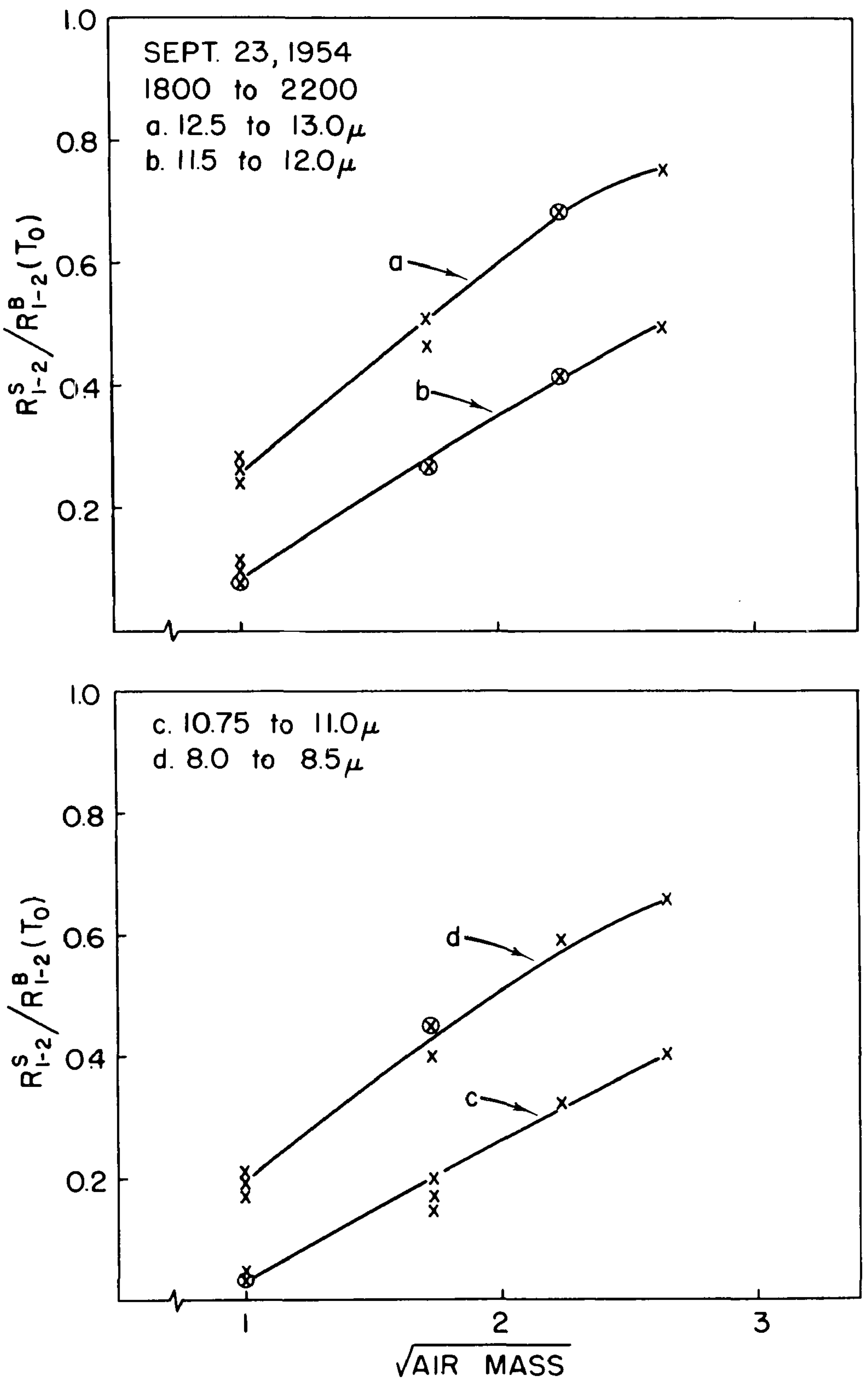
SEPT. 23, 1954
1800 to 2200
a. 12.5 to 13.0μ
b. 11.5 to 12.0μ
c. 10.75 to 11.0μ
d. 8.0 to 8.5μ
a
b
c
d
$R^S_{1-2}/R^B_{1-2}(T_0)$
1.0
0.8
0.6
0.4
0.2
1
2
3
√AIR MASS

Figure 57.

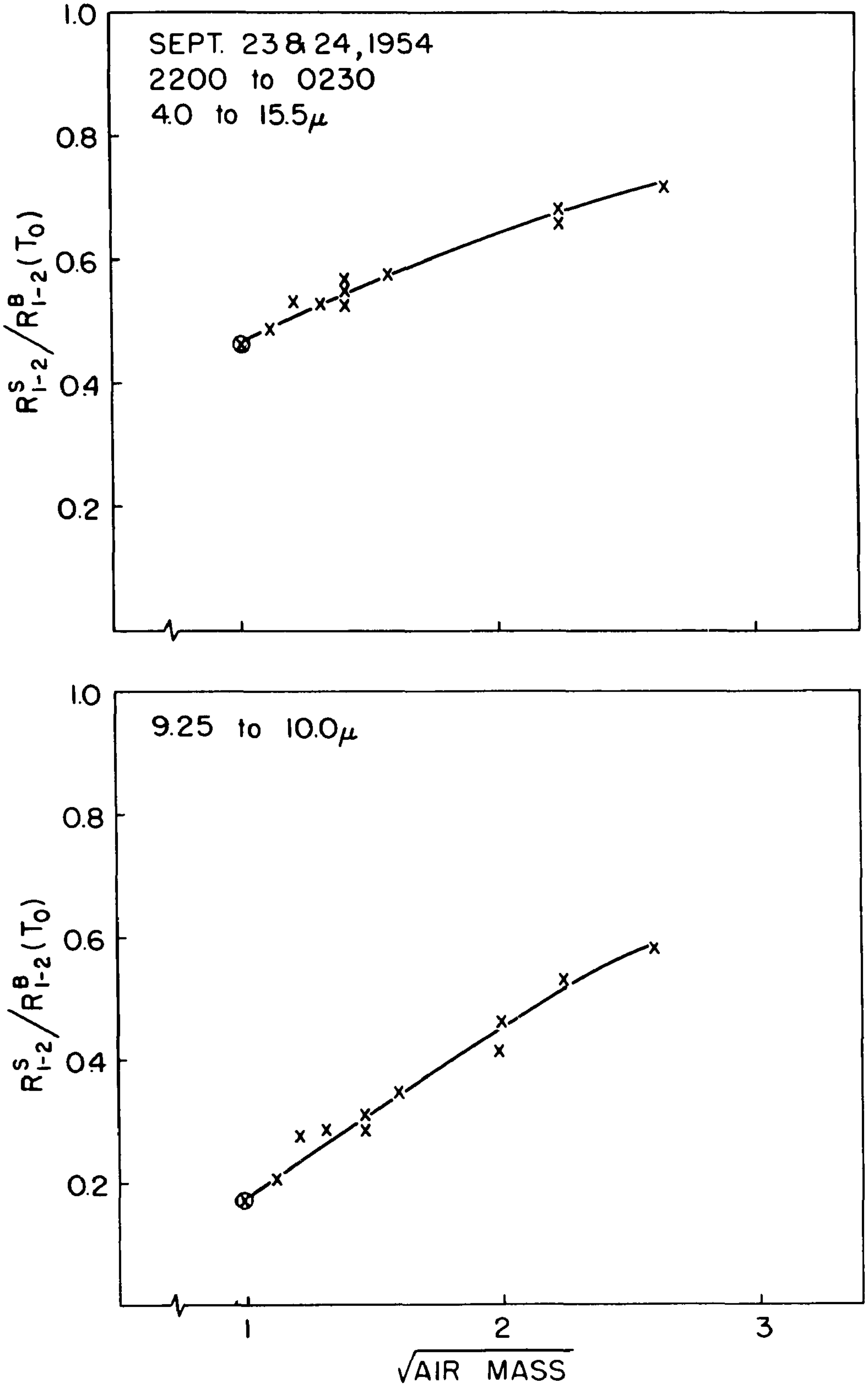
1.0
0.8
0.6
0.4
0.2
$R^S_{1-2}/R^B_{1-2}(T_0)$
SEPT. 23 & 24, 1954
2200 to 0230
4.0 to 15.5μ
1.0
0.8
0.6
0.4
0.2
$R^S_{1-2}/R^B_{1-2}(T_0)$
9.25 to 10.0μ
1
2
3
√AIR MASS

Figure 58.

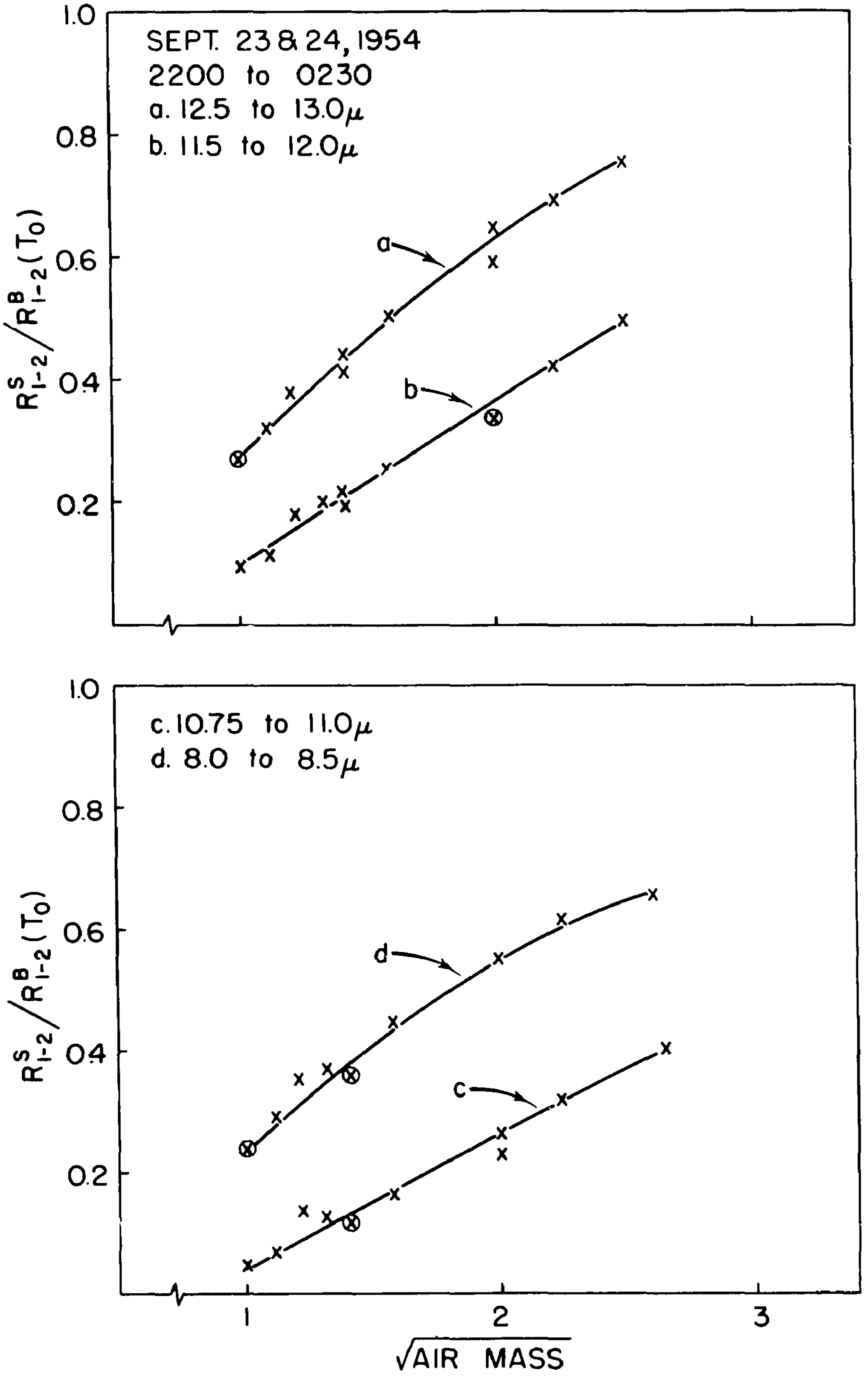
1.0
0.8
0.6
0.4
0.2
SEPT. 23 & 24, 1954
2200 to 0230
a. 12.5 to 13.0μ
b. 11.5 to 12.0μ
a
b
$R^S_{1-2} / R^B_{1-2}(T_0)$
c. 10.75 to 11.0μ
d. 8.0 to 8.5μ
d
c
1
2
3
√AIR MASS

Figure 59.

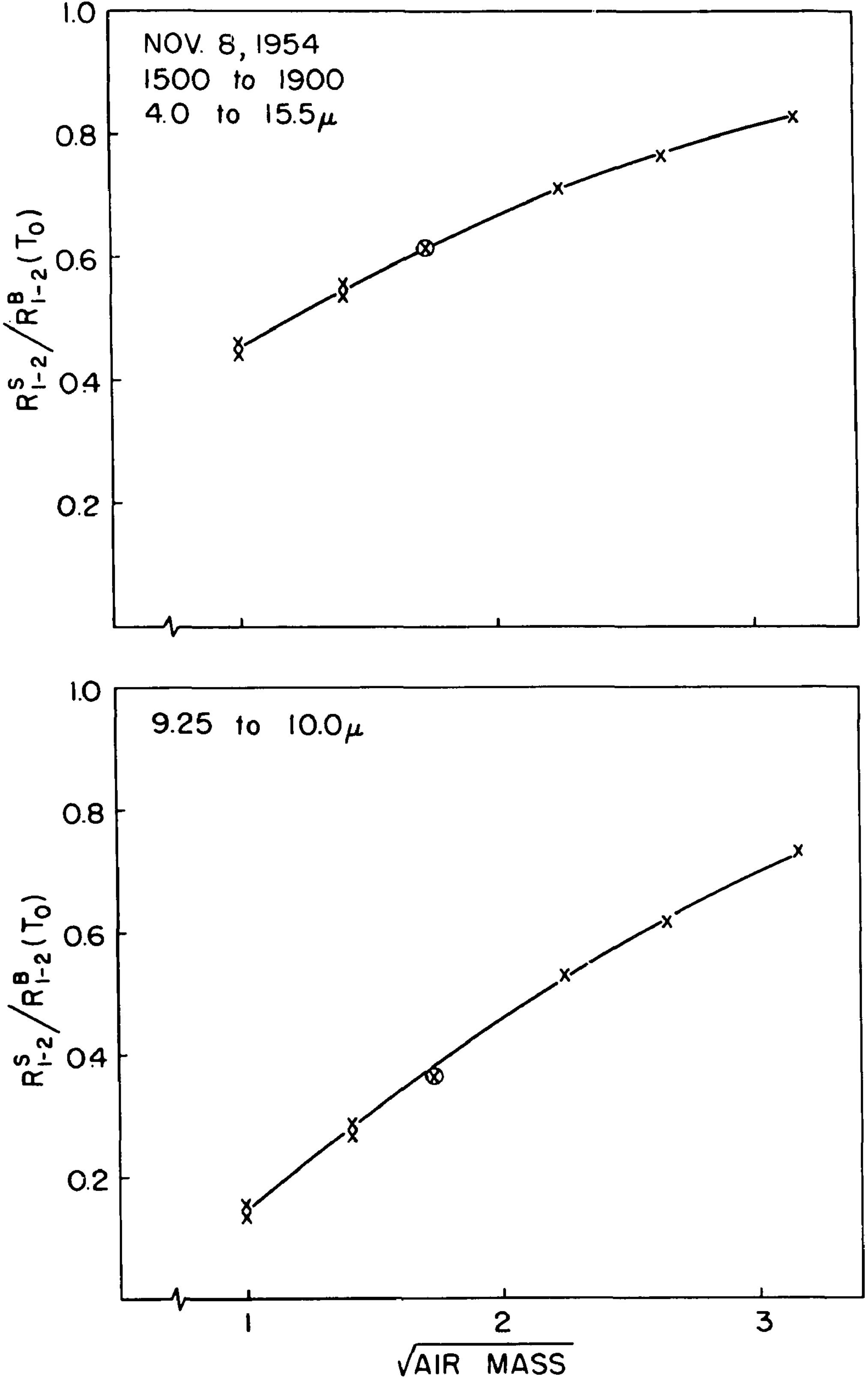
NOV. 8, 1954
1500 to 1900
4.0 to 15.5μ
9.25 to 10.0μ
1.0
0.8
0.6
0.4
0.2
$R^S_{1-2}/R^B_{1-2}(T_0)$
1
2
3
$\sqrt{\text{AIR MASS}}$

Figure 60.

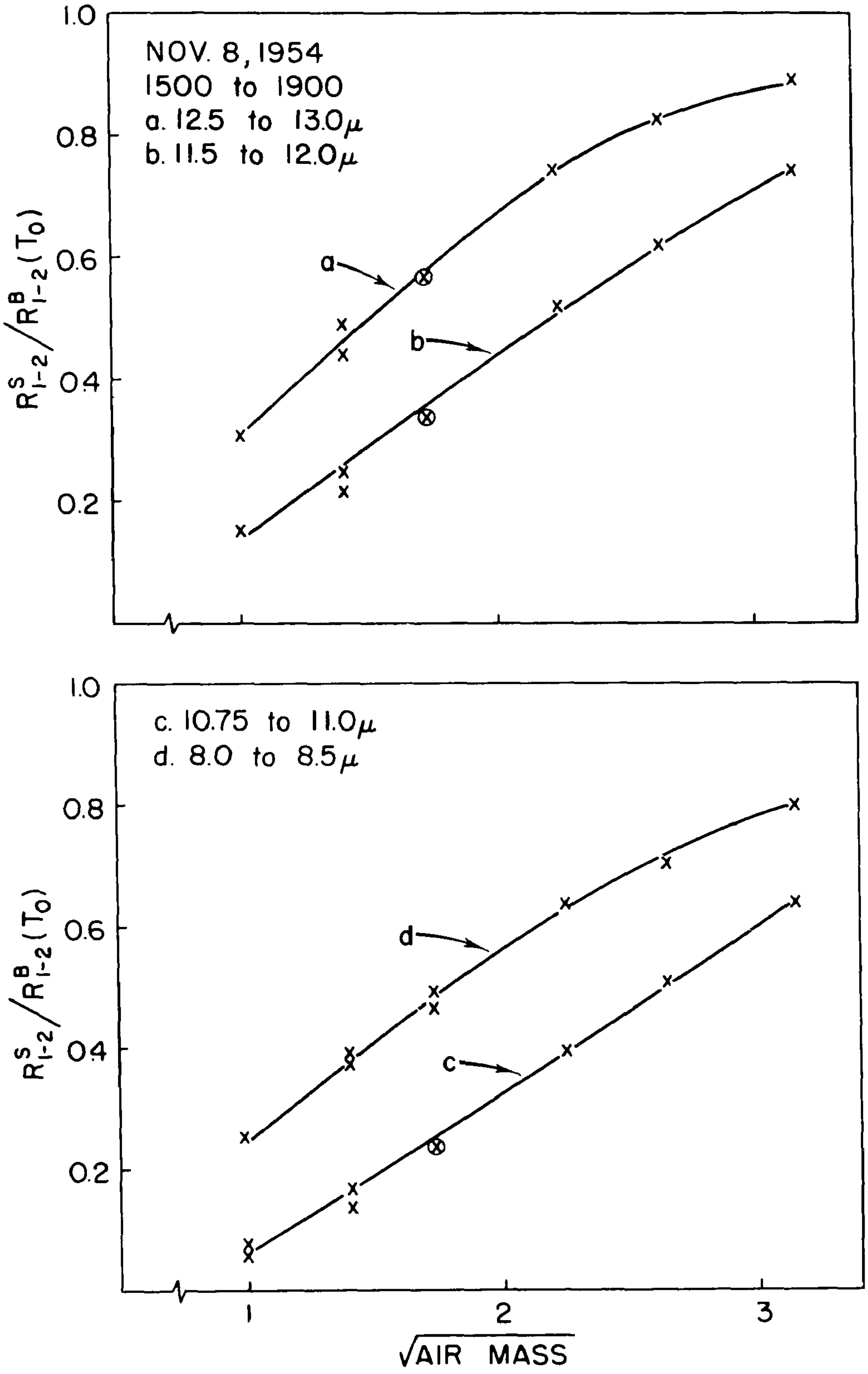
NOV. 8, 1954
1500 to 1900
a. 12.5 to 13.0μ
b. 11.5 to 12.0μ
a
b
1.0
0.8
0.6
0.4
0.2
$R^{S}_{1-2}/R^{B}_{1-2}(T_0)$
c. 10.75 to 11.0μ
d. 8.0 to 8.5μ
d
c
1.0
0.8
0.6
0.4
0.2
$R^{S}_{1-2}/R^{B}_{1-2}(T_0)$
1
2
3
√AIR MASS

Figure 61.

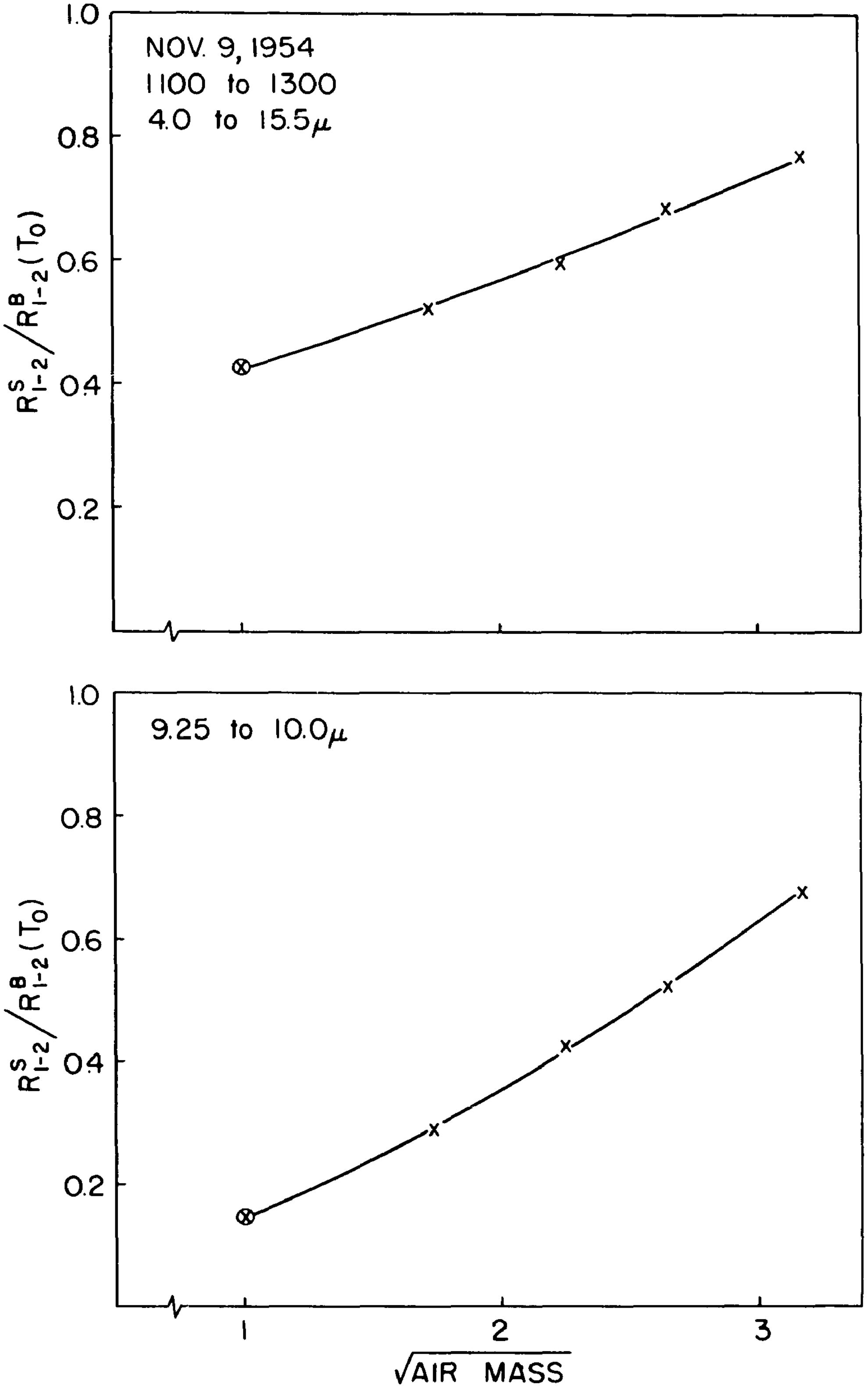
1.0
0.8
0.6
0.4
0.2
$R^S_{1-2}/R^B_{1-2}(T_0)$
NOV. 9, 1954
1100 to 1300
4.0 to 15.5μ
1.0
0.8
0.6
0.4
0.2
$R^S_{1-2}/R^B_{1-2}(T_0)$
9.25 to 10.0μ
1
2
3
$\sqrt{\text{AIR MASS}}$

Figure 62.

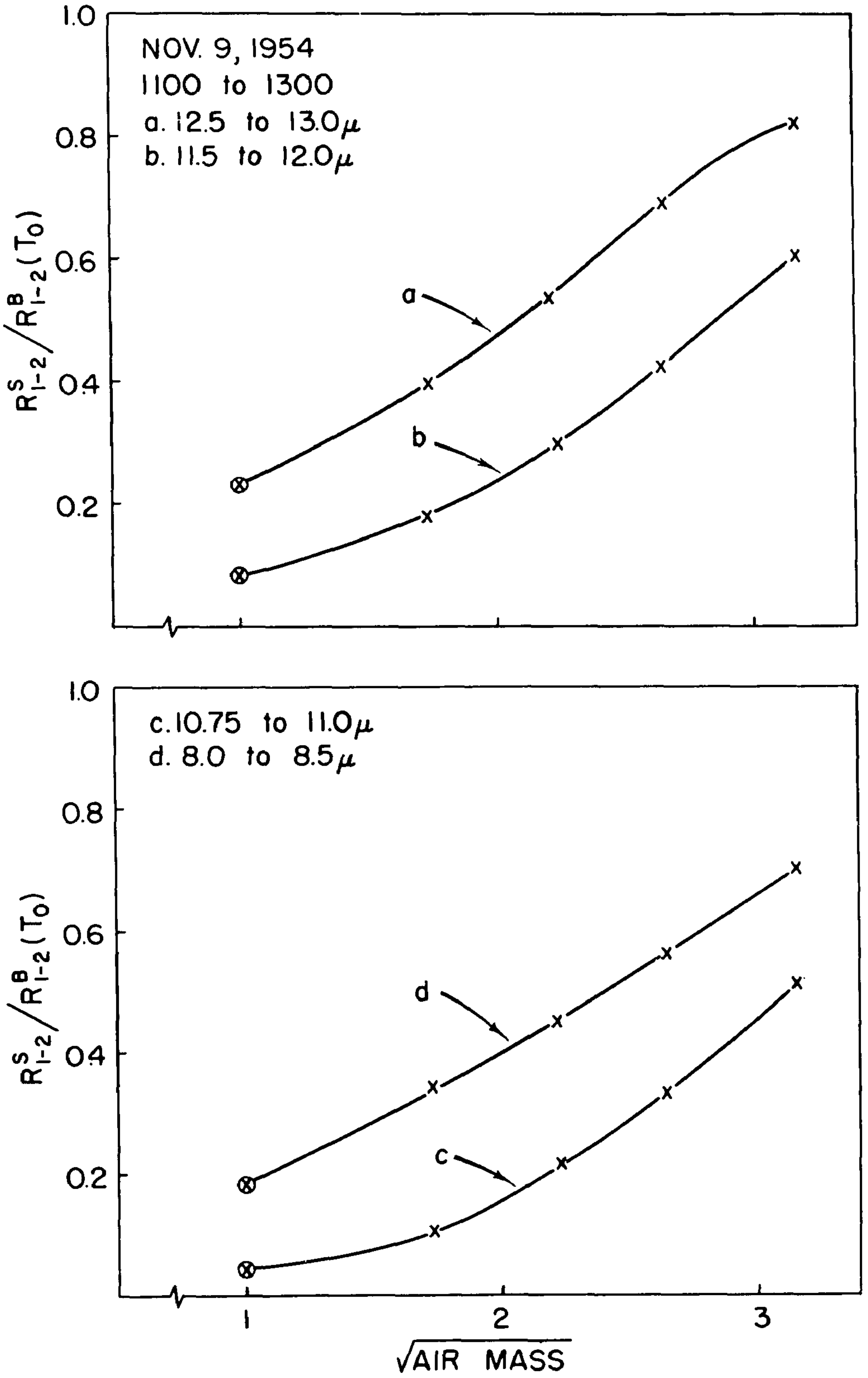
NOV. 9, 1954
1100 to 1300
a. 12.5 to 13.0μ
b. 11.5 to 12.0μ
c. 10.75 to 11.0μ
d. 8.0 to 8.5μ
a
b
c
d
1.0
0.8
0.6
0.4
0.2
1
2
3
$R^S_{1-2} / R^B_{1-2}(T_0)$
$\sqrt{\text{AIR MASS}}$

Figure 63.

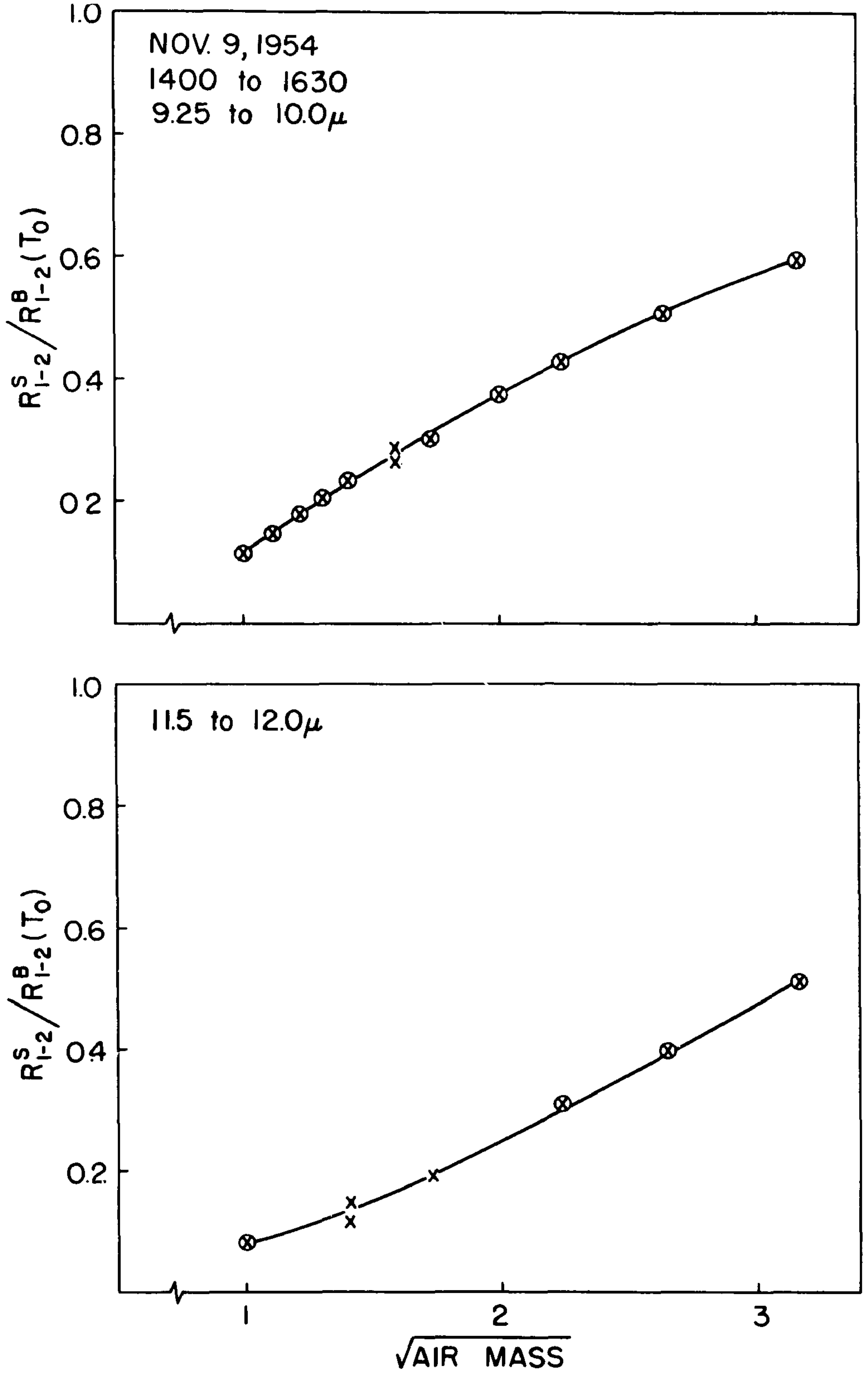
1.0
0.8
0.6
0.4
0.2
NOV. 9, 1954
1400 to 1630
9.25 to 10.0μ
$R^S_{1-2}/R^B_{1-2}(T_0)$
1.0
0.8
0.6
0.4
0.2
11.5 to 12.0μ
$R^S_{1-2}/R^B_{1-2}(T_0)$
1
2
3
$\sqrt{\text{AIR MASS}}$

Figure 64.

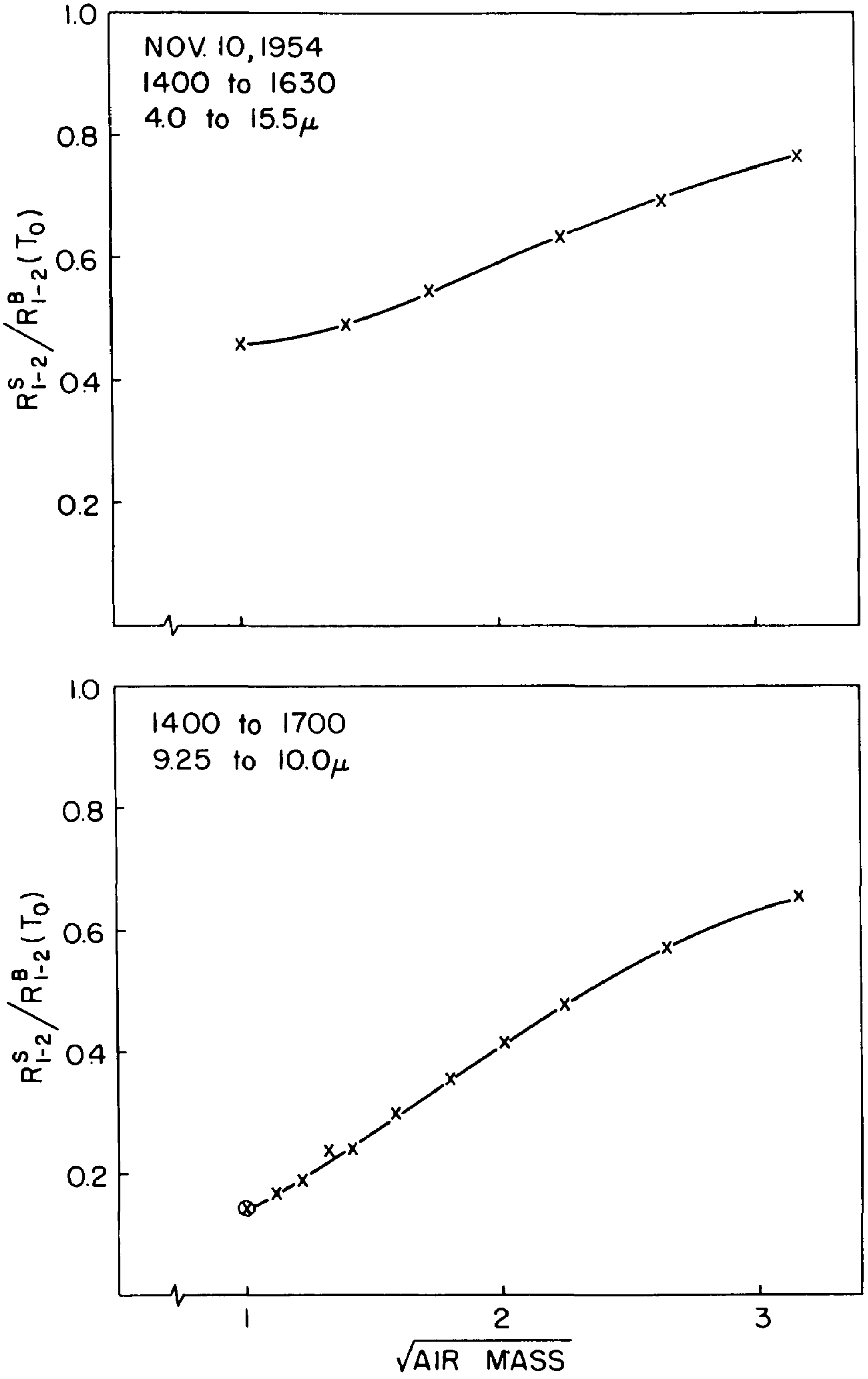
NOV. 10, 1954
1400 to 1630
4.0 to 15.5μ
1400 to 1700
9.25 to 10.0μ
$R^S_{1-2} / R^B_{1-2}(T_0)$
1.0
0.8
0.6
0.4
0.2
1
2
3
$\sqrt{\text{AIR MASS}}$

Figure 65.

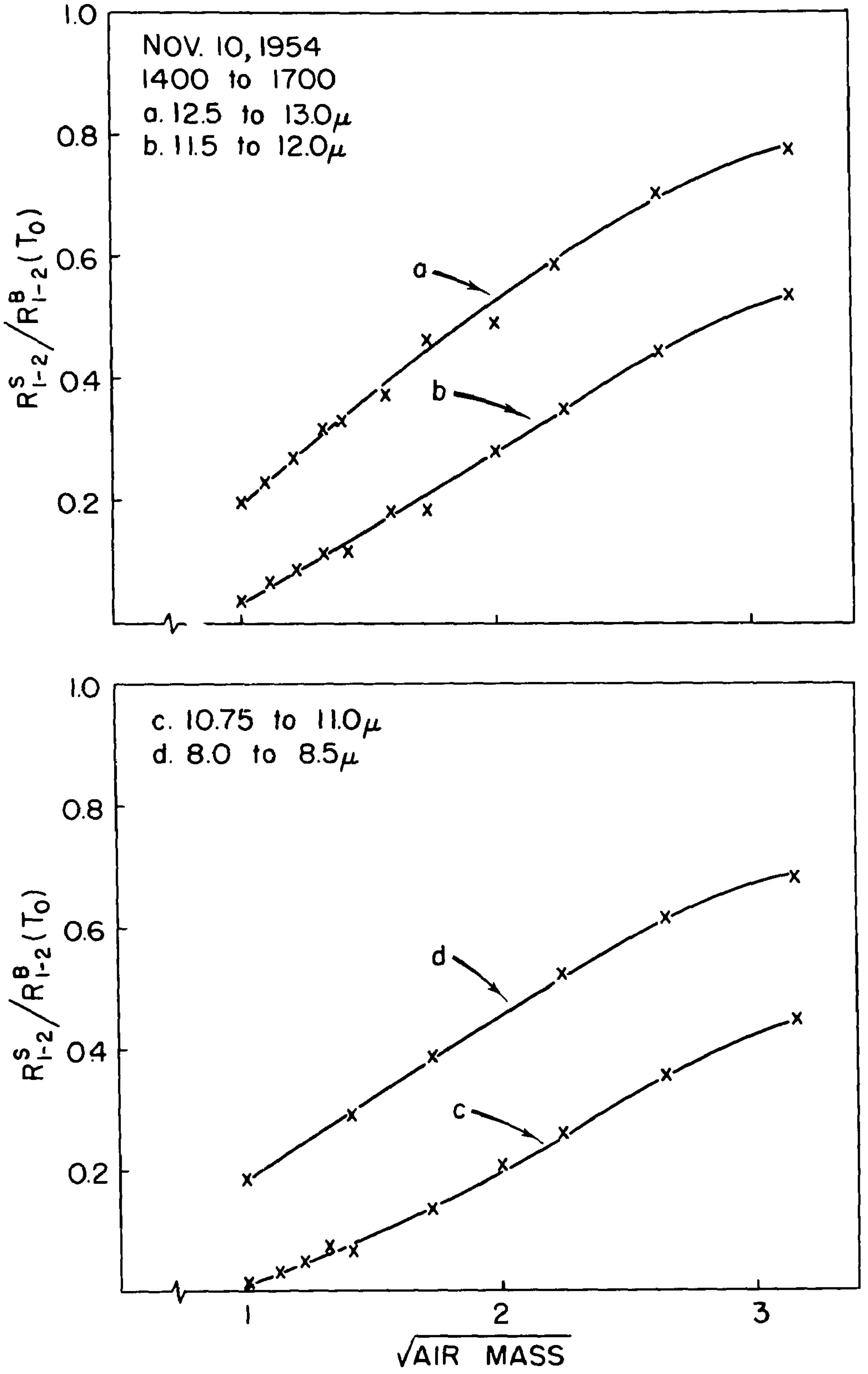
NOV. 10, 1954
1400 to 1700
a. 12.5 to 13.0μ
b. 11.5 to 12.0μ
c. 10.75 to 11.0μ
d. 8.0 to 8.5μ
a
b
c
d
R^S_{1-2}/R^B_{1-2}(T_0)
1.0
0.8
0.6
0.4
0.2
1
2
3
√AIR MASS

Figure 66.

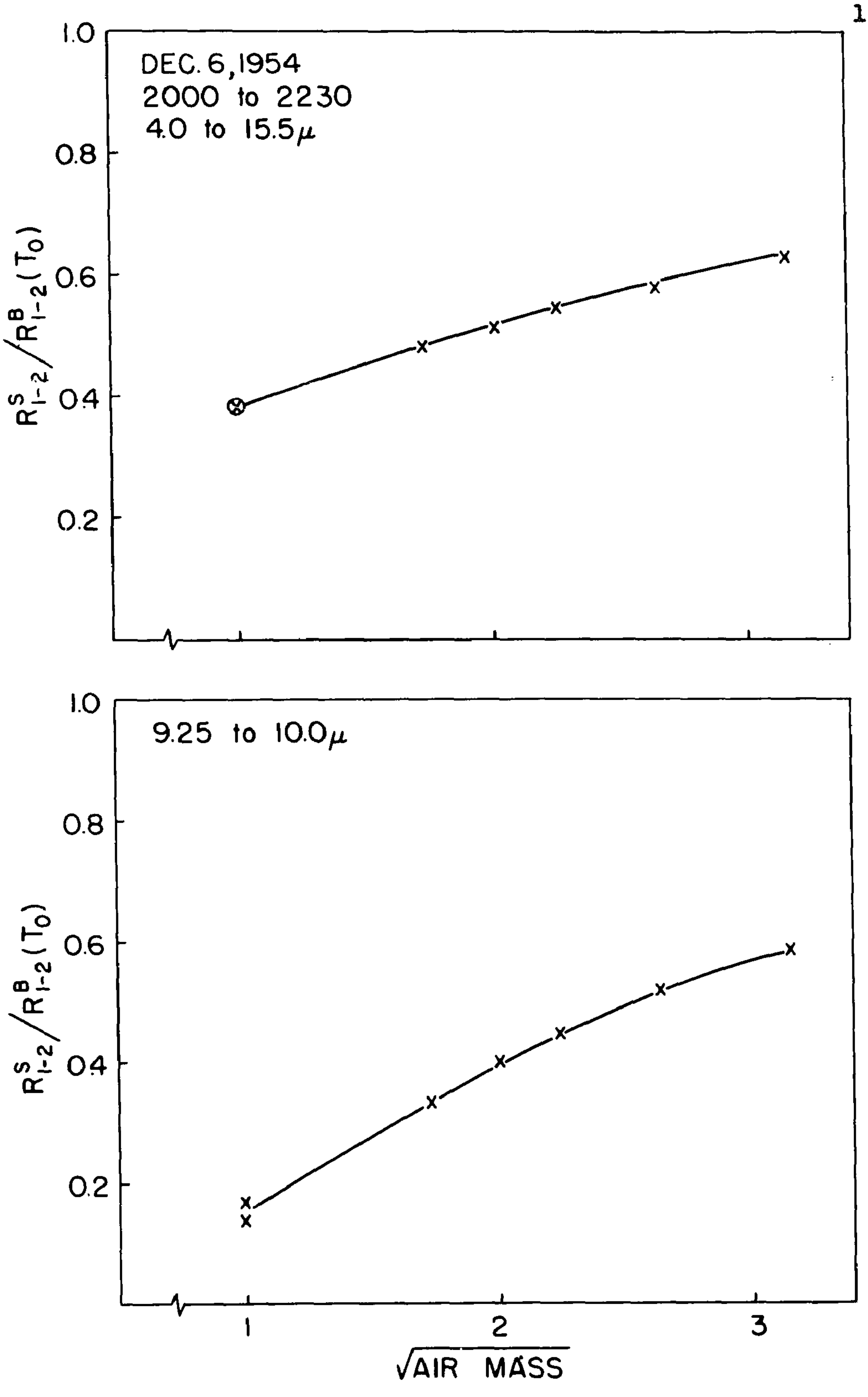
DEC. 6, 1954
2000 to 2230
4.0 to 15.5μ
9.25 to 10.0μ
$R^S_{1-2} / R^B_{1-2}(T_0)$
1.0
0.8
0.6
0.4
0.2
1
2
3
$\sqrt{\text{AIR MASS}}$

Figure 67.

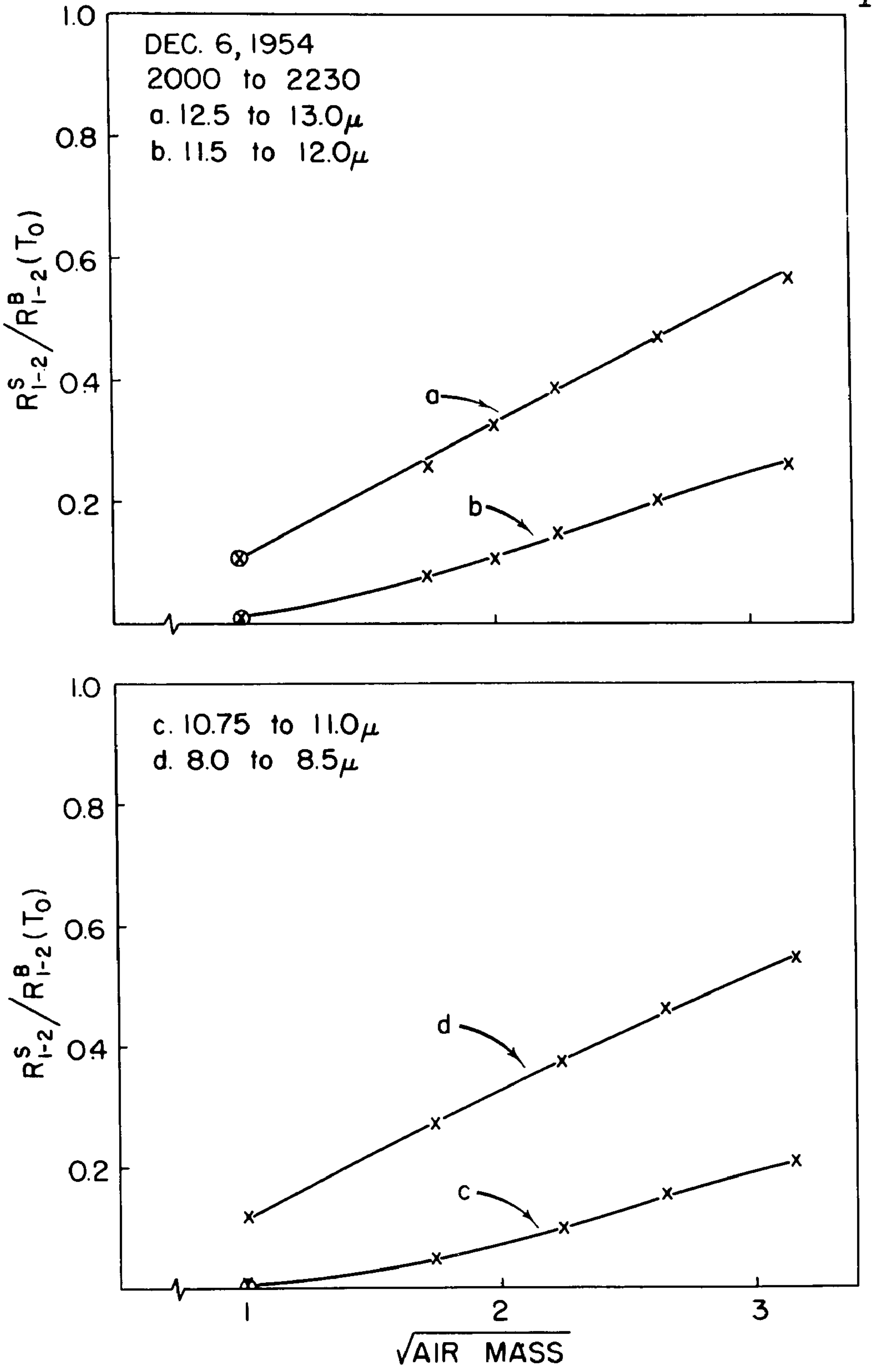
1.0
0.8
0.6
0.4
0.2
$R^S_{1-2}/R^B_{1-2}(T_0)$
DEC. 6, 1954
2000 to 2230
a. 12.5 to 13.0μ
b. 11.5 to 12.0μ
a
b
c. 10.75 to 11.0μ
d. 8.0 to 8.5μ
d
c
1
2
3
√AIR MASS

Figure 68.

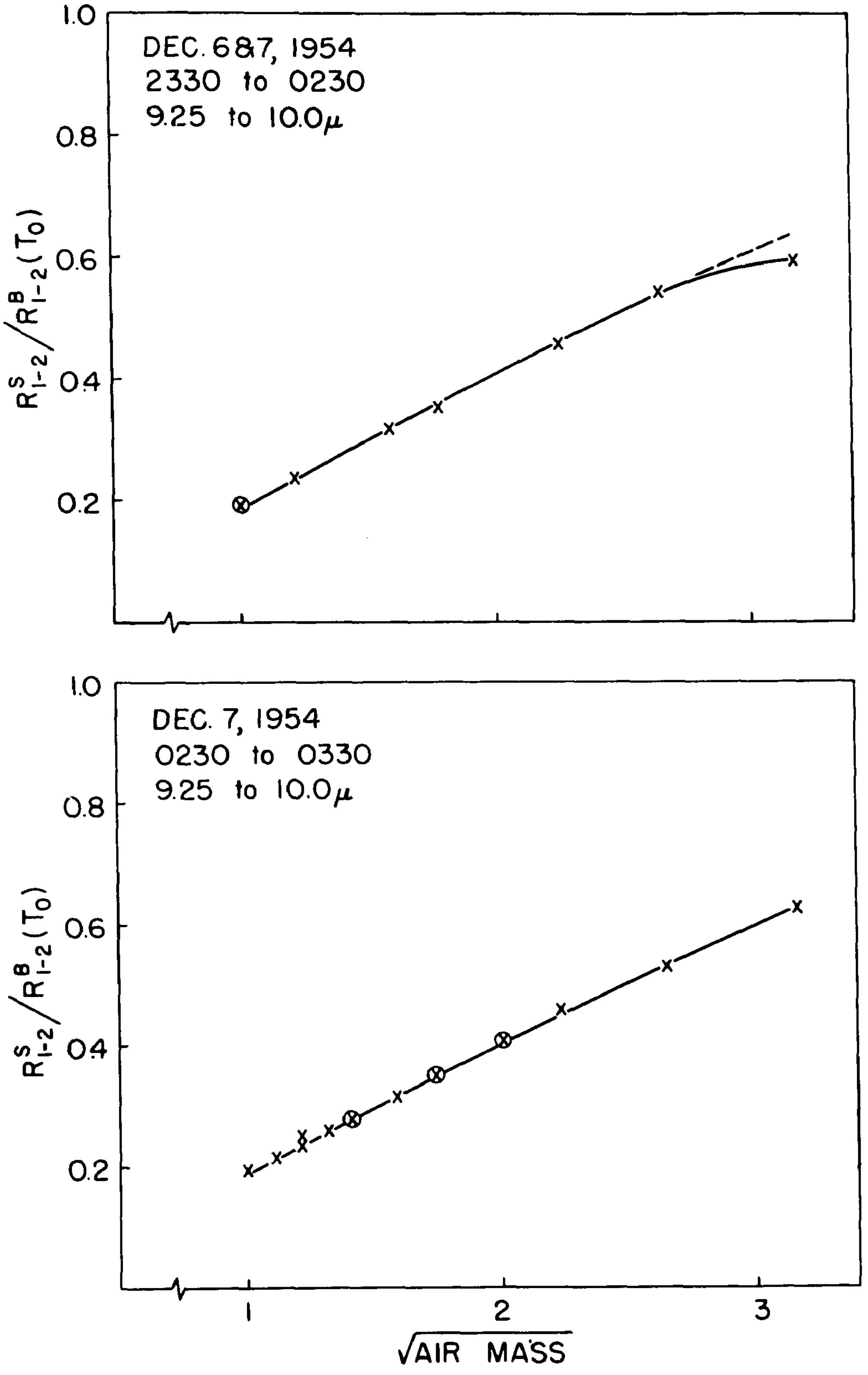
DEC. 6&7, 1954
2330 to 0230
9.25 to 10.0μ
DEC. 7, 1954
0230 to 0330
9.25 to 10.0μ
1.0
0.8
0.6
0.4
0.2
$R^S_{1-2} / R^B_{1-2}(T_0)$
1
2
3
$\sqrt{\text{AIR MASS}}$

Figure 69.

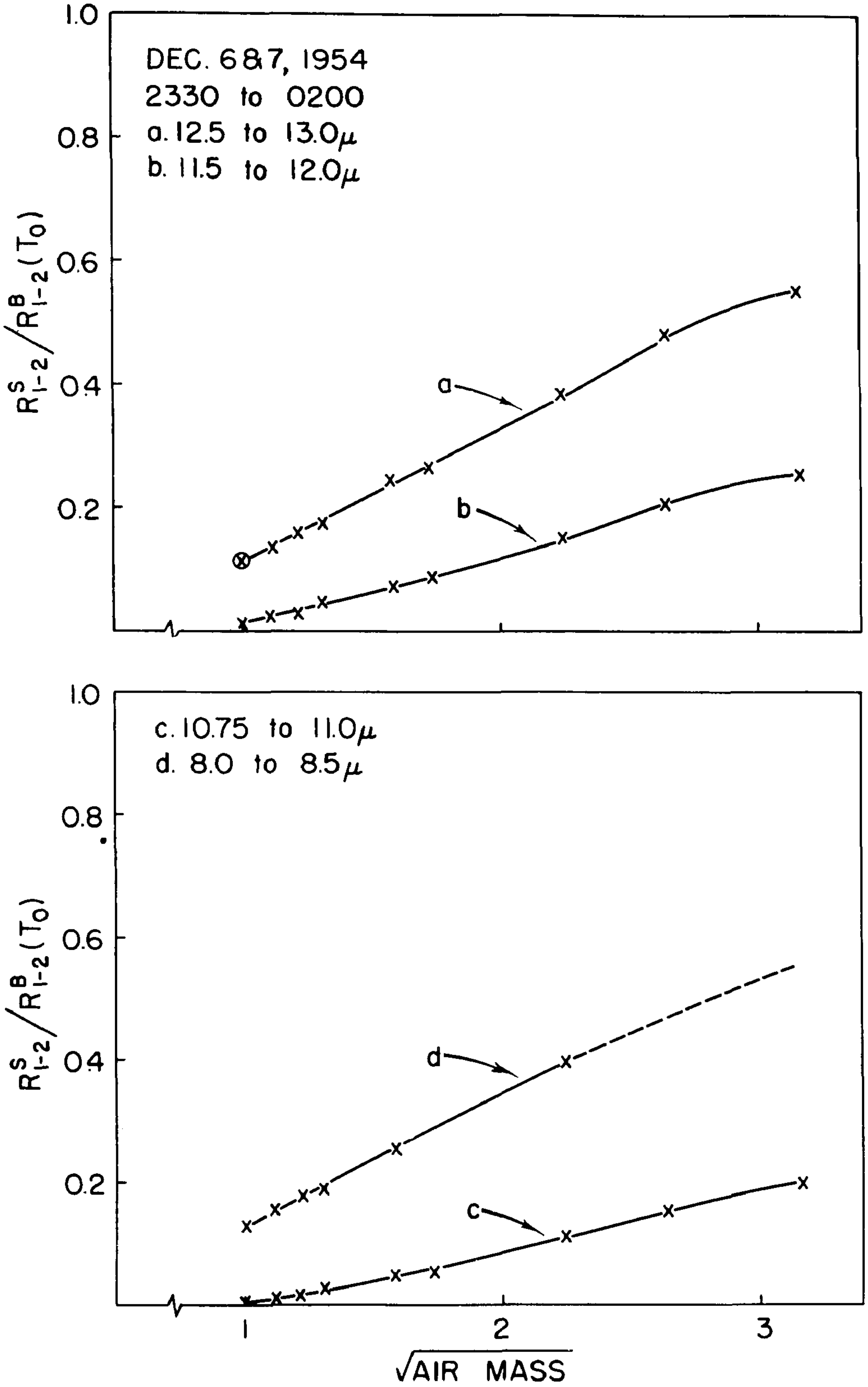
DEC. 6&7, 1954
2330 to 0200
a. 12.5 to 13.0μ
b. 11.5 to 12.0μ
a
b
c. 10.75 to 11.0μ
d. 8.0 to 8.5μ
d
c
1.0
0.8
0.6
0.4
0.2
$R^S_{1-2}/R^B_{1-2}(T_0)$
1
2
3
$\sqrt{\text{AIR MASS}}$

Figure 70.

APPENDIX V Curves of Radiation as a Function of Zenith Distance

This appendix contains Figures 71 through 144 which consist of curves of the radiation as a function of zenith distance for the various wavelength intervals selected. At the bottom in each figure is the corresponding curve for πR^{S}_{1-2} sin 2z which, as described in section VIII of the text, may be integrated over z to find the value $\underline{R}^{S}_{1-2}(\Sigma)$. The area under these curves was planimetered and calibrated to obtain this value which is included in Tables I through VI along with other pertinent data and results. These tables follow immediately after Figure 144.

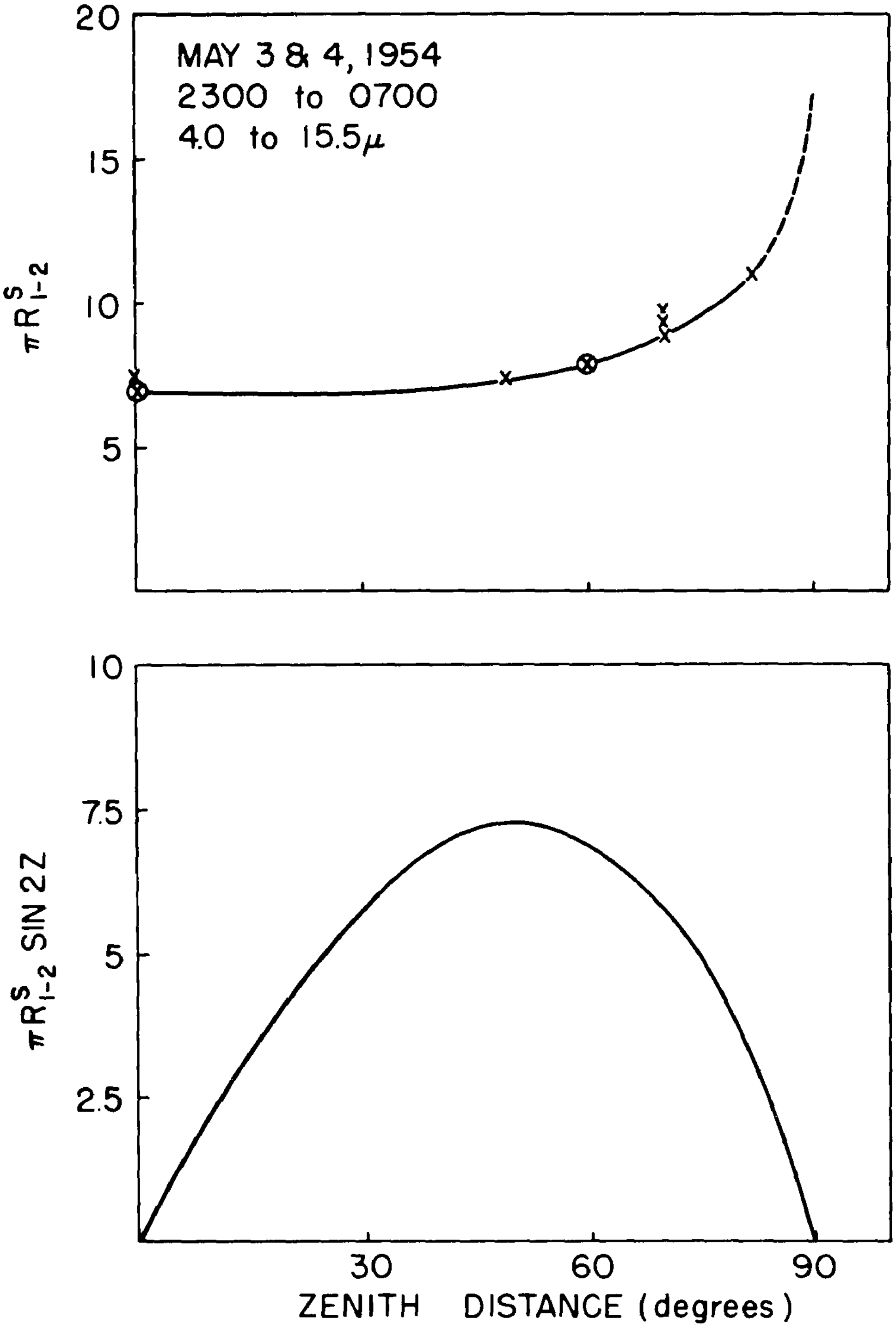
MAY 3 & 4, 1954
2300 to 0700
4.0 to 15.5μ
20
15
10
5
πR^S_{1-2}
10
7.5
5
2.5
πR^S_{1-2} SIN 2Z
30
60
90
ZENITH DISTANCE (degrees)

Figure 71.

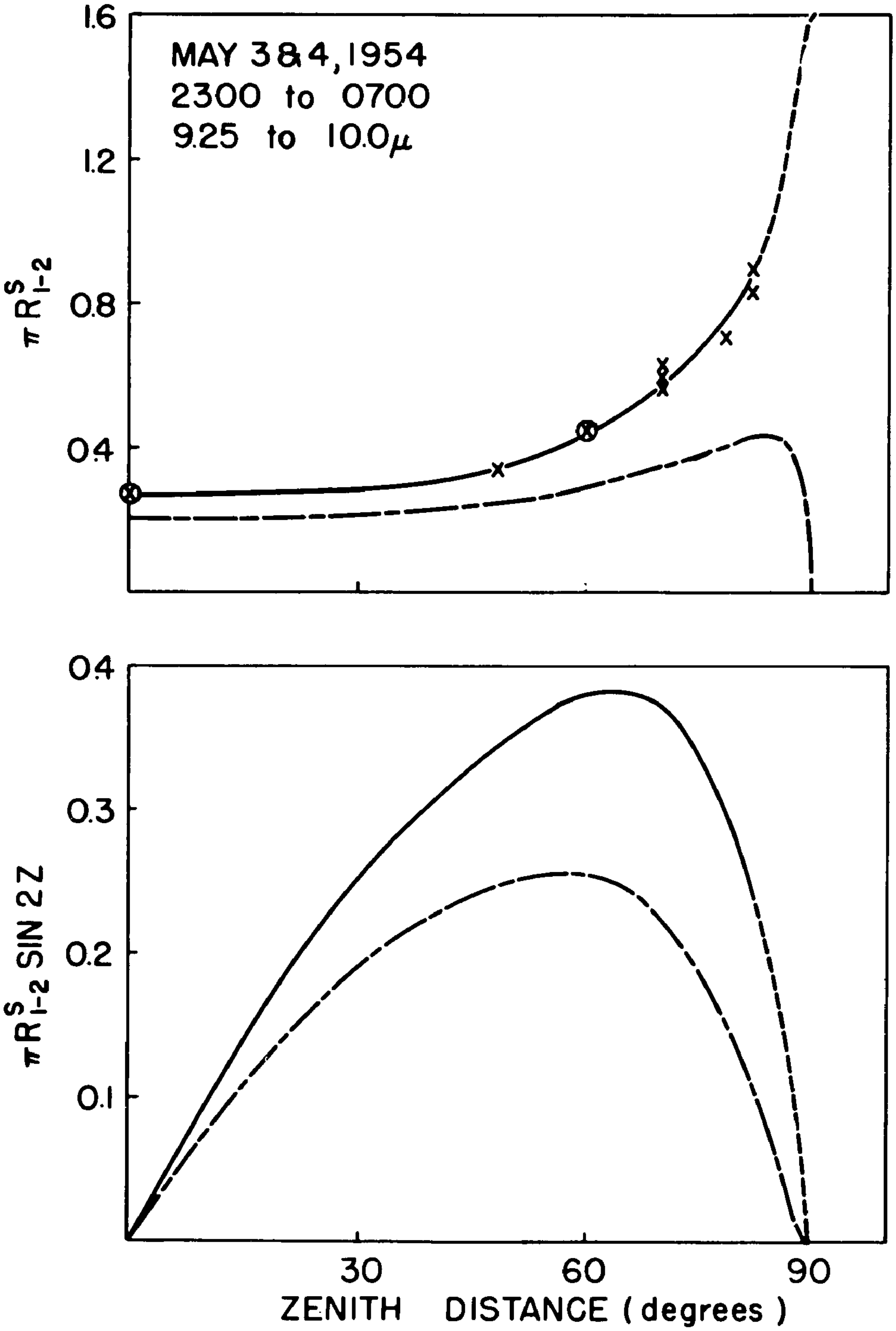
MAY 3&4, 1954
2300 to 0700
9.25 to 10.0μ
1.6
1.2
0.8
0.4
πR^S_{1-2}
0.4
0.3
0.2
0.1
πR^S_{1-2} SIN 2Z
30
60
90
ZENITH DISTANCE (degrees)

Figure 72.

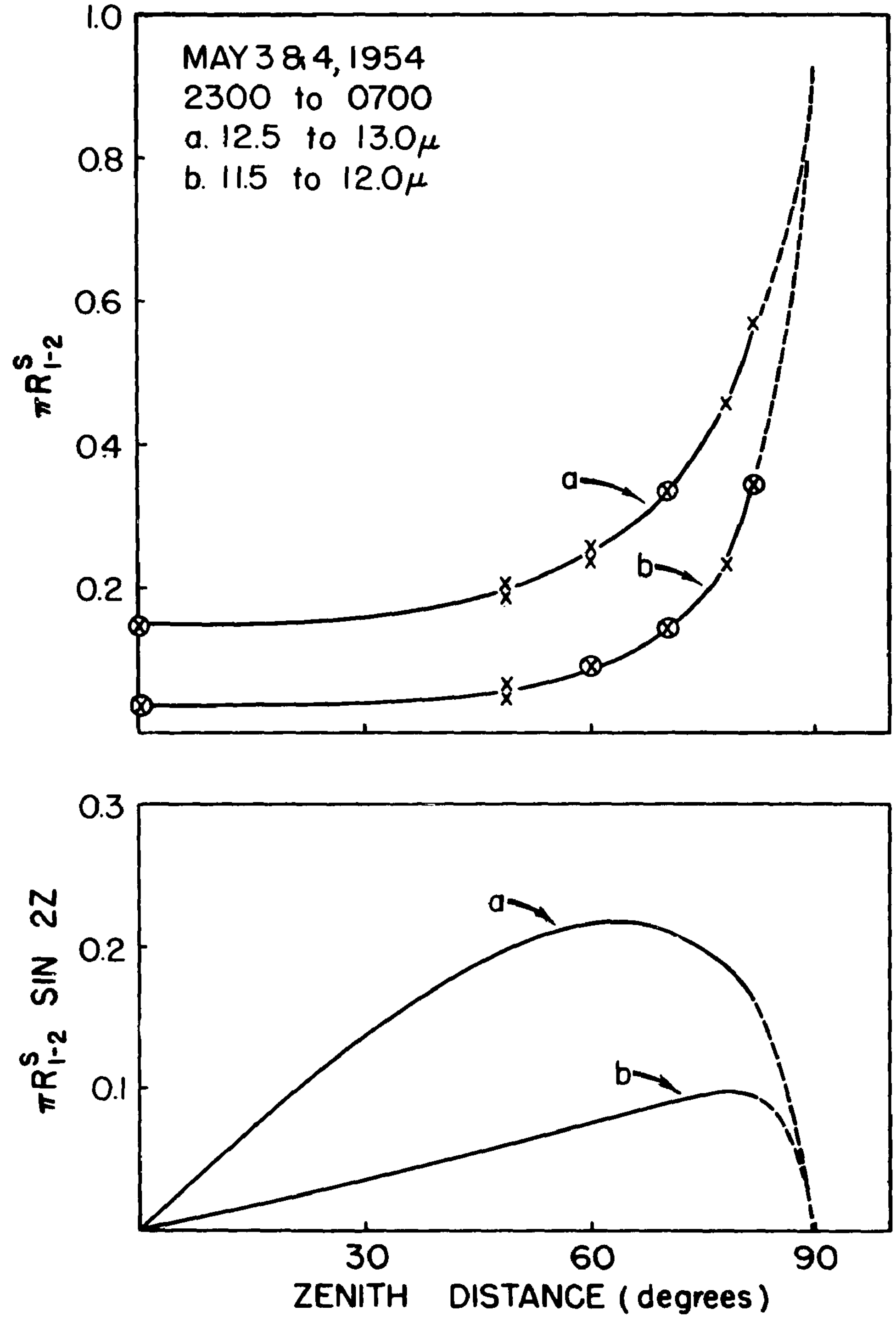
MAY 3 & 4, 1954
2300 to 0700
a. 12.5 to 13.0μ
b. 11.5 to 12.0μ
1.0
0.8
0.6
0.4
0.2
πR^S_{1-2}
a
b
0.3
0.2
0.1
πR^S_{1-2} SIN 2Z
a
b
30
60
90
ZENITH DISTANCE (degrees)

Figure 73.

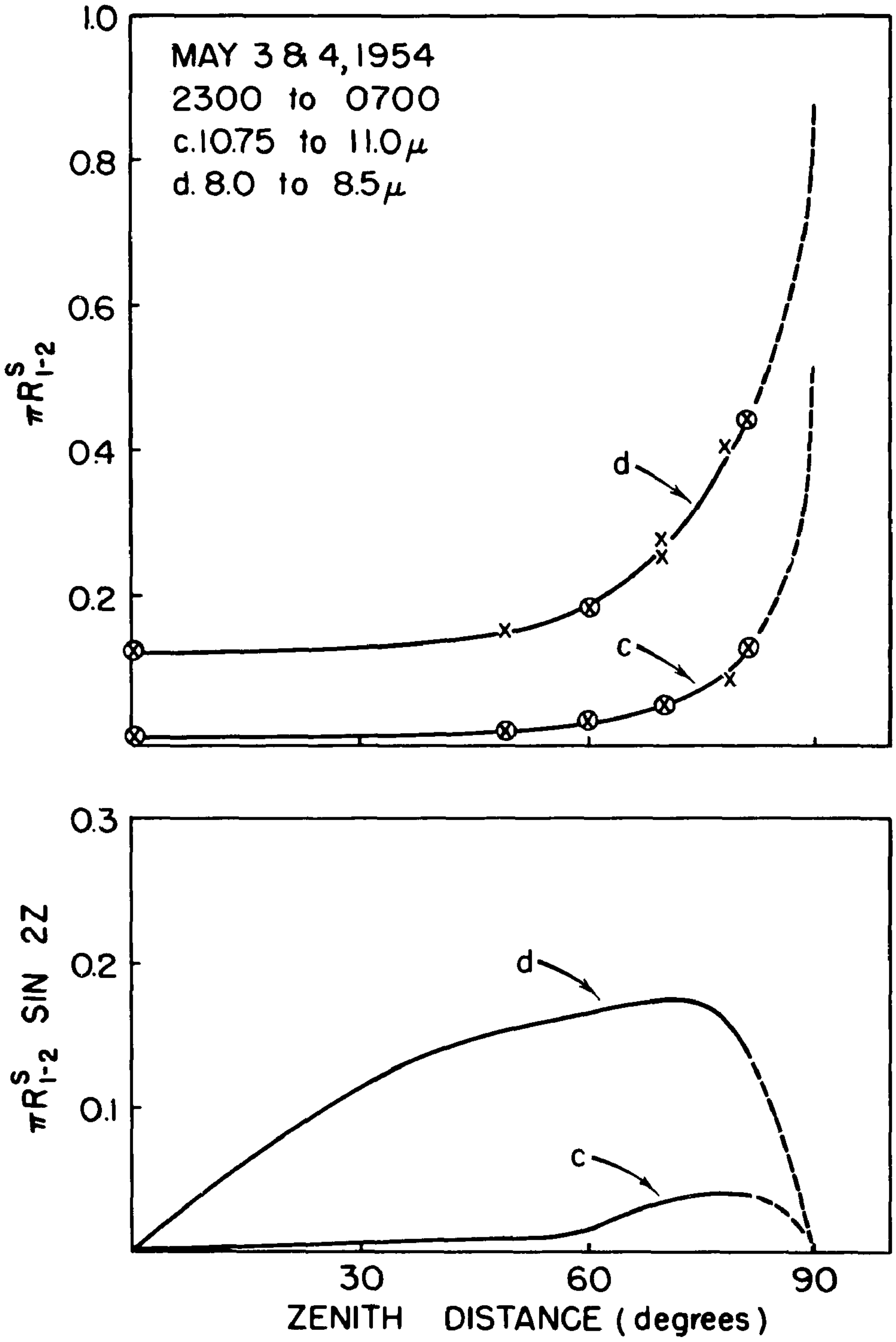
MAY 3 & 4, 1954
2300 to 0700
c. 10.75 to 11.0 μ
d. 8.0 to 8.5 μ
1.0
0.8
0.6
0.4
0.2
πR^{S}_{1-2}
d
c
0.3
0.2
0.1
πR^{S}_{1-2} SIN 2Z
d
c
30
60
90
ZENITH DISTANCE (degrees)

Figure 74.

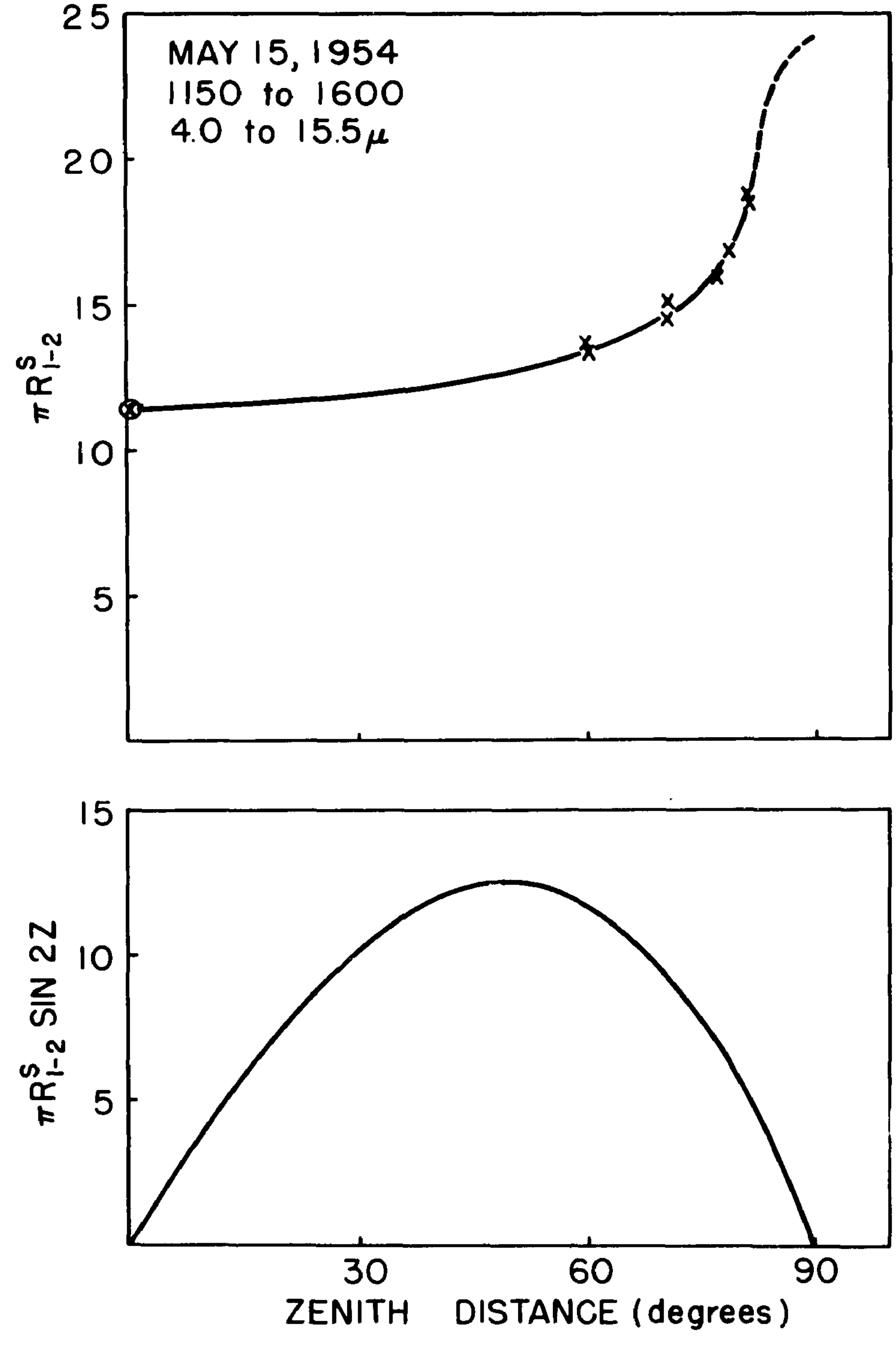
MAY 15, 1954
1150 to 1600
4.0 to 15.5μ
25
20
15
10
5
πR^S_{1-2}
15
10
5
πR^S_{1-2} SIN 2Z
30
60
90
ZENITH DISTANCE (degrees)

Figure 75.

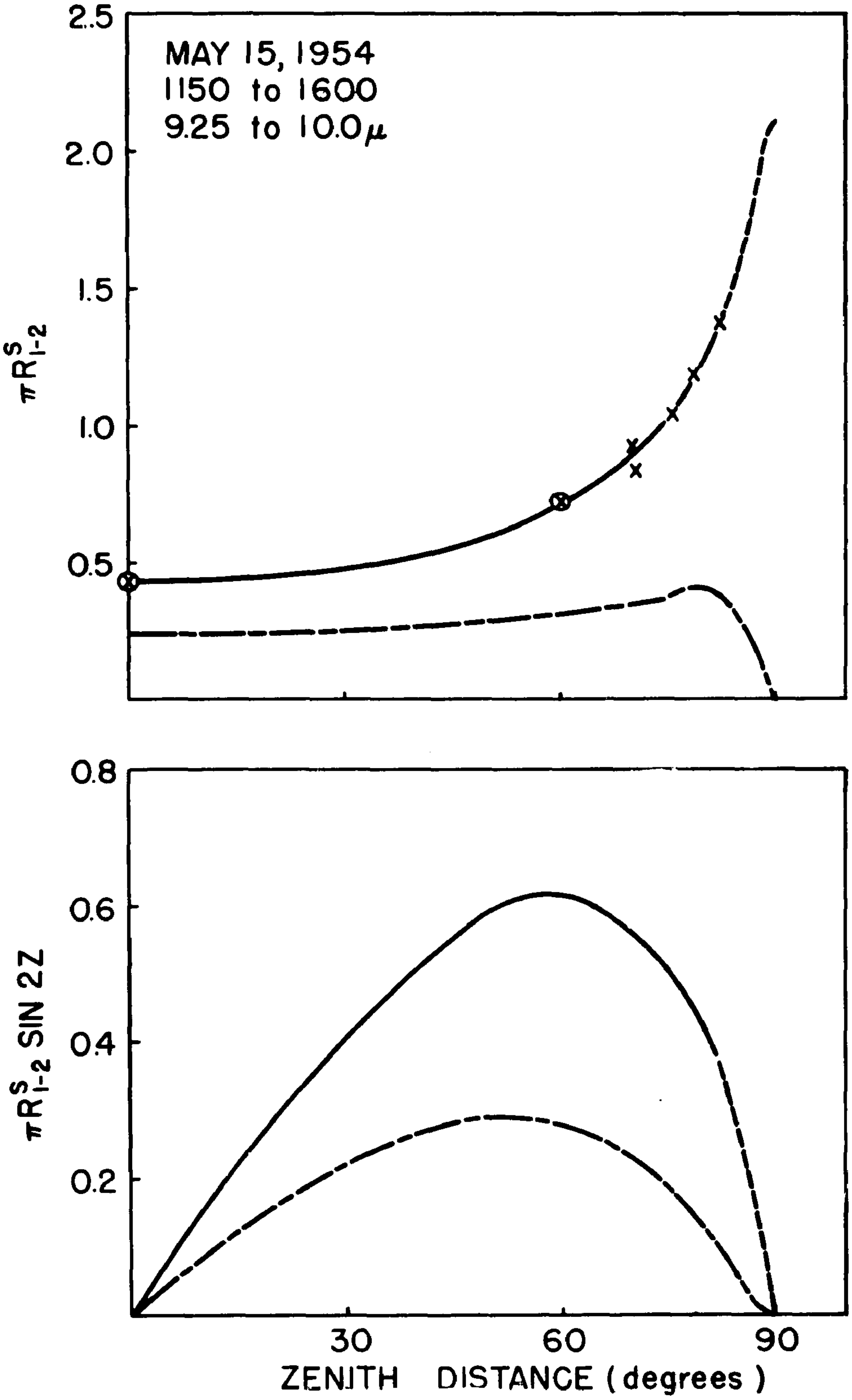
MAY 15, 1954
1150 to 1600
9.25 to 10.0μ
2.5
2.0
1.5
1.0
0.5
πR^S_1-2
0.8
0.6
0.4
0.2
πR^S_1-2 SIN 2Z
30
60
90
ZENITH DISTANCE (degrees)

Figure 76.

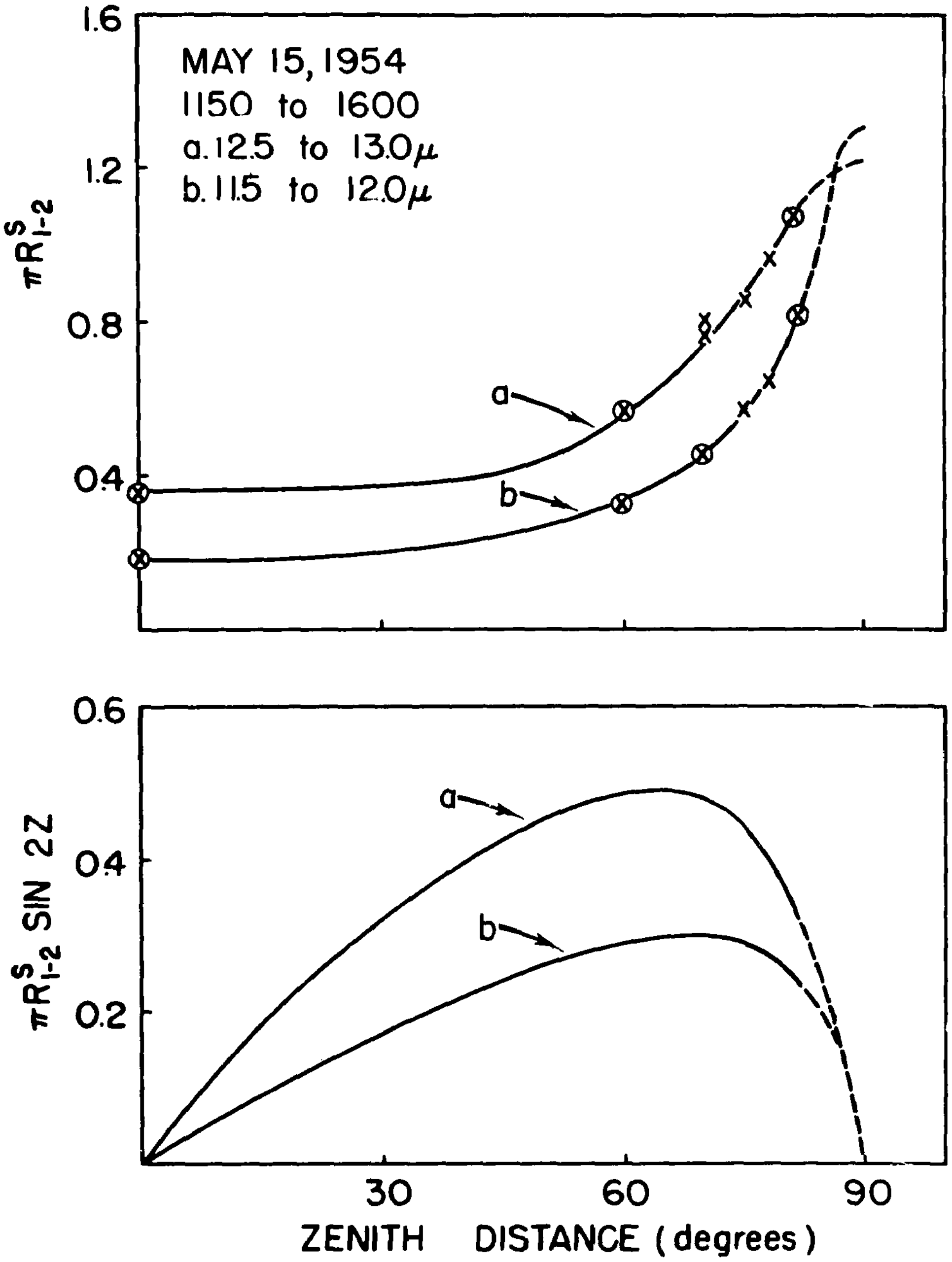
1.6
MAY 15, 1954
1150 to 1600
a. 12.5 to 13.0μ
b. 11.5 to 12.0μ
1.2
πR^S_{1-2}
0.8
a
0.4
b
0.6
a
0.4
πR^S_{1-2} SIN 2Z
b
0.2
30
60
90
ZENITH DISTANCE (degrees)

Figure 77.

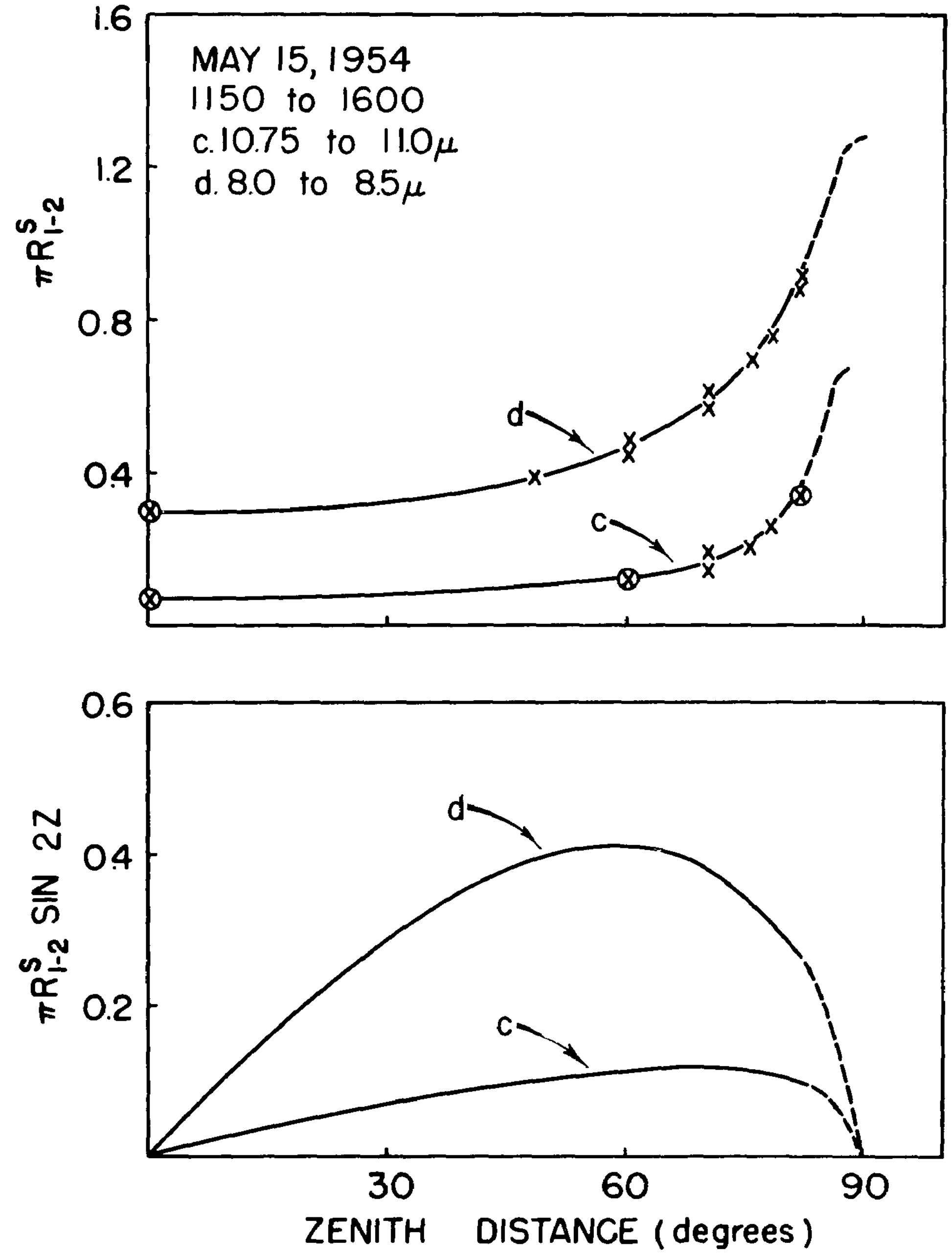
MAY 15, 1954
1150 to 1600
c. 10.75 to 11.0μ
d. 8.0 to 8.5μ
1.6
1.2
0.8
0.4
πR$^S_{1-2}$
d
c
0.6
0.4
0.2
πR$^S_{1-2}$ SIN 2Z
30
60
90
ZENITH DISTANCE (degrees)

Figure 78.

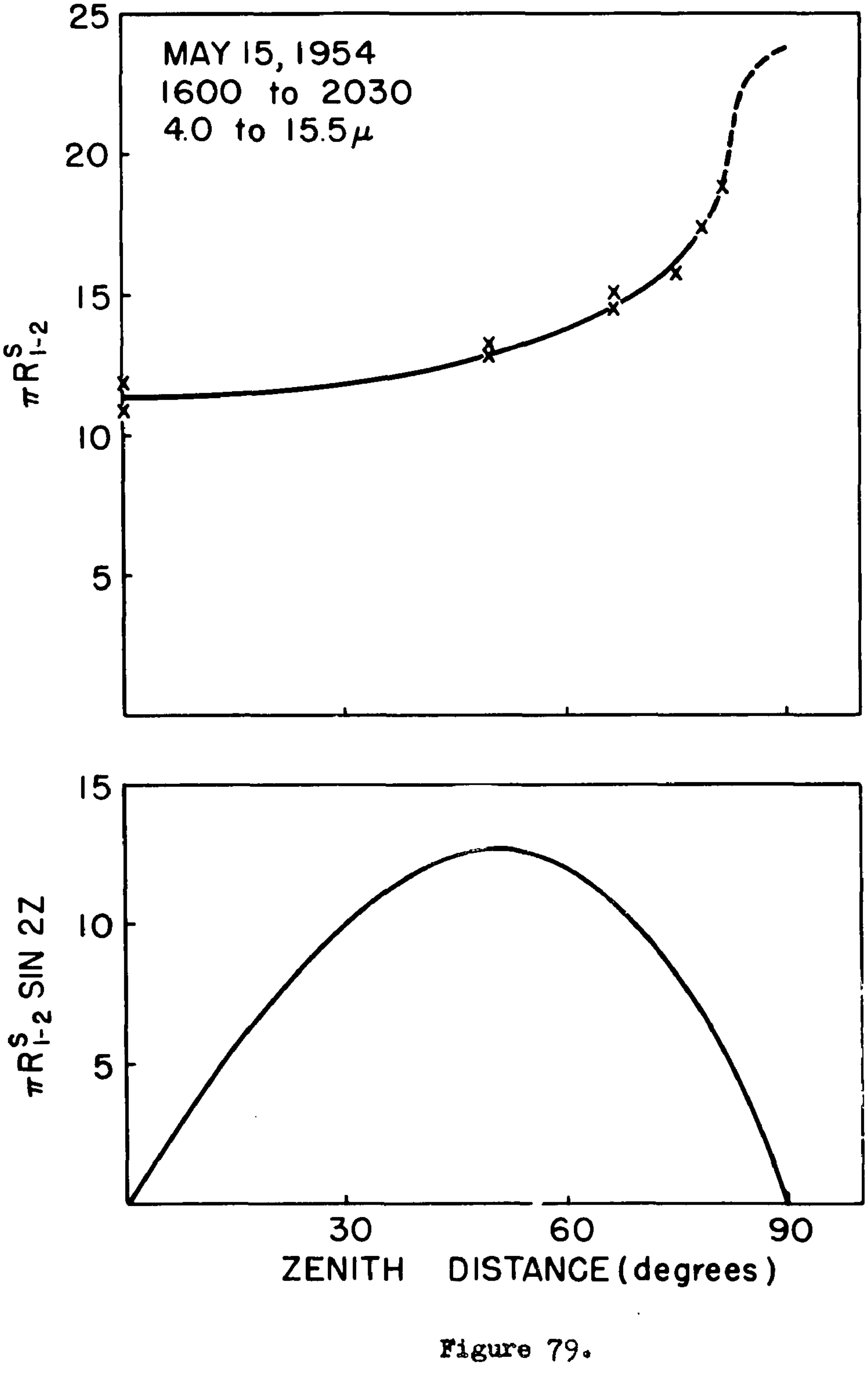
25
20
15
10
5
MAY 15, 1954
1600 to 2030
4.0 to 15.5μ
πR^{S}_{1-2}
15
10
5
πR^{S}_{1-2} SIN 2Z
30
60
90
ZENITH DISTANCE (degrees)

Figure 79.

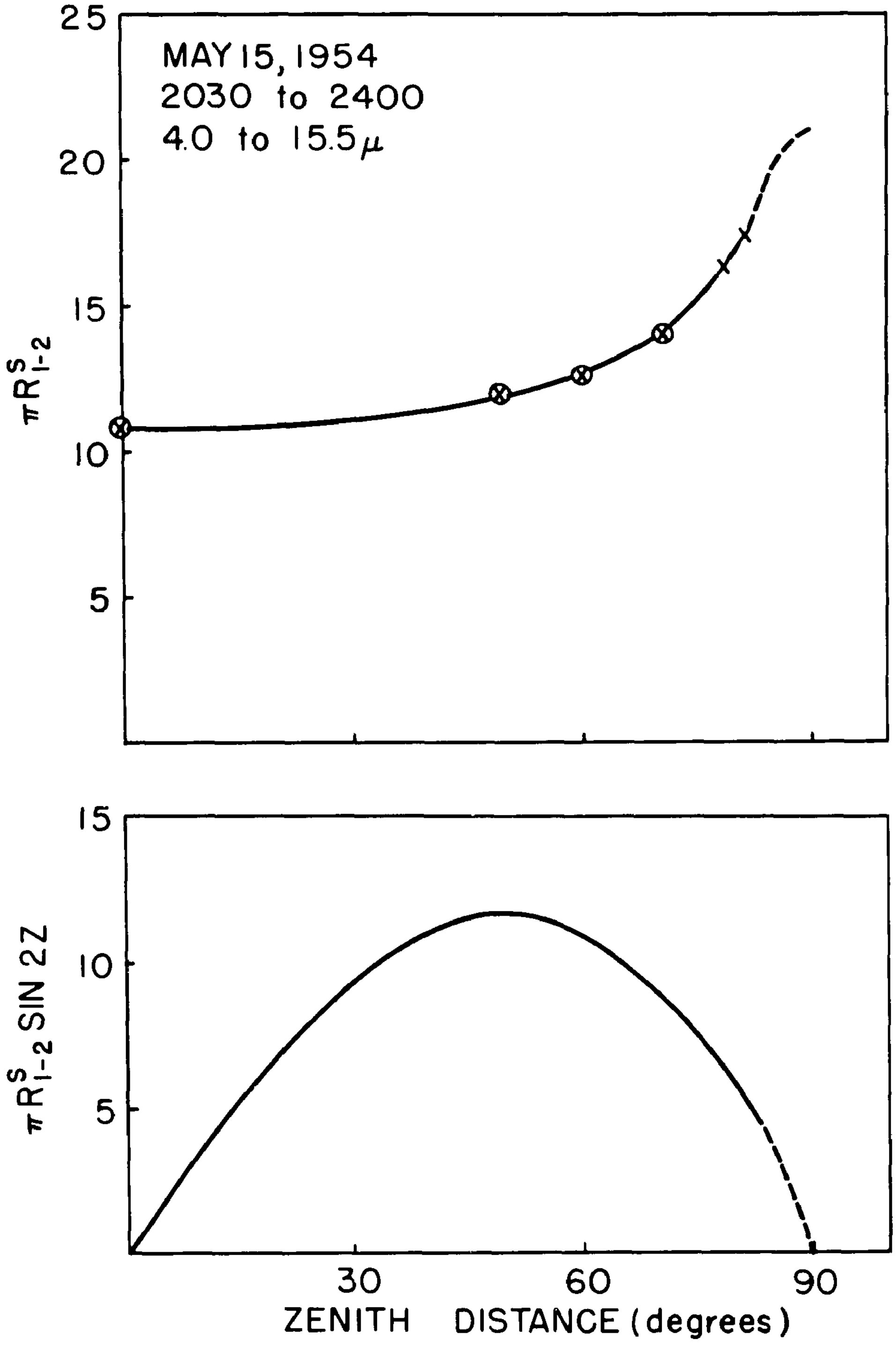
MAY 15, 1954
2030 to 2400
4.0 to 15.5μ
25
20
15
10
5
πR^S_{1-2}
15
10
5
πR^S_{1-2} SIN 2Z
30
60
90
ZENITH DISTANCE (degrees)

Figure 80.

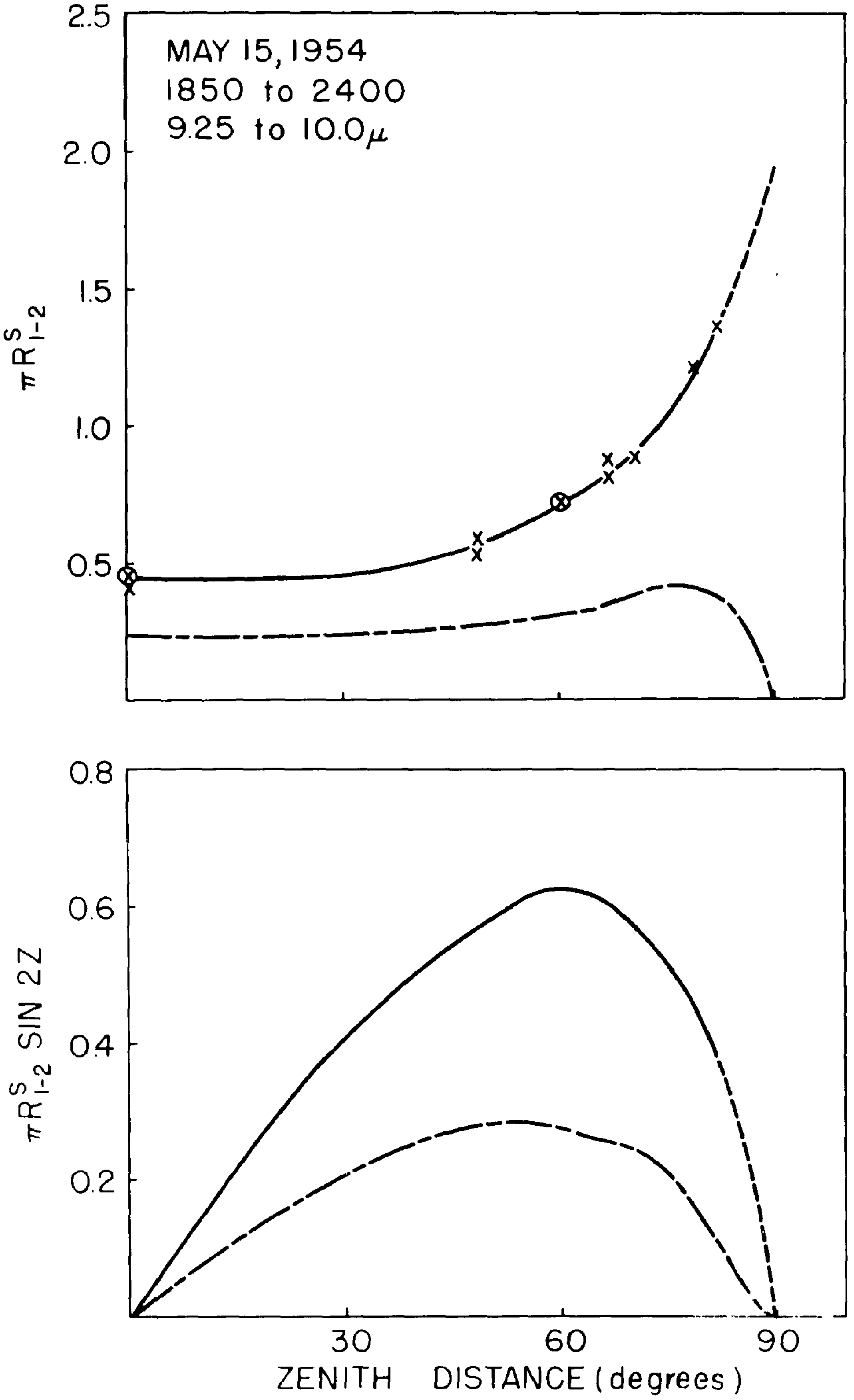
MAY 15, 1954
1850 to 2400
9.25 to 10.0μ
2.5
2.0
1.5
1.0
0.5
πR^{S}_{1-2}
0.8
0.6
0.4
0.2
πR^{S}_{1-2} SIN 2Z
30
60
90
ZENITH DISTANCE (degrees)

Figure 81.

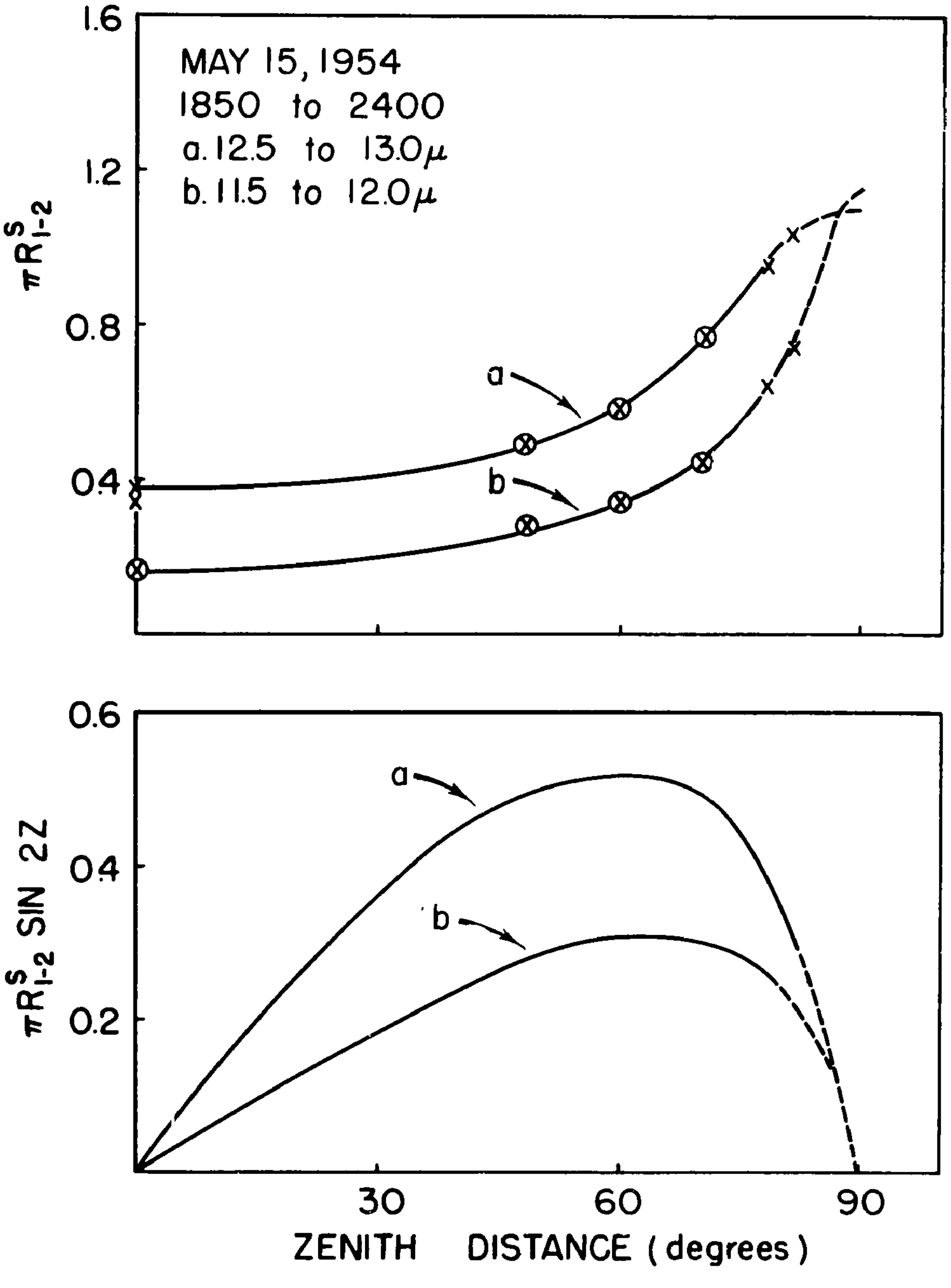
MAY 15, 1954
1850 to 2400
a. 12.5 to 13.0μ
b. 11.5 to 12.0μ
1.6
1.2
0.8
0.4
πR^S_1-2
a
b
0.6
0.4
0.2
πR^S_1-2 SIN 2Z
30
60
90
ZENITH DISTANCE (degrees)

Figure 82.

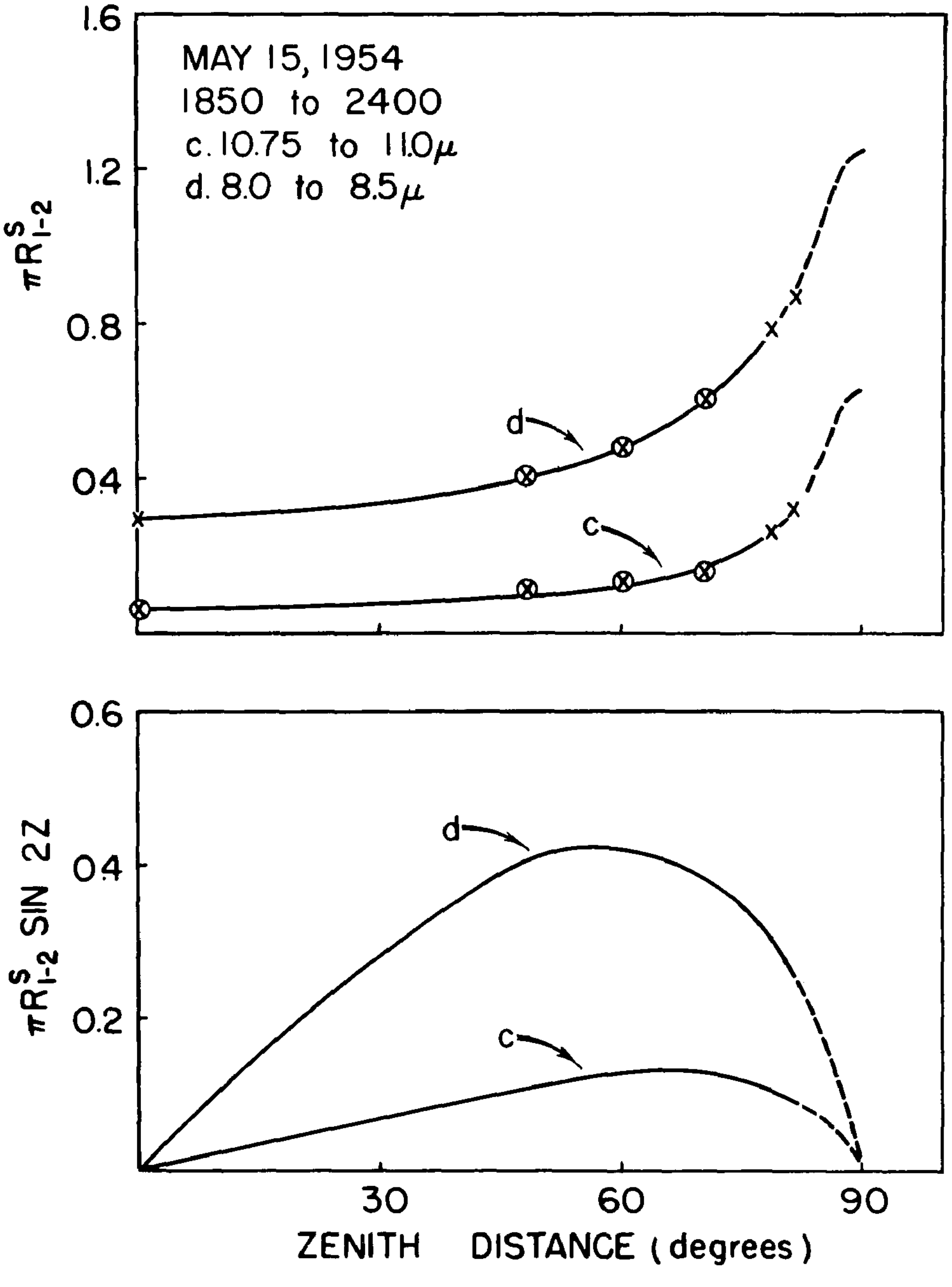
MAY 15, 1954
1850 to 2400
c. 10.75 to 11.0μ
d. 8.0 to 8.5μ
1.6
1.2
0.8
0.4
πR^S_{1-2}
d
c
0.6
0.4
0.2
πR^S_{1-2} SIN 2Z
d
c
30
60
90
ZENITH DISTANCE (degrees)

Figure 83.

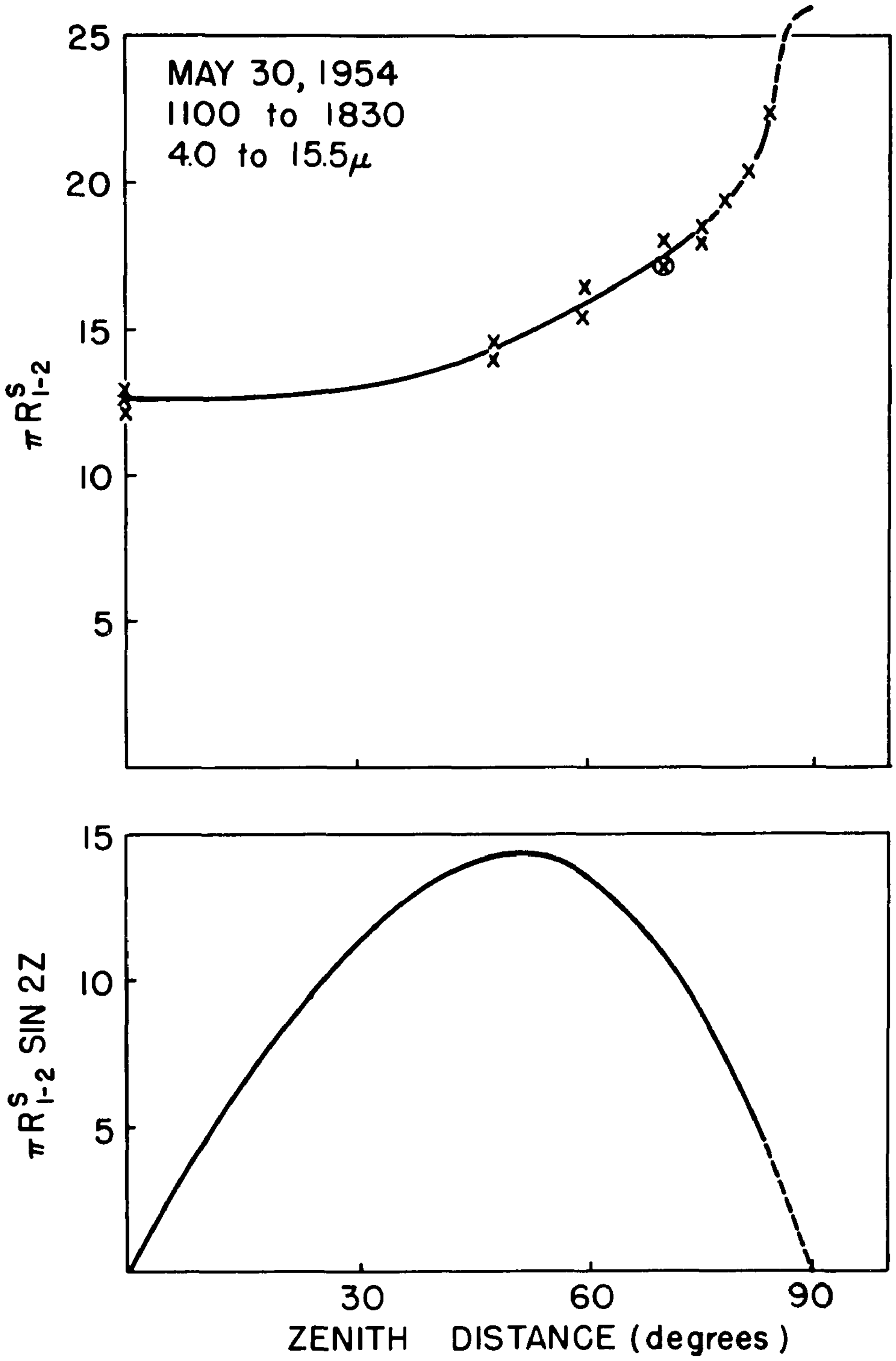
MAY 30, 1954
1100 to 1830
4.0 to 15.5μ
25
20
15
10
5
πR^S_{1-2}
15
10
5
πR^S_{1-2} SIN 2Z
30
60
90
ZENITH DISTANCE (degrees)

Figure 84.

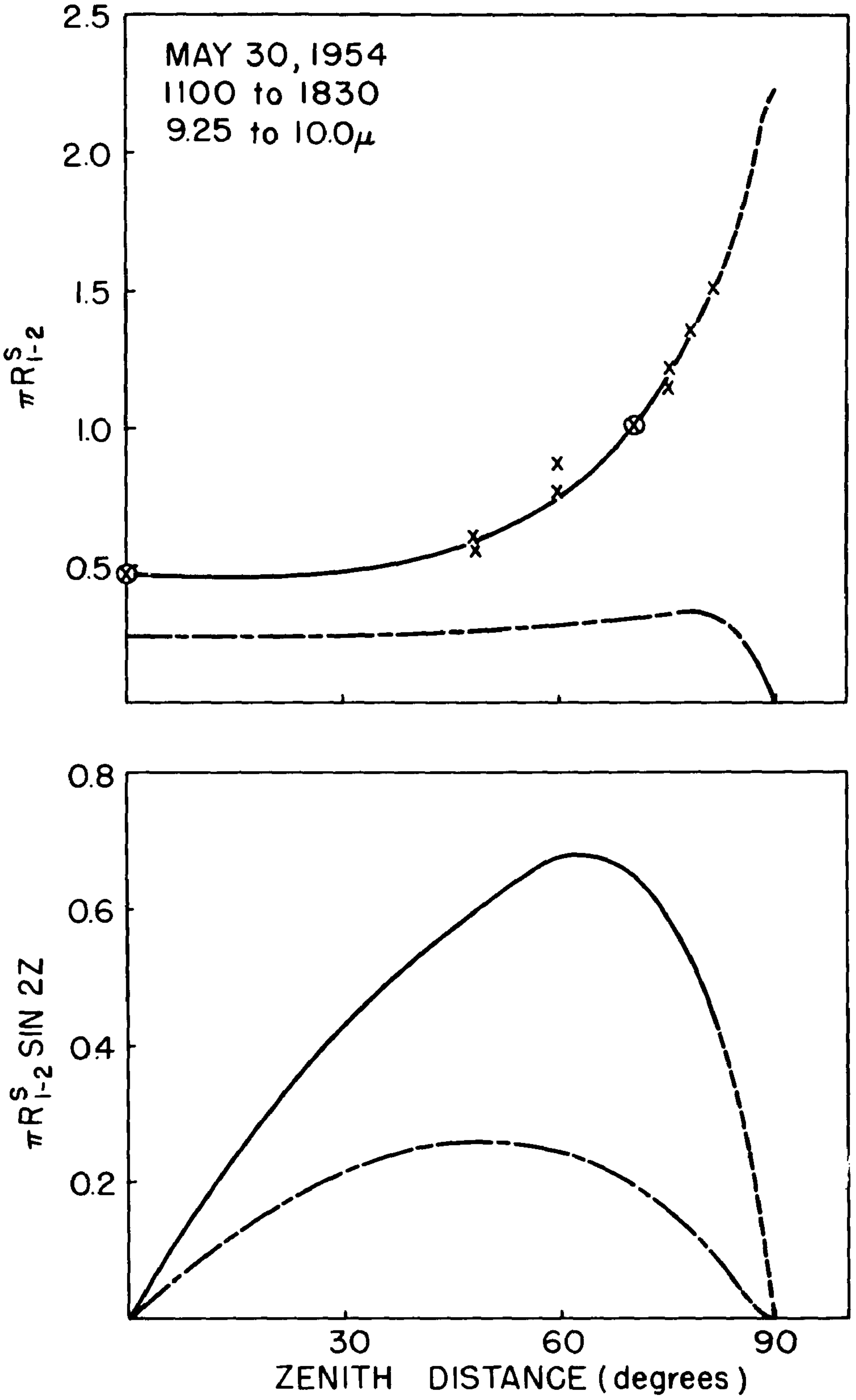
MAY 30, 1954
1100 to 1830
9.25 to 10.0μ
2.5
2.0
1.5
1.0
0.5
πR^{S}_{1-2}
0.8
0.6
0.4
0.2
πR^{S}_{1-2} SIN 2Z
30
60
90
ZENITH DISTANCE (degrees)

Figure 85.

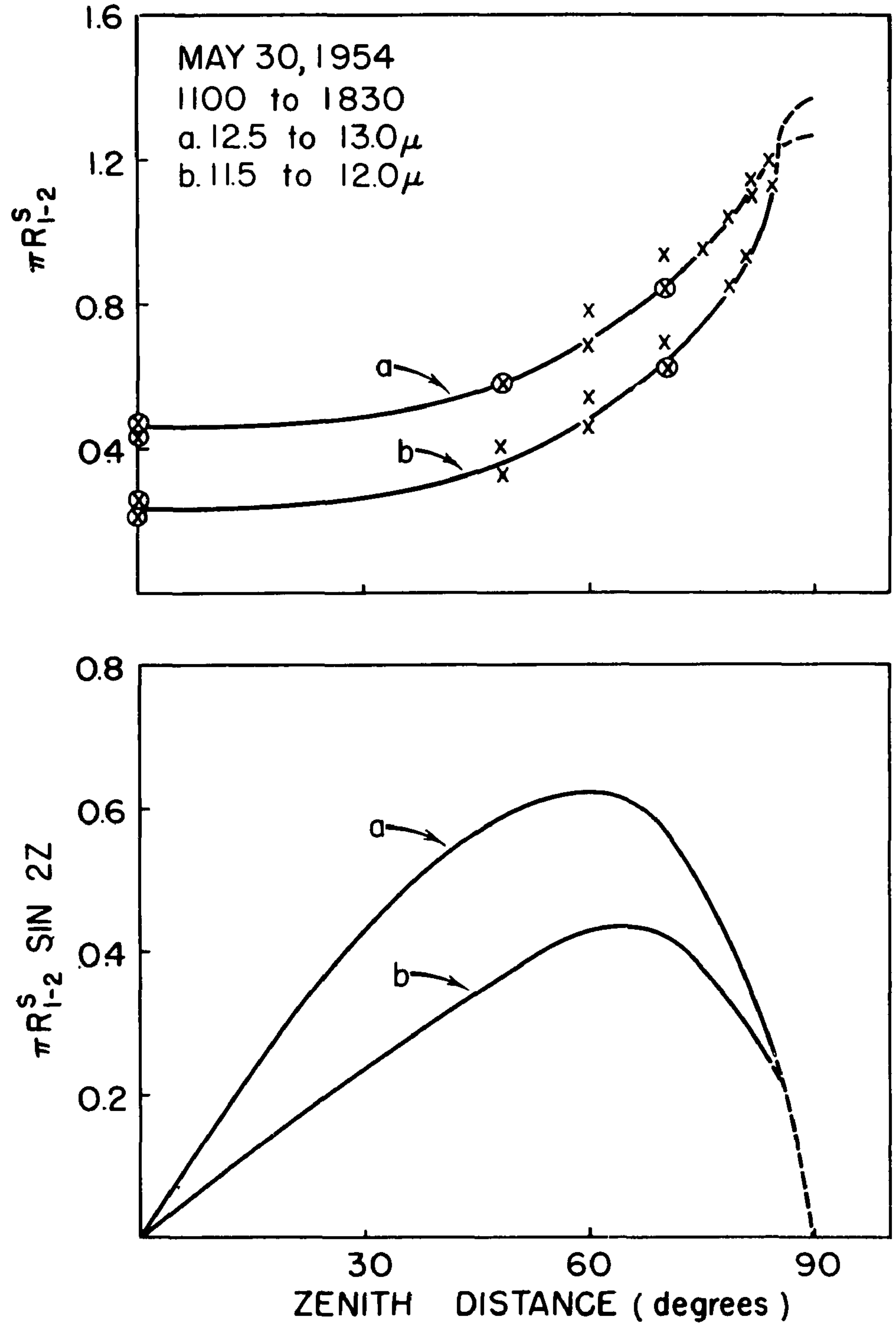
MAY 30, 1954
1100 to 1830
a. 12.5 to 13.0μ
b. 11.5 to 12.0μ
πR^S_{1-2}
1.6
1.2
0.8
0.4
a
b
πR^S_{1-2} SIN 2Z
0.8
0.6
0.4
0.2
30
60
90
ZENITH DISTANCE (degrees)

Figure 86.

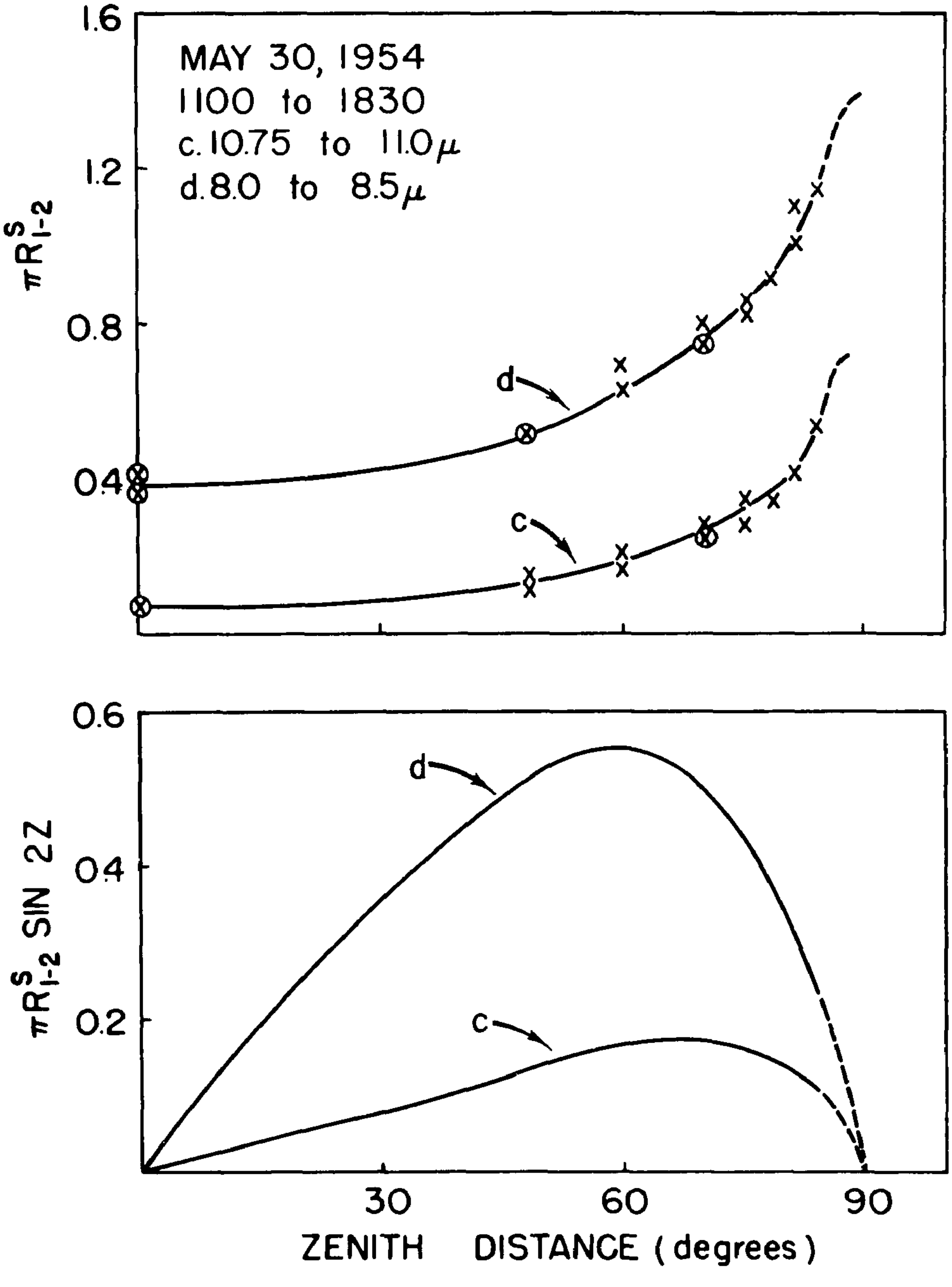
MAY 30, 1954
1100 to 1830
c. 10.75 to 11.0μ
d. 8.0 to 8.5μ
πR^S_{1-2}
1.6
1.2
0.8
0.4
d
c
πR^S_{1-2} SIN 2Z
0.6
0.4
0.2
30
60
90
ZENITH DISTANCE (degrees)

Figure 87.

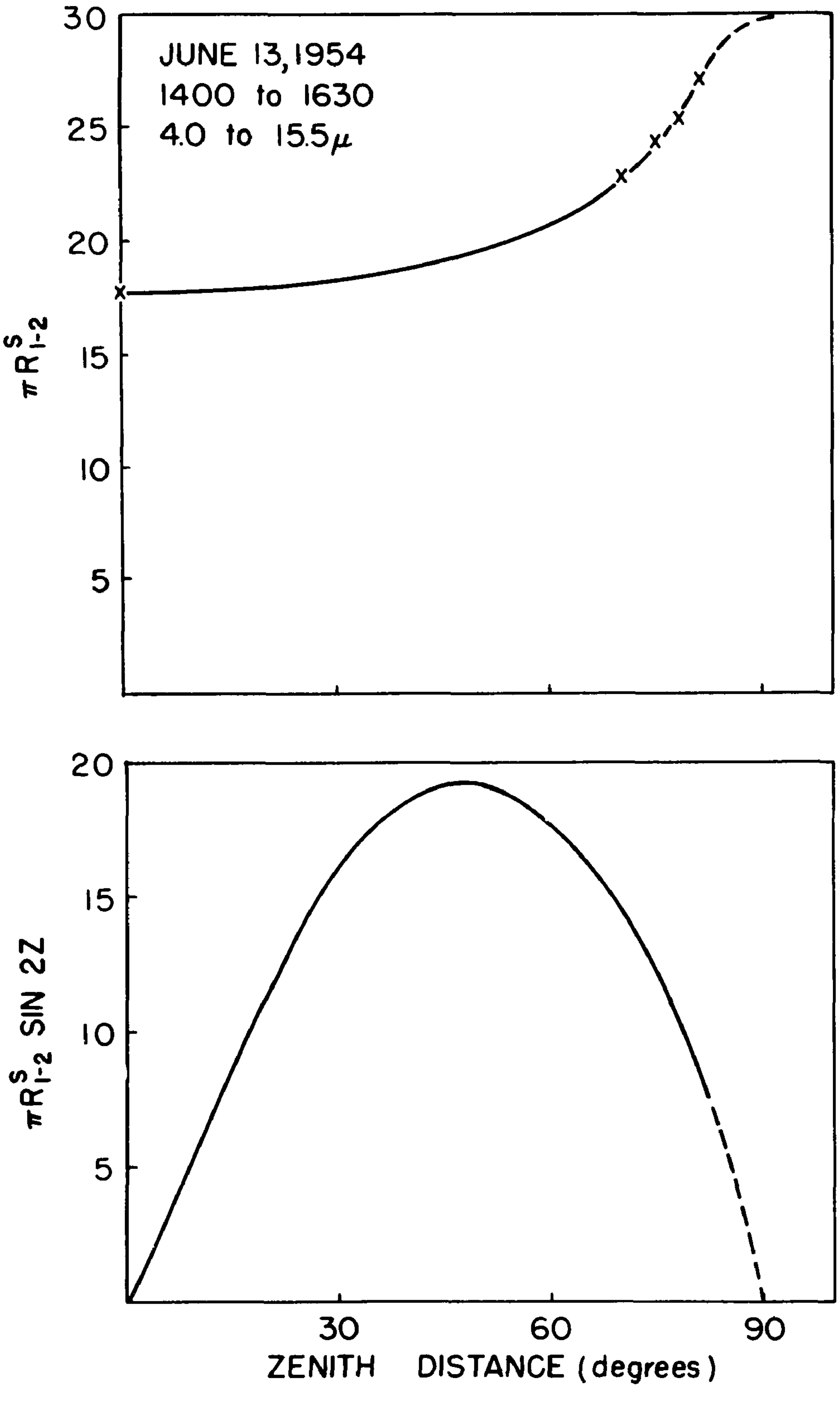
JUNE 13, 1954
1400 to 1630
4.0 to 15.5μ
πR^S_{1-2}
30
25
20
15
10
5
πR^S_{1-2} SIN 2Z
20
15
10
5
30
60
90
ZENITH DISTANCE (degrees)

Figure 88.

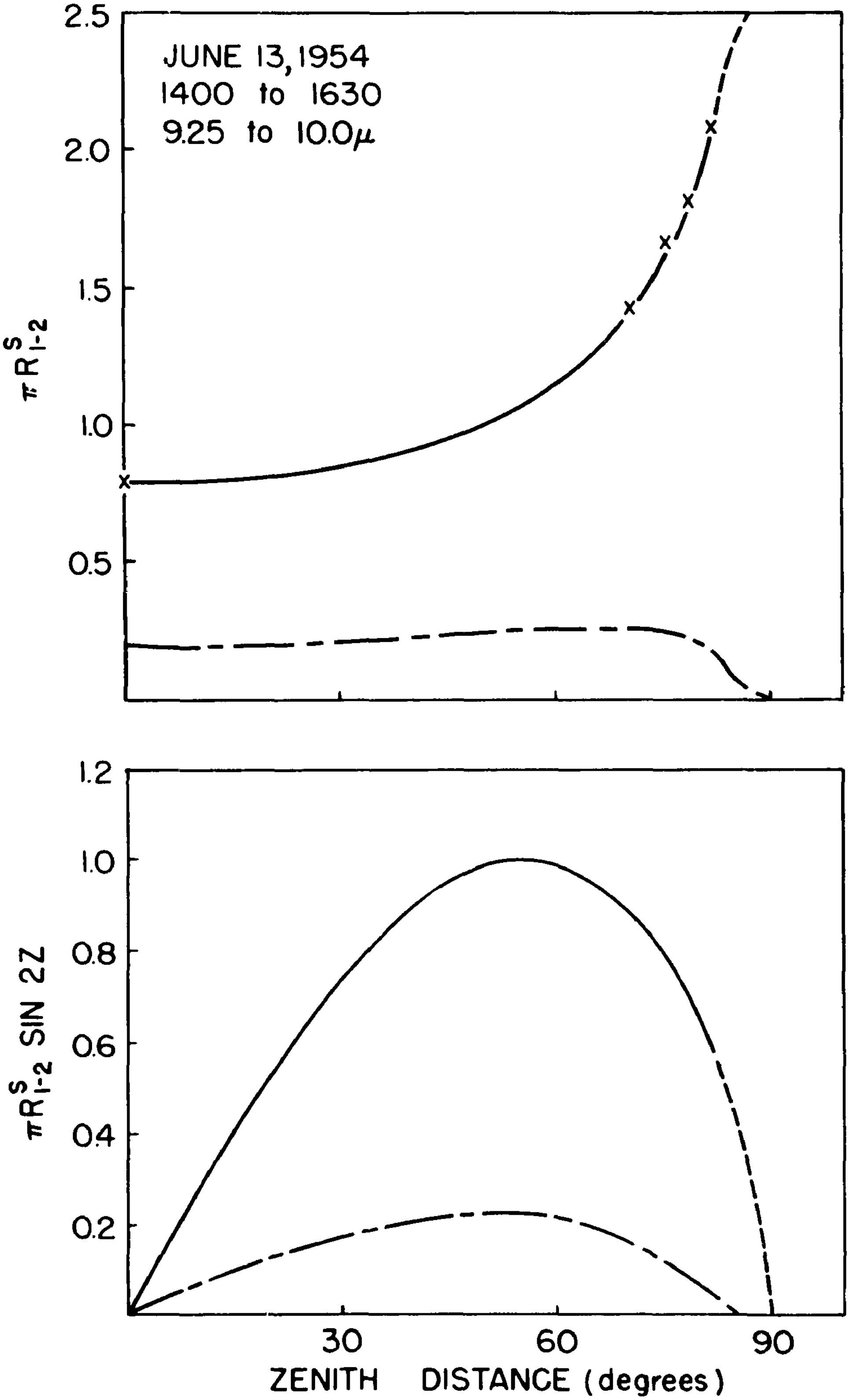
JUNE 13, 1954
1400 to 1630
9.25 to 10.0μ
πR^S_{1-2}
2.5
2.0
1.5
1.0
0.5
πR^S_{1-2} SIN 2Z
1.2
1.0
0.8
0.6
0.4
0.2
30
60
90
ZENITH DISTANCE (degrees)

Figure 89.

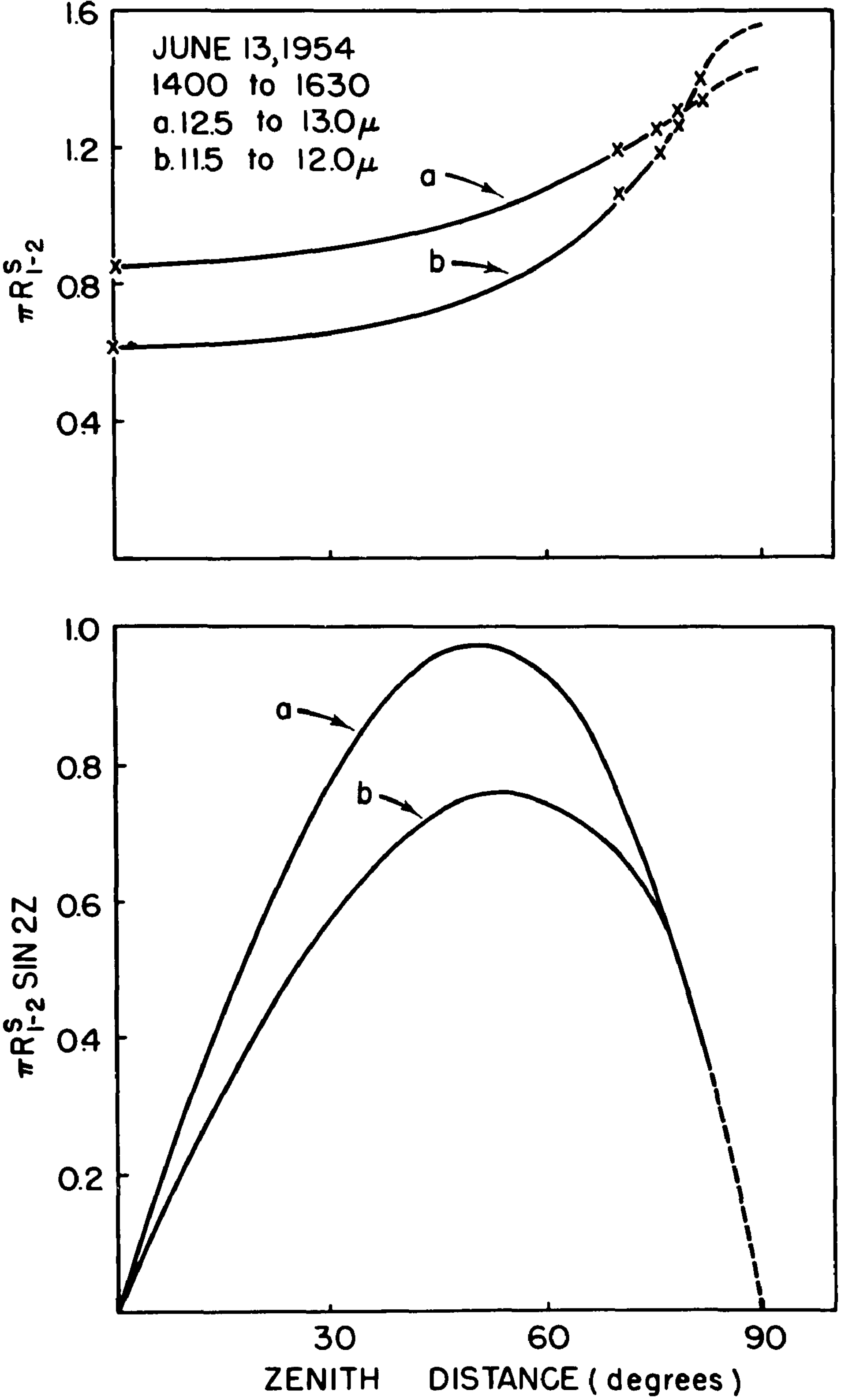
JUNE 13, 1954
1400 to 1630
a. 12.5 to 13.0μ
b. 11.5 to 12.0μ
a
b
1.6
1.2
0.8
0.4
πR^S_{1-2}
1.0
0.8
0.6
0.4
0.2
πR^S_{1-2} SIN 2Z
30
60
90
ZENITH DISTANCE (degrees)

Figure 90.

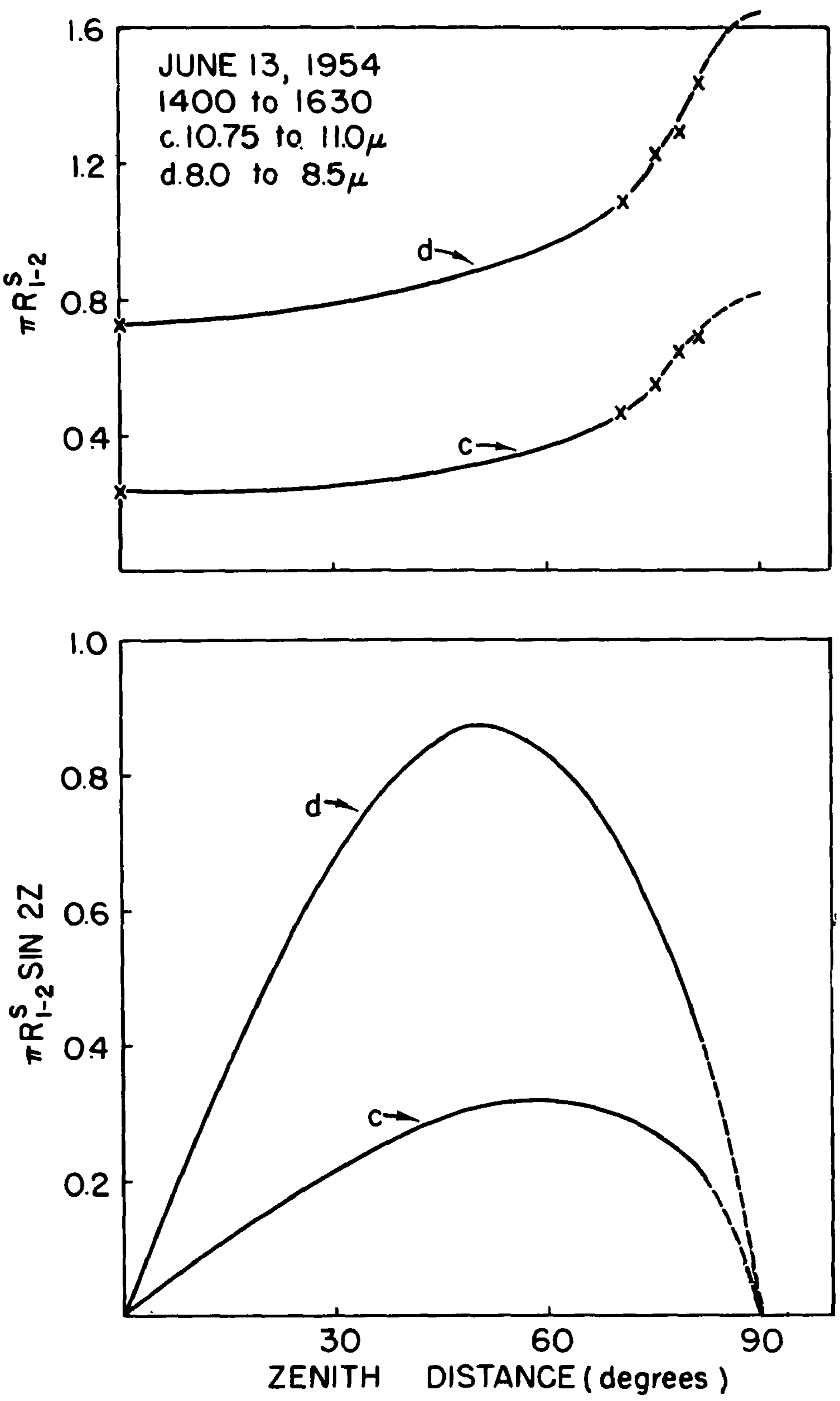
JUNE 13, 1954
1400 to 1630
c. 10.75 to 11.0μ
d. 8.0 to 8.5μ
d
c
πR^S_{1-2}
1.6
1.2
0.8
0.4
πR^S_{1-2} SIN 2Z
1.0
0.8
0.6
0.4
0.2
30
60
90
ZENITH DISTANCE (degrees)

Figure 91.

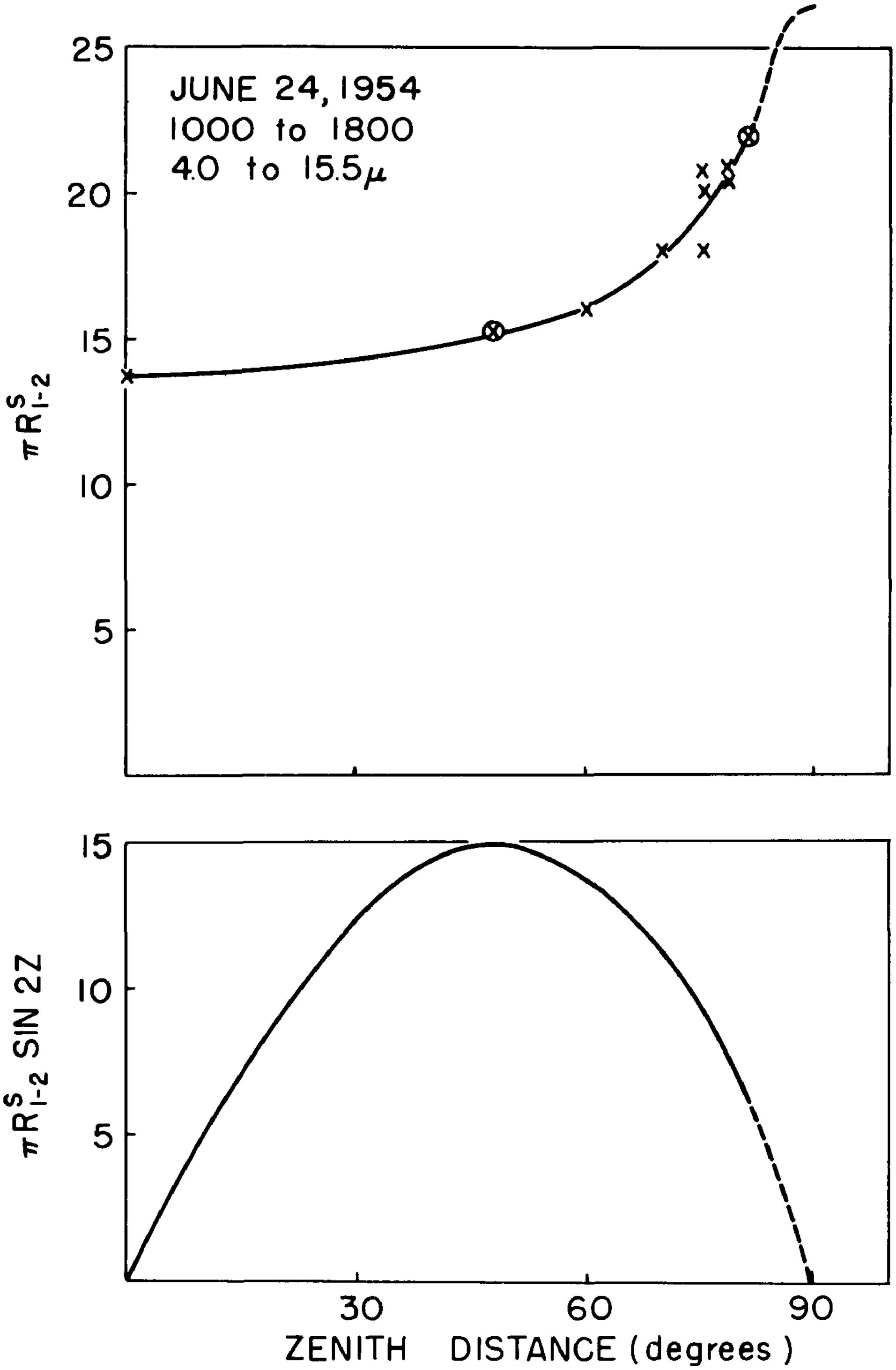
JUNE 24, 1954
1000 to 1800
4.0 to 15.5μ
πR^S_{1-2}
25
20
15
10
5
πR^S_{1-2} SIN 2Z
15
10
5
30
60
90
ZENITH DISTANCE (degrees)

Figure 92.

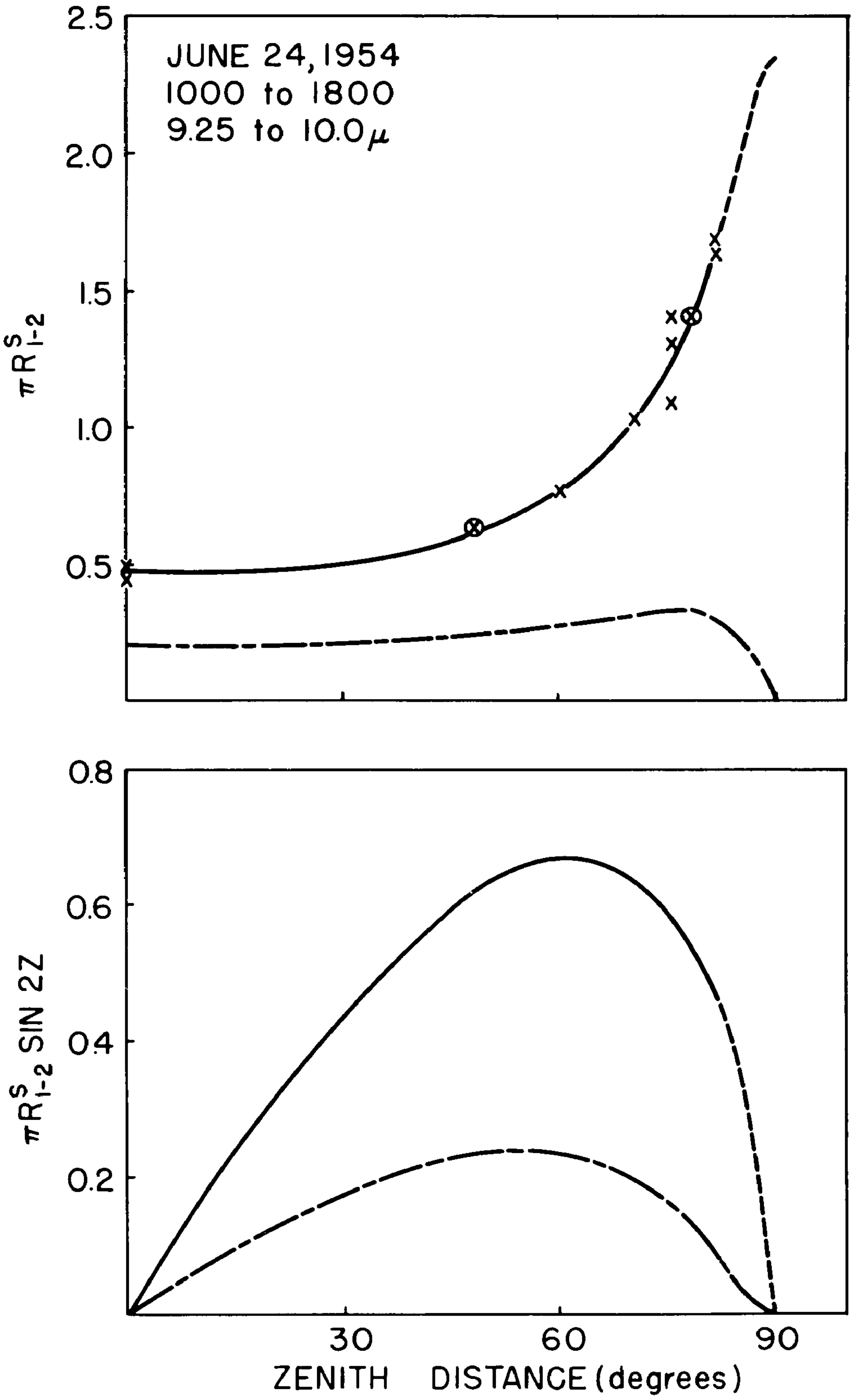
JUNE 24, 1954
1000 to 1800
9.25 to 10.0μ
2.5
2.0
1.5
1.0
0.5
πR^{S}_{1-2}
0.8
0.6
0.4
0.2
πR^{S}_{1-2} SIN 2Z
30
60
90
ZENITH DISTANCE (degrees)

Figure 93.

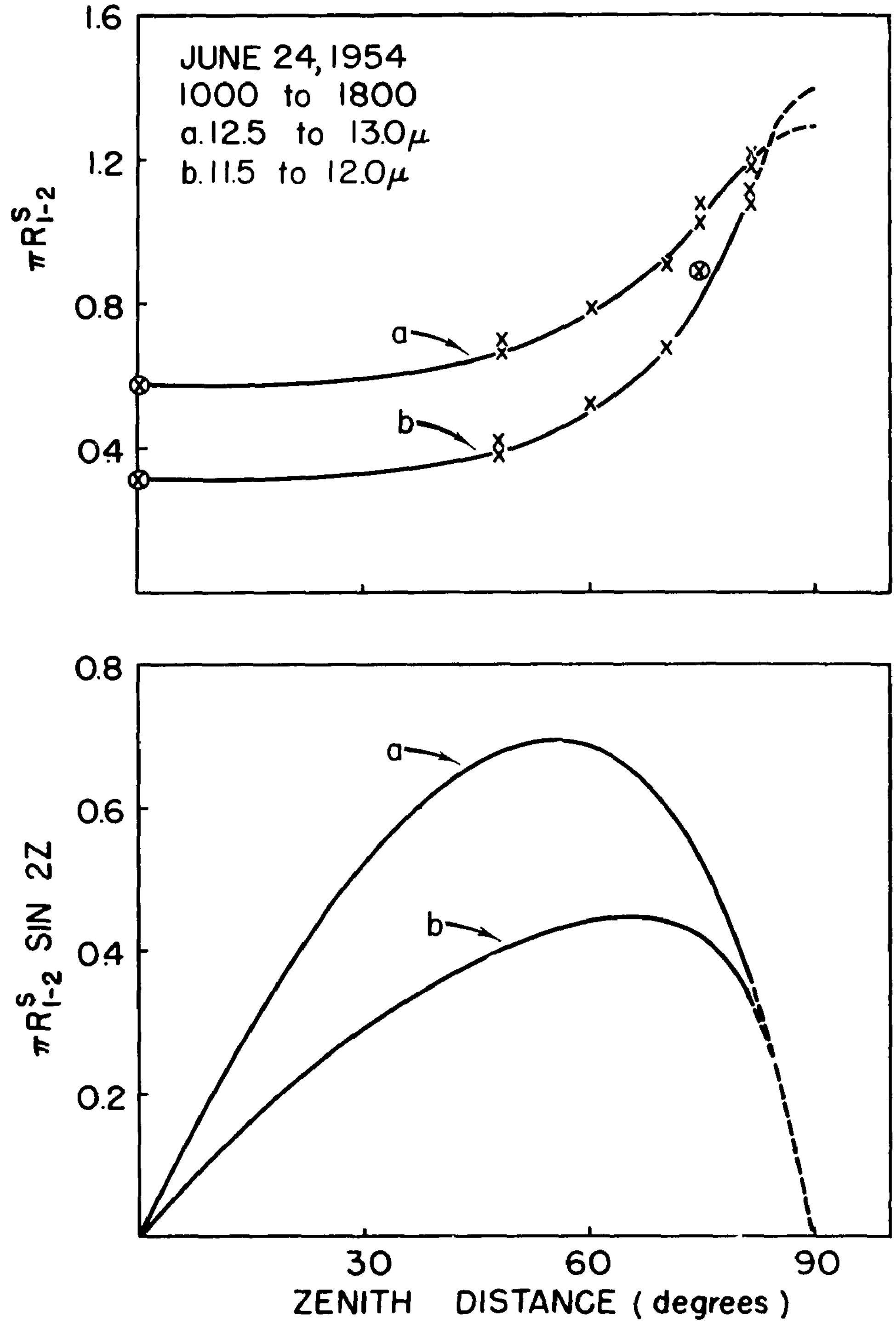
1.6
1.2
0.8
0.4
JUNE 24, 1954
1000 to 1800
a. 12.5 to 13.0μ
b. 11.5 to 12.0μ
πR^S_{1-2}
a
b
0.8
0.6
0.4
0.2
πR^S_{1-2} SIN 2Z
a
b
30
60
90
ZENITH DISTANCE (degrees)

Figure 94.

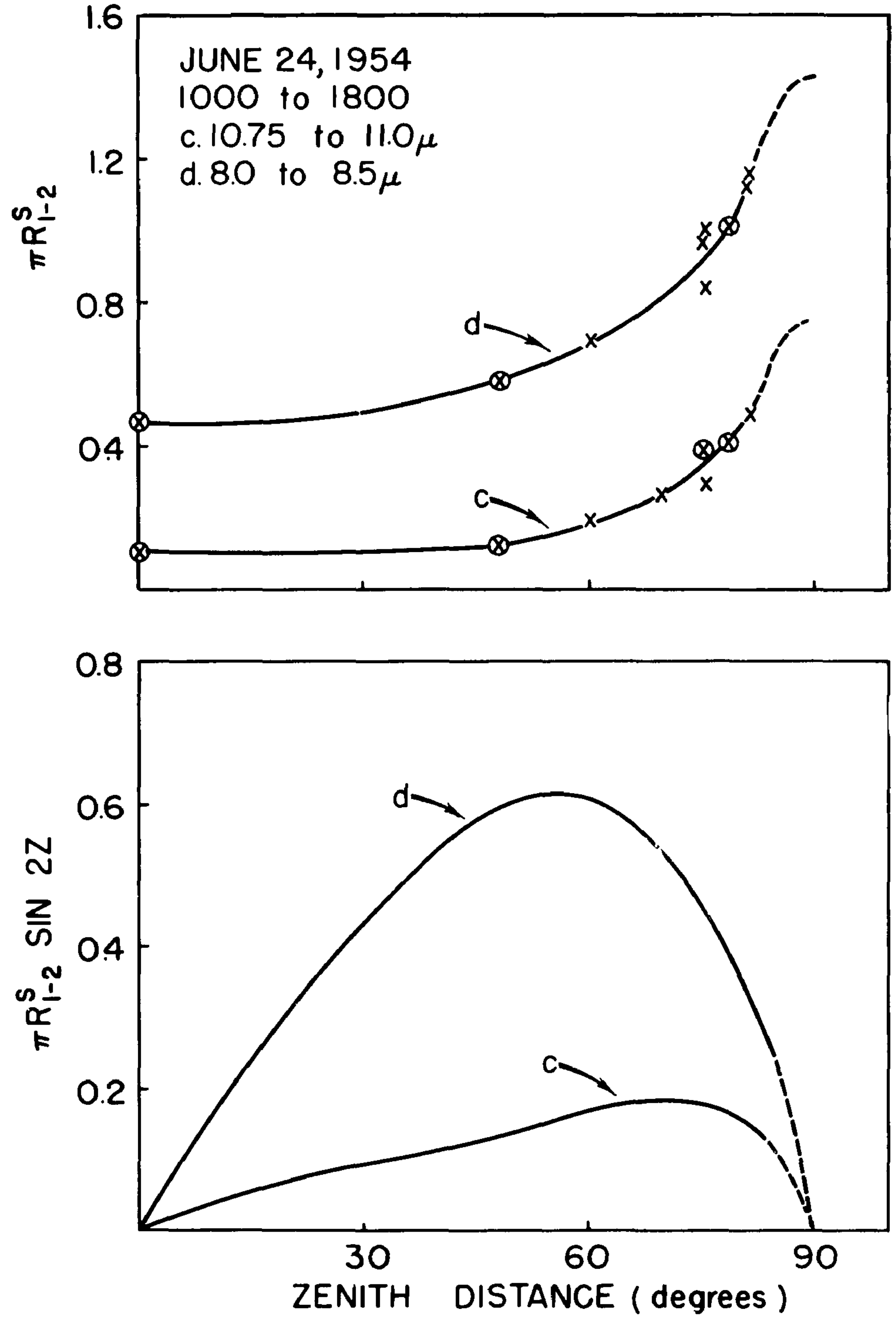
JUNE 24, 1954
1000 to 1800
c. 10.75 to 11.0μ
d. 8.0 to 8.5μ
1.6
1.2
0.8
0.4
πR^S_{1-2}
d
c
0.8
0.6
0.4
0.2
πR^S_{1-2} SIN 2Z
d
c
30
60
90
ZENITH DISTANCE (degrees)

Figure 95.

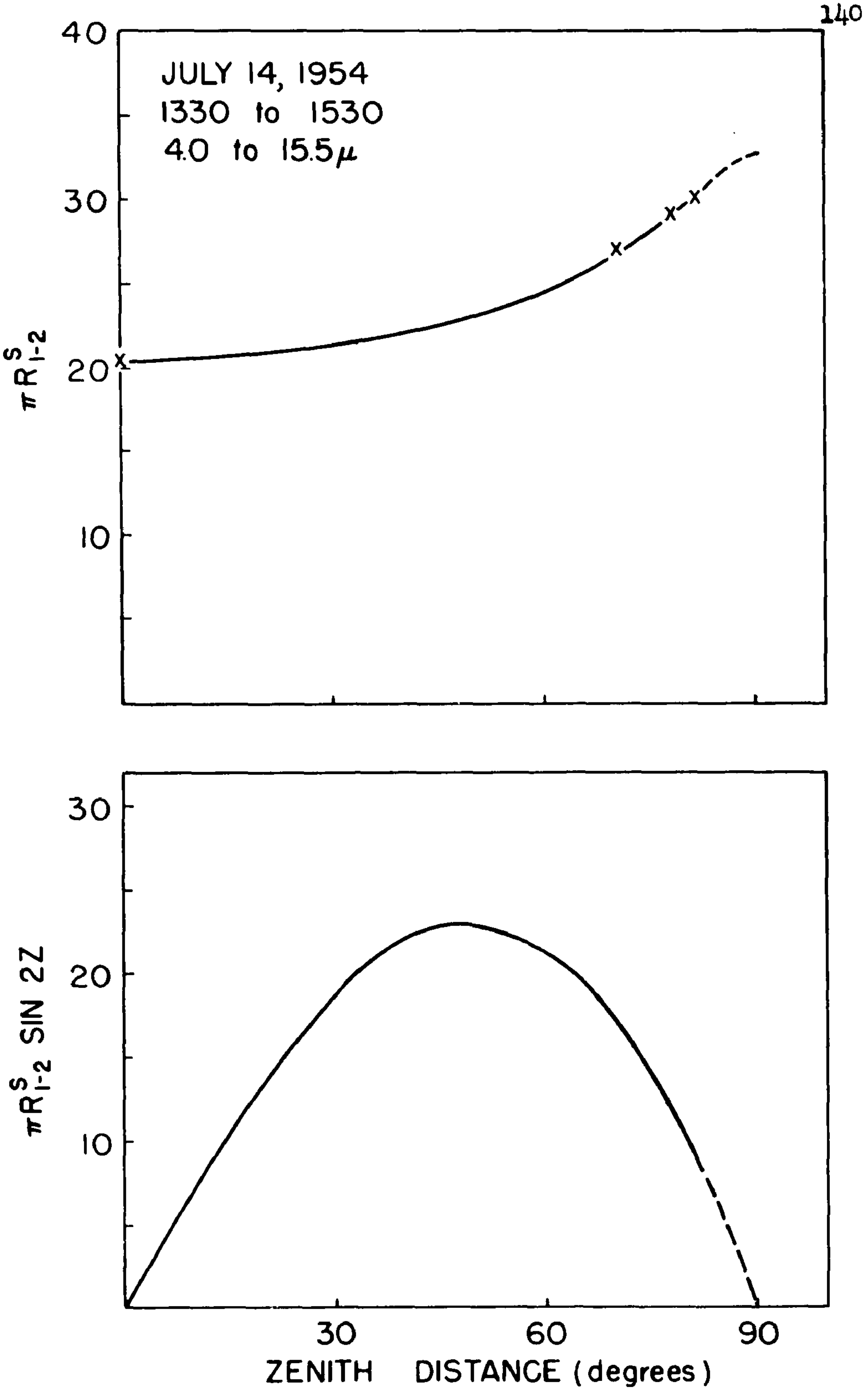
JULY 14, 1954
1330 to 1530
4.0 to 15.5μ
40
30
20
10
πR^S_{1-2}
30
20
10
πR^S_{1-2} SIN 2Z
30
60
90
ZENITH DISTANCE (degrees)

Figure 96.

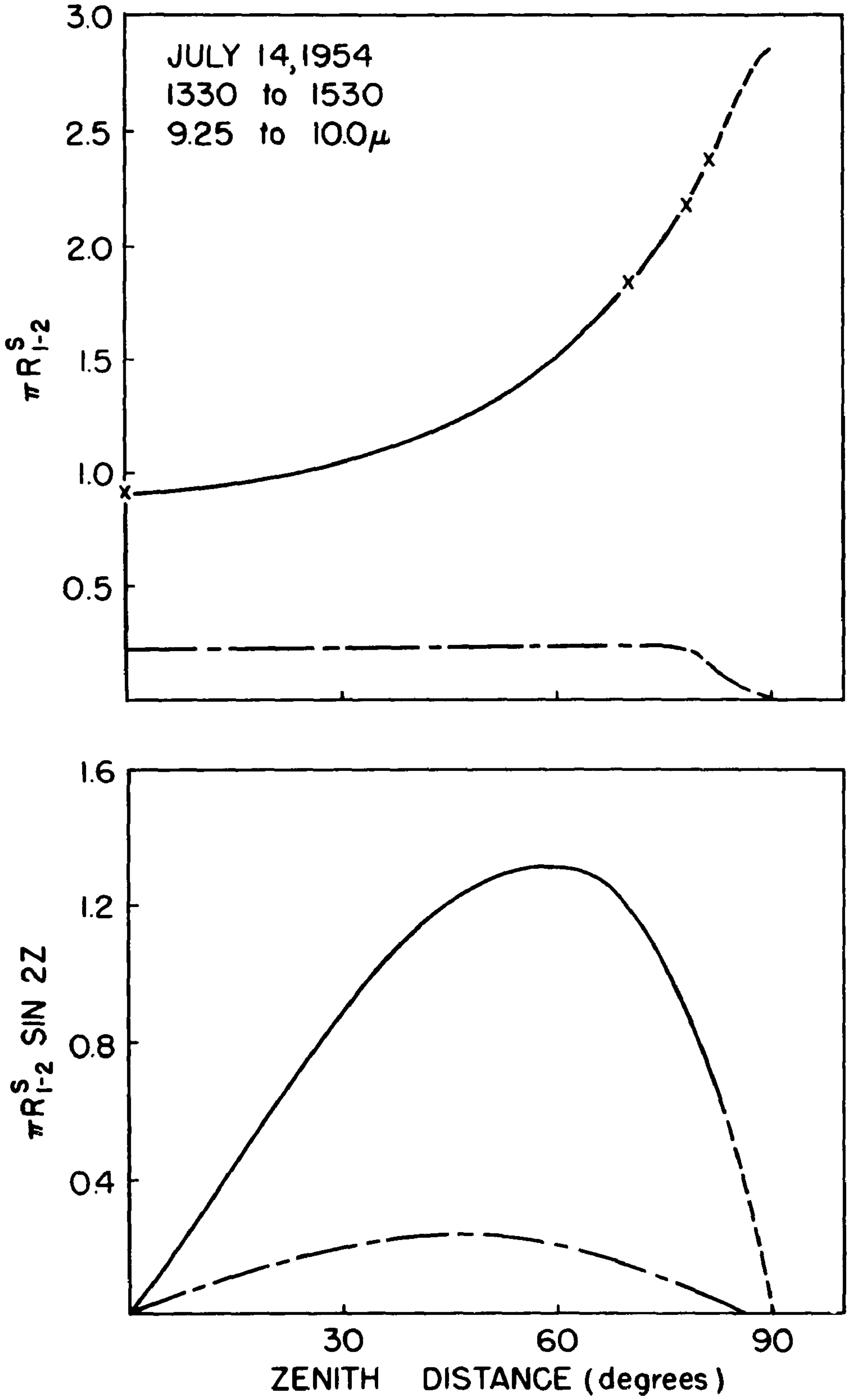

JULY 14, 1954
1330 to 1530
9.25 to 10.0μ
3.0
2.5
2.0
1.5
1.0
0.5
πR^S_{1-2}
1.6
1.2
0.8
0.4
πR^S_{1-2} SIN 2Z
30
60
90
ZENITH DISTANCE (degrees)

Figure 97.

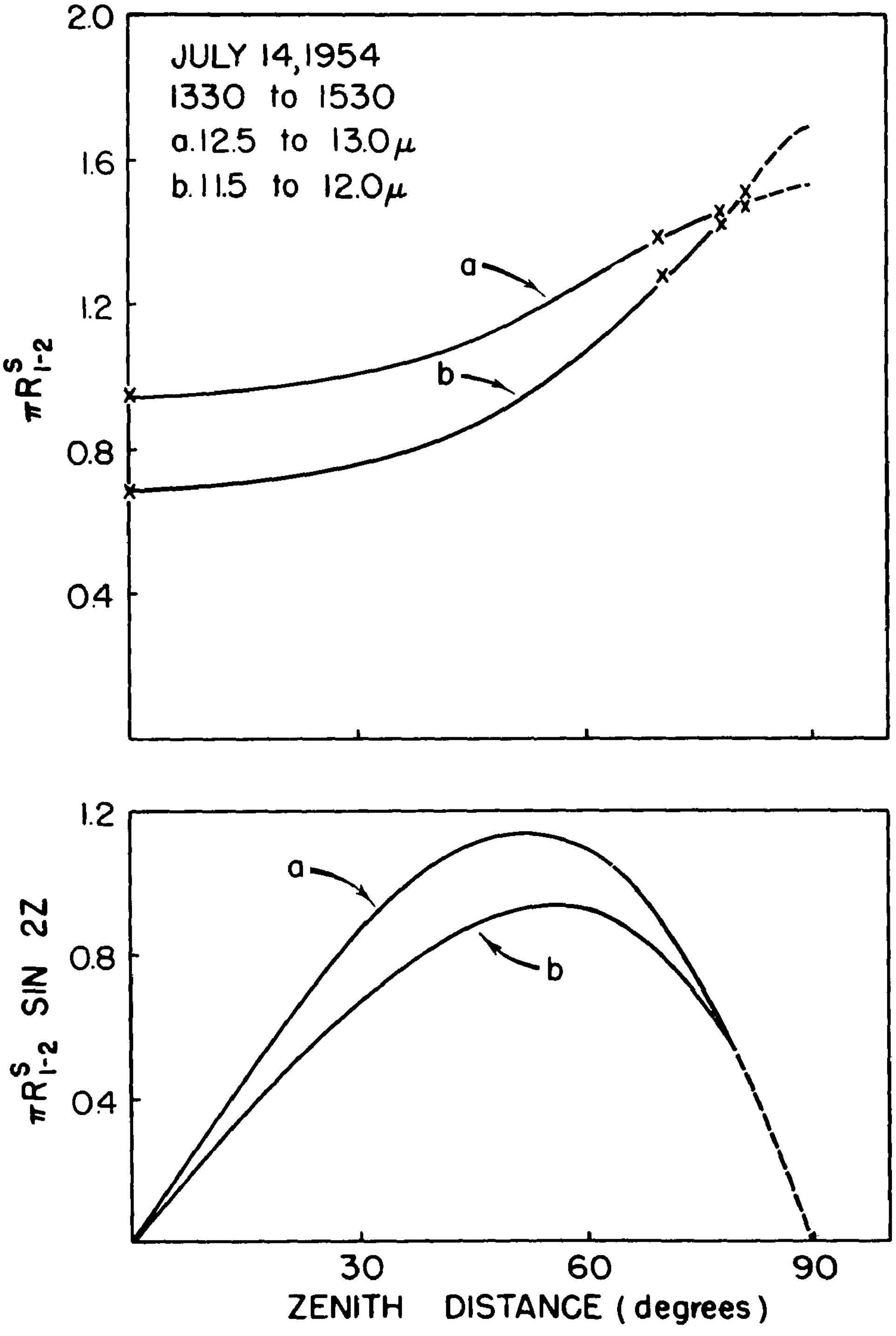
JULY 14, 1954
1330 to 1530
a. 12.5 to 13.0μ
b. 11.5 to 12.0μ
a
b
2.0
1.6
1.2
0.8
0.4
πR^{S}_{1-2}
1.2
0.8
0.4
πR^{S}_{1-2} SIN 2Z
30
60
90
ZENITH DISTANCE (degrees)

Figure 98.

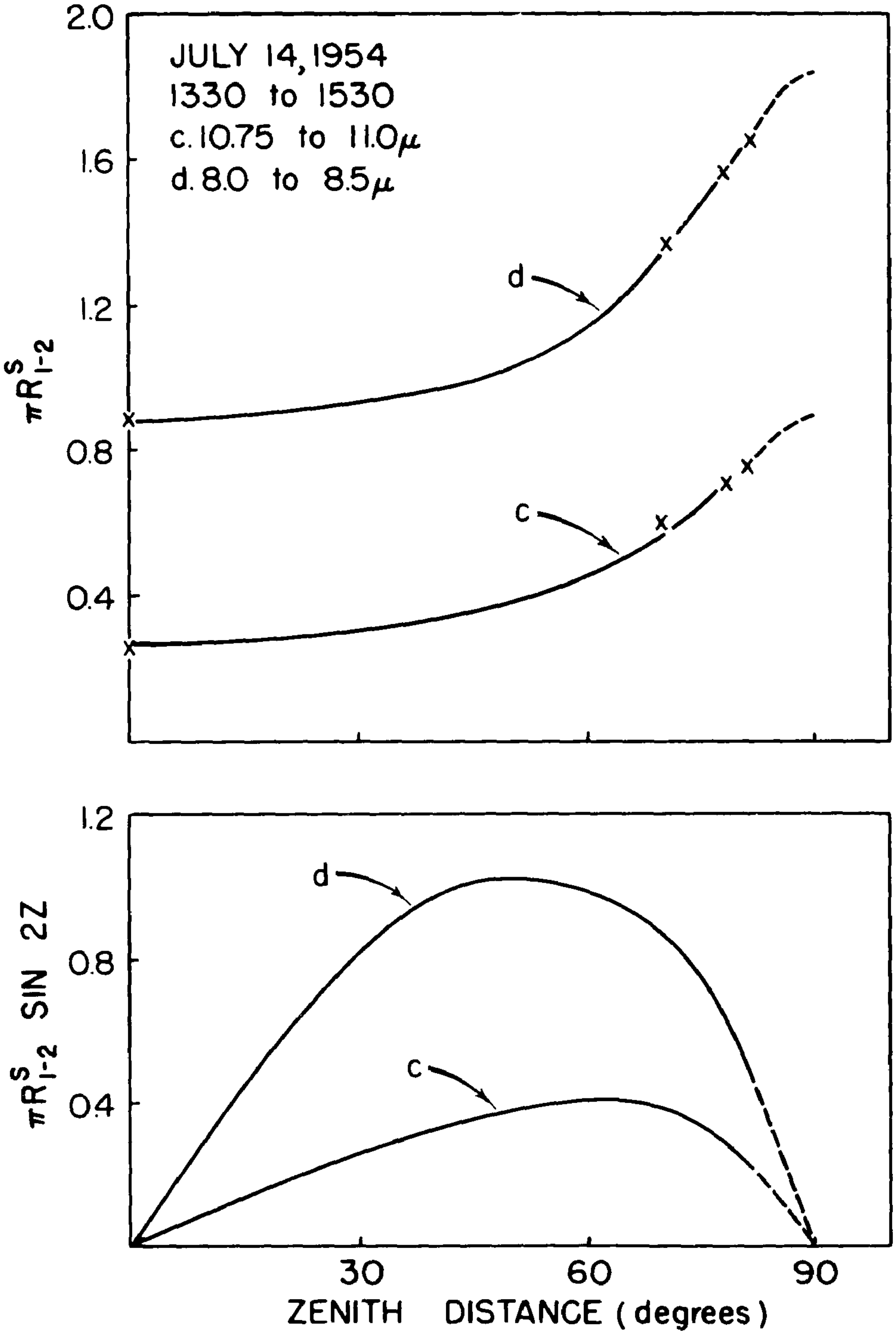
JULY 14, 1954
1330 to 1530
c. 10.75 to 11.0μ
d. 8.0 to 8.5μ
2.0
1.6
1.2
0.8
0.4
πR^{S}_{1-2}
d
c
1.2
0.8
0.4
πR^{S}_{1-2} SIN 2Z
30
60
90
ZENITH DISTANCE (degrees)

Figure 99.

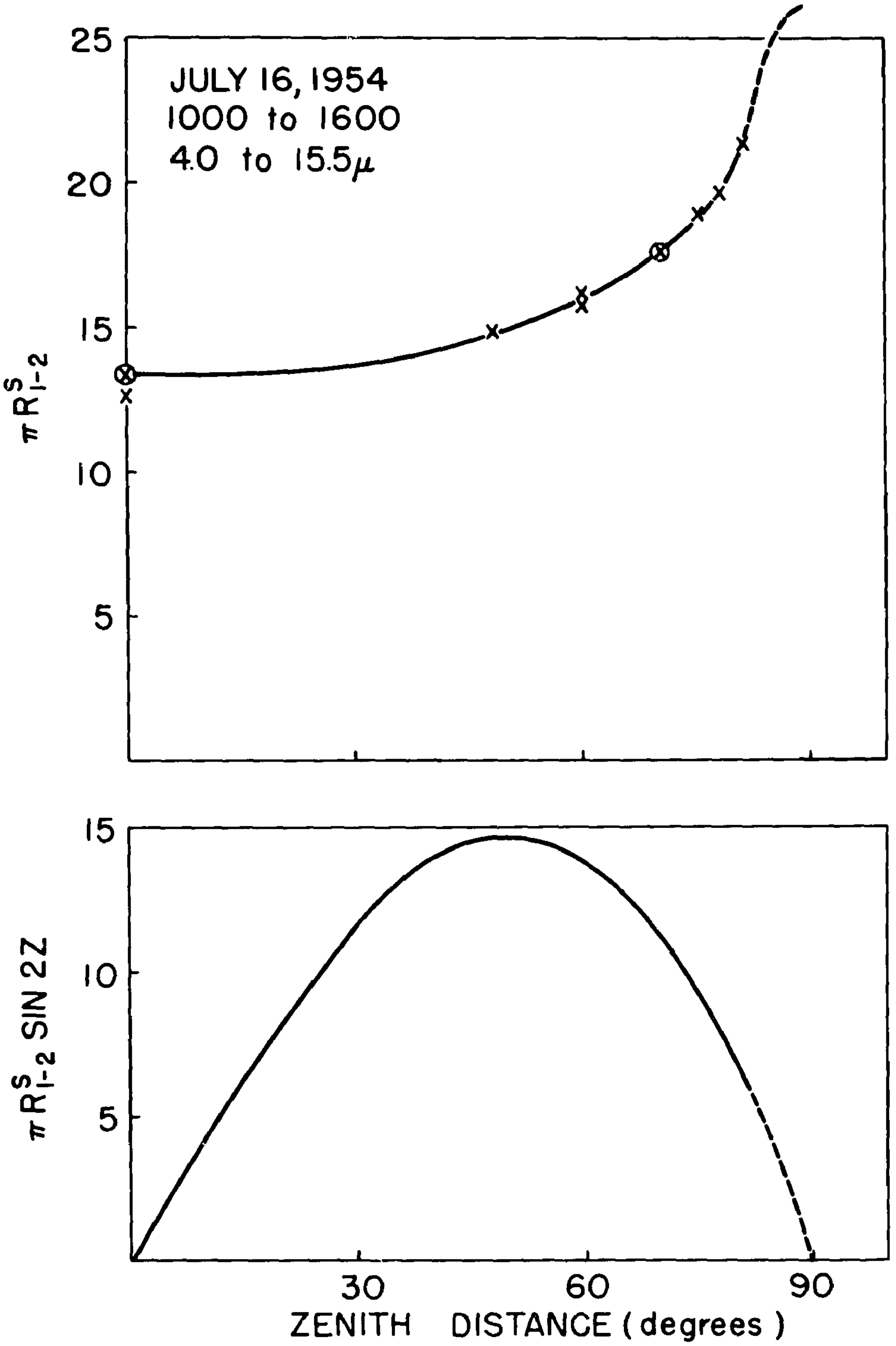
25
20
15
10
5
JULY 16, 1954
1000 to 1600
4.0 to 15.5μ
πR^S_{1-2}
15
10
5
πR^S_{1-2} SIN 2Z
30
60
90
ZENITH DISTANCE (degrees)

Figure 100.

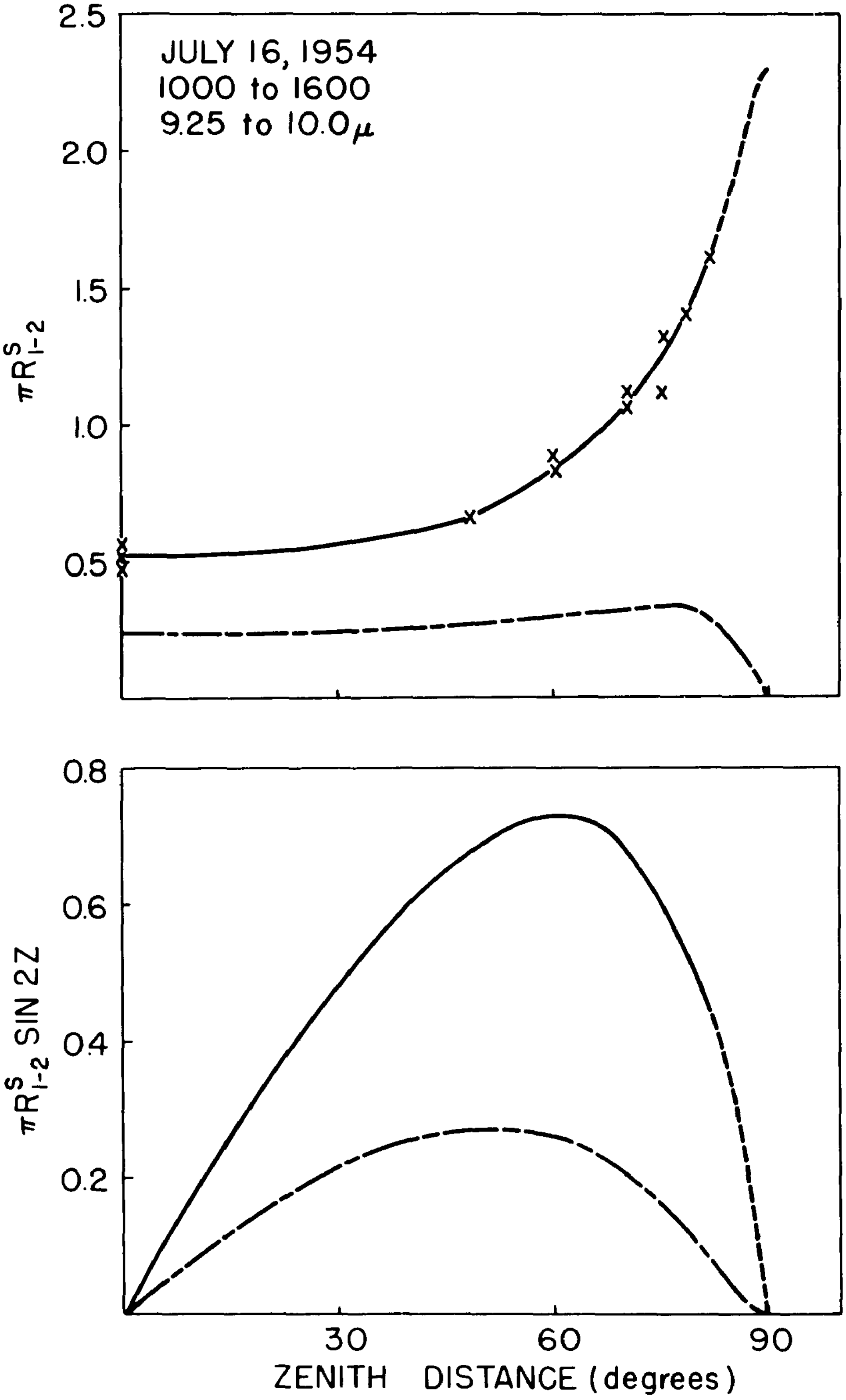
2.5
2.0
1.5
1.0
0.5
πR^S_{1-2}
JULY 16, 1954
1000 to 1600
9.25 to 10.0μ
0.8
0.6
0.4
0.2
πR^S_{1-2} SIN 2Z
30
60
90
ZENITH DISTANCE (degrees)

Figure 101.

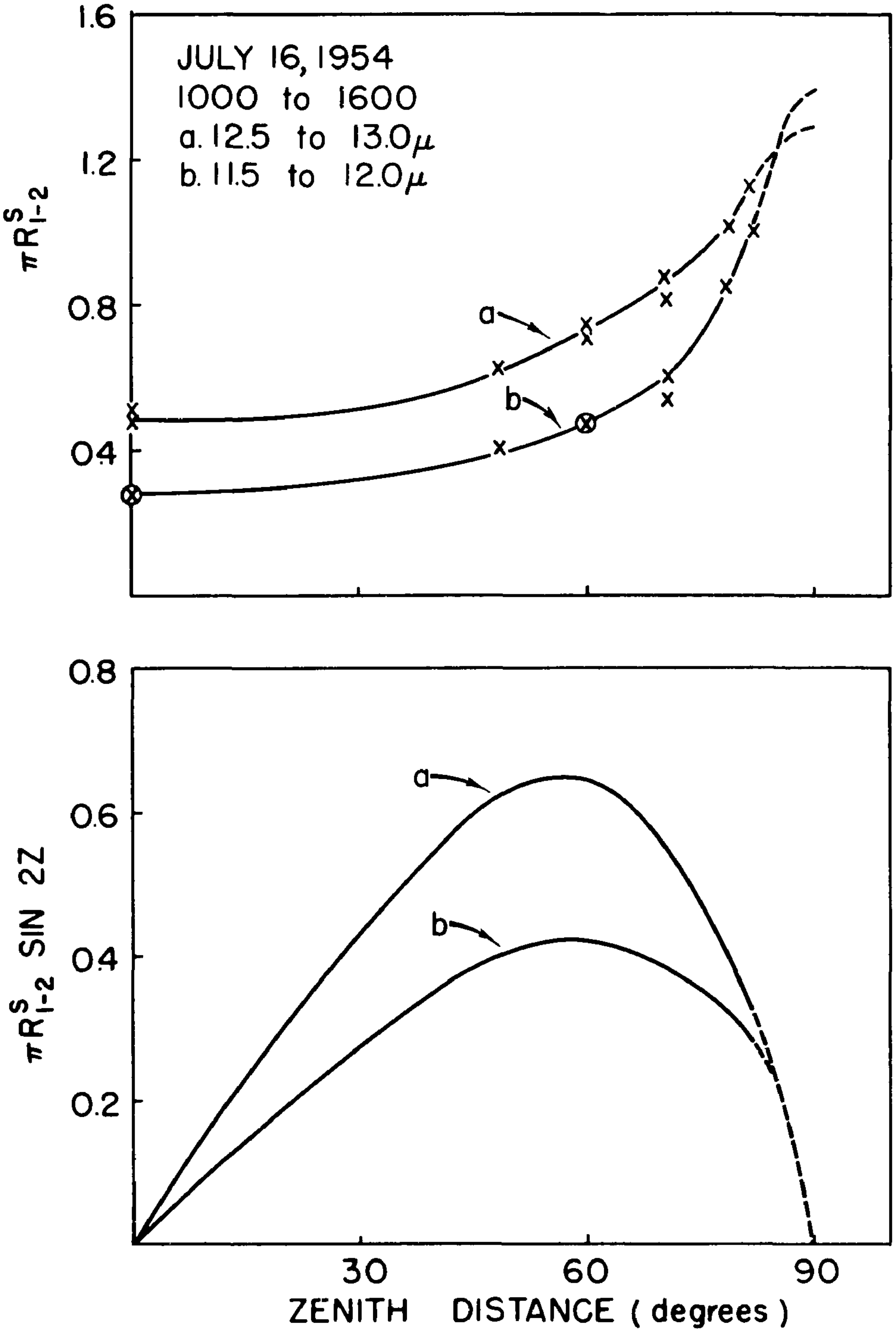
1.6
1.2
0.8
0.4
JULY 16, 1954
1000 to 1600
a. 12.5 to 13.0μ
b. 11.5 to 12.0μ
πR^S_{1-2}
a
b
0.8
0.6
0.4
0.2
πR^S_{1-2} SIN 2Z
a
b
30
60
90
ZENITH DISTANCE (degrees)

Figure 102.

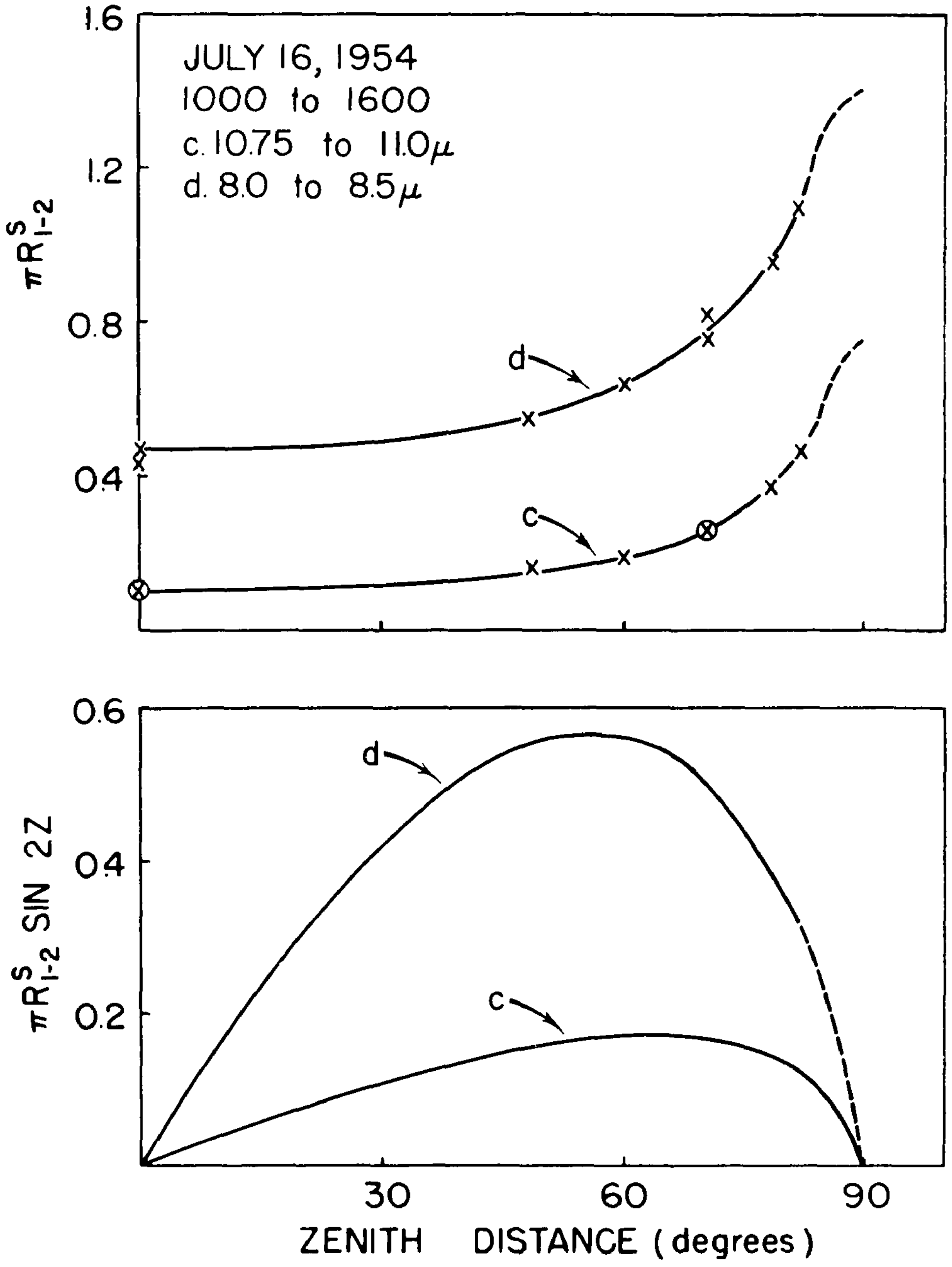
JULY 16, 1954
1000 to 1600
c. 10.75 to 11.0μ
d. 8.0 to 8.5μ
πR^S_{1-2}
1.6
1.2
0.8
0.4
d
c
πR^S_{1-2} SIN 2Z
0.6
0.4
0.2
30
60
90
ZENITH DISTANCE (degrees)

Figure 103.

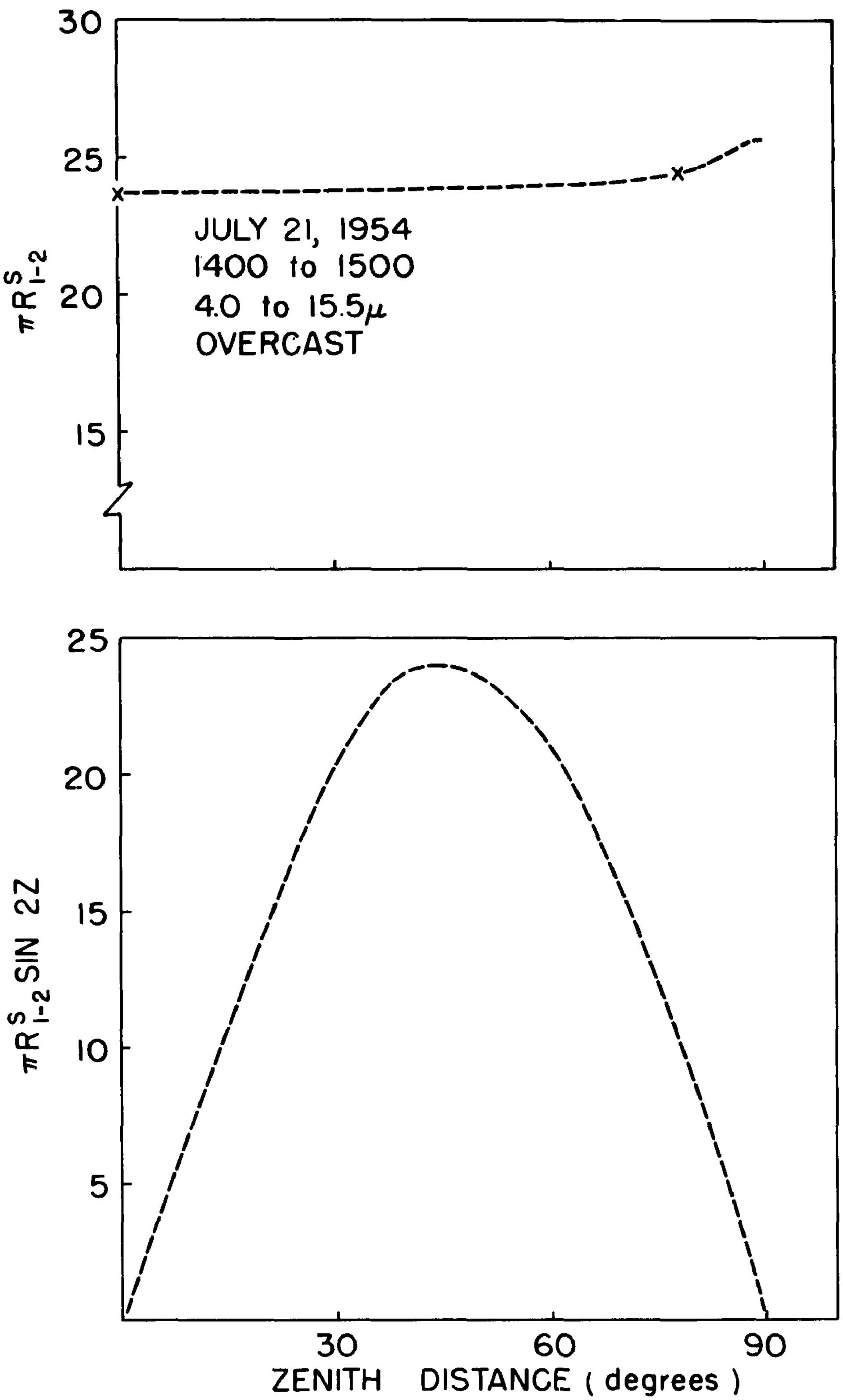
30
25
20
15
πR^S_{1-2}
JULY 21, 1954
1400 to 1500
4.0 to 15.5μ
OVERCAST
25
20
15
10
5
πR^S_{1-2} SIN 2Z
30
60
90
ZENITH DISTANCE (degrees)

Figure 104.

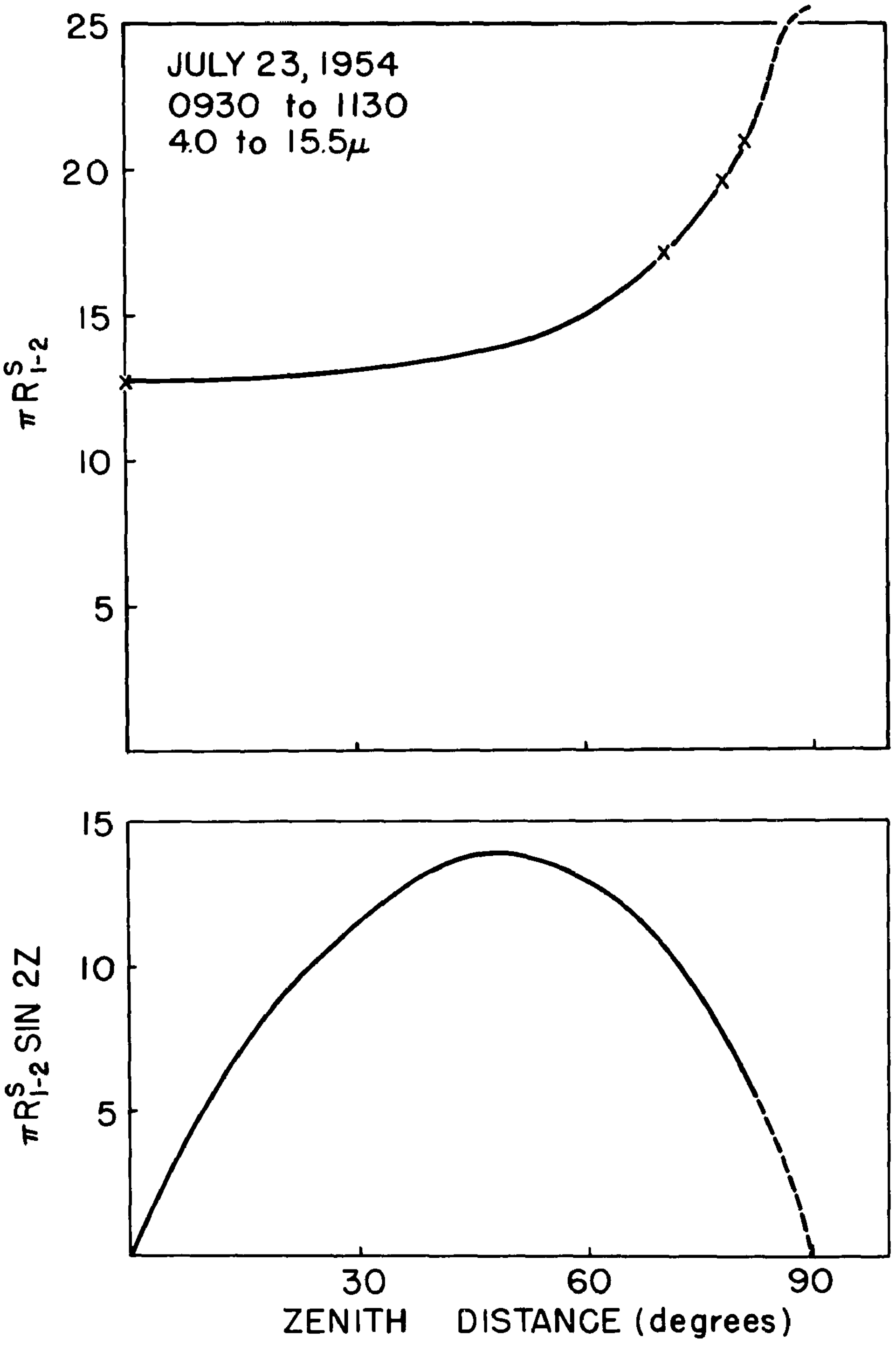
JULY 23, 1954
0930 to 1130
4.0 to 15.5μ
25
20
15
10
5
πR^S_{1-2}
15
10
5
πR^S_{1-2} SIN 2Z
30
60
90
ZENITH DISTANCE (degrees)

Figure 105.

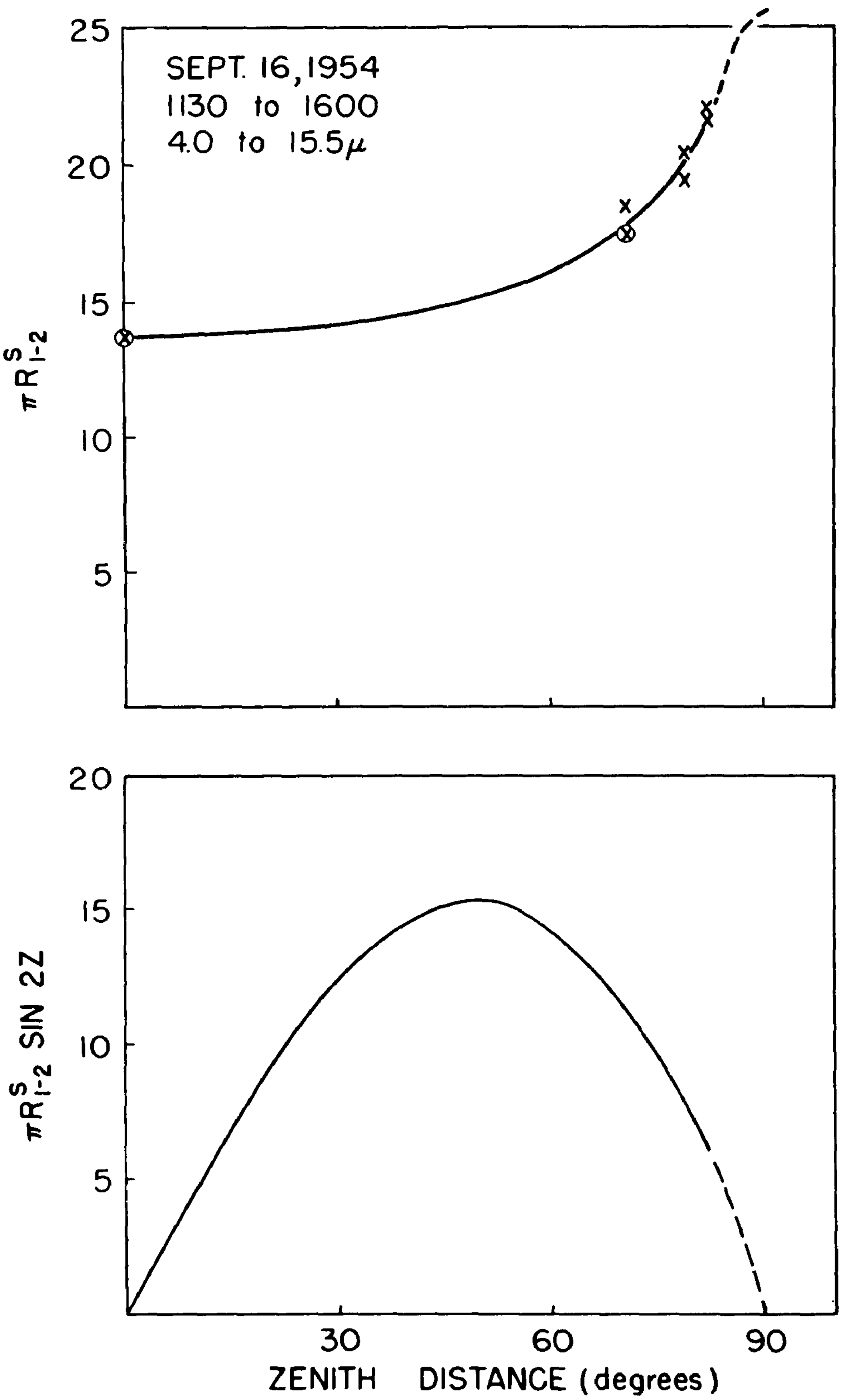
SEPT. 16, 1954
1130 to 1600
4.0 to 15.5μ
25
20
15
10
5
πR^S_{1-2}
20
15
10
5
πR^S_{1-2} SIN 2Z
30
60
90
ZENITH DISTANCE (degrees)

Figure 106.

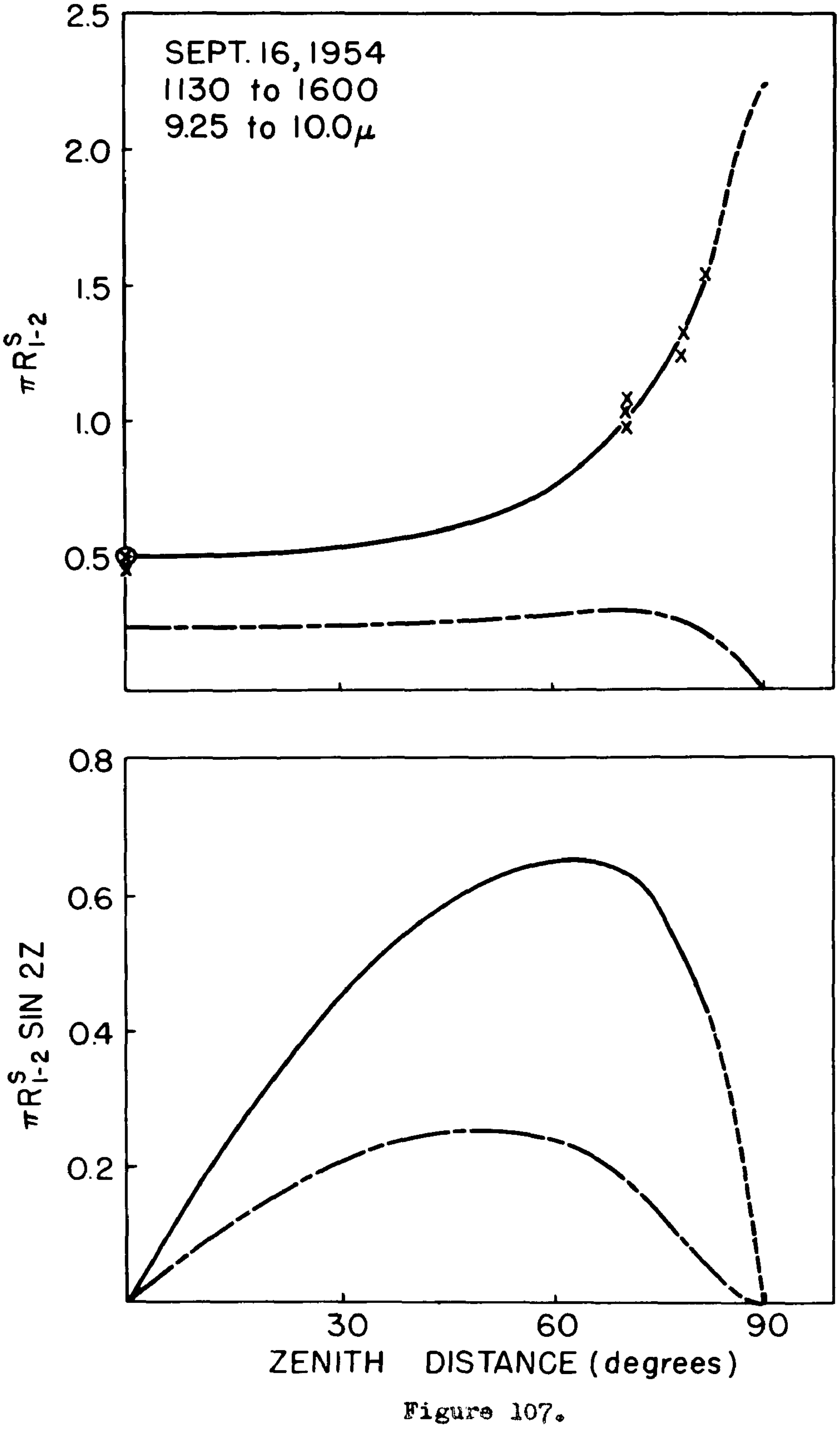
2.5
2.0
1.5
1.0
0.5
SEPT. 16, 1954
1130 to 1600
9.25 to 10.0μ
πR^{S}_{1-2}
0.8
0.6
0.4
0.2
πR^{S}_{1-2} SIN 2Z
30
60
90
ZENITH DISTANCE (degrees)

Figure 107.

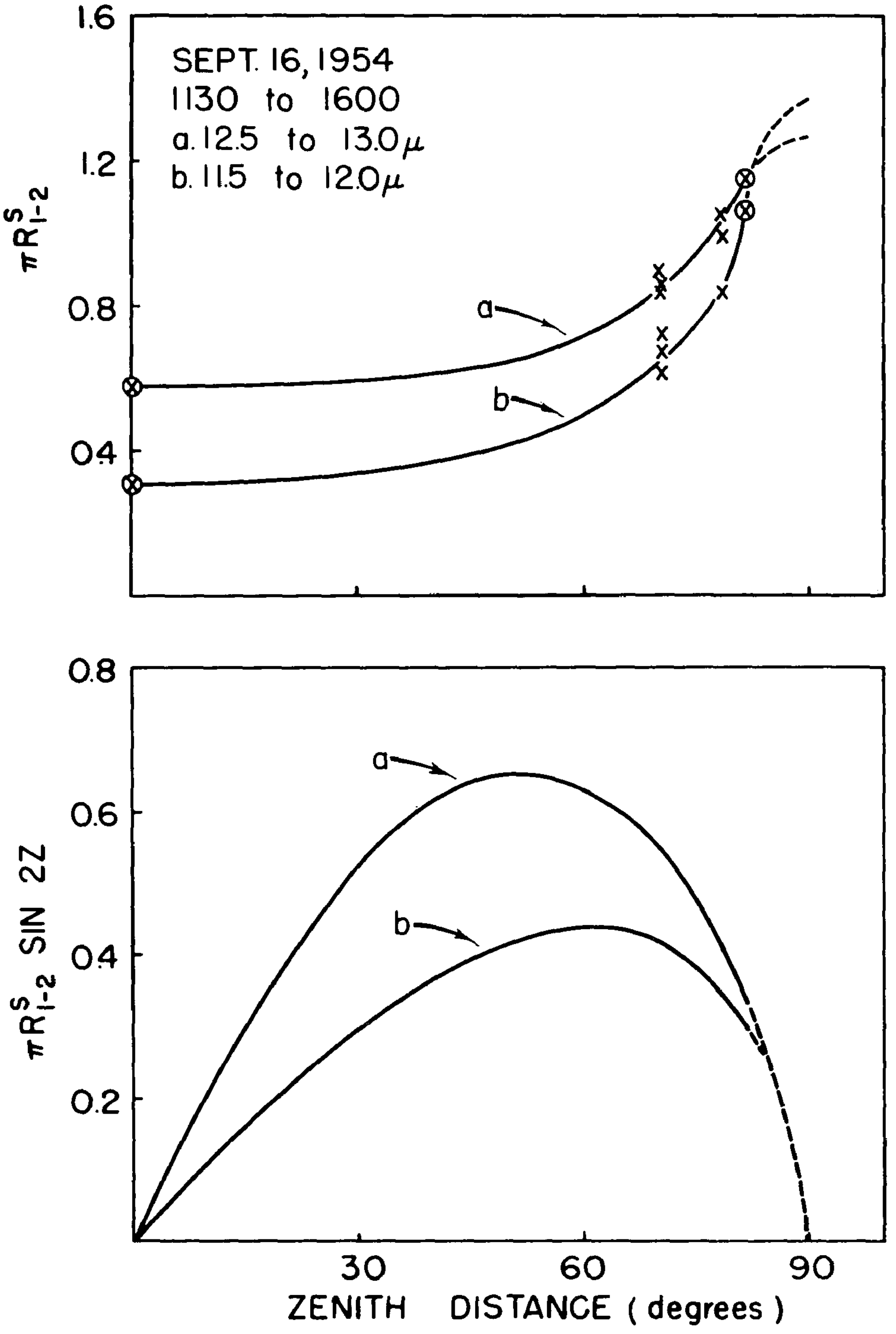
1.6
1.2
0.8
0.4
πR^S_{1-2}
SEPT. 16, 1954
1130 to 1600
a. 12.5 to 13.0μ
b. 11.5 to 12.0μ
a
b
0.8
0.6
0.4
0.2
πR^S_{1-2} SIN 2Z
a
b
30
60
90
ZENITH DISTANCE (degrees)

Figure 108.

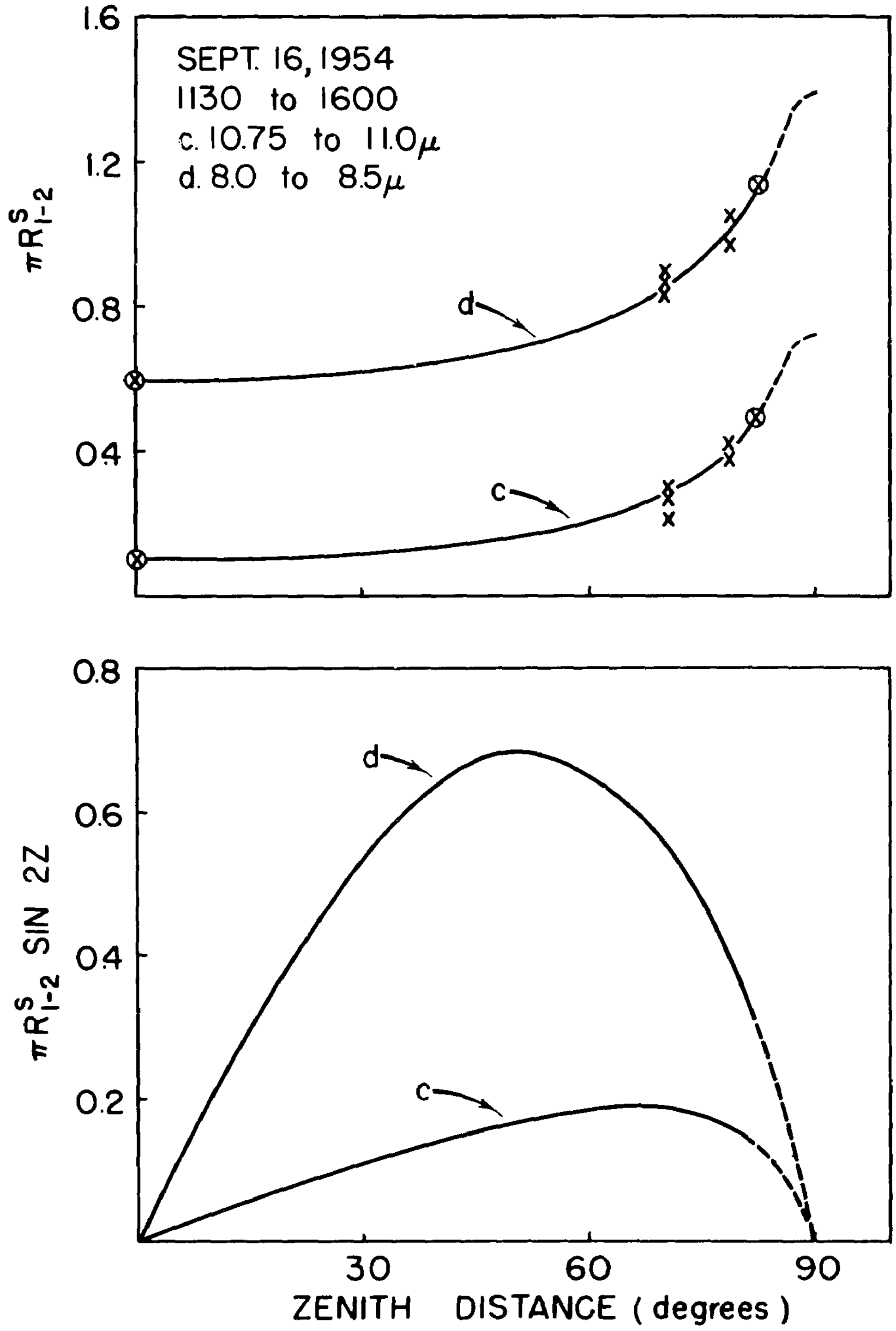
1.6
1.2
0.8
0.4
πR^{S}_{1-2}
SEPT. 16, 1954
1130 to 1600
c. 10.75 to 11.0μ
d. 8.0 to 8.5μ
d
c
0.8
0.6
0.4
0.2
πR^{S}_{1-2} SIN 2Z
d
c
30
60
90
ZENITH DISTANCE (degrees)

Figure 109.

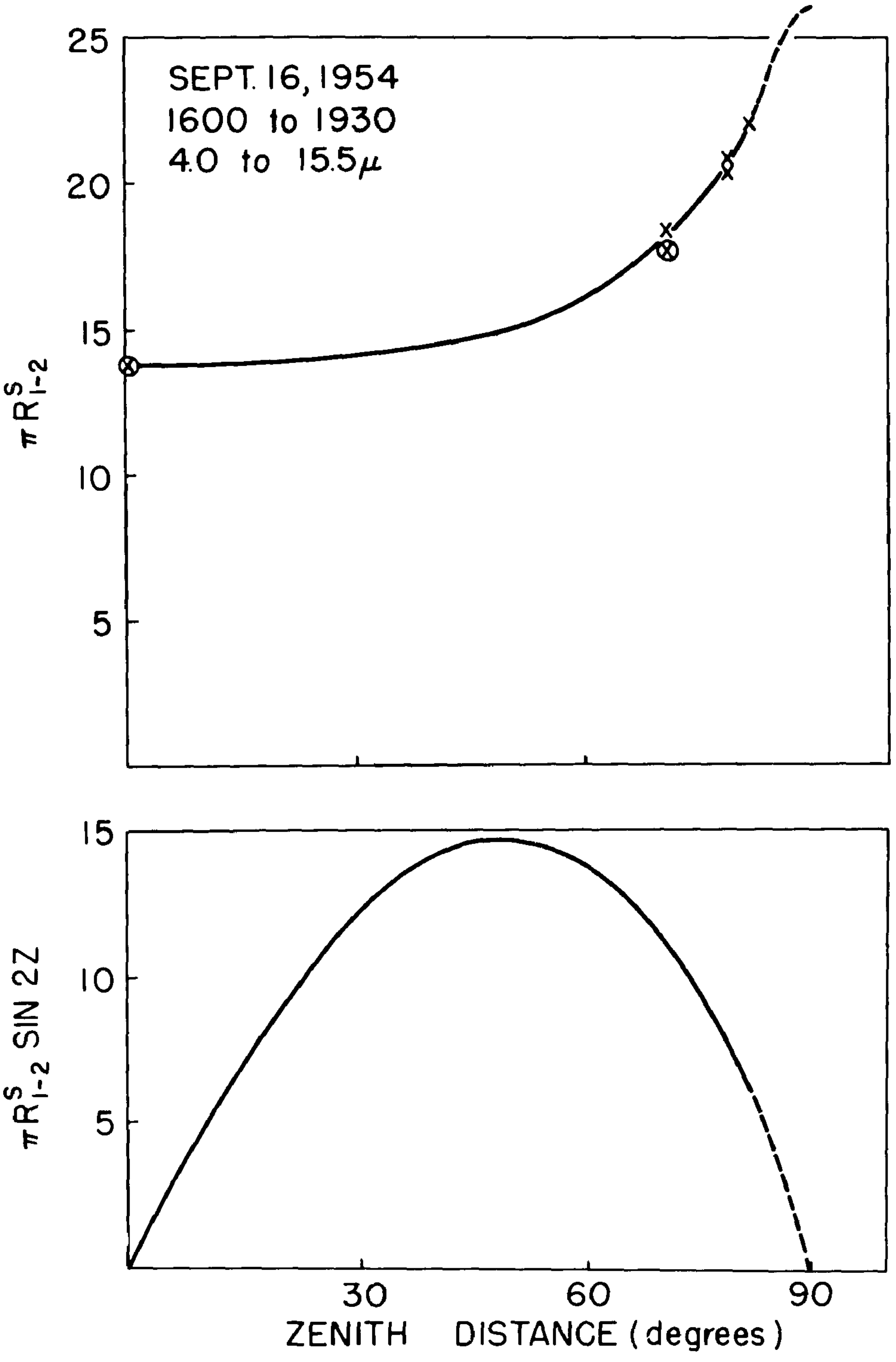
25
20
15
10
5
SEPT. 16, 1954
1600 to 1930
4.0 to 15.5μ
πR^S_1-2
15
10
5
πR^S_1-2 SIN 2Z
30
60
90
ZENITH DISTANCE (degrees)

Figure 110.

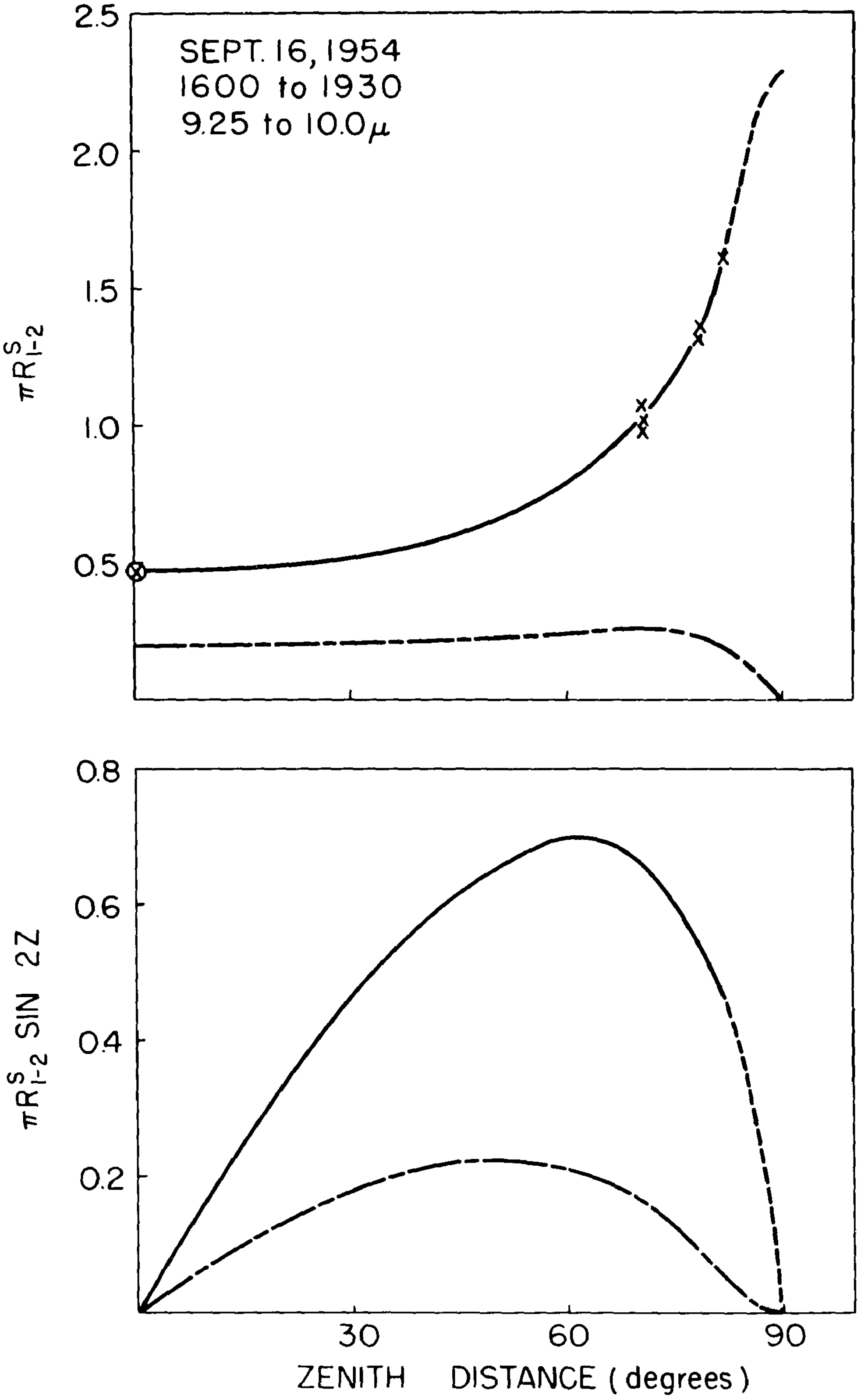
2.5
2.0
1.5
1.0
0.5
πR^{S}_{1-2}
SEPT. 16, 1954
1600 to 1930
9.25 to 10.0μ
0.8
0.6
0.4
0.2
πR^{S}_{1-2} SIN 2Z
30
60
90
ZENITH DISTANCE (degrees)

Figure 111.

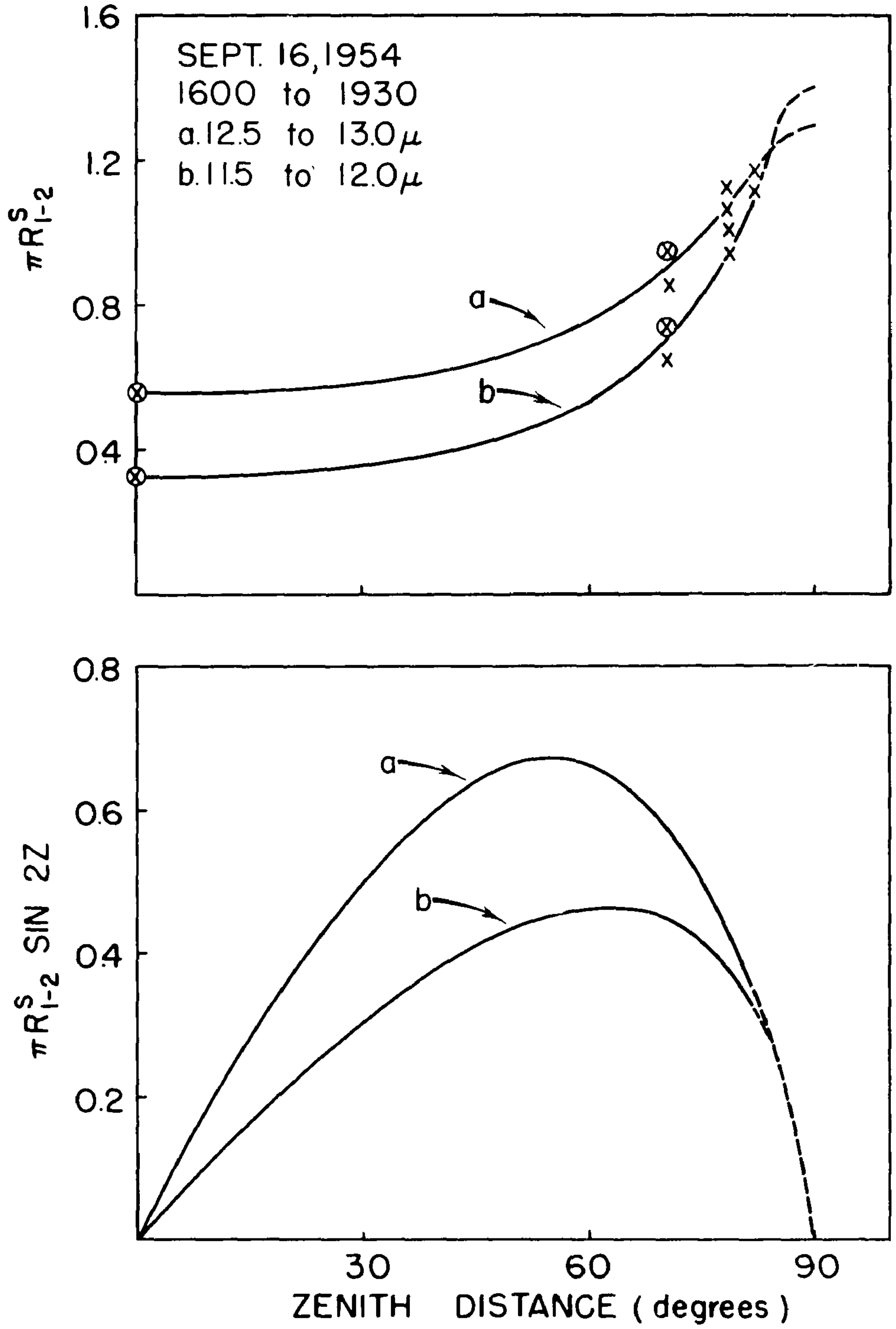
SEPT. 16, 1954
1600 to 1930
a. 12.5 to 13.0μ
b. 11.5 to 12.0μ
1.6
1.2
0.8
0.4
πR^S_1-2
a
b
0.8
0.6
0.4
0.2
πR^S_1-2 SIN 2Z
a
b
30
60
90
ZENITH DISTANCE (degrees)

Figure 112.

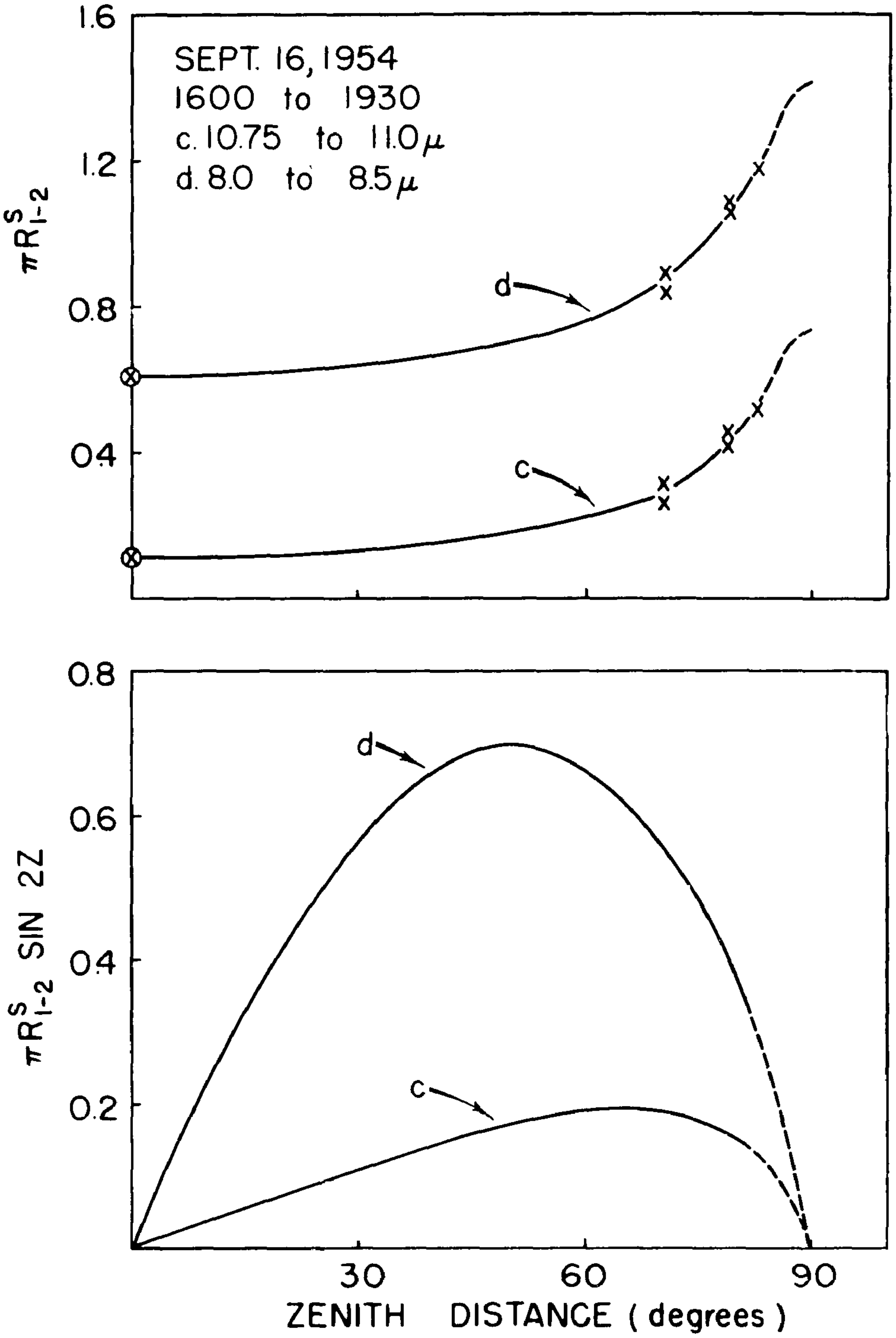
1.6
1.2
0.8
0.4
πR^S_{1-2}
SEPT. 16, 1954
1600 to 1930
c. 10.75 to 11.0μ
d. 8.0 to 8.5μ
d
c
0.8
0.6
0.4
0.2
πR^S_{1-2} SIN 2Z
d
c
30
60
90
ZENITH DISTANCE (degrees)

Figure 113.

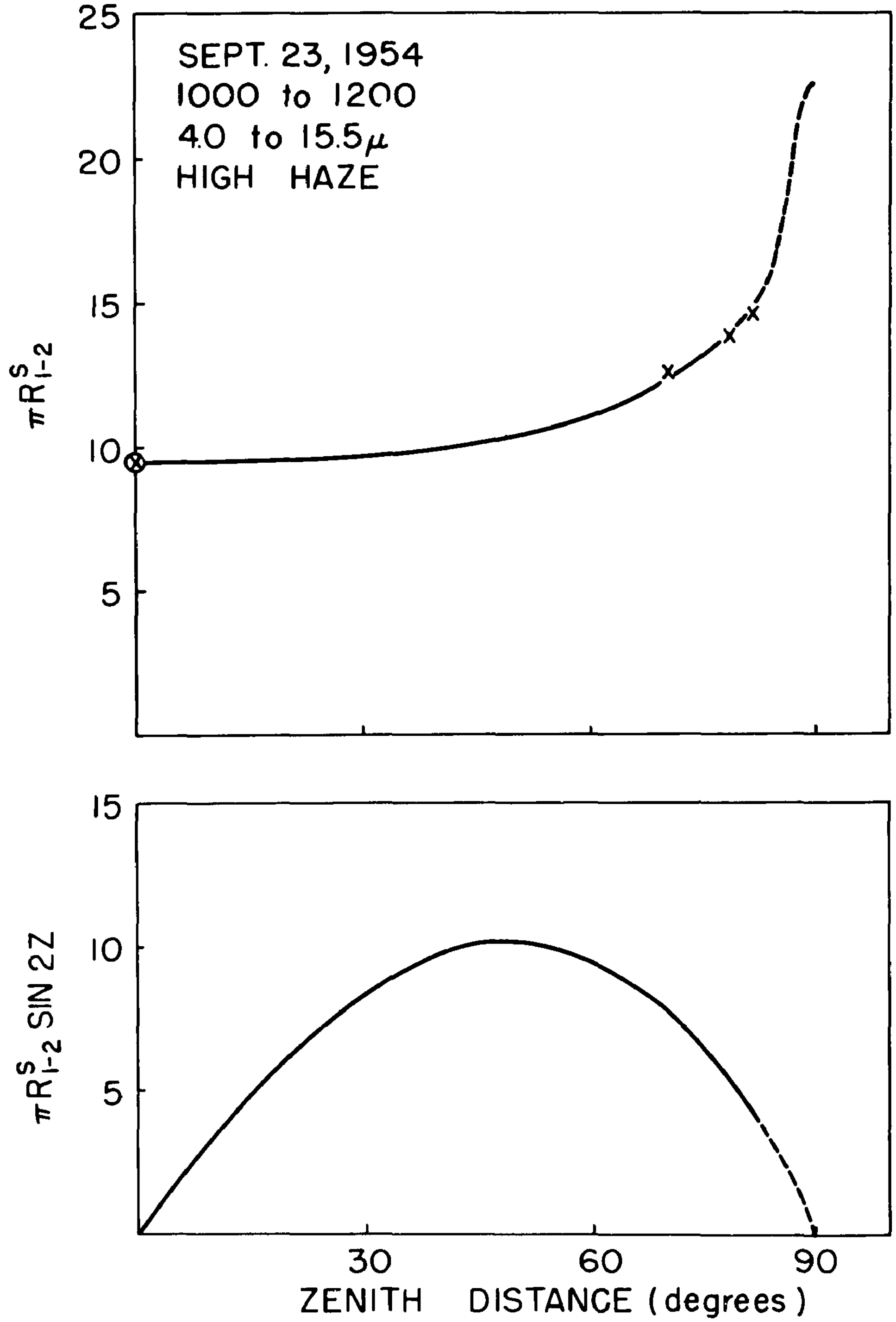
25
20
15
10
5
πR^S_{1-2}
SEPT. 23, 1954
1000 to 1200
4.0 to 15.5μ
HIGH HAZE
15
10
5
πR^S_{1-2} SIN 2Z
30
60
90
ZENITH DISTANCE (degrees)

Figure 114.

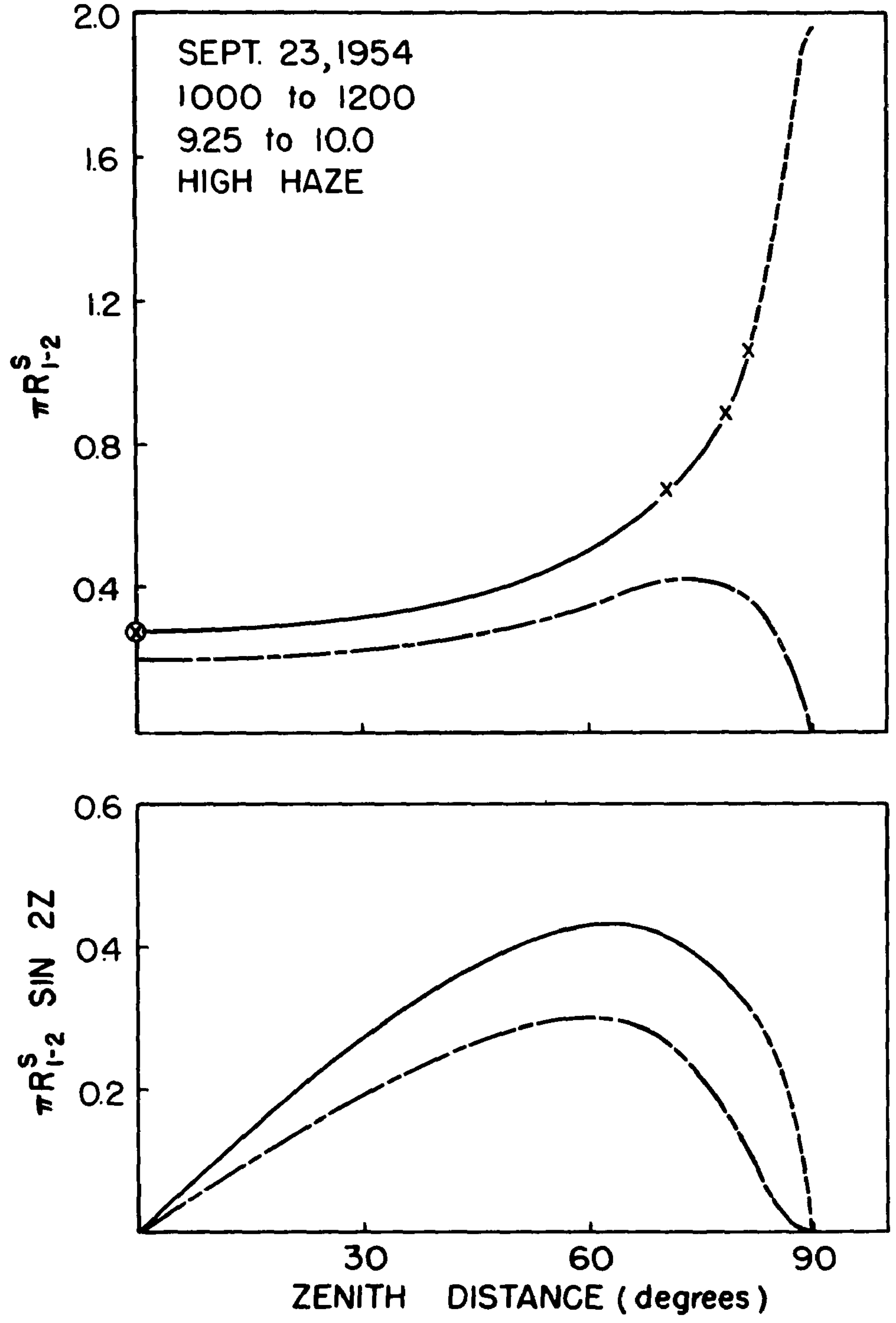
SEPT. 23, 1954
1000 to 1200
9.25 to 10.0
HIGH HAZE
2.0
1.6
1.2
0.8
0.4
πR^S_{1-2}
0.6
0.4
0.2
πR^S_{1-2} SIN 2Z
30
60
90
ZENITH DISTANCE (degrees)

Figure 115.

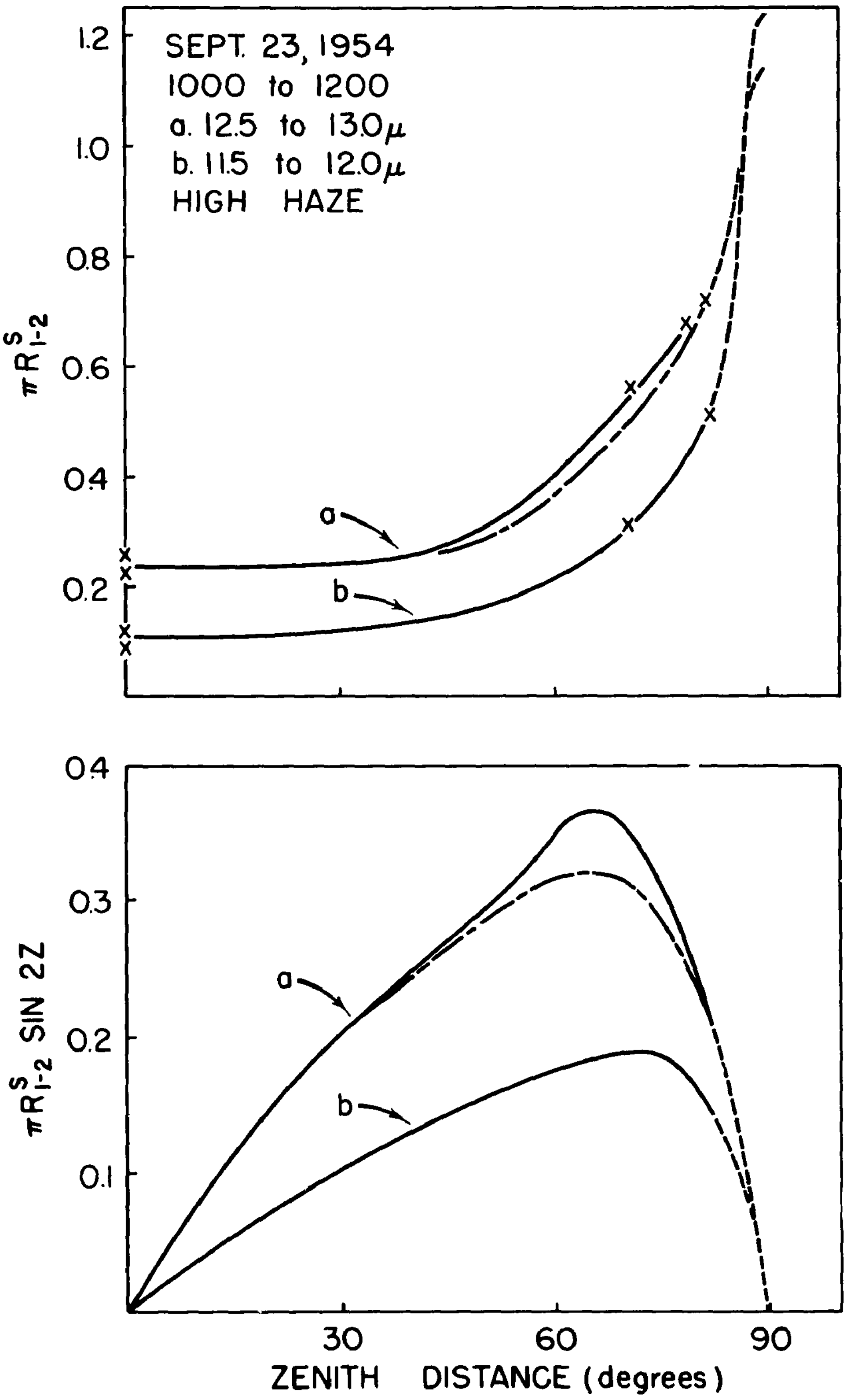
SEPT. 23, 1954
1000 to 1200
a. 12.5 to 13.0μ
b. 11.5 to 12.0μ
HIGH HAZE
1.2
1.0
0.8
0.6
0.4
0.2
πR^S_{1-2}
a
b
0.4
0.3
0.2
0.1
πR^S_{1-2} SIN 2Z
a
b
30
60
90
ZENITH DISTANCE (degrees)

Figure 116.

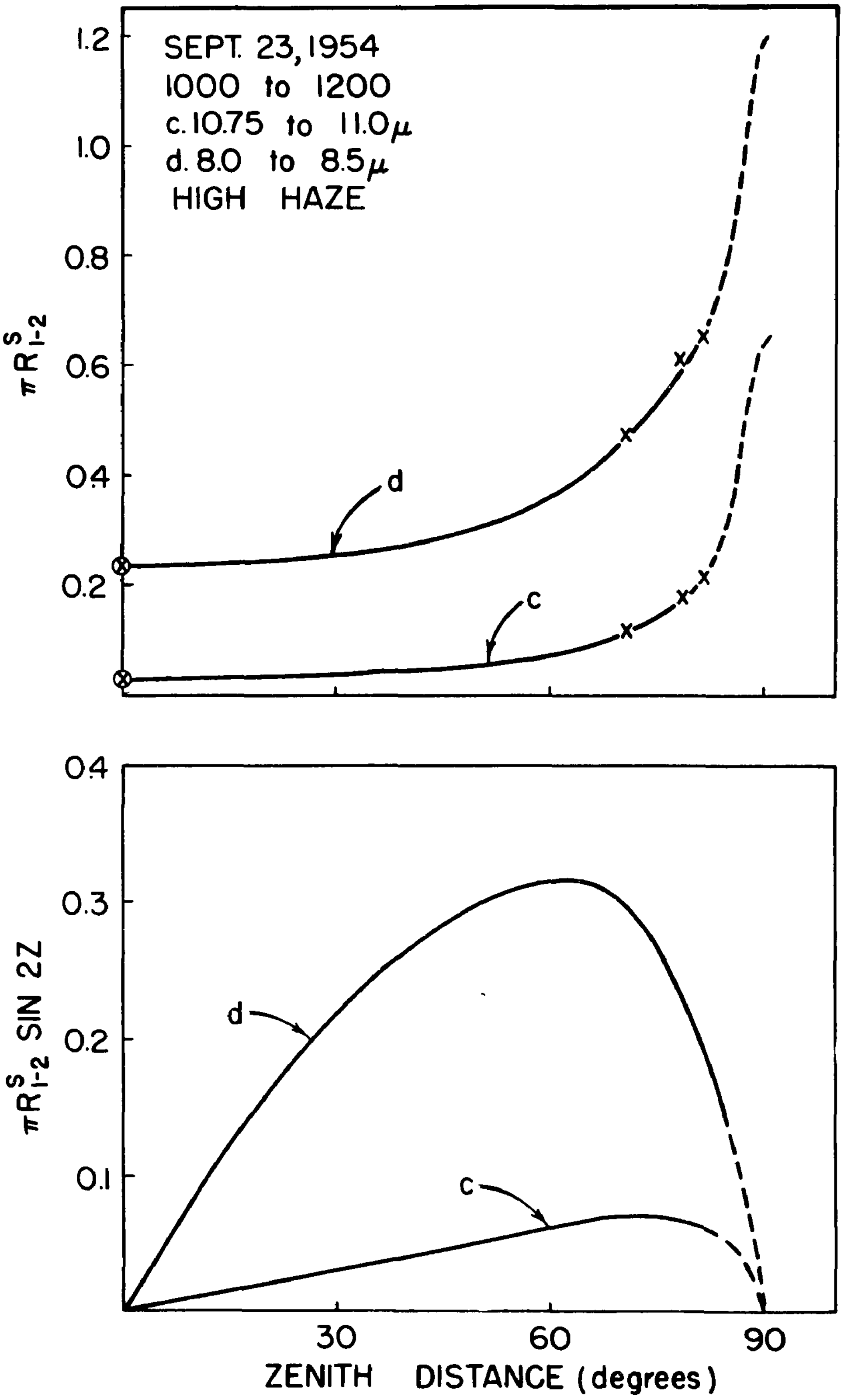
SEPT. 23, 1954
1000 to 1200
c. 10.75 to 11.0μ
d. 8.0 to 8.5μ
HIGH HAZE
πR^{S}_{1-2}
1.2
1.0
0.8
0.6
0.4
0.2
d
c
πR^{S}_{1-2} SIN 2Z
0.4
0.3
0.2
0.1
d
c
30
60
90
ZENITH DISTANCE (degrees)

Figure 117.

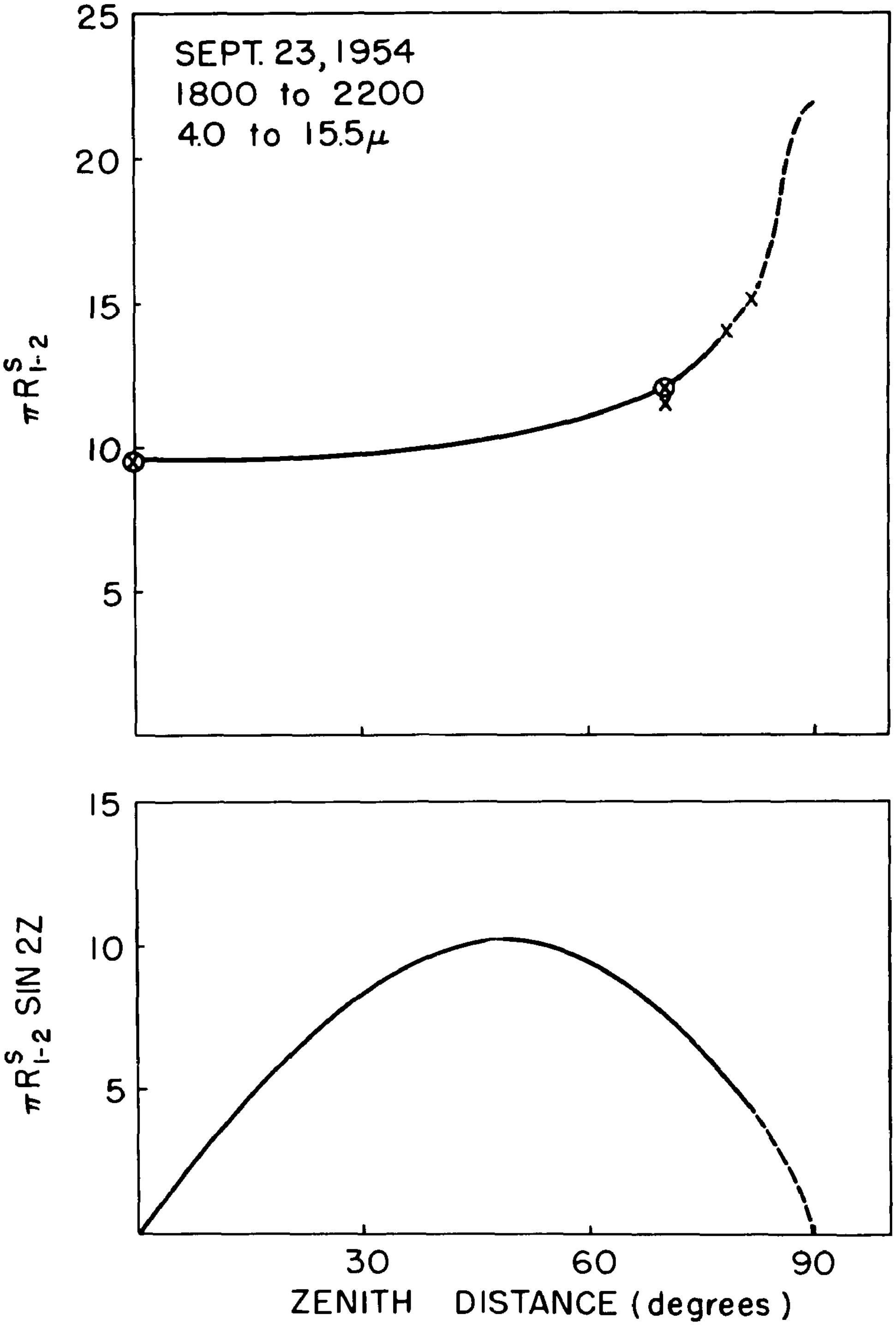
SEPT. 23, 1954
1800 to 2200
4.0 to 15.5μ
25
20
15
10
5
πR^S_1-2
15
10
5
πR^S_1-2 SIN 2Z
30
60
90
ZENITH DISTANCE (degrees)

Figure 118.

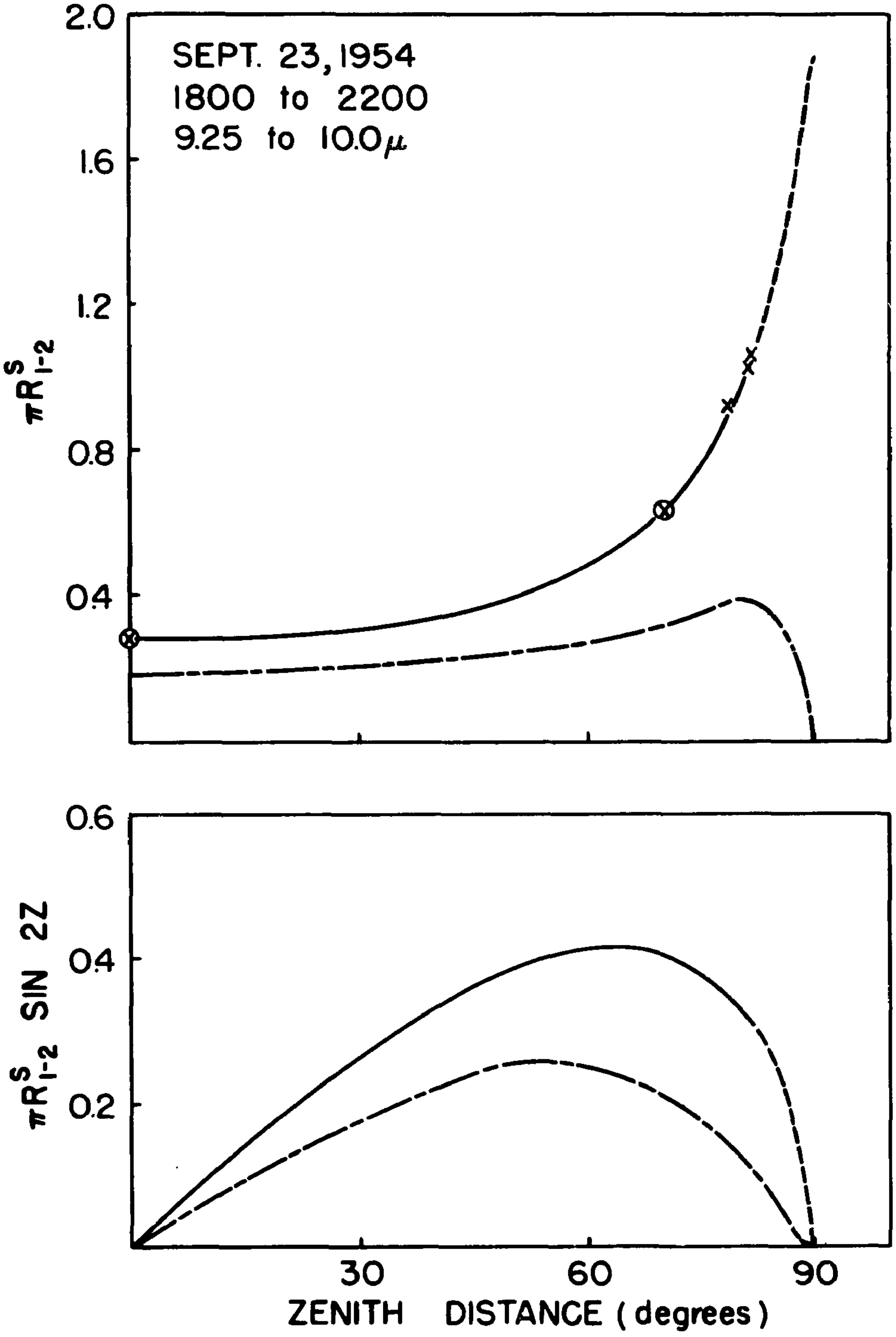
SEPT. 23, 1954
1800 to 2200
9.25 to 10.0μ
2.0
1.6
1.2
0.8
0.4
πR^S_{1-2}
0.6
0.4
0.2
πR^S_{1-2} SIN 2Z
30
60
90
ZENITH DISTANCE (degrees)

Figure 119.

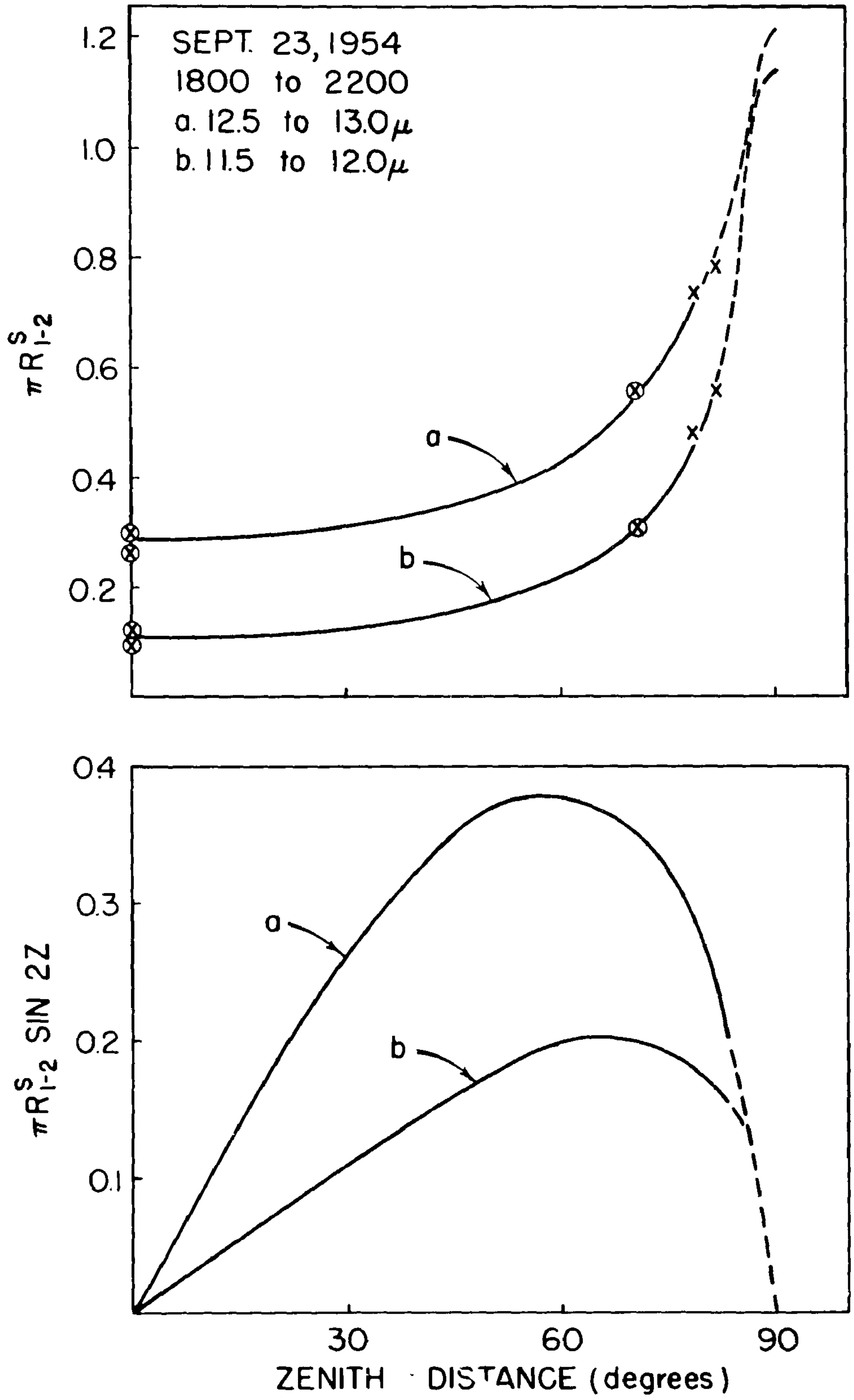
SEPT. 23, 1954
1800 to 2200
a. 12.5 to 13.0μ
b. 11.5 to 12.0μ
1.2
1.0
0.8
0.6
0.4
0.2
πR^S_{1-2}
a
b
0.4
0.3
0.2
0.1
πR^S_{1-2} SIN 2Z
30
60
90
ZENITH DISTANCE (degrees)

Figure 120.

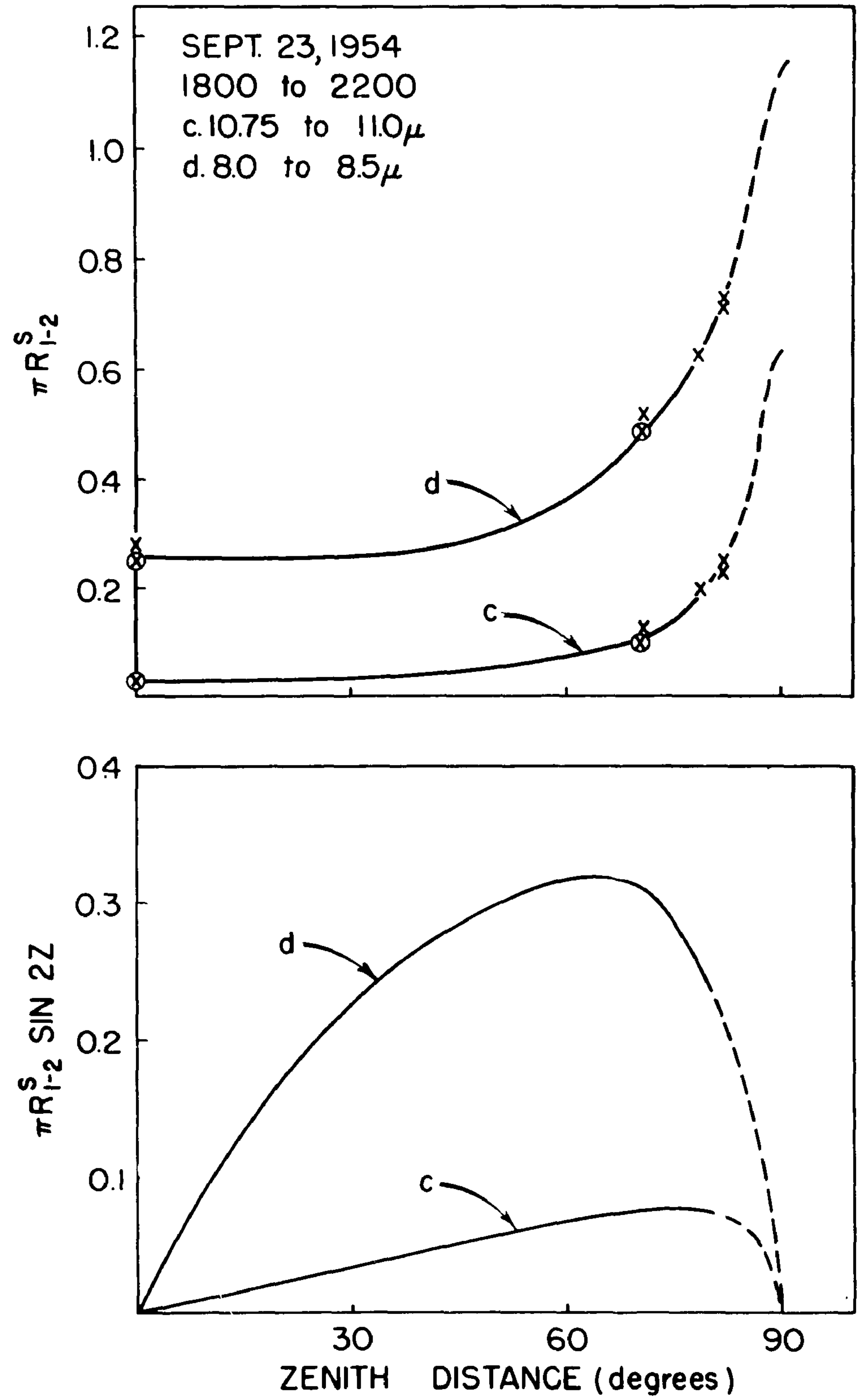
SEPT. 23, 1954
1800 to 2200
c. 10.75 to 11.0μ
d. 8.0 to 8.5μ
πR^S_{1-2}
1.2
1.0
0.8
0.6
0.4
0.2
d
c
πR^S_{1-2} SIN 2Z
0.4
0.3
0.2
0.1
d
c
30
60
90
ZENITH DISTANCE (degrees)

Figure 121.

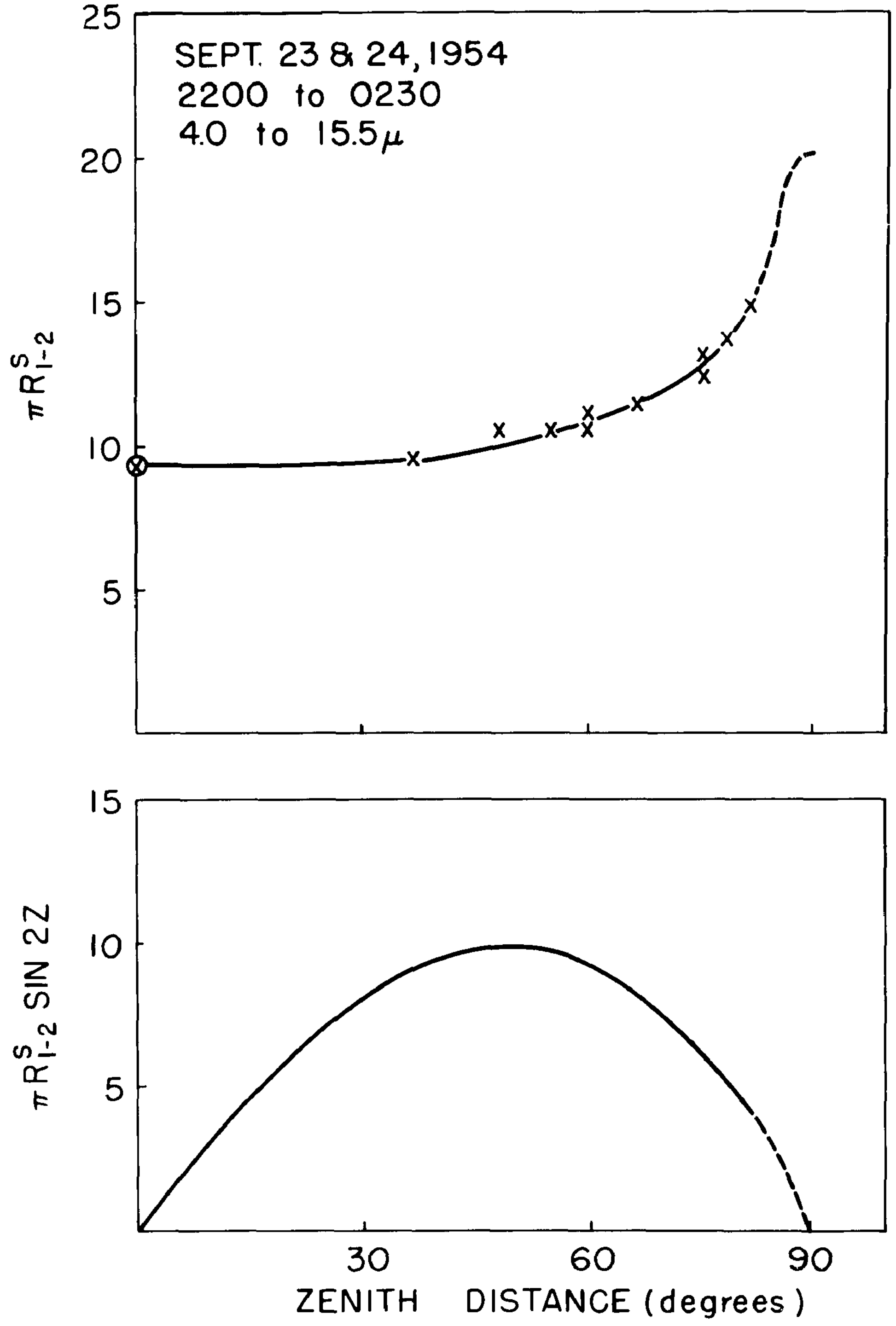
25
20
15
10
5
πR^S_{1-2}
SEPT. 23 & 24, 1954
2200 to 0230
4.0 to 15.5μ
15
10
5
πR^S_{1-2} SIN 2Z
30
60
90
ZENITH DISTANCE (degrees)

Figure 122.

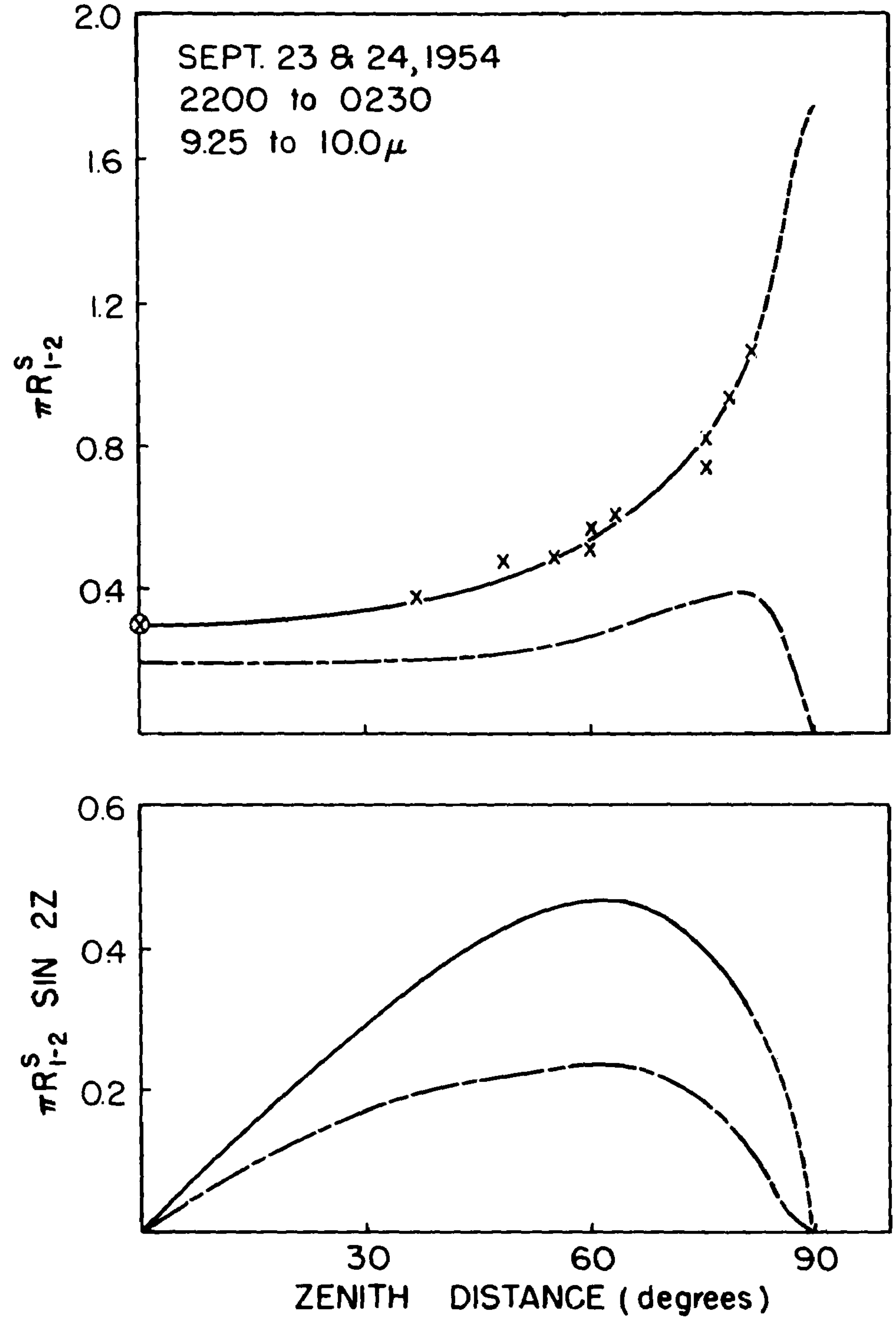
2.0
1.6
1.2
0.8
0.4
πR^S_{1-2}
SEPT. 23 & 24, 1954
2200 to 0230
9.25 to 10.0μ
0.6
0.4
0.2
πR^S_{1-2} SIN 2Z
30
60
90
ZENITH DISTANCE (degrees)

Figure 123.

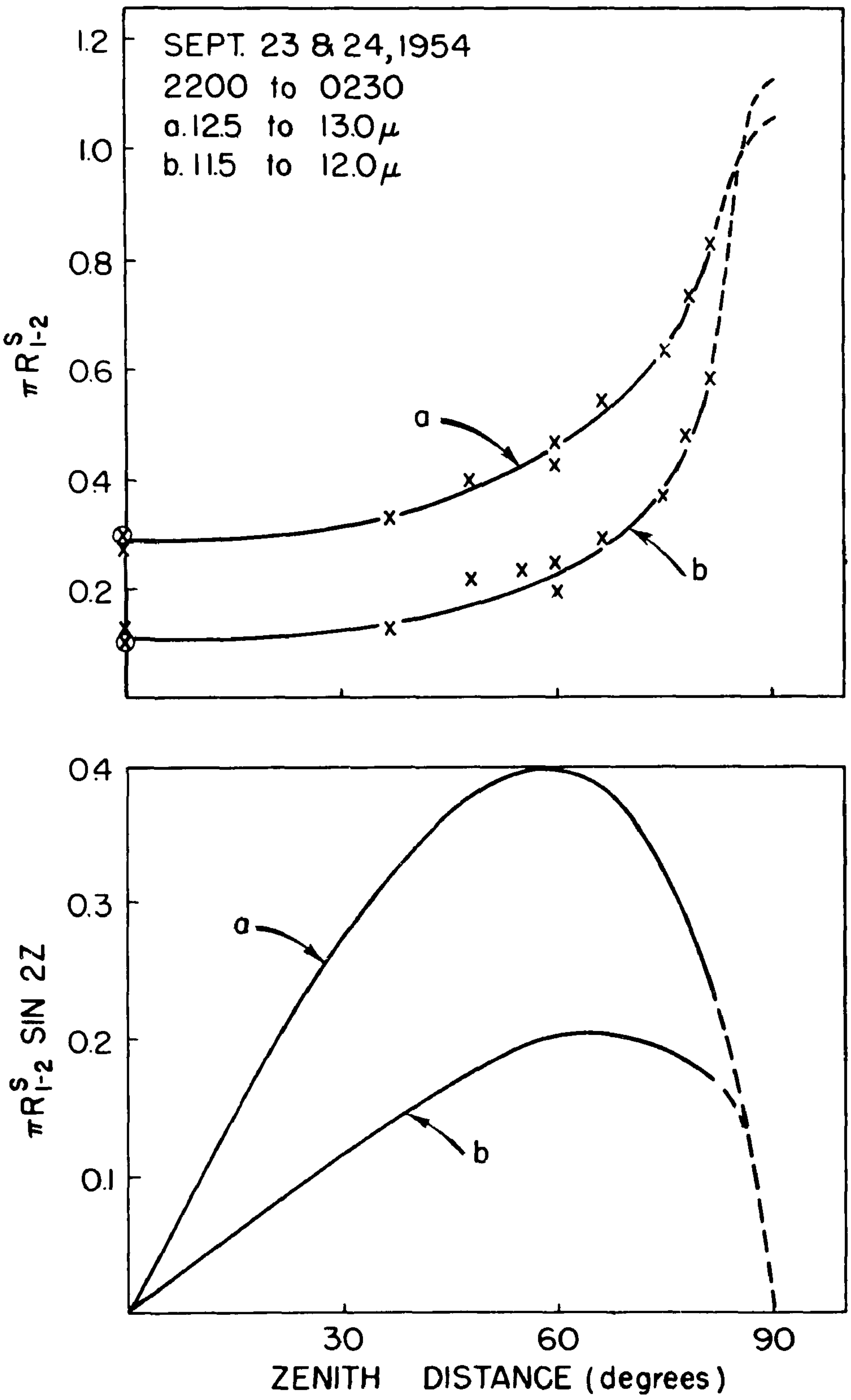
SEPT. 23 & 24, 1954
2200 to 0230
a. 12.5 to 13.0μ
b. 11.5 to 12.0μ
1.2
1.0
0.8
0.6
0.4
0.2
πR^S_{1-2}
a
b
0.4
0.3
0.2
0.1
πR^S_{1-2} SIN 2Z
a
b
30
60
90
ZENITH DISTANCE (degrees)

Figure 124.

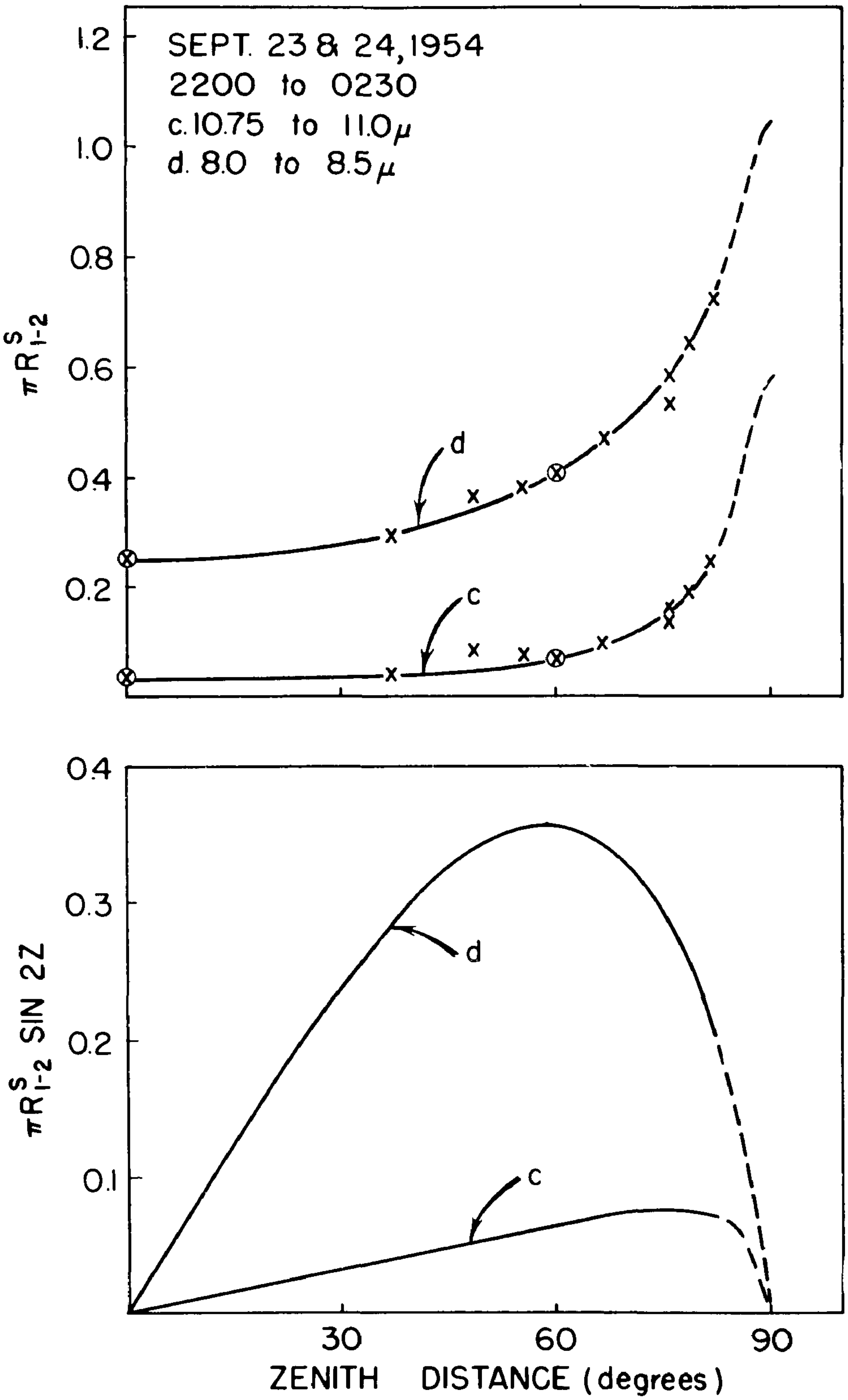
SEPT. 23 & 24, 1954
2200 to 0230
c. 10.75 to 11.0μ
d. 8.0 to 8.5μ
πR^S_{1-2}
1.2
1.0
0.8
0.6
0.4
0.2
d
c
πR^S_{1-2} SIN 2Z
0.4
0.3
0.2
0.1
d
c
30
60
90
ZENITH DISTANCE (degrees)

Figure 125.

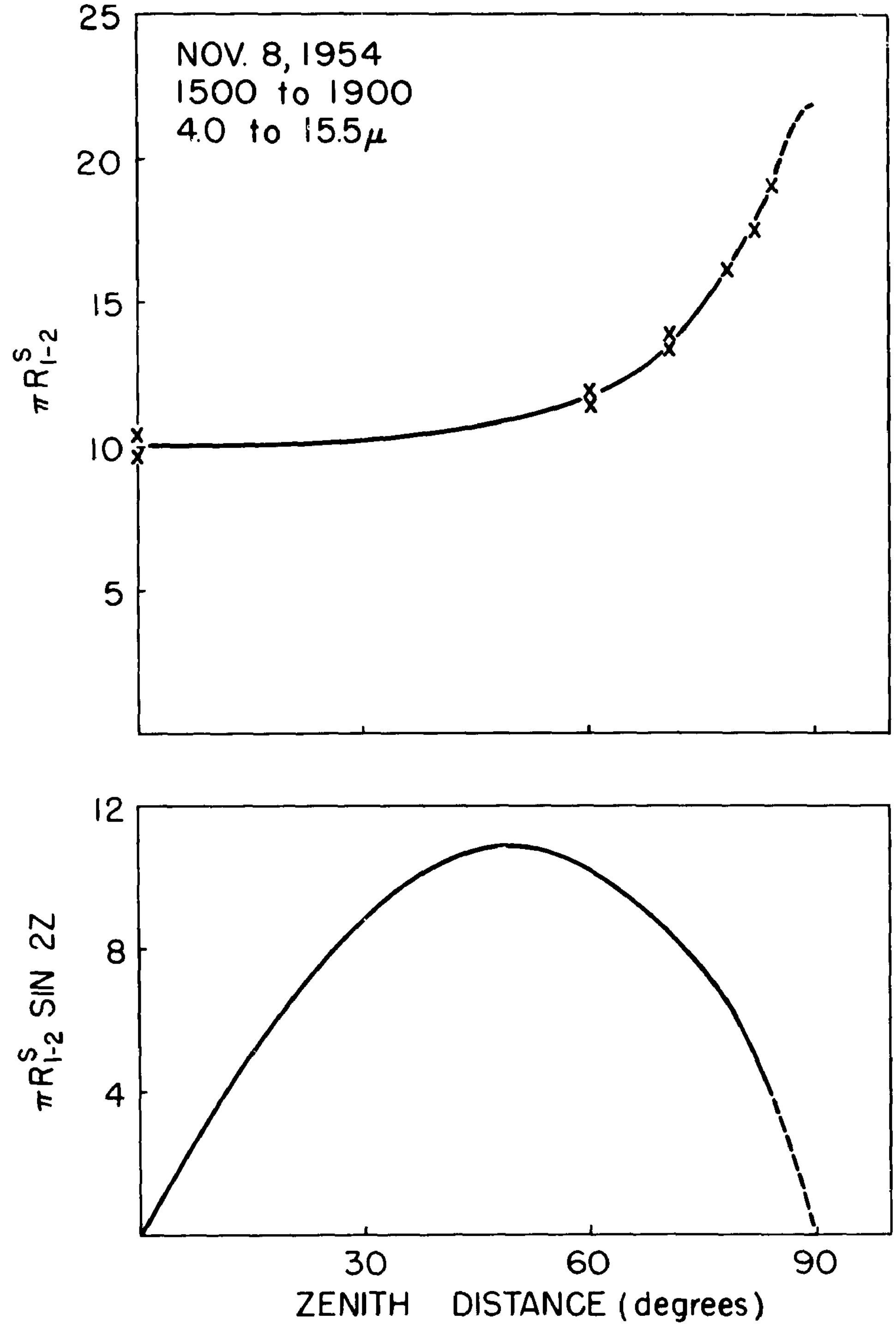
NOV. 8, 1954
1500 to 1900
4.0 to 15.5μ
πR^S_{1-2}
25
20
15
10
5
πR^S_{1-2} SIN 2Z
12
8
4
30
60
90
ZENITH DISTANCE (degrees)

Figure 126.

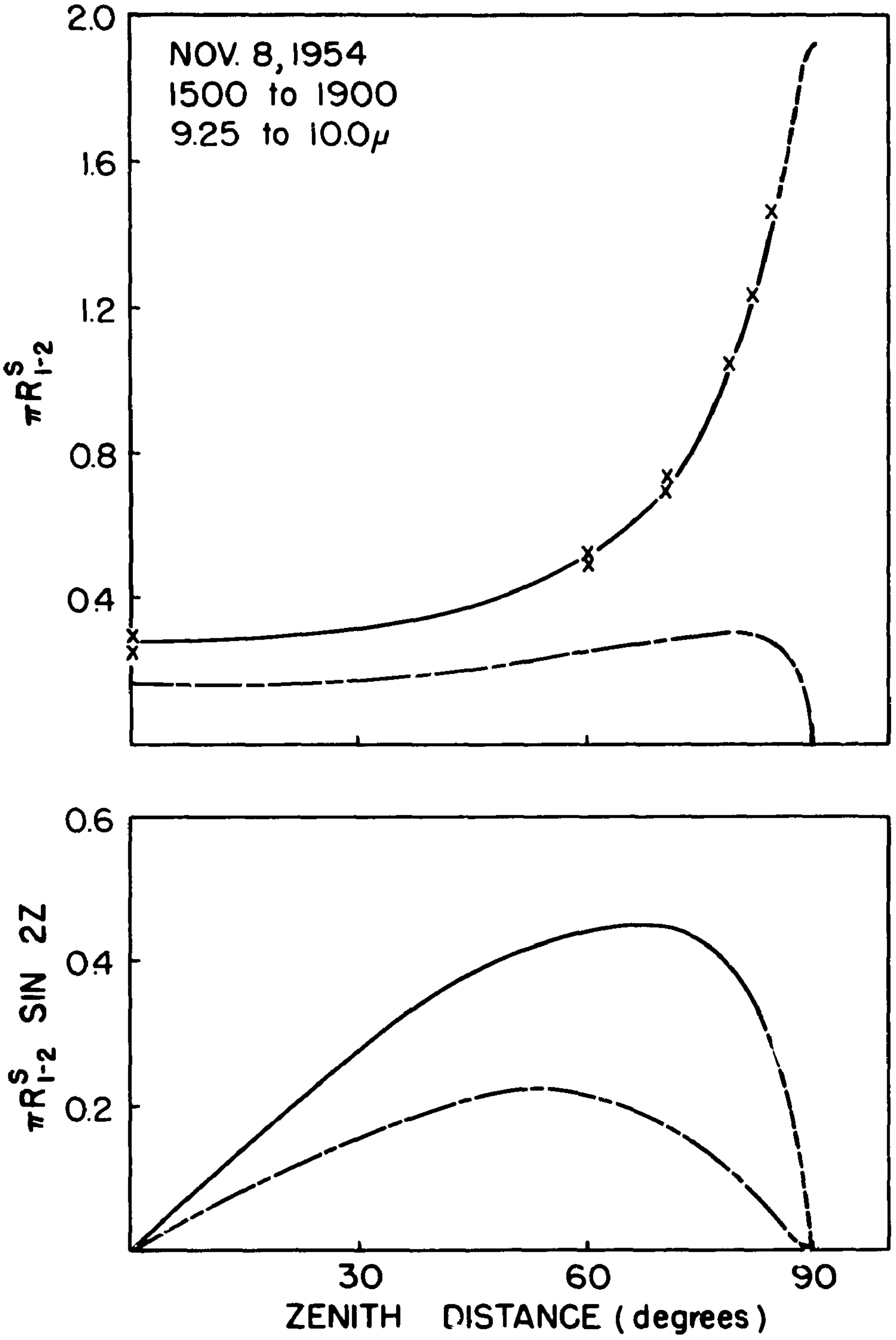
NOV. 8, 1954
1500 to 1900
9.25 to 10.0μ
2.0
1.6
1.2
0.8
0.4
πR^S_{1-2}
0.6
0.4
0.2
πR^S_{1-2} SIN 2Z
30
60
90
ZENITH DISTANCE (degrees)

Figure 127.

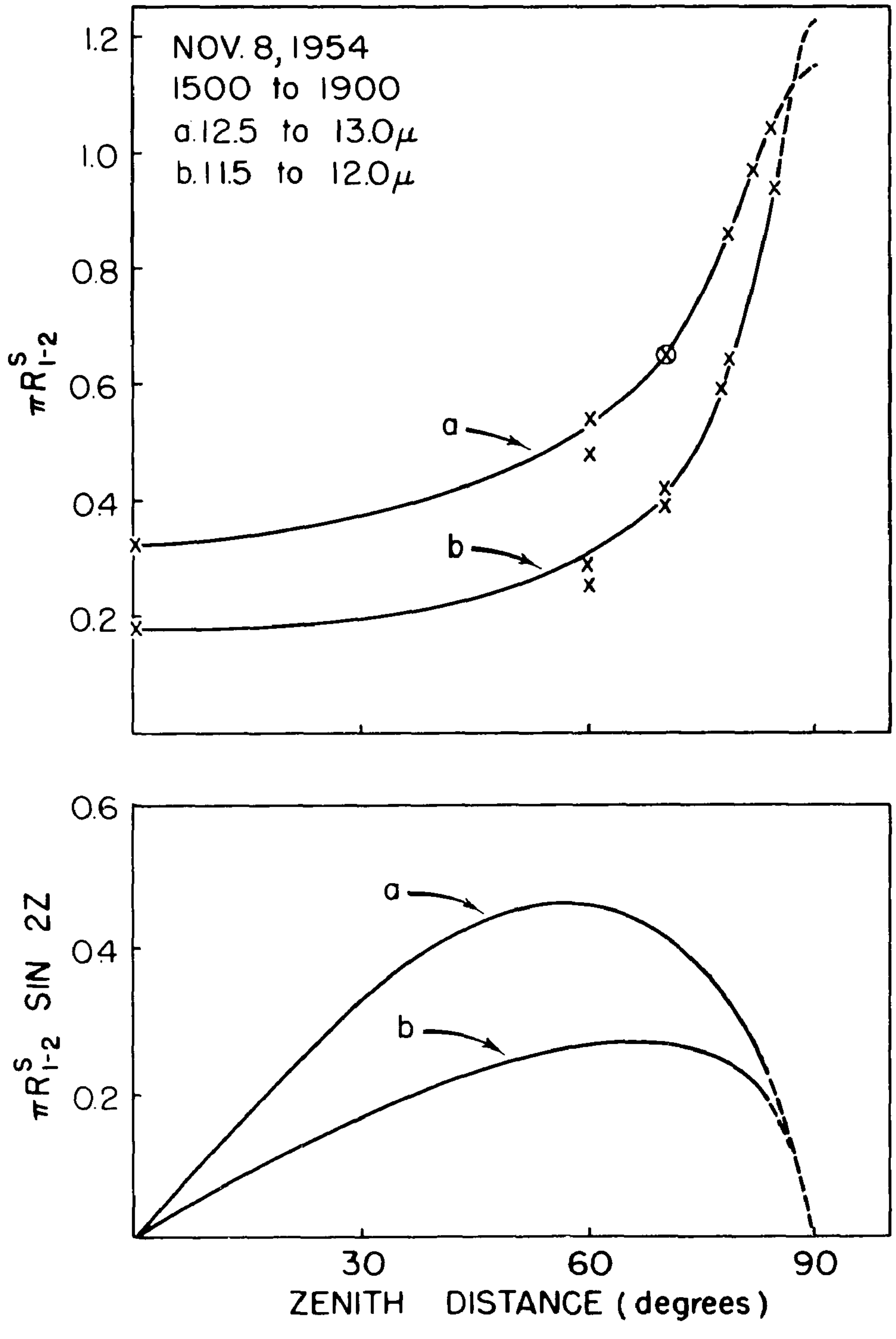
NOV. 8, 1954
1500 to 1900
a. 12.5 to 13.0μ
b. 11.5 to 12.0μ
1.2
1.0
0.8
0.6
0.4
0.2
πR^S_1-2
a
b
0.6
0.4
0.2
πR^S_1-2 SIN 2Z
30
60
90
ZENITH DISTANCE (degrees)

Figure 128.

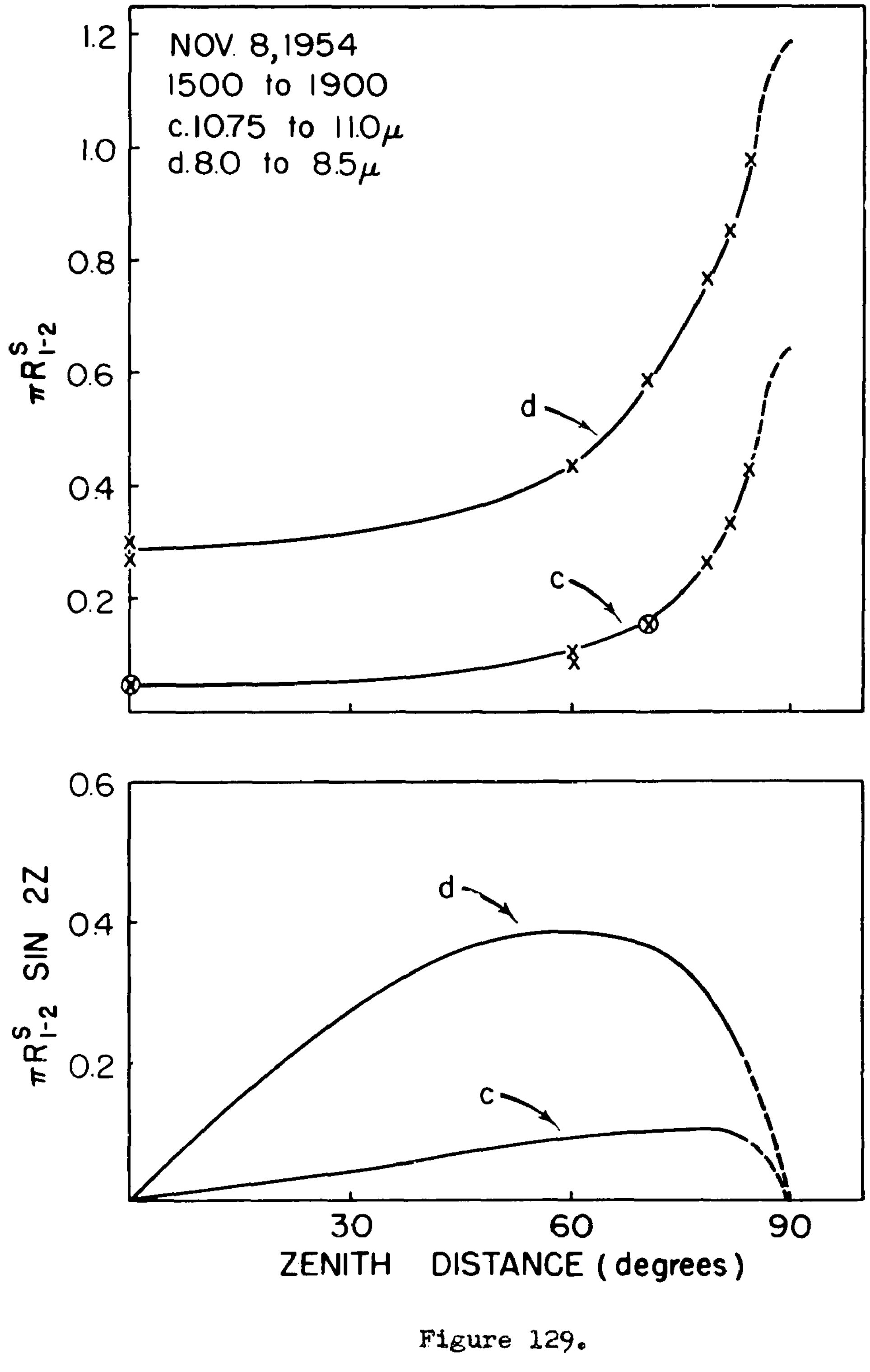
NOV. 8, 1954
1500 to 1900
c. 10.75 to 11.0μ
d. 8.0 to 8.5μ
πR^S_{1-2}
1.2
1.0
0.8
0.6
0.4
0.2
d
c
πR^S_{1-2} SIN 2Z
0.6
0.4
0.2
d
c
30
60
90
ZENITH DISTANCE (degrees)

Figure 129.

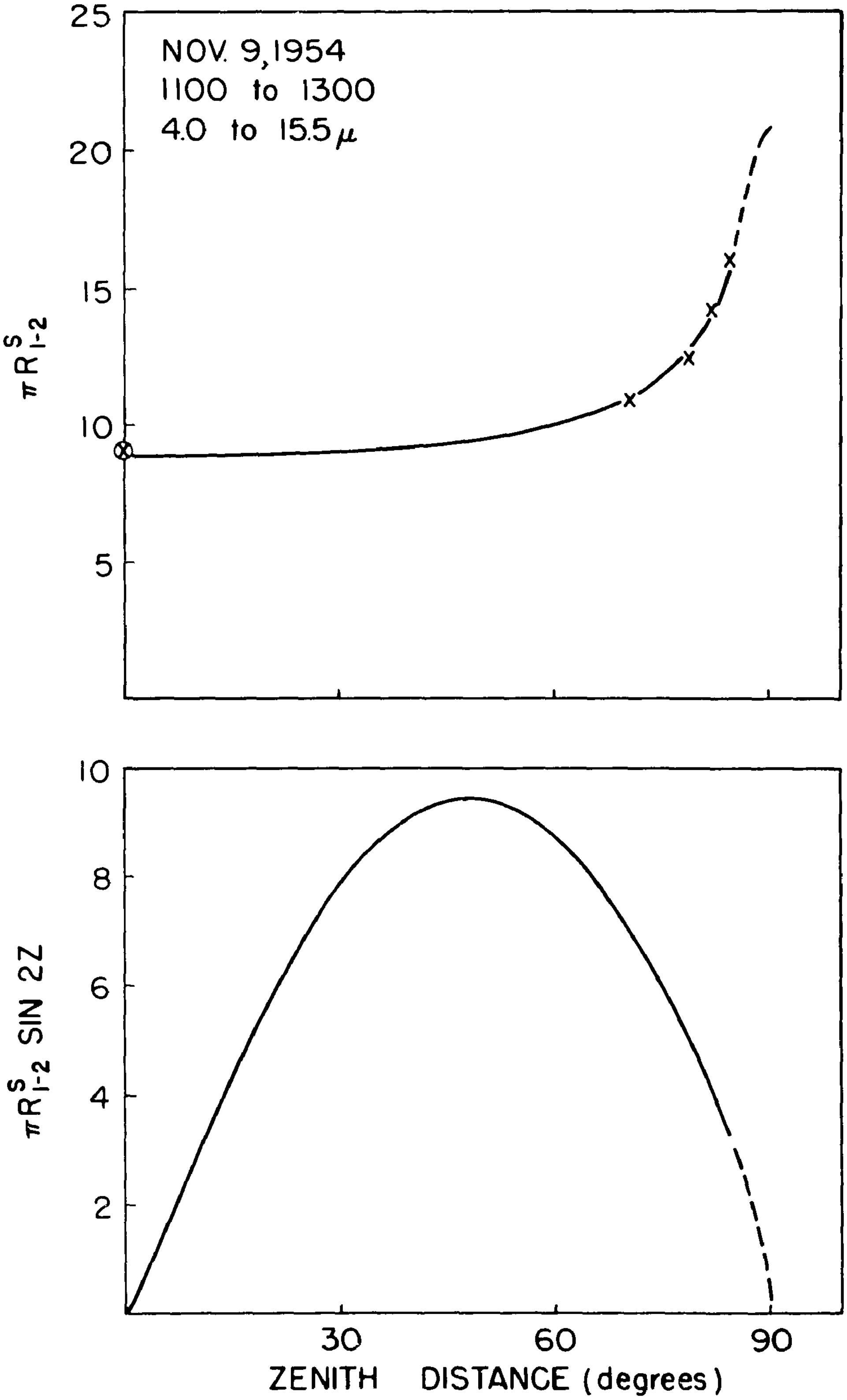
NOV. 9, 1954
1100 to 1300
4.0 to 15.5 μ
25
20
15
10
5
πR^S_1-2
10
8
6
4
2
πR^S_1-2 SIN 2Z
30
60
90
ZENITH DISTANCE (degrees)

Figure 130.

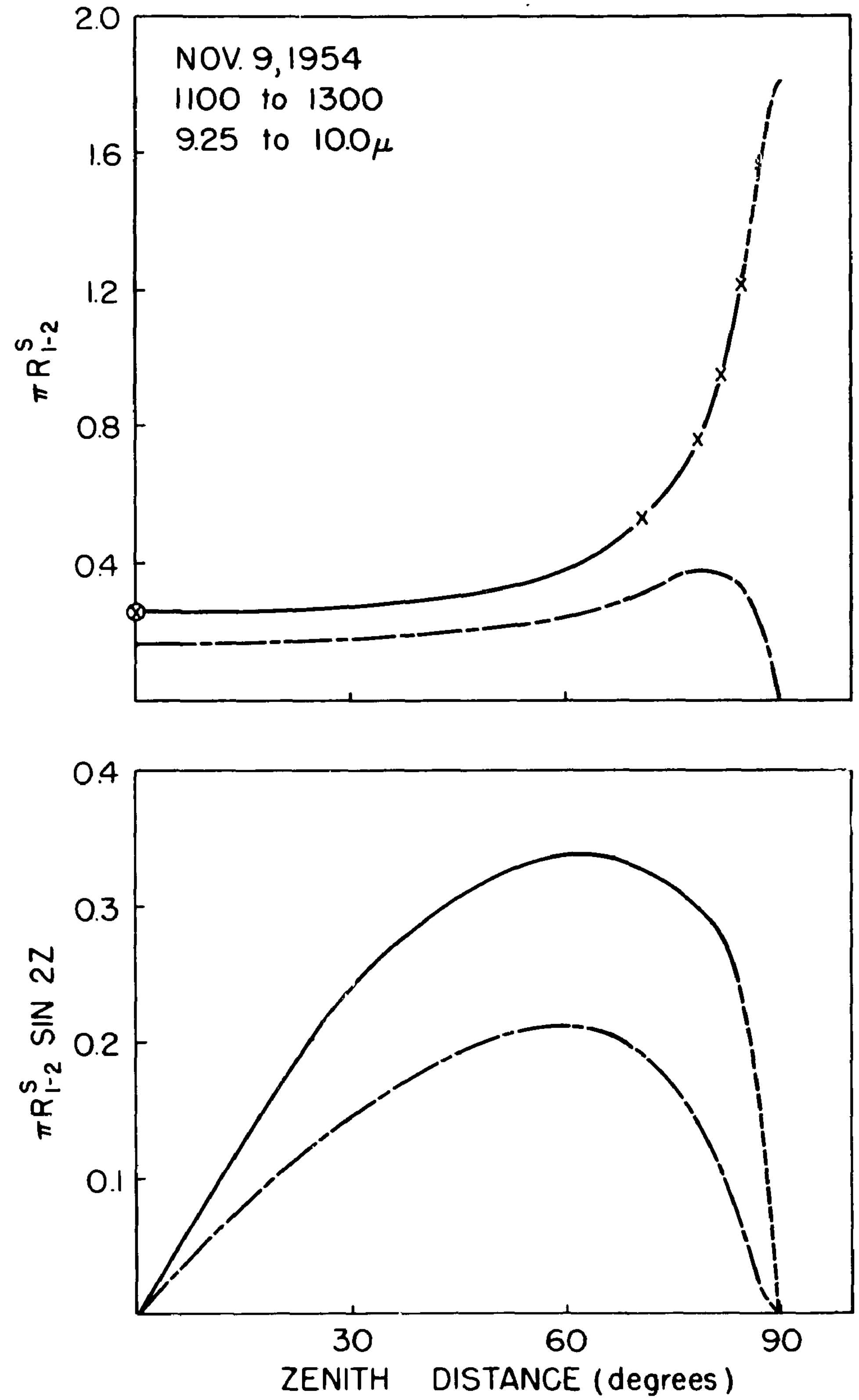
NOV. 9, 1954
1100 to 1300
9.25 to 10.0μ
2.0
1.6
1.2
0.8
0.4
πR^S_{1-2}
0.4
0.3
0.2
0.1
πR^S_{1-2} SIN 2Z
30
60
90
ZENITH DISTANCE (degrees)

Figure 131.

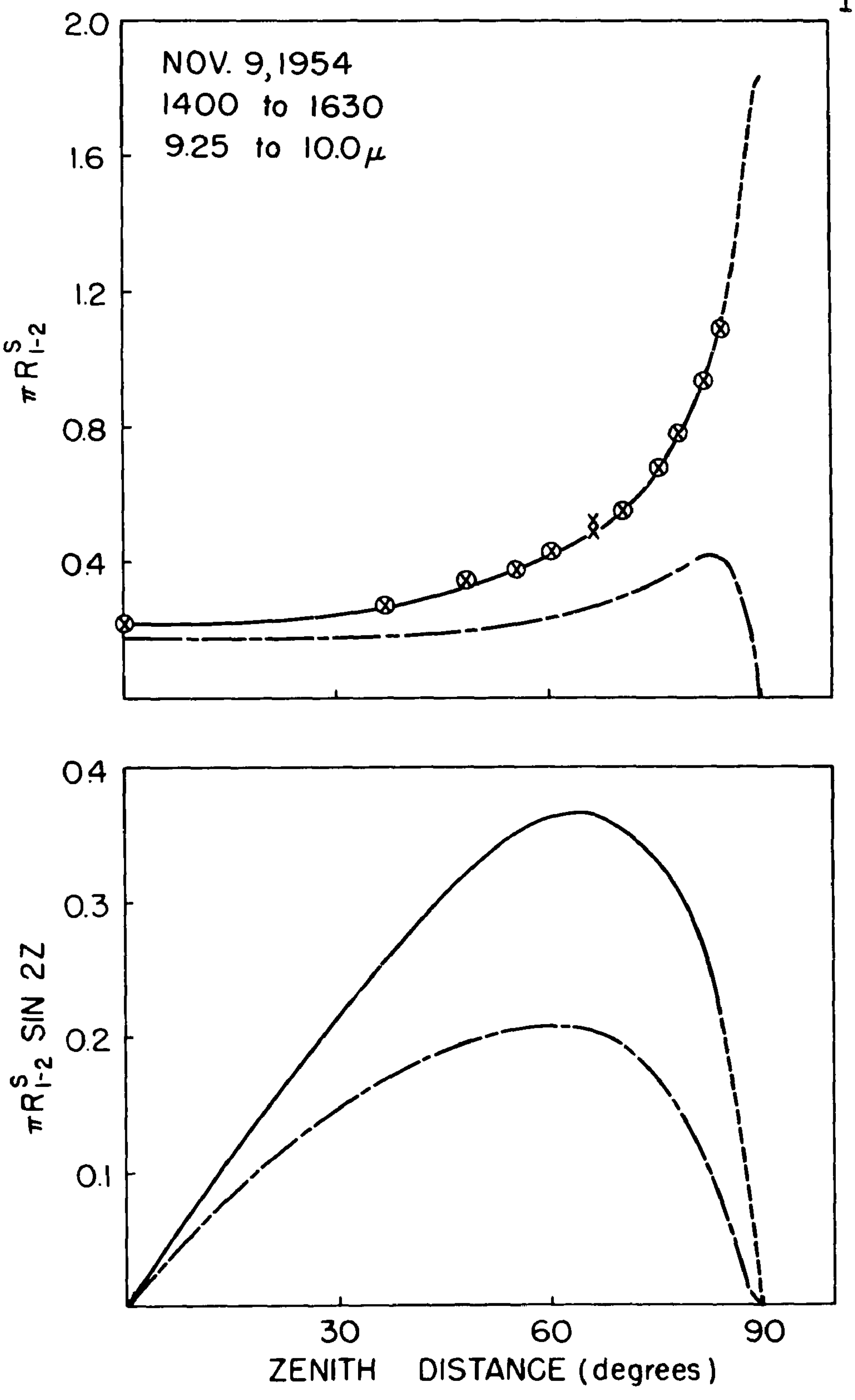
NOV. 9, 1954
1400 to 1630
9.25 to 10.0μ
2.0
1.6
1.2
0.8
0.4
πR^{S}_{1-2}
0.4
0.3
0.2
0.1
πR^{S}_{1-2} SIN 2Z
30
60
90
ZENITH DISTANCE (degrees)

Figure 132.

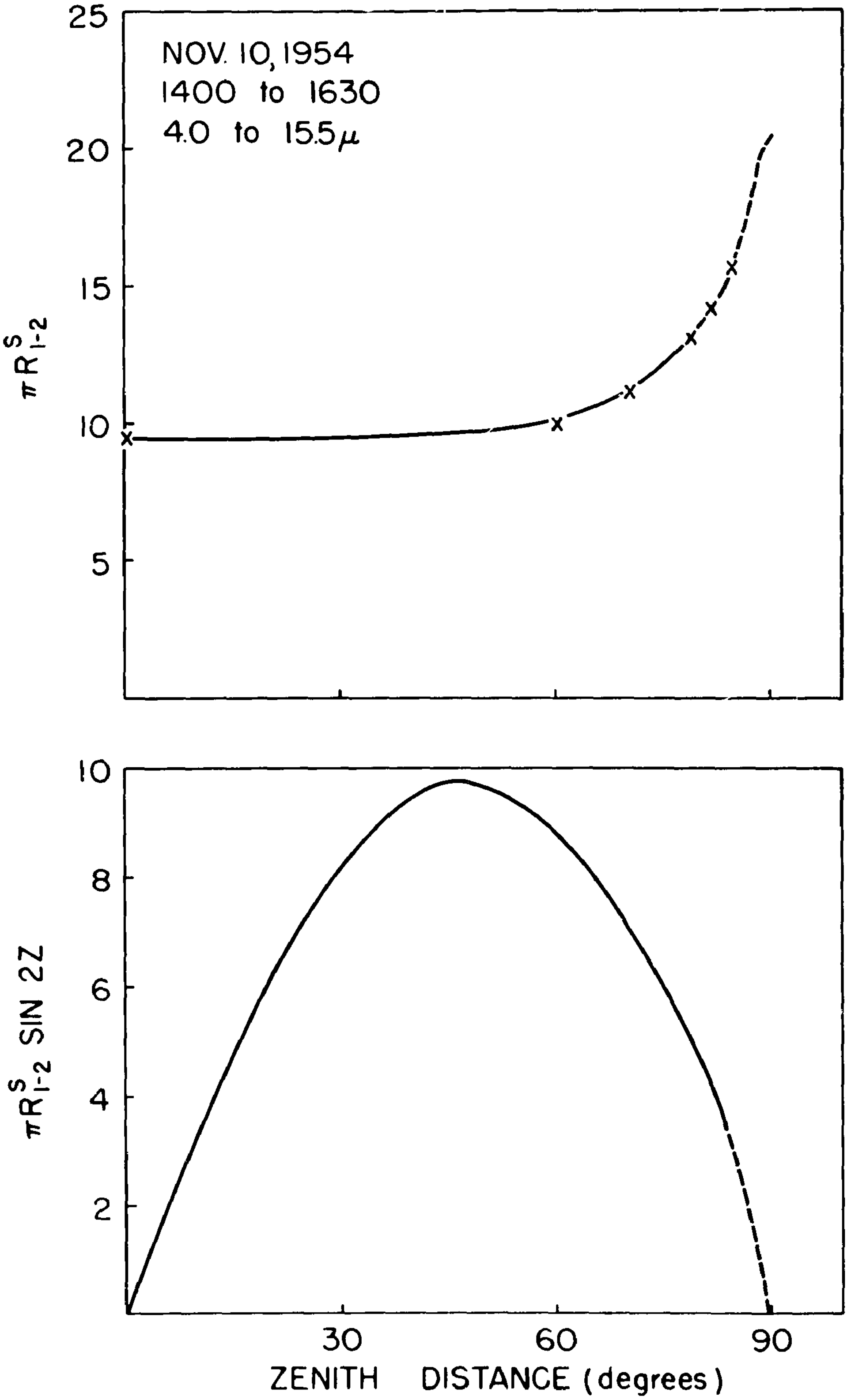

25
20
15
10
5
NOV. 10, 1954
1400 to 1630
4.0 to 15.5μ
πR^S_1-2
10
8
6
4
2
πR^S_1-2 SIN 2Z
30
60
90
ZENITH DISTANCE (degrees)

Figure 133.

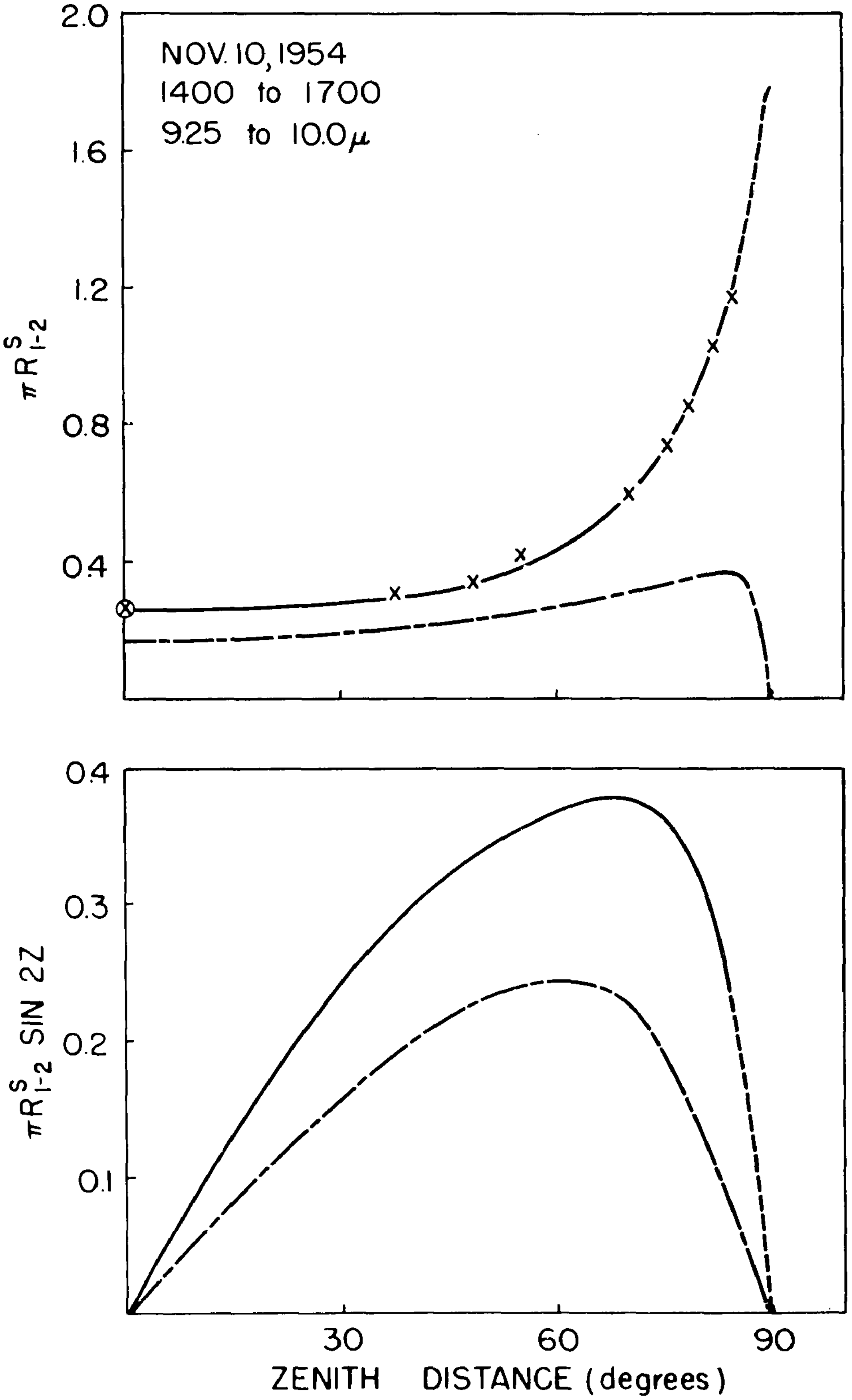
2.0
1.6
1.2
0.8
0.4
πR^{S}_{1-2}
NOV. 10, 1954
1400 to 1700
9.25 to 10.0μ
0.4
0.3
0.2
0.1
πR^{S}_{1-2} SIN 2Z
30
60
90
ZENITH DISTANCE (degrees)

Figure 134.

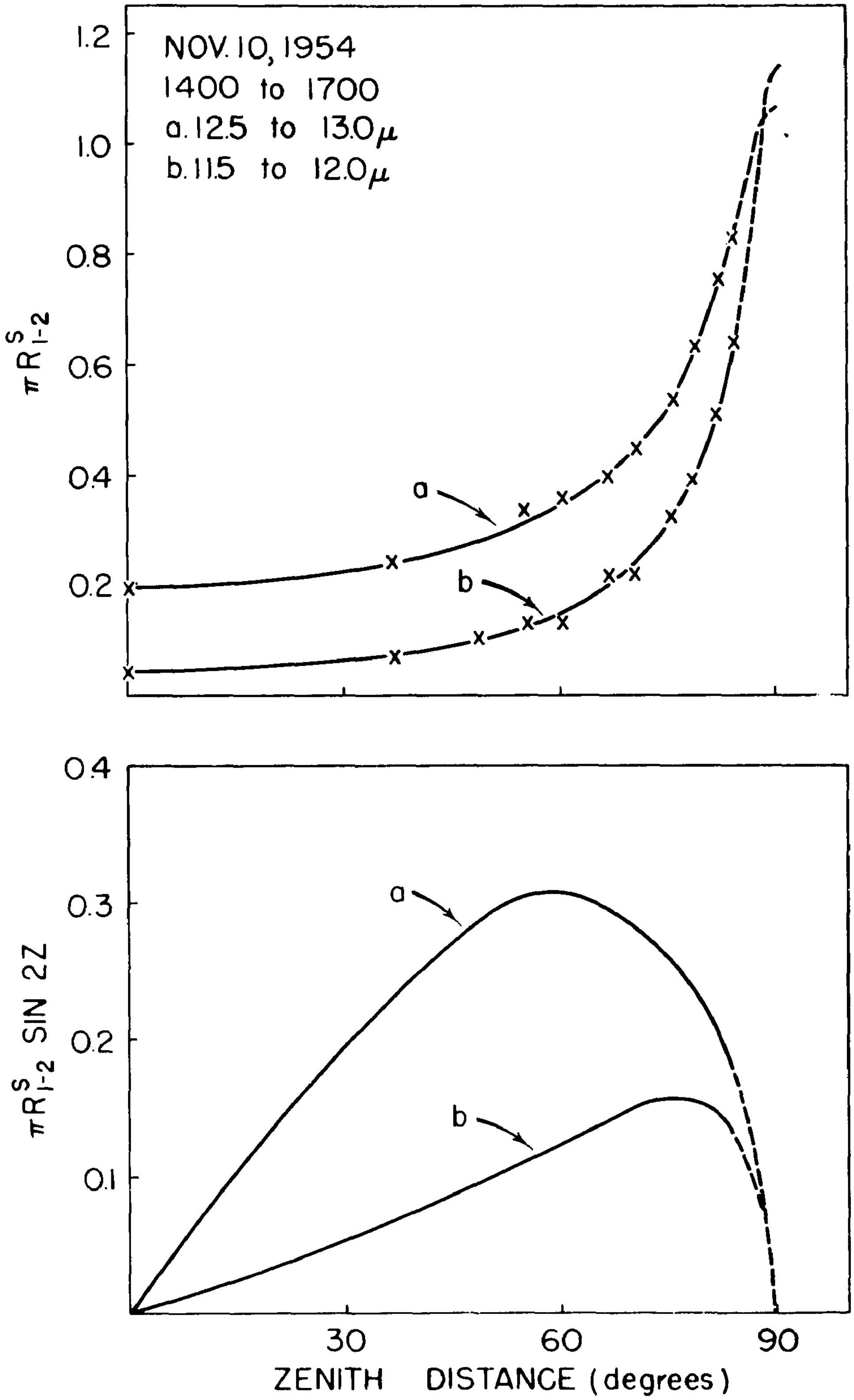
NOV. 10, 1954
1400 to 1700
a. 12.5 to 13.0μ
b. 11.5 to 12.0μ
1.2
1.0
0.8
0.6
0.4
0.2
πR^S_{1-2}
a
b
0.4
0.3
0.2
0.1
πR^S_{1-2} SIN 2Z
a
b
30
60
90
ZENITH DISTANCE (degrees)

Figure 135.

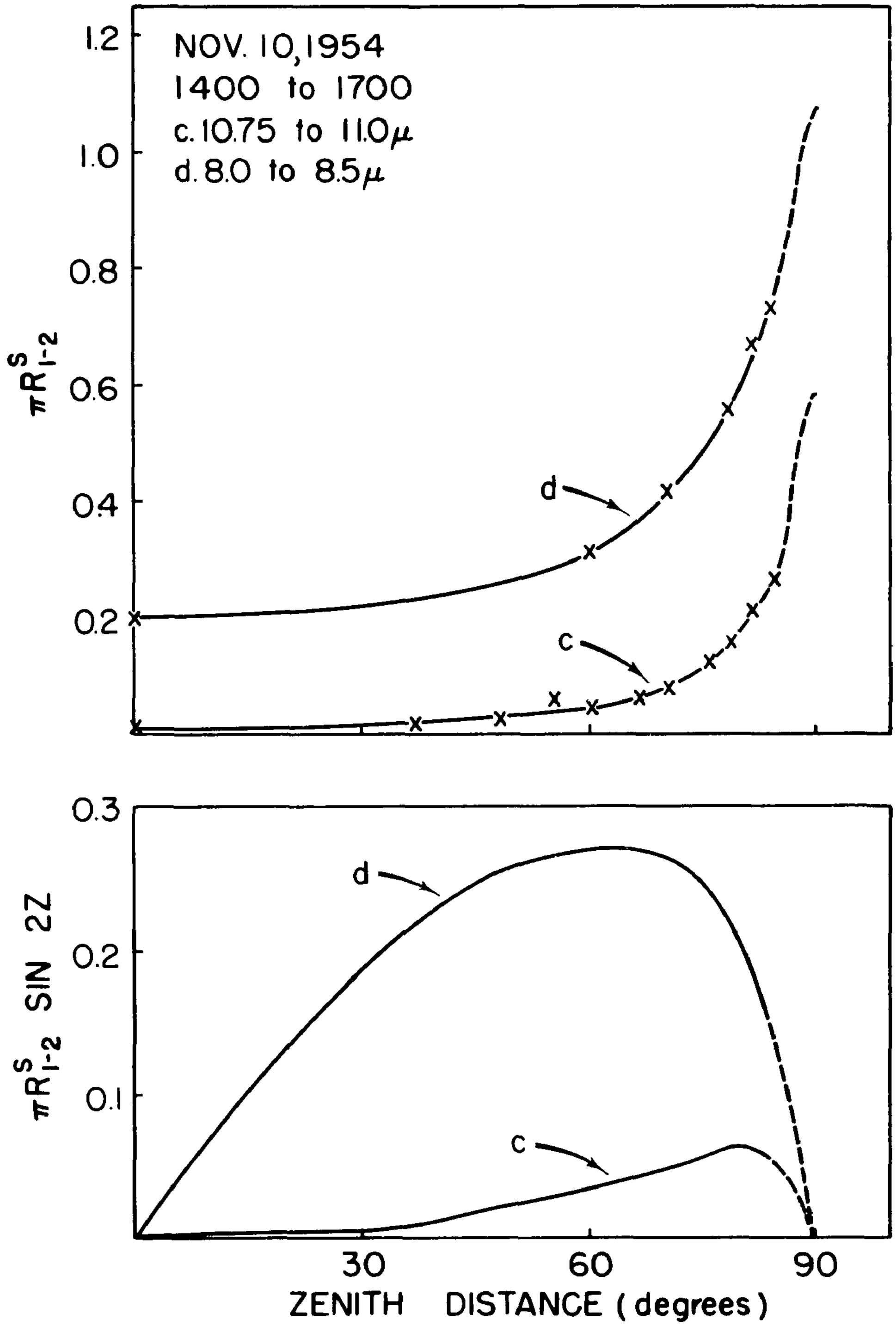
NOV. 10, 1954
1400 to 1700
c. 10.75 to 11.0μ
d. 8.0 to 8.5μ
1.2
1.0
0.8
0.6
0.4
0.2
0.3
0.2
0.1
d
c
d
c
πR^S_{1-2}
πR^S_{1-2} SIN 2Z
30
60
90
ZENITH DISTANCE (degrees)

Figure 136.

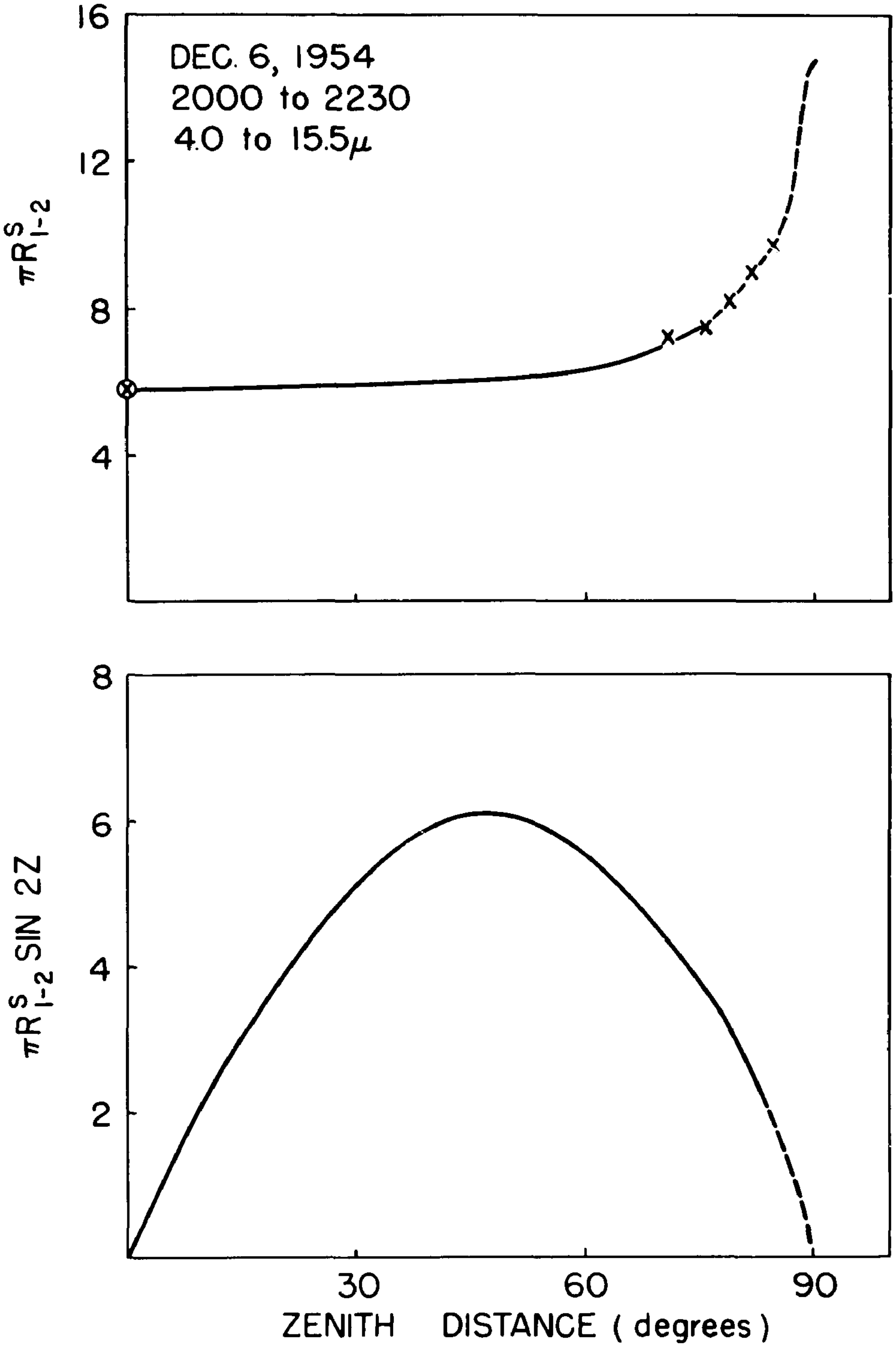
16
12
8
4
πR^{S}_{1-2}
DEC. 6, 1954
2000 to 2230
4.0 to 15.5μ
8
6
4
2
πR^{S}_{1-2} SIN 2Z
30
60
90
ZENITH DISTANCE (degrees)

Figure 137.

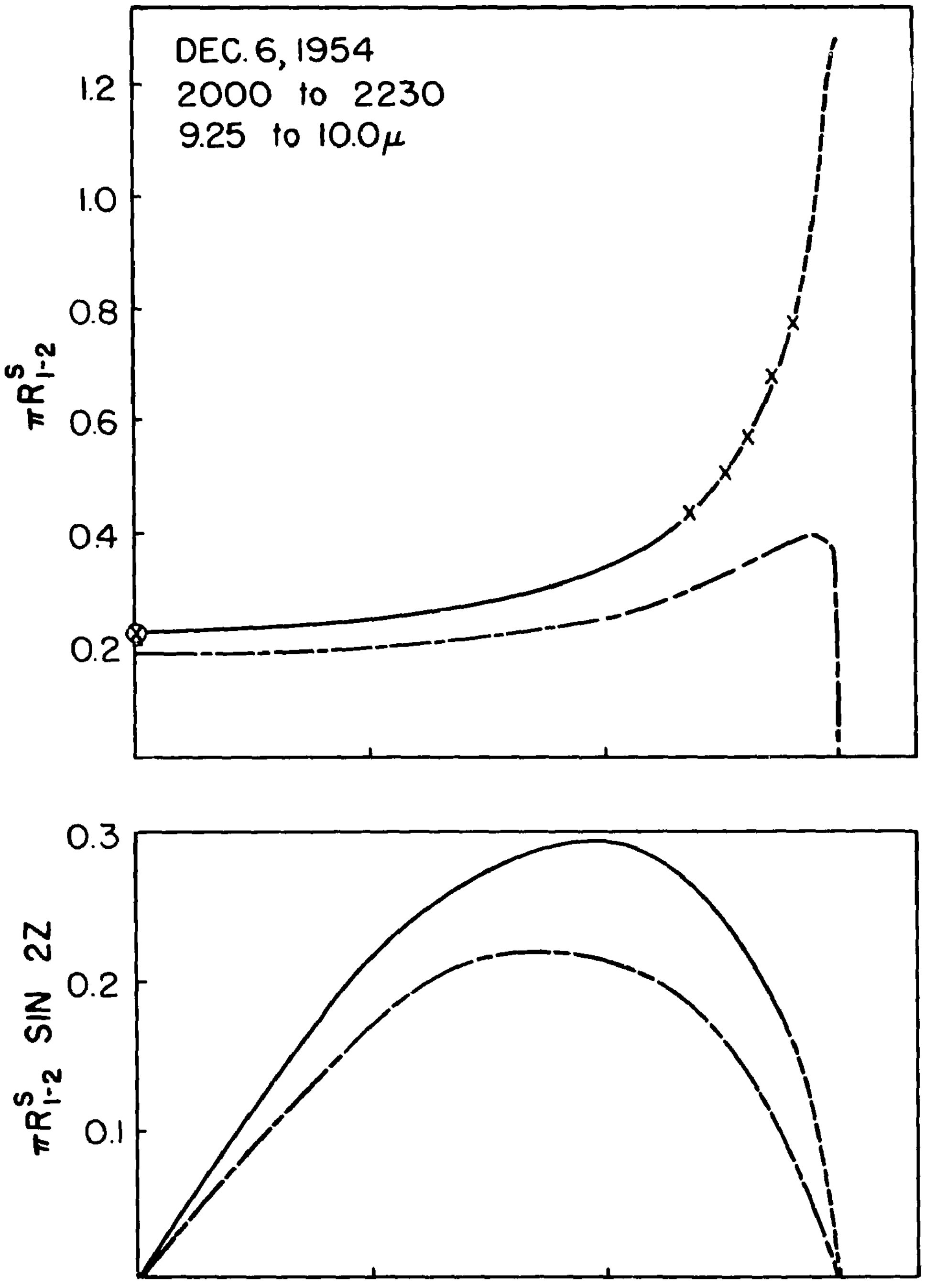
DEC. 6, 1954
2000 to 2230
9.25 to 10.0μ
1.2
1.0
0.8
0.6
0.4
0.2
πR^S_{1-2}
0.3
0.2
0.1
πR^S_{1-2} SIN 2Z
30
60
90
ZENITH DISTANCE (degrees)

Figure 138.

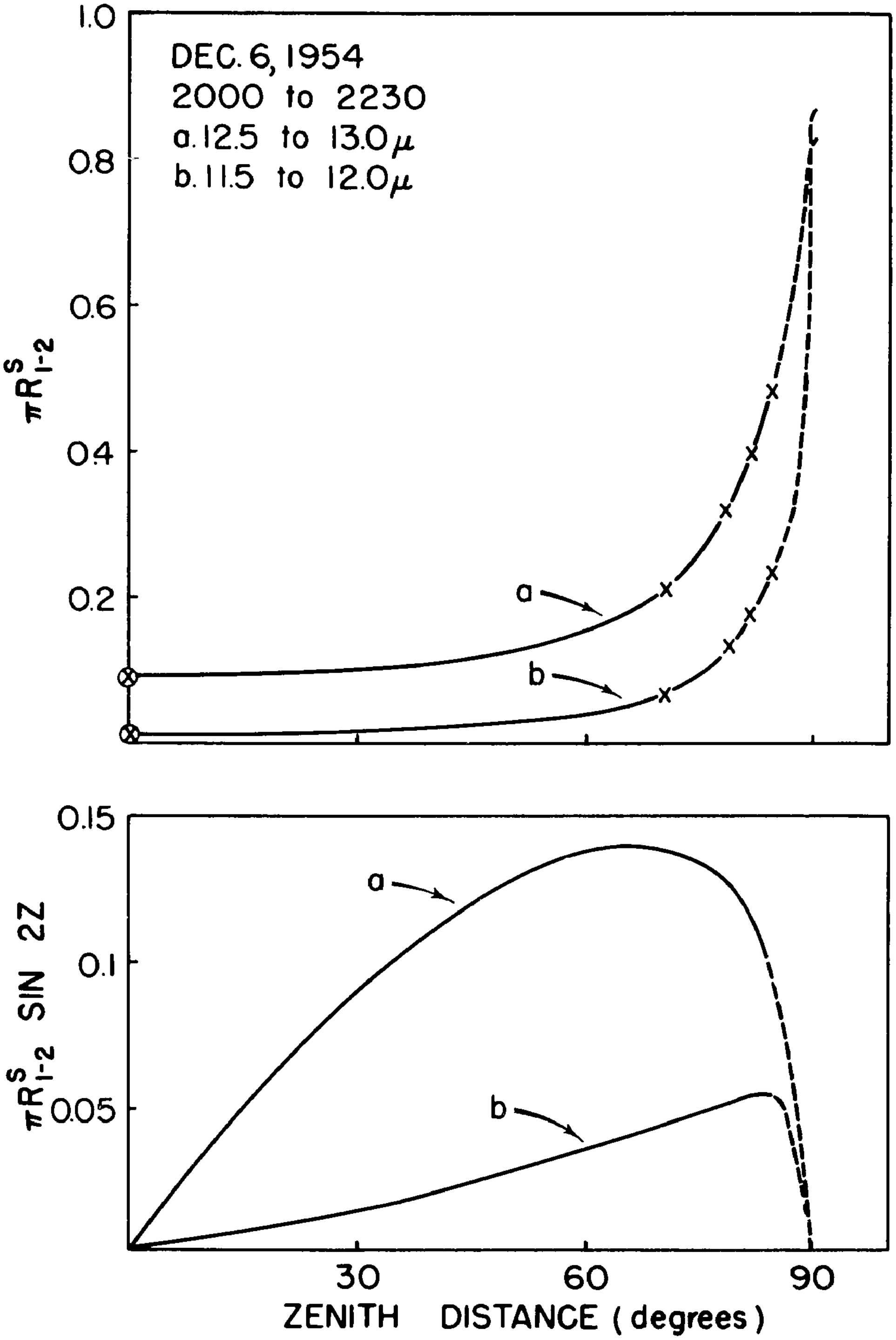
1.0
0.8
0.6
0.4
0.2
πR^{S}_{1-2}
DEC. 6, 1954
2000 to 2230
a. 12.5 to 13.0μ
b. 11.5 to 12.0μ
a
b
0.15
0.1
0.05
πR^{S}_{1-2} SIN 2Z
a
b
30
60
90
ZENITH DISTANCE (degrees)

Figure 139.

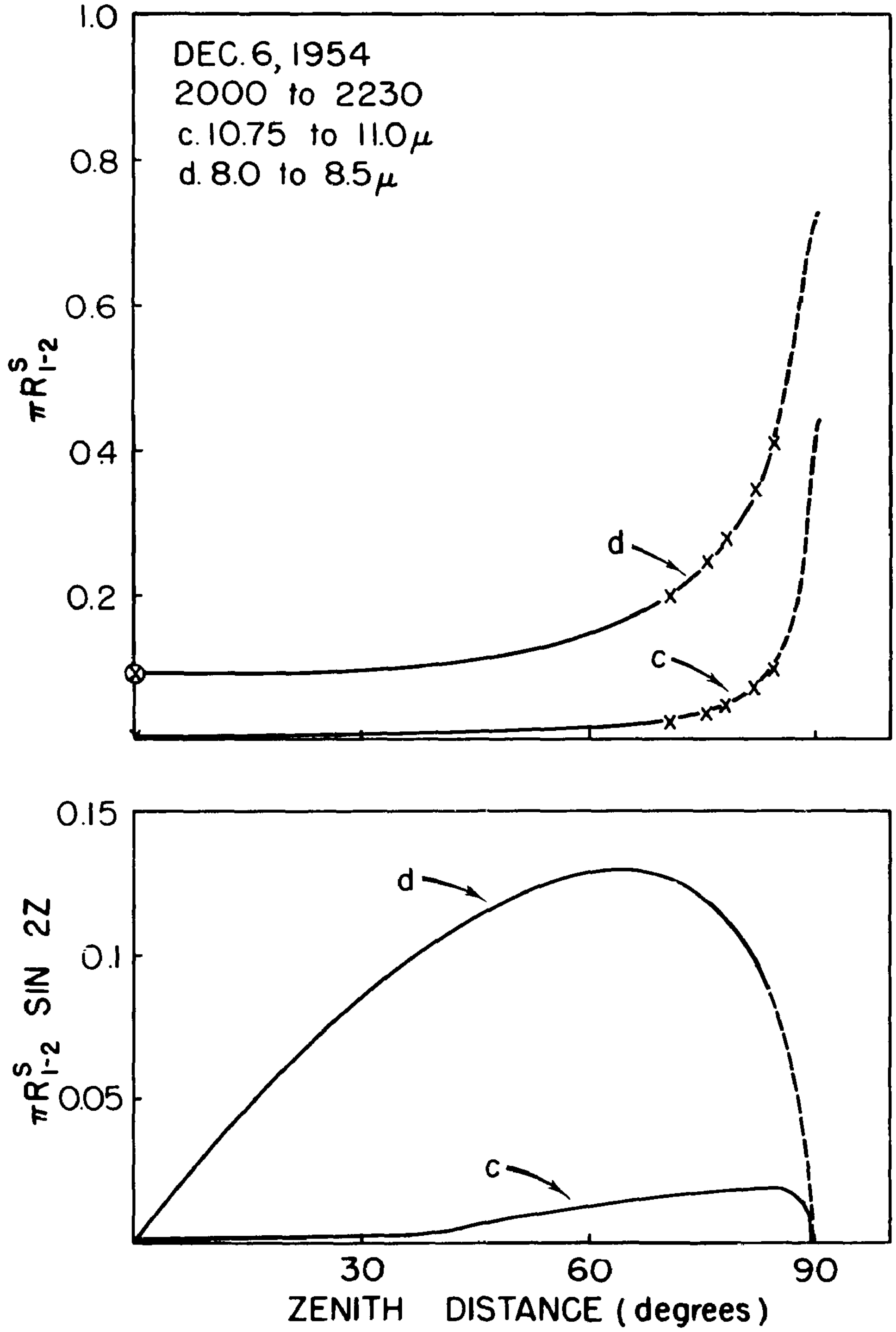
DEC. 6, 1954
2000 to 2230
c. 10.75 to 11.0μ
d. 8.0 to 8.5μ
1.0
0.8
0.6
0.4
0.2
πR^{S}_{1-2}
d
c
0.15
0.1
0.05
πR^{S}_{1-2} SIN 2Z
d
c
30
60
90
ZENITH DISTANCE (degrees)

Figure 140.

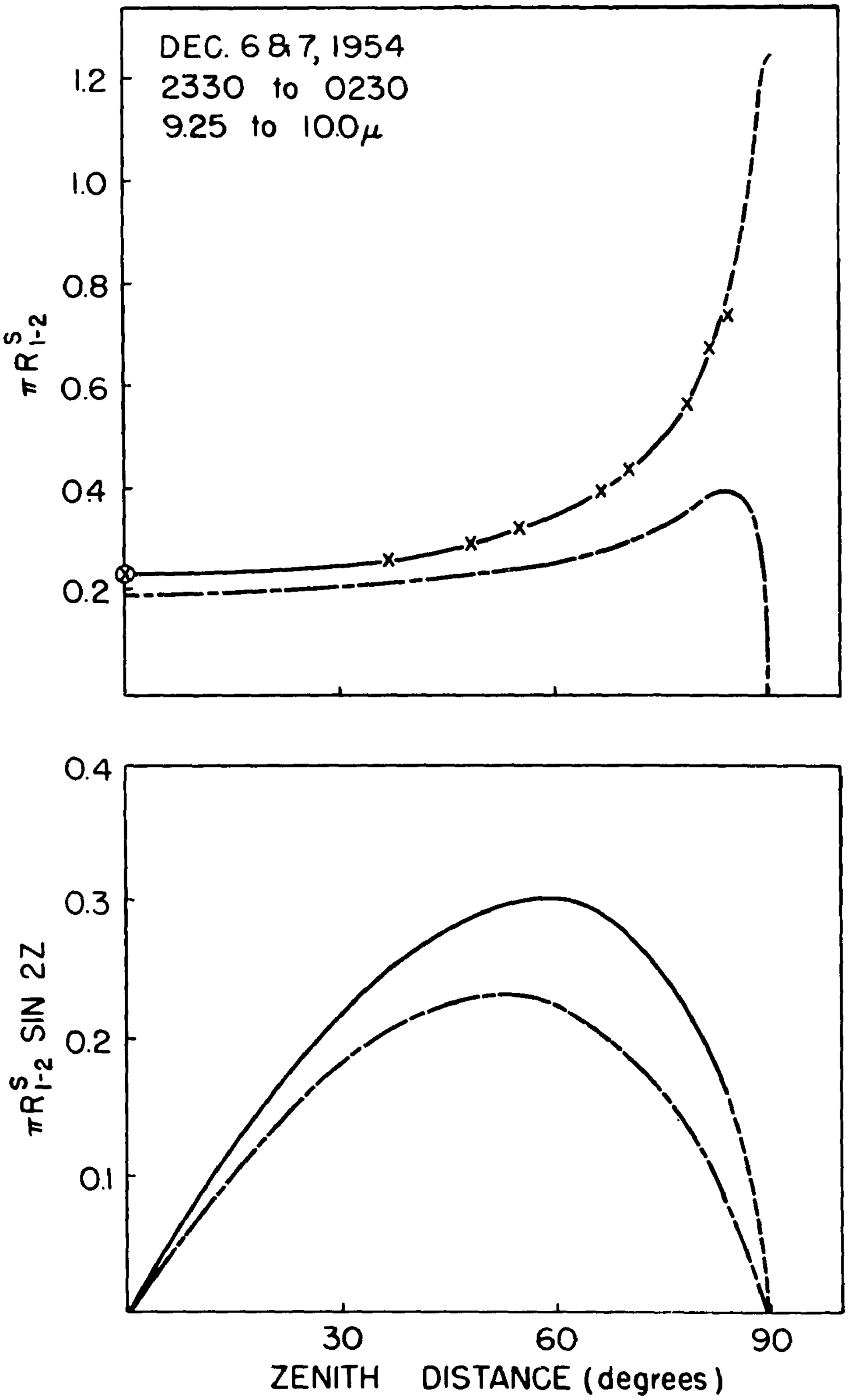
DEC. 6 & 7, 1954
2330 to 0230
9.25 to 10.0μ
1.2
1.0
0.8
0.6
0.4
0.2
πR^S_{1-2}
0.4
0.3
0.2
0.1
πR^S_{1-2} SIN 2Z
30
60
90
ZENITH DISTANCE (degrees)

Figure 141.

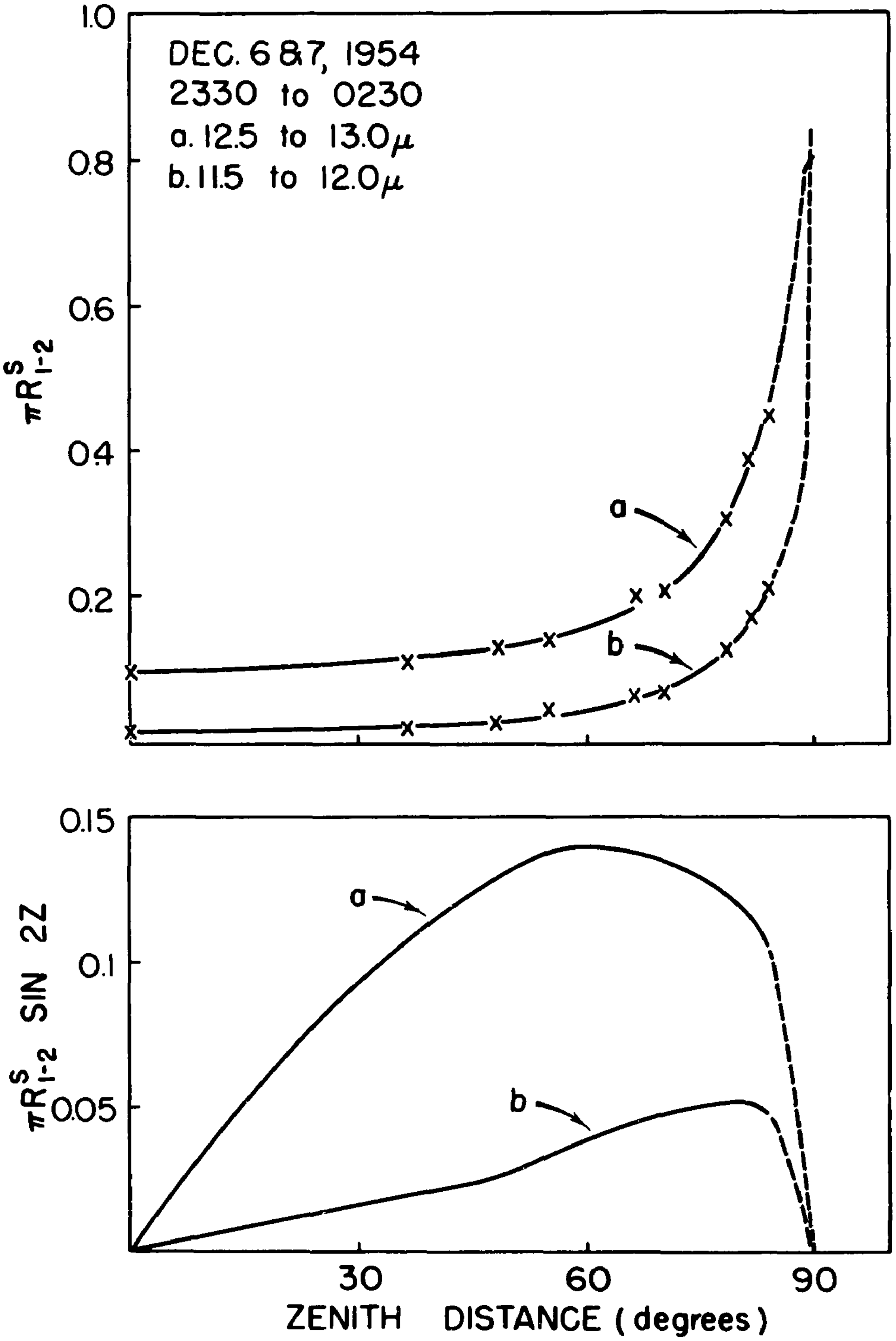
DEC. 6 & 7, 1954
2330 to 0230
a. 12.5 to 13.0μ
b. 11.5 to 12.0μ
1.0
0.8
0.6
0.4
0.2
πR^S_{1-2}
a
b
0.15
0.1
0.05
πR^S_{1-2} SIN 2Z
a
b
30
60
90
ZENITH DISTANCE (degrees)

Figure 142.

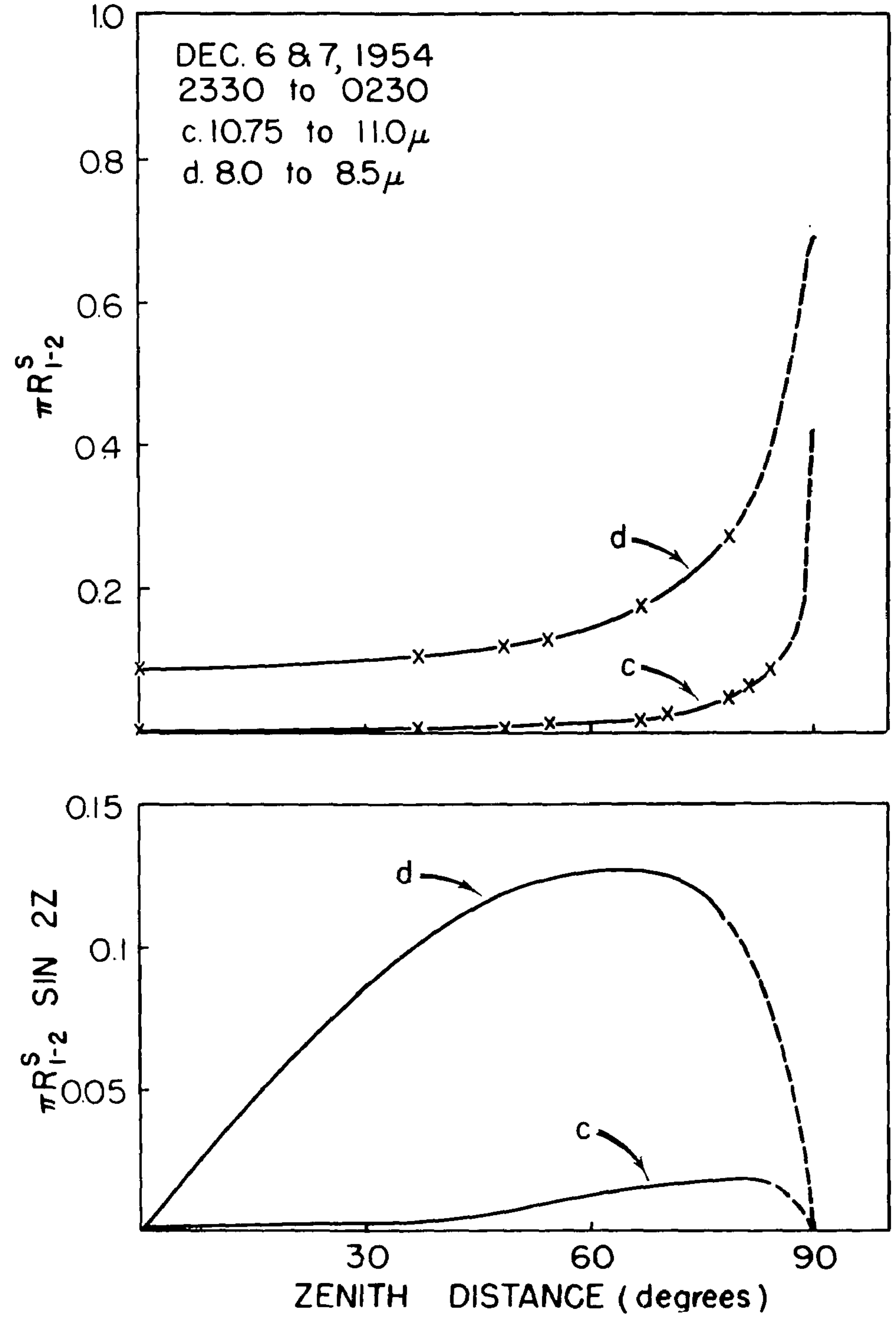
1.0
0.8
0.6
0.4
0.2
$\pi R^{S}_{1\text{-}2}$
DEC. 6 & 7, 1954
2330 to 0230
c. 10.75 to 11.0μ
d. 8.0 to 8.5μ
d
c
0.15
0.1
0.05
$\pi R^{S}_{1\text{-}2}$ SIN 2Z
d
c
30
60
90
ZENITH DISTANCE (degrees)

Figure 143.

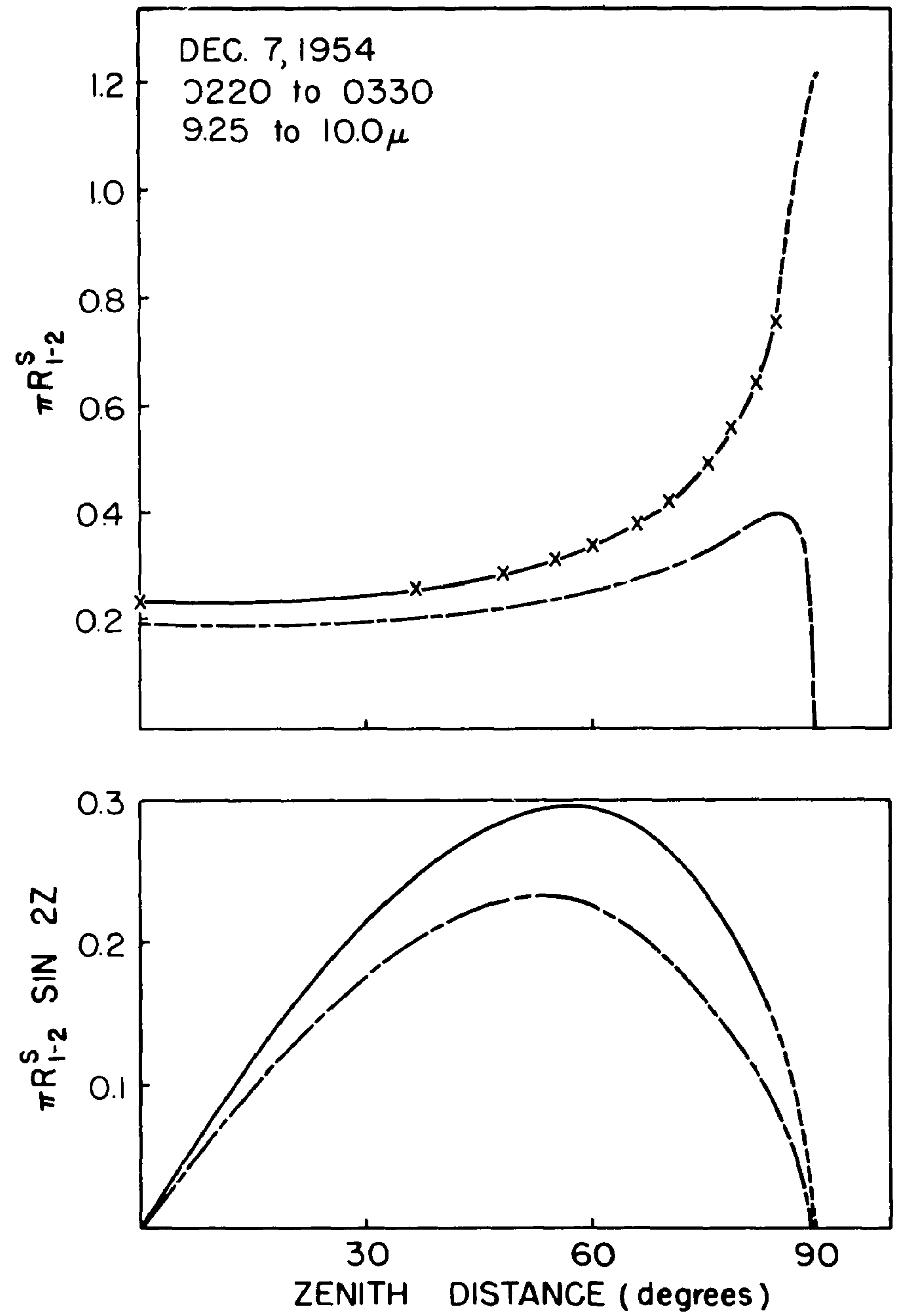
DEC. 7, 1954
0220 to 0330
9.25 to 10.0μ
πR^S_{1-2}
1.2
1.0
0.8
0.6
0.4
0.2
πR^S_{1-2} SIN 2Z
0.3
0.2
0.1
30
60
90
ZENITH DISTANCE (degrees)

Figure 144.

TABLE I

RADIATION VALUES FOR THE TOTAL SKY AND APPROPRIATE DATA FOR THE WAVELENGTH REGION 4.0 TO 15.5 μ

Date	Time	Humidity (g/m^3)	Temp. (°C)	$\underline{R}^S_{1-2}(\Sigma)$	$\dfrac{\underline{R}^S_{1-2}(\Sigma)}{\pi R^B_{1-2}(T_o)}$
May 3 & 4	2300-0700	4.0- 4.3	1.7- 4.2	7.60	43.2
May 15	1150-1600	7.6- 8.4	18.9-21.7	12.9	53.6
	1600-2030	8.4- 9.1	20.8-21.7	13.0	54.8
	2030-2400	8.4- 9.1	11.7-20.8	12.0	57.2
May 30	1100-1830	8.4- 9.4	22.2-25.6	14.6	56.3
June 13	1400-1630	15.7	31.9-32.7	19.8	66.7
June 24	1000-1800	11.9-13.3	23.3-28.3	15.7	59.2
July 14	1330-1530	17.8-18.5	38.3-39.7	23.4	71.8
July 16	1000-1600	10.5-11.0	22.8-27.5	15.0	57.6
*July 21	1400-1500	17.0	23.9-23.9	23.7	92.2
July 23	0930-1130	10.4-10.9	22.5-24.4	14.7	57.4
Sept. 16	1130-1600	12.4-12.7	22.2-25.6	15.7	61.3
	1600-1930	12.7-12.9	24.7-25.6	15.5	59.3
Sept. 23	1000-1200	6.5- 7.2	15.6-17.2	10.6	47.0
	1800-2200	7.2- 7.6	10.8-18.3	10.6	48.4
Sept. 23 & 24	2200-0230	6.6- 7.2	9.2-10.8	10.3	51.4
Nov. 8	1500-1900	7.1- 7.4	12.5-17.2	11.4	52.3
Nov. 9	1100-1300	5.0- 5.4	11.4-12.2	9.80	47.1
Nov. 10	1400-1630	5.4- 5.6	11.1-11.1	10.1	53.2
Dec. 6	2000-2230	2.3	(-6.9)-(-4.2)	6.33	42.5

*Overcast Sky

TABLE II

RADIATION VALUES FOR THE TOTAL SKY AND APPROPRIATE DATA FOR THE WAVELENGTH REGION 9.25 TO 10.0 μ

Date	Time	Humidity	Temp. (°C)	$\underline{R}^{S}_{1-2}(\Sigma)$	$\underline{R}^{S}_{1-2}(O_3)$
May 3 & 4	2300-0700	4.0- 4.3	1.7- 4.2	0.395	0.265
May 15	1150-1600	7.6- 8.4	18.9-21.7	0.630	0.292
	1850-2400	8.4- 9.1	11.7-21.7	0.629	0.287
May 30	1100-1830	8.4- 9.4	22.2-25.6	0.682	0.269
June 13	1400-1630	15.7-15.7	31.9-32.7	1.057	0.225
June 24	1000-1800	11.9-13.3	23.3-28.3	0.692	0.238
July 14	1330-1530	17.8-18.5	38.3-39.7	1.326	0.235
July 16	1000-1600	10.5-11.0	22.8-27.5	0.746	0.272
Sept. 16	1130-1600	12.4-12.7	22.2-25.6	0.694	0.255
	1600-1930	12.7-12.9	24.7-25.6	0.716	0.222
Sept. 23	1000-1200	6.5- 7.2	15.6-17.2	0.447	0.286
	1800-2200	7.2- 7.6	10.8-18.3	0.434	0.249
Sept. 23 & 24	2200-0230	6.6 - 7.2	9.2-10.8	0.475	0.240
Nov. 8	1500-1900	7.1- 7.4	12.5-17.2	0.468	0.219
Nov. 9	1100-1300	5.0- 5.4	11.4-12.2	0.371	0.217
	1400-1630	5.1- 5.3	12.2-12.8	0.366	0.216
Nov. 10	1400-1700	5.3- 5.6	10.3-11.1	0.396	0.239
Dec. 6	2000-2230	2.3- 2.3	(-6.9)-(-4.2)	0.315	0.229
Dec. 6 & 7	2330-0230	2.4- 2.4	(-8.1)-(-7.2)	0.321	0.241
Dec. 7	0220-0230	2.4- 2.4	(-8.9)-(-8.3)	0.314	0.242

TABLE III

RADIATION VALUES FOR THE TOTAL SKY AND APPROPRIATE DATA FOR THE WAVELENGTH REGION 12.5 TO 13.0 μ

Date	Time	Humidity (g/m^3)	Temp. ($^\circ C$)	$\underline{R}^S_{1-2}(\Sigma)$	$\frac{\underline{R}^S_{1-2}(\Sigma)}{\pi R^S_{1-2}(T_o)}$
May 3 & 4	2300-0700	4.0- 4.3	1.7- 4.2	0.225	22.7
May 15	1150-1600	7.6- 8.4	18.9-21.7	0.498	41.2
	1850-2400	8.4- 9.1	11.7-21.7	0.535	48.6
May 30	1100-1830	8.4- 9.4	22.2-25.6	0.631	49.3
June 13	1400-1630	15.7	31.9-32.7	1.000	70.4
June 24	1000-1800	11.9-13.3	23.3-28.3	0.718	54.8
July 14	1330-1530	17.8-18.5	38.3-39.7	1.142	74.2
July 16	1000-1600	10.5-11.0	22.8-27.5	0.645	49.4
Sept. 16	1130-1600	12.4-12.7	22.2-25.6	0.687	53.7
	1600-1930	12.7-12.9	24.7-25.6	0.698	53.7
Sept. 23	1000-1200	6.5- 7.2	15.6-17.2	0.341	29.5
	1800-2200	7.2- 7.6	10.8-18.3	0.397	35.1
Sept. 23 & 24	2200-0230	6.6- 7.2	9.2-10.8	0.411	38.8
Nov. 8	1500-1900	7.1- 7.4	12.5-17.2	0.481	41.5
Nov. 10	1400-1700	5.3- 5.6	10.3-11.1	0.314	29.5
Dec. 6	2000-2230	2.3	(-6.9)-(-4.2)	0.147	17.6
Dec. 6 & 7	2330-0230	2.4	(-8.1)-(-7.2)	0.150	18.6

TABLE IV

RADIATION VALUES FOR THE TOTAL SKY AND APPROPRIATE DATA FOR THE WAVELENGTH REGION 11.5 TO 12.0 μ

Date	Time	Humidity (g/m^3)	Temp. ($^\circ C$)	$\underline{R}^{S}_{1-2}(\Sigma)$	$\frac{\underline{R}^{S}_{1-2}(\Sigma)}{\pi \underline{R}^{B}_{1-2}(T_o)}$
May 3 & 4	2300-0700	4.0- 4.3	1.7- 4.2	0.081	7.3
May 15	1150-1600	7.6- 8.4	18.9-21.7	0.301	23.0
	1850-2400	8.4- 9.1	11.7-21.7	0.306	26.4
May 30	1100-1830	8.4- 9.4	22.2-25.6	0.410	29.7
June 13	1400-1630	15.7	31.9-32.7	0.793	51.2
June 24	1000-1800	11.9-13.3	23.3-28.3	0.460	30.5
July 14	1330-1530	17.8-18.5	38.3-39.7	0.938	55.2
July 16	1000-1600	10.5-11.0	22.8-27.5	0.434	28.8
Sept. 16	1130-1600	12.4-12.7	22.2-25.6	0.459	33.3
	1600-1930	12.7-12.9	24.7-25.6	0.485	34.4
Sept. 23	1000-1200	6.5- 7.2	15.6-17.2	0.186	15.0
	1800-2200	7.2- 7.6	10.8-18.3	0.202	16.7
Sept. 23 & 24	2200-0230	6.6- 7.2	9.2-10.8	0.204	18.1
Nov. 8	1500-1900	7.1- 7.4	12.5-17.2	0.281	22.8
Nov. 10	1400-1700	5.3- 5.6	10.3-11.1	0.130	11.4
Dec. 6	2000-2230	2.3	(-6.9)-(-4.2)	0.039	4.4
Dec. 6 & 7	2330-0230	2.4	(-8.1)-(-7.2)	0.041	4.9

TABLE V

RADIATION VALUES FOR THE TOTAL SKY AND APPROPRIATE DATA FOR THE WAVELENGTH REGION 10.75 TO 11.0 μ

Date	Time	Humidity (g/m^3)	Temp. (^oC)	$\underline{R}^S_{1-2}(\Sigma)$	$\frac{\underline{R}^S_{1-2}(\Sigma)}{\pi R^B_{1-2}(T_o)}$
May 3 & 4	2300-0700	4.0- 4.3	1.7- 4.2	0.022	4.3
May 15	1150-1600	7.6- 8.4	18.9-21.7	0.121	17.7
	1850-2400	8.4- 9.1	11.7-21.7	0.122	22.8
May 3 0	1100-1830	8.4- 9.4	22.2-25.6	0.156	21.5
June 13	1400-1630	15.7	31.9-32.7	0.328	39.8
June 24	1000-1800	11.9-13.3	23.3-28.3	0.171	22.6
July 14	1330-1530	17.8-18.5	38.3-39.7	0.400	44.7
July 16	1000-1600	10.5-11.0	22.8-27.5	0.179	24.0
Sept. 16	1130-1600	12.4-12.7	22.2-25.6	0.186	25.4
	1600-1930	12.7-12.9	24.7-25.6	0.194	26.3
Sept. 23	1000-1200	6.5- 7.2	15.6-17.2	0.063	9.8
	1800-2200	7.2- 7.6	10.8-18.3	0.069	10.9
Sept. 23 & 24	2200-0230	6.6- 7.2	9.2-10.8	0.068	11.7
Nov. 8	1500-1900	7.1- 7.4	12.5-17.2	0.095	14.8
Nov. 10	1400-1700	5.3- 5.6	10.3-11.1	0.038	6.4
Dec. 6	2000-2230	2.3	(-6.9)-(-4.2)	0.012	2.8
Dec. 6 & 7	2330-0230	2.4	(-8.1)-(-7.2)	0.012	2.9

TABLE VI

RADIATION VALUES FOR THE TOTAL SKY AND APPROPRIATE DATA FOR THE WAVELENGTH REGION 8.0 TO 8.5 μ

Date	Time	Humidity (g/m^3)	Temp. (^oC)	$\underline{R}^S_{1-2}(\Sigma)$	$\frac{\underline{R}^S_{1-2}(\Sigma)}{\pi R^B_{1-2}(T_o)}$
May 3 & 4	2300-0700	4.0- 4.3	1.7- 4.2	0.181	20.6
May 15	1150-1600	7.6- 8.4	18.9-21.7	0.430	33.5
	1850-2400	8.4- 9.1	11.7-21.7	0.432	34.7
May 30	1100-1830	8.4- 9.4	22.2-25.6	0.548	39.3
June 13	1400-1630	15.7	31.9-32.7	0.896	54.5
June 24	1000-1800	11.9-13.3	23.3-28.3	0.628	43.6
July 14	1330-1530	17.8-18.5	38.3-39.7	1.077	58.5
July 16	1000-1600	10.5-11.0	22.8-27.5	0.598	42.6
Sept. 16	1130-1600	12.4-12.7	22.2-25.6	0.732	52.3
	1600-1930	17.7-12.9	24.6-25.6	0.704	49.2
Sept. 23	1000-1200	6.5- 7.2	15.6-17.2	0.332	27.8
	1800-2200	7.2- 7.6	10.8-18.3	0.341	29.7
Sept. 23 & 24	2200-0230	6.6- 7.2	9.2-10.8	0.364	34.8
Nov. 8	1500-1900	7.1- 7.4	12.5-17.2	0.410	34.4
Nov. 10	1400-1700	5.3- 5.6	10.3-11.1	0.289	26.9
Dec. 6	2000-2230	2.3	(-6.9)-(-4.2)	0.137	18.7
Dec. 6 & 7	2330-0230	2.4	(-8.1)-(-7.2)	0.136	19.4

BIBLIOGRAPHY

Adel, A. Astrophys. J. 103, 19 (1946).

______. Astrophys. J. 105, 406 (1947).

______. Cent. Proc. Roy. Meteor. Soc. London, p 5 (1950).

______. "Effective Radiation Temperatures of the Ozoneosphere Over New Mexico." Geophysical Research Papers No. 2 (1949).

Benedict, W. S., Claasen, H. H., and Shaw, J. H. J. Res. Nat. Bu. Stan. 49, 91-132 (1952).

Butler, C. P. "On the Exchange of Radiant Energy Between the Earth and Sky." NRL Report 3984, June 11, 1952.

Herzberg, G. Infrared and Raman Spectra of Polyatomic Molecules. (D. Van Nostrand Company, New York, New York, 1945), p 274.

Lowan, A. N., and Blanch, G. J. Opt. Soc. Amer. 30, 70 (1940).

Shaw, J. H., Oxholm, M. L., and Claassen, H. H. Astrophys. J. 116, 554 (1952).

Strong, J. J. Frank. Inst. 232, 1 (1941).

______. J. Opt. Soc. Amer. 29, 520 (1939).

Compendium of Meteorology. Am. Met. Soc., Boston, Mass., 34-49 (1951).

"Instruction Manual, Infrared Spectrometer, Model 12c." Appendix (The Perkin-Elmer Corporation, Glenbrook, Connecticut, 1950).

AUTOBIOGRAPHY

I, Raymond William Sloan, was born in Wakeeney, Kansas, March 12, 1923. I received my primary and secondary education in the laboratory schools of the Emporia State Teachers College, Emporia, Kansas. I received undergraduate training at the Emporia State Teachers College for a period of two and one half years and at Kansas State Teachers College, Pittsburg, Kansas, from which I received the degree Bachelor of Arts in 1944. In 1950 I received the degree Master of Science from the Ohio State University. Since 1950 I have served in the capacity of a research associate for the Research Foundation of the Ohio State University while completing the requirements for the degree Doctor of Philosophy.